Process design for high throughput Laser Powder Bed Fusion

Alex Gullane, MEng

Thesis submitted to the University of Nottingham for the degree of Doctor of Philosophy

September 2022

Abstract

Laser Powder Bed Fusion (LPBF) suffers from modest build rates. A powder bed component typically requires many hours to produce; hence for LPBF to become time and cost effective, batch sizes are limited to especially low volumes. By reducing build times, components can be realised much faster and it is possible to increase the number of components for which LPBF remains economical, in turn broadening the scope of applications for which the technology is viable.

LPBF has received growing attention in industry for significant benefits when compared with traditional manufacturing methods, namely high geometrical design freedom and sub-millimetre local process control. The latter, however, is seldom exercised within the literature, whereby authors typically adopt a single set of laser parameters to consolidate a component. This one-size-fits-all approach solely satisfies one metric, most commonly mechanical performance, while failing to accommodate other beneficial metrics such as manufacturing productivity. By harnessing the local process control possible through LPBF, a given component can be optimised for multiple metrics simultaneously.

The work in the present thesis exploits these process design freedoms, by varying parameters within sub-volumes of components to achieve the optimal part for both service conditions and manufacturing productivity. This involves prioritising mechanical strength in areas of structural significance and high volumetric build rates in areas of low structural significance. In theory, a component with similar mechanical behaviour to that seen in standard LPBF parts can be built with reduced time and cost. In practice however, this method is yet to be investigated and the boundaries between sub-volumes are yet to be understood.

Two methods have been highlighted, in which build times can be significantly reduced. These are coarser layer thicknesses, and Hot Isostatic Pressing (HIPing) of shelled components. Used in isolation, each incurs a notable reduction in mechanical properties. However, these techniques are introduced to LPBF parts as sub-volumes, enabling the remaining volume of the components to be fabricated by standard laser processing parameters to maintain mechanical properties, while still benefitting from reduced build times.

An initial study demonstrates parts can be additively built using multiple layer thickness regions with similar ultimate tensile strength (1110 - 1135 MPa) and elastic moduli

to standard LPBF specimens. Varying penalties to ductility were observed, depending on layer thickness and interface design (elongation to failure reductions up to one-third in the most extreme case). New pore formations were discovered along the interface between sub-volumes that were understood to dominate failure.

In the following study, XCT revealed that sub-volume interface orientation has a great effect on porosity formation along the boundary, with interfaces perpendicular to the substrate experiencing the largest pore formations, while interfaces parallel to the substrate experienced no additional porosity. Realtime evidence was observed that these defects lead to fracture at the interface. By combining pre-test XCT and Focus Variation data of fracture surfaces, a novel 3D reconstruction technique has been demonstrated, enabling post-mortem evaluation of additively manufactured parts and tracking of pore deformation during subsequent mechanical testing.

The final study designs and tests new-class laser scan strategies, to enable the laser to raster back and forth between regions of varying parameters, changing parameters both instantaneously and using a ramped region, as well as using secondary rework passes. Rework passes were successful in halving the number of interfacial pores, however, the introduction of laser vectors that pass through sub-volumes continuously presented new pore formations at parameter increment planes. HIPing of semi-hollow specimens achieved high density material with only a small volume of < 10 µm pores and superior ductility. Both methods were effective in significantly increasing productivity, however, each presented notable issues in part quality when characterised for porosity using XCT and mechanical performance by way of fatigue testing.

Build times can be reduced as much as 31.2% and 34.6% using coarse layer or shelled regions respectively, while still dedicating at least a quarter of the component volume to optimal parameters to maintain part performance. It is also possible to increase annual profits by one-third by adopting this method – this may increase or decrease depending on the size and number of builds. By producing entirely shelled components with coarse layers and using a post-process HIP treatment to enclose the void, it is possible to reduce build times by up to 76% and increase annual profit by 259%.

Publications

- A. Gullane, S. Faron, J. W. Murray, C. J. Hyde, S. Sankare, A. Evirgen, and A. T. Clare, “Failure modes in dual layer thickness Laser Powder Bed Fusion components using a novel post-mortem reconstruction technique,” Additive Manufacturing, vol. 59, November 2022, doi: 10.1016/j.addma.2022.103186
- A. Gullane, J. W. Murray, C. J. Hyde, S. Sankare, A. Evirgen, and A. T. Clare, “On the use of multiple layer thicknesses within laser powder bed fusion and the effect on mechanical properties,” *Mater. Des.*, vol. 212, p. 110256, Dec. 2021, doi: 10.1016/J.MATDES.2021.110256.
- Clare, A. Gullane, C. Hyde, J. W. Murray, S. Sankare, and W. W. Wits, “Interlaced layer thicknesses within single laser powder bed fusion geometries,” *CIRP Ann.*, Mar. 2021, doi: 10.1016/j.cirp.2021.03.001.

Acknowledgements

I wish to express my gratitude towards my primary supervisor, Prof. Adam Clare, for guiding my development as a researcher and for providing sage, expert advice day and night. Thank you to my secondary supervisors, Dr Chris Hyde for sharing his invaluable mechanical and materials knowledge and continued affirmations, and finally Dr James Murray for routinely making additional efforts to guide myself and my research.

I am incredibly grateful to my industry supervisors, Dr Simon Sankare and Dr Alper Evirgen, with my sponsor company, Oerlikon AM GmbH. The expertise and advice of Simon and Alper has ensured industry-relevant and greater quality research. Our relationship has also allowed me to hone my professional skills. Thank you to both Oerlikon and EPSRC for their financial contributions to my project, enabling me to conduct the research and provide a fantastic PhD experience.

Thank you to the wealth of technical staff that have provided invaluable advice, time and training during my PhD. Namely Mark Hardy, Martin Roe, Alex Jackson-Crisp, Jason Greeves, Richard Homer, Kieran Orange and many more.

Lastly, I am forever grateful to my parents for their unwavering support during my PhD and all other endeavours. I hope to make them proud.

Table of Contents

List of Figures

List of Tables

Abbreviations

AM	Additive Manufacturing
BCC	Body-Centred Cubic
CAD	Computer Aided Design
DED	Directed Energy Deposition
DMLS	Direct Metal Laser Sintering
EBPBF	Electron Beam Powder Bed Fusion
EBSD	Electron Backscatter Diffraction
EDM	Electrical Discharge Machining
FVM	Focus Variation Microscope/Microscopy
HCP	Hexagonal Close-Packed
HF	Hydrofluoric (acid)
HIP	Hot Isostatic Pressing
ID	Identification
LPBF	Laser Powder Bed Fusion
MHD	Magneto-Hydro dynamic
PBF	Powder Bed Fusion
PSD	Particle Size Distribution
SEM	Scanning Electron Microscope/Microscopy
SLM	Selective Laser Melting
STL	Stereolithography (file type)
UTS	Ultimate Tensile Strength
XCT	X-ray Computed Tomography

Nomenclature

s_c	total build laser vector length of coarse layer region
s_f	total build laser vector length of fine layer region
t_{build}	total build time
t_{wiper}	time taken to recoat the powder bed
v_c	coarse layer laser scan speed
v_f	fine layer laser scan speed
h	hatch distance
l	layer thickness
N	number of layers
P	laser power
v	scan speed
VED	Volumetric Energy Density

1 Introduction

Laser Powder Bed Fusion (LPBF), also commonly referred to as Selective Laser Melting (SLM) or Direct Metal Laser Sintering (DMLS), is a metal additive manufacturing technology introduced in the 1990s. The technology makes use of a laser optics system to fuse select regions of a preplaced bed of powder feedstock. Once the select areas have been fused for the current layer, the build platform is lowered by a nominal layer height and recoated with the next powder layer to be processed by the laser. LPBF is typically reserved for low volume, high value components, for which it remains more economical than traditional methods of manufacture. Powder bed fabrication has received growing attention in industry for a wealth of benefits over traditional manufacturing techniques. Namely:

- Geometrical design freedoms that are impossible through subtractive or formative manufacturing, such as internal lattice structures and cooling channels, owing to layer-by-layer build up of component geometry.
- Local process control to impart varying characteristics such as microstructure, mechanical properties and surface roughness, owing to high level control of laser parameters.
- Technology that is immediately ready to produce a design with simple slicing of 3D part files.
- Technology that is capable of producing custom components at no additional cost or time, since any part file can be sliced and loaded to an LPBF machine with relative ease.

Consequently, LPBF is subject to a multitude of research topics within the field. The literature has highlighted the key limitations of the technology, and these limitations have prevented researchers and industry from realising the full potential of LPBF. The primary limitations consist of:

- Variable and anisotropic microstructure leading to poor repeatability in part performance.
- Process-inherent porosity that causes poor repeatability in part performance.
- Slow volumetric build rates as each laser pass and each layer increments to the order of tens-of-microns to manufacture components to the order of centimetres.

Due to focussing on the issues above, and being limited by the process functions available in proprietary software, the literature seldom explores the high-level local process control available in LPBF. This control can be used to vary process parameters in different areas of single components for optimisation for both application and production, instead of opting for a 'one size fits all' single set of parameters for the entire part volume (the predominant approach in the literature). Exploiting the use of variable parameters within parts can be a powerful technique in addressing one the primary limitations of LPBF: slow volumetric build rates. By discretising components into sub volumes, based on areas of high versus low mechanical requirements for a given application, process parameters can be optimised for both production rate and mechanical performance. Volumes with high mechanical requirements can be processed with optimal parameters for mechanical properties, whereas volumes with low mechanical requirements can be optimised for high build rates while maintaining acceptable mechanical properties. In theory, a component of similar performance can be produced in a fraction of the time.

The present thesis aims to explore the viability of discretising LPBF components into sub volumes of varying processing conditions, introducing coarse layer thickness regions and shelled regions while still maintaining optimal parameters for performance in necessary volumes. This allows for significant increases in build rates while reserving the same material properties in areas of high stress concentration.

1.1 Aims of Thesis

The initial aim of the present thesis is to establish the viability of producing LPBF components comprised of sub-volumes, processed using combinations of standard processing conditions, coarse layer thicknesses, and shelled regions to be enclosed by hot isostatic pressing. Once the method is proven valid, the following aims are to produce a detailed characterisation of the interface among sub-volumes and use this information to inform a further process adaptation to improve the mechanical performance of the components. Lastly, the thesis aims to quantify the build time and cost savings that are possible through adopting the presented build methods.

To achieve these aims, the following three topics are presented, that comprise the three experimental chapters of the thesis:

i) Discretising LPBF components into disparate layer thickness sub-volumes to optimise productivity while maintaining mechanical performance.

While there is evidence in the literature of researchers adopting different layer thicknesses for the core of components compared with the shell, there are no studies in which core volumes are discretised into multiple layer thicknesses. Hence this study designs and manufactures single LPBF components produced with multiple layer thickness sub-volumes, in order to prove the concept and to characterise the resultant components. Test specimens are produced comprising of half standard layer thickness (30 μm) and half thicker layers (60 and 90 μm), as well as investigating different geometries at the interface for improved blending. Porosity, grain structure, tensile and fatigue properties are all compared with standard LPBF specimens to measure the quality of components. This initial study serves as the basis for the following chapters.

ii) Deeper understanding of interfaces between sub-volume regions, including pore formation and failure modes.

This chapter aims to further understand the interface among sub-volumes of the components, to identify the root cause of fracture and any issues identified in the initial study. Micro tensile testing with in-situ optical microscopy is used to focus on the interfaces at the microscopic level and observe failure modes, as well as XCT data to identify and characterise pores at the interface. Micro tensile testing allows for the role of individual defects to be tracked under tension and a novel 3D fracture reconstruction technique is demonstrated to further understand the role of said defects. This knowledge surrounding failure modes of the specimens is crucial to then inform a solution to improve the interface quality between sub-volumes in the following chapter.

iii) Improving interfaces through process design adaptations.

The lessons from the previous chapter regarding interface integrity and failure modes are used to target methods within the LPBF process that are likely to improve the performance of the test specimens in the initial study. Custom laser scan strategies are designed and manufactured with the aim of progressing from processing each sub-area in sequence, instead enabling laser vectors to continuously pass back and forth across the interface to process all areas in one continuous pass, changing parameters both instantaneously and ramping them across borders. A secondary rework pass is also investigated as a means to improve interface integrity.

As well as multiple layer thicknesses, this chapter aims to observe semi-hollow specimens that have been subjected to hot isostatic pressing to densify the hollow sub-volume. Similar techniques have been demonstrated by authors in the literature only for entire components. This study aims to maintain a fully-dense sub-volume for areas of complex geometry and superior properties, since shrinkage after hot isostatic pressing is detrimental to complex structures. This method mitigates some issues with laser processing using post-process heat treatment, however, there are new issues to address. Densification of entrapped powder in the hollow region and shrinkage relative to the solid region remains to be understood and is investigated in this study.

The final chapter also aims to quantify build time and cost savings possible through adopting the build methods. This section summarises the benefits of adopting coarse layer and shelled sub-volumes. The primary benefits are significant increases in volumetric build rates, and significant decreases in build cost. The achievable build time and cost reductions are calculated and presented.

1.2 Outline of Thesis

Details of LPBF and literature that is relevant to the work found in the present thesis is discussed in detail in chapter 2. The literature review briefly describes other metal additive manufacturing technologies before focussing on LPBF in detail. An account of the fundamental process is given, as well as relevant research findings regarding: laser-material interaction, porosity and process defects, residual stress, surface roughness and common feedstock materials. All work within the thesis has been undertaken using Ti6Al4V feedstock, hence section 2.3 discusses the microstructure and mechanical properties of LPBF Ti6Al4V, including heat treated material and comparisons to wrought material. Finally, the literature review describes various methods found in the literature, in which authors and machine suppliers have made efforts to improve the productivity of the powder bed process; including coarse layer thicknesses and hot isostatic pressing of porous material.

Chapter 3 comprises the methodology section, giving a detailed description of the experimental and characterisation techniques used to achieve the data presented throughout the thesis. This includes: materials selection, mechanical characterisations such as tensile, micro tensile and fatigue testing, as well as imaging techniques such as optical microscopy, scanning electron microscopy, focus variation microscopy and x-ray computed tomography.

Chapter 4 contains the initial research chapter, presenting the fundamental study for which the following research chapters are built on. This study describes a proof of concept, in terms of building LPBF components subdivided into volumes of disparate layer thicknesses and geometrical interfaces. Test specimens are characterised by way of porosity and grain structure analysis, and mechanical testing, to be compared with standard LPBF material.

Chapter 5 follows on from this study by examining the issues identified at the interface between sub-volumes in detail. Micro tensile testing with in-situ microscopy and XCT is used to track the role of interfacial defects and characterise failure modes of dual-layer thickness test specimens. Identifying the root cause of interfacial porosity is crucial to the inform a processing solution to alleviate the issues in the following research chapter.

The final experimental chapter (chapter 6) interprets the lessons from the previous study with regards to interface issues being a likely cause of laser scanning order and thermal history. In accordance, custom scan paths are designed and manufactured to enable laser vectors to pass continuously across the border, changing parameters both instantaneously and ramping parameters over a small region, as well as investigating laser remelting to reduce large pores. Semi-hollow specimens are also investigated, using hot isostatic pressing to enclose the hollow regions and examine the interface between solid and hollow post-HIP.

This chapter also summarises the benefits of adopting the presented build methods (introducing coarse layer and hollow sub-volumes to LPBF components). This is achieved by quantifying the build time and cost reductions by calculating total laser vector lengths, as well as collecting costing data from the literature and commercial suppliers and applying the data to the various build scenarios.

Lastly, chapter 7 presents the overall conclusions from the research presented in the thesis and discusses the future work premises that would allow the research topics to be progressed further. A flow chart describing the thesis structure and primary chapters (1 – 7) can be seen below in Figure 1.

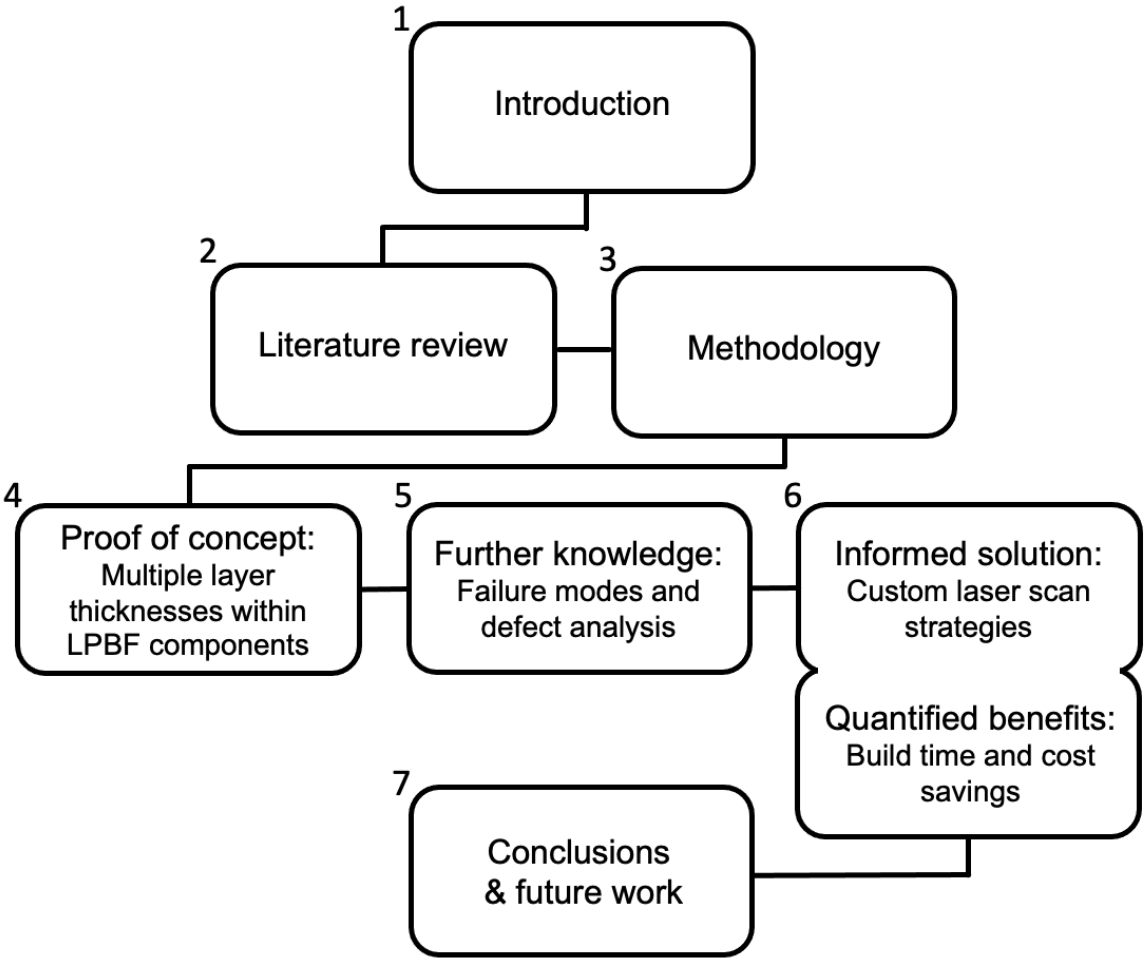

Figure 1 - Flowchart to show the structure of the thesis and the primary chapters

2 Literature Review

2.1 Overview of metal Additive Manufacturing technologies

Additive Manufacturing (AM) is the "process of joining materials to make objects from three-dimensional (3D) model data, usually layer upon layer, as opposed to subtractive manufacturing methodologies" according to the ASTM standard terminology for Additive Manufacturing (AM) technologies [1]. Three of the seven ASTM AM categories are regularly used to fabricate components from metals and metal alloys. These are Powder Bed Fusion, Directed Energy Deposition and Material Jetting (Metal Jetting); brief descriptions of the processes are described in the following sections.

2.1.1 Powder Bed Fusion

Powder Bed Fusion (PBF) is an AM technique used to fuse select areas of a bed of metal powder, building layer upon layer to achieve a final part. PBF requires a heat source, typically a laser (LPBF) or electron beam (EBPBF) coupled with an optical beam focussing system, to selectively melt local areas of a preplaced bed of powder material. A schematic for LPBF can be seen in Figure 2. The build platform is then dropped by a nominal layer thickness (30 – 60 µm), powder is deposited from a hopper and a wiper blade recoats the build platform with a new layer of powder to be processed. The process is performed under an inert atmosphere (typically Argon) to prevent oxidation of the material. Parts are limited in size since the standard system houses a 250 x 250 x 250 mm build volume. Component feature resolutions (such as lattice strut thickness) have been demonstrated as low as 150 µm [2]. LPBF is best suited to high value, small volume components with complex geometries [3], such as aerospace components [4] or biomedical implants [5], since feedstock is expensive (£250/kg for Ti6Al4V) and traditional manufacturing techniques are typically more cost effective for larger batch sizes. A comprehensive description of the LPBF process can be found in the Additive Manufacturing Handbook [6], and further details of laser interaction, materials considerations and process adaptations are discussed in sections 2.2 – 2.4 of the present literature review.

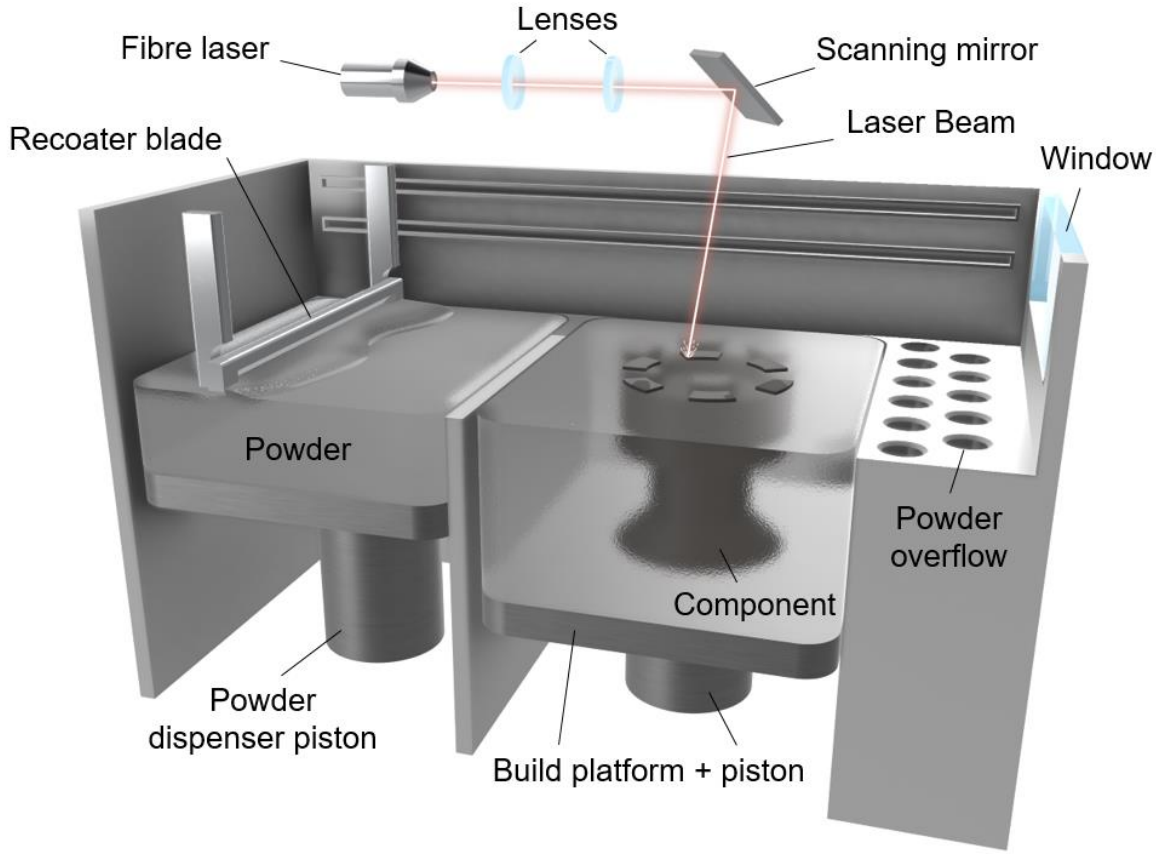

Figure 2 – Laser Powder Bed Fusion schematic, showing laser processing of a layer and recoating of the powder bed – the two repeating sequences that comprise the total build time

2.1.2 Directed Energy Deposition

Directed Energy Deposition (DED) differs from PBF, in that weld tracks are locally deposited as opposed to processing preplaced material. Powder or wire feedstock is fed into the path of a high power laser emitted from a nozzle. The nozzle is translated by a gantry system according to the 3D model data. The weld tracks are much coarser than PBF, meaning features are typically considered to the order of millimetres as opposed to hundreds of microns; however, this enables greater material deposition rates and, coupled with the gantry system, fabrication of parts to the order of metres are possible. Due to the size capabilities and versatility of DED systems, they can be used for in-situ repairs [7] and multi-material fabrication [8], however, the coarse resolution typically invokes a need for post processing. A common application of DED is typically joining of dissimilar alloys, since the technology offers the benefit of introducing gradience to joints as opposed to traditional joining methods. For example, tungsten is a highly suitable material for use in plasma-facing walls of nuclear fusion power plants [9], due to having a high melting temperature, high thermal conductivity, and excellent erosion resistance. Since tungsten is incredibly difficult to both machine and join to

dissimilar alloys, DED is currently being considered for joining tungsten to steel for armouring [10]. By controlling material feed rates, functionally graded materials can be manufactured. A detailed description of the DED process, component characteristics, challenges and applications has been produced by Svetlizky et al. [11].

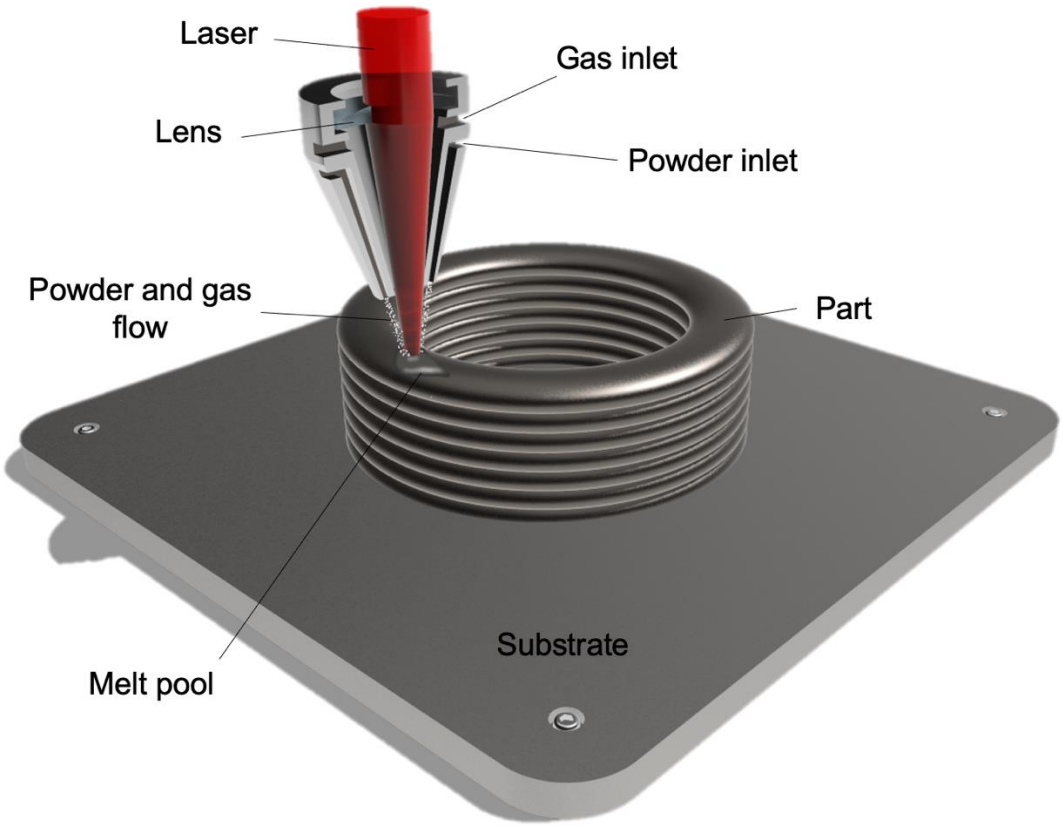

Figure 3 - Powder fed Directed Energy Deposition (Laser Engineered Net Shaping) process schematic

2.1.3 Metal Jet

Metal jetting involves deposition of molten metal droplets onto an appropriate substrate (such as copper onto a copper substrate), through either a drop-on-demand [12] or continuous [13] droplet nozzle. Typical systems use piezoelectric [14], pneumatic [15], or Magento-Hydro-Dynamic (MHD) [16] actuators to control individual droplet deposition. A drop-on-demand system with MHD actuation can be seen in Figure 4. Piezoelectric and pneumatic nozzles are generally limited to > 200 µm droplet diameter and < 200 Hz droplet generation, for materials up to 700°C melting temperature; however, MHD nozzles have been shown to exhibit droplets < 80 µm at frequencies up to 2kHz for materials up to 2000°C melting temperature [17], meaning these systems have been the subject of more research focus in recent years.

Due to operating in single droplets, metal jetting features superior resolution compared with LPBF, at the cost of deposition rate. Other benefits include the lack of pre and post processing, whereby molten metal is simply used as feedstock without the need for atomised powders and the as-built surface finish is typically acceptable. This method is also capable of multi-material fabrication through the use of multiple nozzles depositing disparate alloys. However, issues with droplet coalescence, residual stress and substrate adhesion are evident in the literature and remain to be well understood. A comprehensive review of the metal jetting process has been conducted by Ansell (2021)[18].

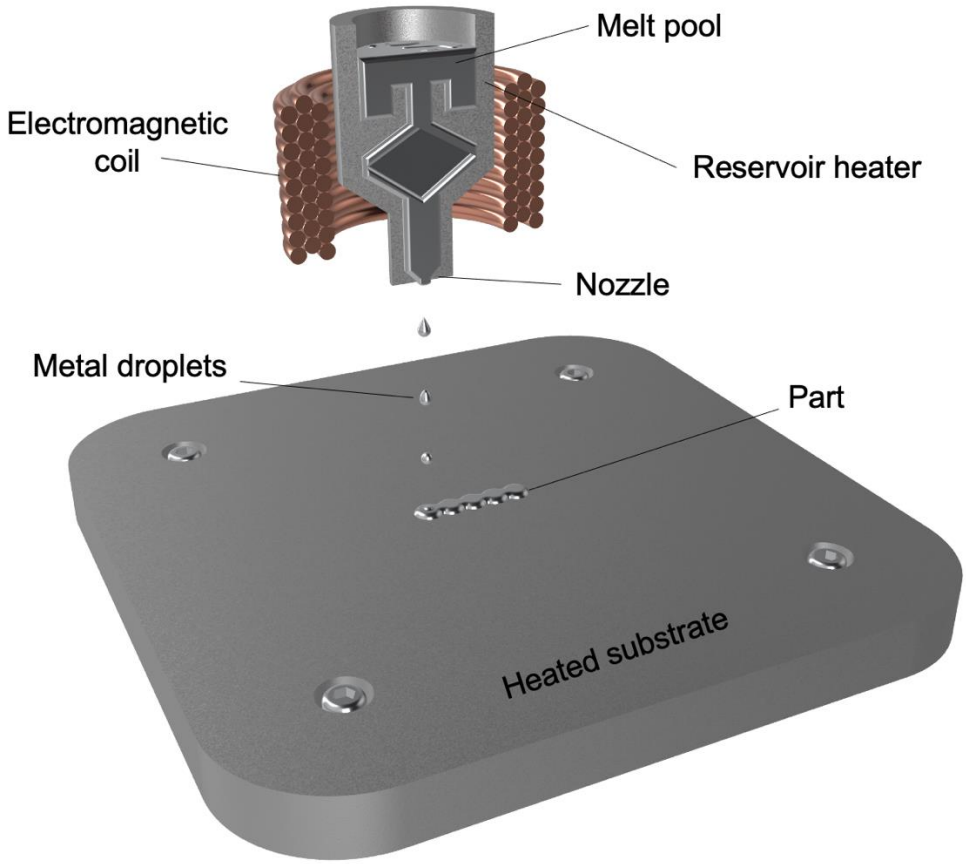

Figure 4 - Metal jetting process schematic

2.2 Laser Powder Bed Fusion

2.2.1 Laser-material interaction and consolidation

'Laser' is an acronym for Light Amplification of Stimulated Emission of Radiation, describing the process in which light or electrical current is used to excite atoms in an optical medium to release photons. The wavelength of said photons is selected by controlling the energy level of electrons within the atoms of the optical medium – electrons in the same state will release

photons of the same wavelength. Some of this light passes through a mirror at one end of the device to create the laser beam, while some light is reflected in order to stimulate further photon emission within the optical medium.

As light from the laser beam hits metal material, the photons interact with electrons 10 – 100 nm deep into the surface of the metal, transferring energy into the atomic lattice structure and increasing the temperature. This process serves as the basis for selective melting of material. The energy transferred to the material surface is greatly influenced by choice of material (the frequency with which electrons in the atoms vibrate), laser wavelength, and photon incident angle [19]. Influencing factors considered within Powder Bed Fusion are primarily laser parameters and powder feedstock characteristics [20]. Primary laser parameters consist of power, scan speed (or exposure time and point distance for pulsed lasers), spot size, beam focus and hatch distance; however, Yadroitsava et al. states there are up to 130 variables that can influence the properties of laser processed alloys [21]. Operators often retain the standard configuration of commercial systems for laser spot size and focal plane offset – typically an 80 µm spot diameter with a near-Gaussian beam distribution and a focal plane offset of 0 mm (i.e. in focus). This configuration is well-suited to achieving high feature resolution and deep melt pools with high energy density, however, larger spot sizes can be used to generate more stable, larger melt pools to achieve greater productivity through use of thicker layers and scan tracks, as energy is distributed over a larger area [22]. Similarly, the beam focal plane can be shifted above the powder bed to defocus the laser as it interacts with the material surface. This shallows and widens the beam profile to supply a more homogenous, lower intensity, energy input across the laser spot. This can also be useful for improving melt stability in higher energy scans [23], as well as improved surface roughness [24].

Complex physical phenomena occur during laser-powder interaction to incur and sustain a resultant melt pool, required to fuse successive tracks to form a layer, and successive layers to form a part. The laser interaction dictates the melt pool characteristics (size, morphology, stability)[25], which determines the microstructure and relative density of consolidated material, which in turn defines the mechanical properties of components. The amount of energy absorbed by the material will dictate the width and depth of the melt pool, playing a large role in whether pores form within the melt region or between successive laser passes; and the energy absorbed will also dictate the temperature and hence the cooling rate

of the melt pool, having a primary effect on the resultant microstructure and thus mechanical properties. Hence there is a wealth of literature focussing solely on laser absorptivity and melt behaviour.

The initial interaction between laser and powder enables high irradiance, as light experiences numerous reflections amongst powder particles within the small gaps of air. Once the powder melts and agglomerates, the laser forms a 'steady state' scan whereby light from the laser interacts with a moderately uniform melt pool for the remainder of the laser vector. Depending on the energy density, this steady state regime will exhibit either conduction or keyhole mode melting [26]. Conduction mode melting occurs in lower energy processing, below the boiling point of the material. In this mode, heat is predominantly transferred via conduction and a shallow melt pool is generated in which the depth is no more than half the width [27]. See Figure 5 for a comparison of conduction and keyhole mode melt pool geometries. Keyhole mode melting occurs in higher energy processing, in which the temperature exceeds the vaporisation point and a deep, keyhole-shaped depression forms in the melt pool, enabling further light irradiation through reflections and thus greater absorptivity [28]. This cavity allows the melt pool to penetrate much deeper into the material; however, a vapour plume is generated above the melt region that can shield and attenuate the laser, affecting steady state energy transfer to the melt pool and hence stability [29]. Higher energy densities can also ionise the vapour plume and create a plasma. For coarser layer thicknesses, such as those explored in the present thesis, keyhole mode melting is necessary to achieve sufficient energy transfer and penetration depth to consolidate a thick layer and fuse to the previous layer below. However, where possible, transition mode melting is often preferable and most prevalent in commercial systems, to strike a balance between melt depression stability and sufficient melt penetration depth. The transition from a shallow conduction mode depression to a deep keyhole cavity occurs around 1 ms after laser light interacts with the material surface, and can increase the melt penetration depth approximately 4 – 10 times [30].

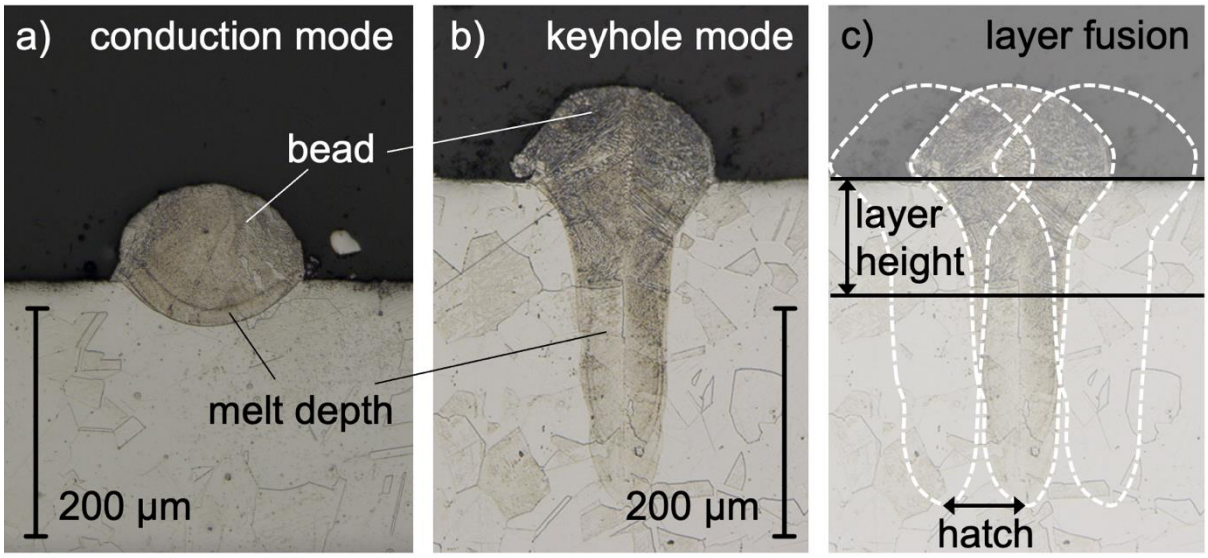

Figure 5 - Melt pool geometry for each melt mode: (a) conduction mode, (b) keyhole mode, and (c) an example of laser track and layer build up; adapted from [31]

Figure 5 also shows an example of how successive laser scan tracks and successive powder layers are used to build up component geometry (image c). Each laser pass translates by a nominal hatch distance, selected to ensure the overlap of the melt region remains below the layer height and thus all fresh powder is melted. Keyhole mode melting is often necessary to reach sufficient melt penetration depths, especially in the case of coarser layer thicknesses such as those explored within the present thesis.

Feedstock characteristics that impact thermal behaviour consist of particle size, particle size distribution (PSD) and the absorptivity and thermal properties of the alloy itself. Powder properties can have a great effect on the quality of LPBF parts in terms of density, mechanical performance [32] and surface roughness [33], since the powder geometry influences laser irradiation, affecting melt pool size and morphology. It is well documented that the large surface area provided by inclusion of fine particles aids laser absorption, while an excessive fraction of fine particles leads to agglomeration and poor flowability of the powder [34]. Flowability describes the propensity of granular material to flow smoothly [35], this is important for LPBF to recoat homogeneous layers of powder. LPBF powders are typically processed with an upper particle size limit close to the nominal layer thickness, so as to maintain flowability while including a maximum volume of fine particles for laser absorption - for example, a 15 – 45 µm particle size feedstock is relatively standard to process a 50 µm layer. In the case of coarser layers, there is scope for higher volumes of fine particles to improve laser absorption further, since the upper particle size limit can be raised (as high

as the nominal layer thickness) to maintain sound flow of powder. However, this has not been properly explored in the literature.

Particle size distribution refers to the volume fraction of particle sizes throughout the particle size range. Figure 5 below displays the various types of PSD available. The majority of literature uses feedstock with a Gaussian PSD [36], yet there are very few studies to explore multi-modal PSDs and where their use may be appropriate, despite the fact there is evidence in the literature of process and property enhancements. Farzadfar et al. used bi-modal IN718 powder to increase productivity by 10% and improve tensile strength, for example [37]. The inter-particle spacing was reduced by introduction of finer particles, which allowed for greater absorptivity. This meant less energy input was required to reach sufficient relative density and the lower energy input also gave rise to faster cooling rates, creating a higher strength material with a penalty to ductility. Tailoring feedstock properties has potential to allow researchers to explore process regimes outside of those that are seen routinely. Altering PSD is likely to improve consolidation of coarse layer thicknesses for example, since the upper limit of particle size can be increased to improve flowability while a similar method to Farzadfar et al. can be adopted to increase the volume of fine particles to enhance absorptivity. A comprehensive review article on powders for PBF has been produced by Vock et al. [38].

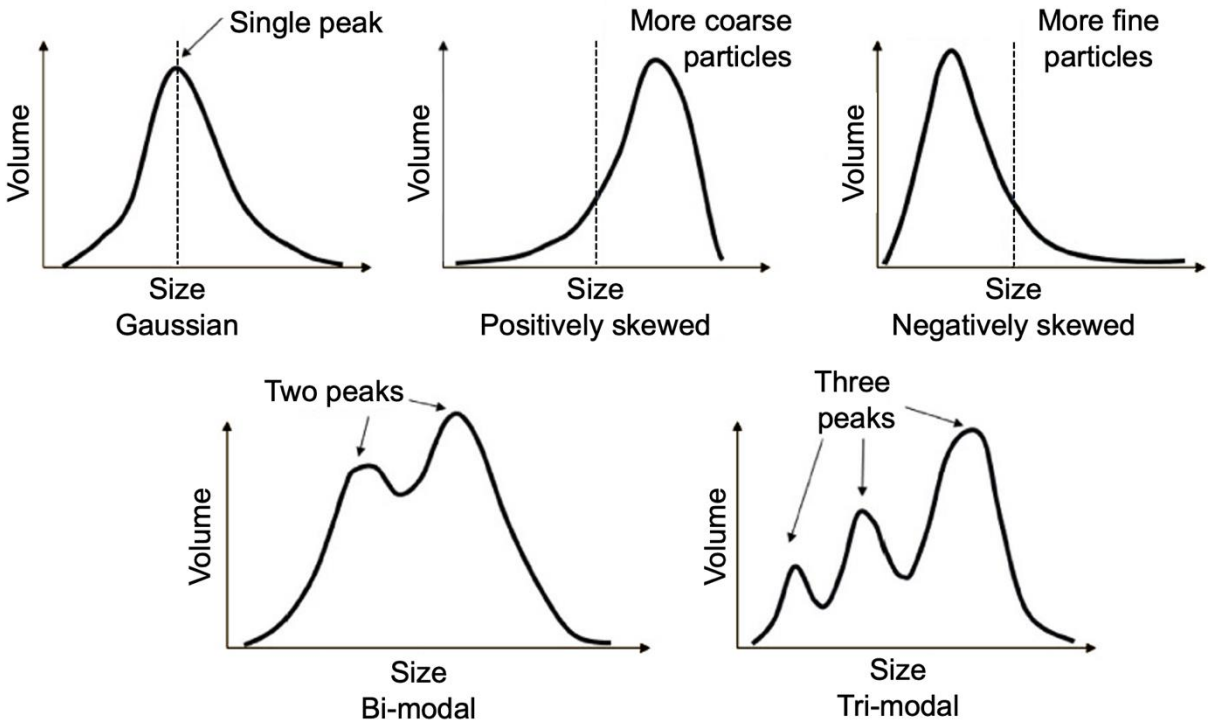

Figure 6 - Examples of different LPBF powder particle size distributions: Gaussian, negatively skewed, positively skewed, bi-modal and tri-modal [39]

The other feedstock characteristic that plays a crucial role in the laser-material interaction and consequent material consolidation is the absorptivity of the alloy itself. Energy absorption can vary as much as 50% throughout the LPBF process [40]. Initial absorption is high due to powder feedstock enabling lots of light reflections and essentially trapping photons in the powder bed; however, once the melt pool has been established and the laser vector is in a 'steady state', laser absorption is mostly dictated by the reflectivity of laser light from the melt pool. Highly reflective materials will reflect more light away from the melt pool surface, meaning the material absorbs less energy and proves more difficult to generate a stable and sizeable melt track. Typically this means greater energy input is required to offset lower absorptivity, however, this can cause further issues. Magnesium, for example, has low absorptivity and a low evaporation temperature, hence increasing the energy input often induces excessive vaporisation of material making it one of the most difficult metals to laser process [41].

Typically in LPBF, absorption is represented as the percentage or fraction of laser energy input that is absorbed by the material. Figure 7 below shows the absorptivity for common metals and how energy absorption varies as the angle of incidence of the laser changes, where normal incidence is equal to 0°. Titanium exhibits superior absorptivity when compared with other common LPBF materials, such as 316L stainless steel and nickel. This means titanium alloys are some of the more robust materials for LPBF processing, hence Ti6Al4V is selected for use in the present thesis to avoid materials processing issues and focus solely on process adaptations. Materials with high reflectivity and thus low absorptivity are aluminium, copper and magnesium. The low absorptivity values for aluminium are a prevalent issue in the literature, since aluminium is an incredibly common material with a wide range of applications. Aluminium is regularly alloyed with other elements to improve the absorptivity and thus 'printability' of a predominantly aluminium-based material - most commonly these are Al-Si alloys [42]. The scanning mirror will reflect the laser with small variations in angle to reach different areas of the powder bed. However, Figure 7 shows that the absorptivity values are very robust for low angles of incidence (< 30°).

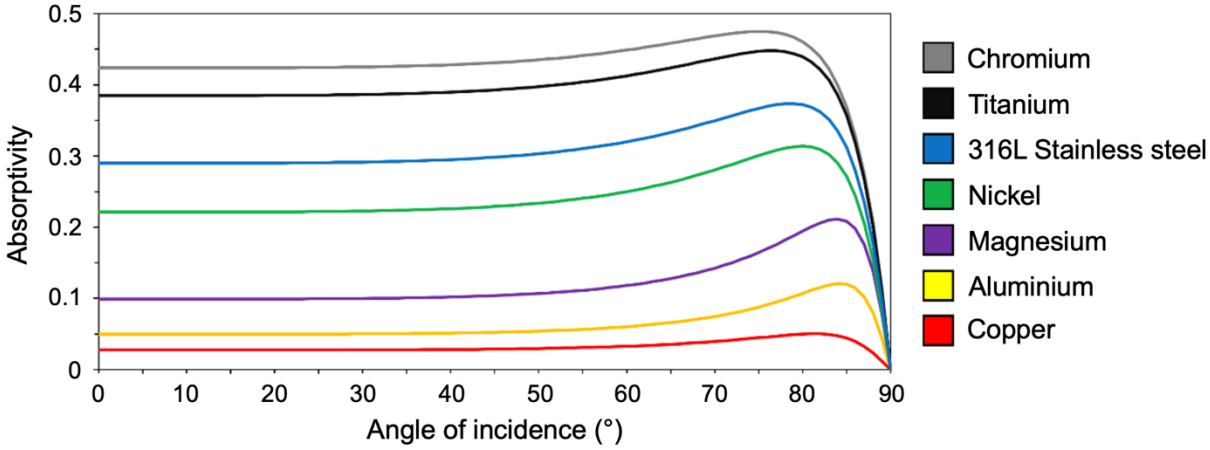

Figure 7 - The absorptivity of common metals, and the variance of absorptivity with photon angle of incidence, from Reynolds [43]

2.2.2 Porosity and process defects

As described above, the melt mechanisms inherent in the LPBF process are crucial to the quality of consolidated powder material. This requires sufficient melting and a stable melt pool by using parameters with a suitable volumetric energy density and normalised enthalpy, as well as appropriate melt pool dimensions for the nominal layer thickness and hatch distance. Volumetric energy density (VED) describes the energy supplied per unit volume of material and normalised enthalpy describes the ratio of energy density to melt enthalpy. The latter has been regularly reported as a crucial metric to maintain melt stability and size [44]. Optimal parameters are regularly reported to produce near-fully-dense material (>99.9% relative density). However, the melt pool is sensitive to small variations in process parameters such as laser power, scan speed, laser spot size, layer thickness and hatch distance, and voids within the consolidated material are increasingly evident when using sub-optimal parameters [45]. These voids are typically referred to as 'pores'.

Internal pores are one of the primary concerns preventing wider adoption of Powder Bed manufacturing. It is well understood that these defects can be responsible for initiating fracture under mechanical loading [46]. Such defects are particularly detrimental under cyclic loading [47], contributing to the poor repeatability exhibited by components built by LPBF. These internal defects fall into three categories: i) keyhole pores [48], ii) gas entrapment [49] and iii) lack of fusion [50].

Keyhole pores form when the recoil pressure from the laser allows molten material to travel upwards along the wall of a 'keyhole' during keyhole mode melting and seal over a large and misshapen cavity, as has been understood within the laser welding literature [51].

‘Recoil pressure’ refers to the vaporisation of material, after laser energy absorption, causing a recoil force at the surface of the melt region [52]. Keyhole pores typically form when excess energy is supplied from the laser to the melt pool and melt flow seals the lower region of the cavity, or when the keyhole briefly collapses, due to interference from a spatter particle (described below) for example. A depiction of keyhole pore formation can be seen in a CFD model in Figure 8, in which large misshapen pores are formed and size can increase with greater energy input. Typical LPBF keyhole pores range in diameter from 50 – 200 µm, however, extreme cases can reach 400 µm. Owing to their size, keyhole pores are significant stress raisers and have been shown to negatively impact mechanical properties [53]. There is little information in the literature compounding pore characteristics (size, morphology, angle, proximity) to define a ‘critical’ pore. These defects mainly form stochastically due to random keyhole collapses. Keyhole depressions can collapse due to brief moments of energy supply drops caused by laser shielding or attenuation from spatter and plasma. There are, however, examples of periodicity due to laser scan strategy phenomena. Martin et al. (2019) reported periodic keyhole pores repeating at the border of laser strategies as one vector ends and the successive vector returns in the opposite direction [54]. The galvanometer laser scanning mirror decelerates as it reaches the turning point, before accelerating in the opposite direction, allowing a large keyhole cavity to generate before subsequently collapsing. This phenomenon forms a keyhole pore and large variations in normalised enthalpy of the melt pool.

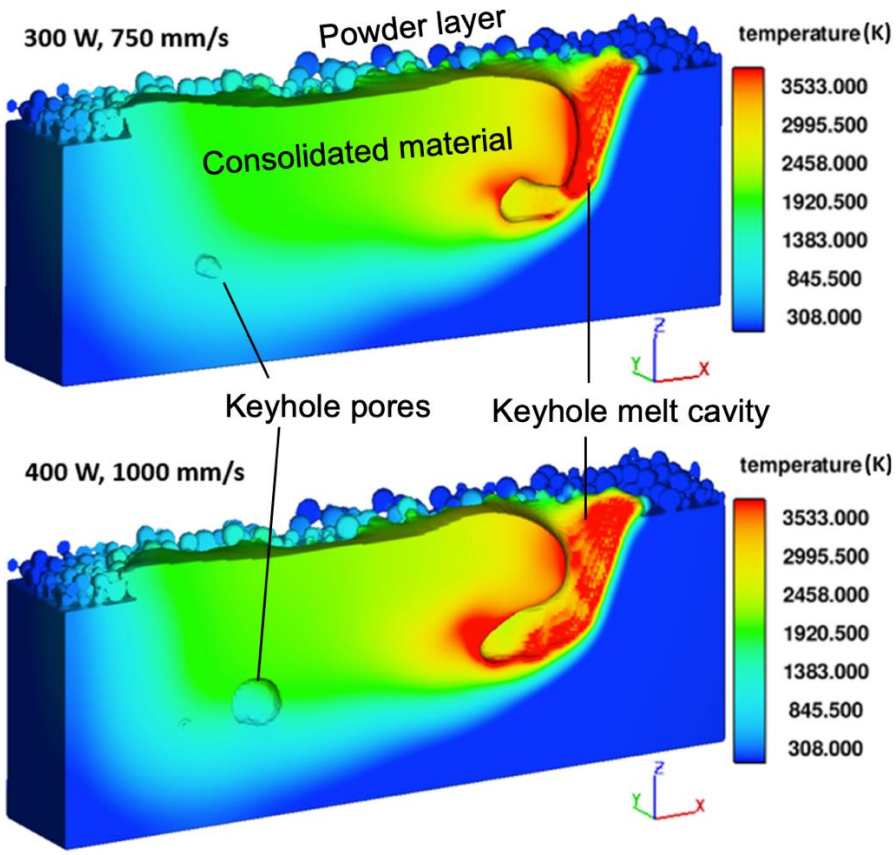

Figure 8 - Keyhole pore formation, taken from a CFD model by Shrestha et al. [55]*, including temperature colour scale to display the heat-affected zone*

Gas pores occur when pockets of air present in the powder feedstock are unable to escape the melt pool due to rapid cooling rates and hence small spherical pores remain within consolidated material [56] – see Figure 9 (b). Entrapped gas can occur during the gas atomisation process of the powder, in which a stream of liquid metal is expelled through a nozzle and is dispersed into droplets by an argon or nitrogen gas flow. Surface tension causes the droplets to adopt a spherical morphology and solidify rapidly, enabling some particles to solidify before gas has escaped [57]. These pores typically measure between 5 – 20 µm in LPBF [58]; they are of low concern since they are strictly a product of gas atomisation, whereby the plasma atomisation process does not yield gas pores [59].

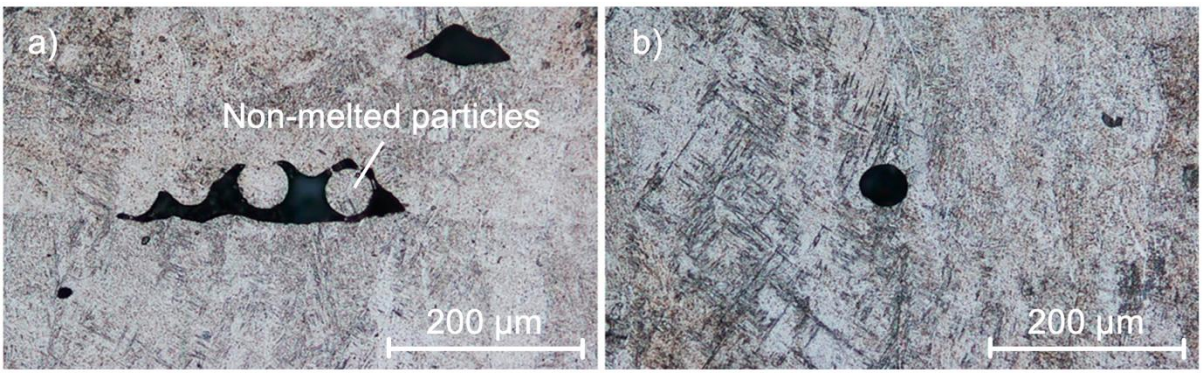

Figure 9 – Typical morphology of (a) a lack of fusion defect, and (b) a gas pore; adapted from [60]

Lack of fusion defects are attributed to insufficient energy causing a smaller melt pool, and in turn poor inter-layer fusion, primarily through coarse hatch distances providing insufficient overlap of the melt region between successive passes and leaving a pocket of non-melted material [61]; as well as spatter particles [62] shielding the powder bed from the laser. These defects exist between layers and exhibit a flat morphology with sharp edges, with the long axis parallel to the layer plane. Typically, they span to the order of hundreds of microns and can be seen displayed in Figure 9 (a). Due to experiencing small pockets of poor melting, partially sintered powder particles are often evident in regions that experience lack of fusion. While these pores are detrimental to mechanical properties, selecting an appropriate hatch distance or layer thickness is a simple solution and can be calculated from known melt pool dimensions or more complex fluid dynamics calculations [63]. The effect of pores on mechanical properties is discussed in more detail in section 2.3.2.

Spatter is material ejected from the melt pool by the vapour plume that forms as a result of material evaporation upon laser absorption, as is also commonly seen in laser welding [64]. In LPBF, a similar phenomenon occurs whereby clusters of partially melted powder particles or molten droplets, much larger than the original powder size [65], are dispersed across the powder bed. Particles can cluster before or after being ejected from the melt pool if the temperature remains high enough. Due to their large size compared with virgin powder, these spatter particles require greater energy input to melt and hence prevent sufficient melting in successive layers by shielding the laser, leading to lack of fusion defects [62]. Spatter is most prevalent in high laser power process regimes, since more pressure is generated in the vapour plume. Consequently, less aggressive melt regimes are the primary solution to reducing spatter generation. Figure 10 shows an example of thermal imaging used to trace dispersion of spatter particles and an example proximity map displaying the dispersion location on the

powder bed with respect to the laser spot. The recoil force of vaporisation is predominantly normal to the powder bed, however, a component of the force is oriented in the opposing direction to the laser scan. This is due to the laser interacting with the front-facing wall of the melt depression as the scan advances and the vapor plume bouncing back. Hence the majority of spatter particles are ejected in the wake of the laser. The majority of particles are also blown laterally by the inert gas flow across the build chamber, meaning areas of the powder bed closest to the gas inlet will be least affected by spatter induced defects. A recent description of the formation mechanisms of spatter has been produced by Young et al. [66].

Powder denudation porosity is a related phenomenon to spatter induced porosity. Denudation of powder describes the process in which powder adjacent to a scan track is removed from the powder bed. This leaves a deficit of powder in active areas of the bed that can potentially breed porosity. Powder denudation is predominantly caused by gas flow in the immediate vicinity of the melt pool. High speed vaporisation of material creates a pressure drop around the melt pool, after which the Bernoulli effect allows argon flow to be drawn in and entrain adjacent powder particles [67]. These particles are either added to the melt pool or ejected by the vapour plume.

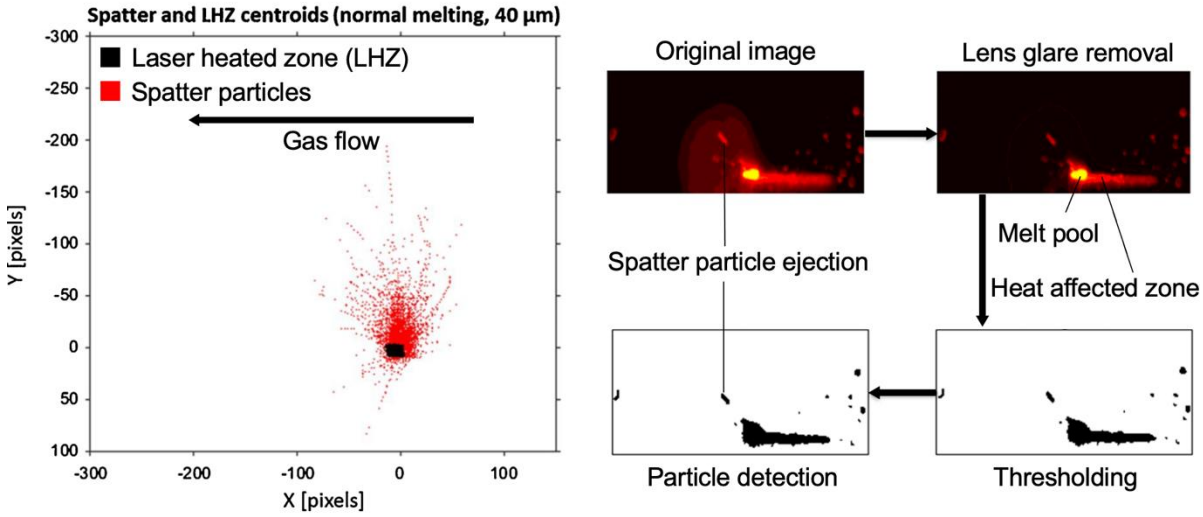

Figure 10 - Example of spatter dispersion on the powder bed with spatial proximity relative to the laser spot (left), adapted from [68]*; and an example of thermal imaging for in situ spatter detection, adapted from* [69]

Keyhole pores and lack of fusion can be seen in Figure 11 with trends in formation relative to energy input, whereby high power, slow scans produce keyhole pores and low power, fast scans produce lack of fusion. Despite porosity issues, through optimisation of process parameters, scan strategy and use of high energy densities, near fully-dense (99.99%) components have been demonstrated in AM processable alloys such as Ti6Al4V [70]. More

recently, Hot Isostatic Pressing (HIPing) has been demonstrated as an effective heat treatment to reduce the volume of pores in some LPBF alloys [71]. However, there is little understanding in the literature regarding where the trapped inert gas is redistributed, and the mechanical properties are altered significantly with grain transformation. It stands to reason that the gas must remain in the components after the HIP process, hence the post-HIP state of the gas pockets and their role on mechanical behaviour is an area of the literature that requires more understanding.

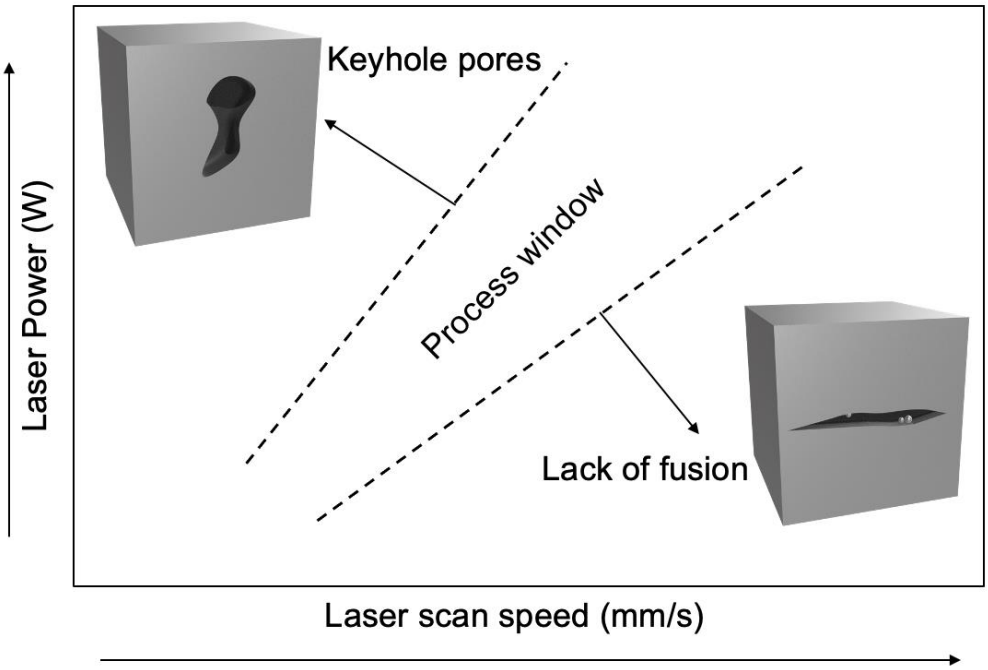

Figure 11 – Trends in pore formations as a function of laser power and scan speed

2.2.3 Residual stress

Residual stress describes stress within a material without any external loading and in a uniform temperature environment. The steep temperature gradients and very high cooling rates (10^3 – 10^8 K/s [72]) associated with LPBF give rise to large internal residual stresses [73] (100 – 500 MPa [74]), as the molten material solidifies and shrinkage is restricted by the solid material below. These stresses become worse as the number of layers increases [75]. Liu et al. reported that residual stress is greatest at the surface of the final layer, as well as increasing with scan track length and along the scan direction leading to an anisotropic stress concentration in components [76].

Residual stresses have been shown to approach the yield stress of some materials [77] (such as aluminium alloys with yield stresses < 300 MPa), often causing warping of

components in-process [78], occasionally to the extent of colliding with the recoater blade [79] or total build failure [80]. Hence short support structures are routinely built to anchor flat geometries down to prevent them from delaminating from the substrate, however, interlayer delamination remains a risk. Leuders et al. reported that, while cracks under fatigue testing typically initiate at pore locations, residual stress causes a greater rate of propagation when compared with wrought material and thus reduces fatigue life further [53]. This has also been reported elsewhere in the literature, providing evidence that crack growth rate and fracture toughness are also affected by the anisotropy of the residual stress state of the component [81]. The relationship between tensile residual stress and crack growth rate for LPBF components is approximately linear [82].

The literature shows that increasing energy density can reduce residual stress [83], since larger melt pools exhibit lower thermal gradients, which in turn produces less non-uniform shrinkage as the material shrinks more slowly with a deeper heat-affected volume. Preheating the build chamber has also proven effective in reducing residual stress, by decreasing thermal gradients [84]. Lastly, laser scan strategies can be engineered to reduce residual stress and directionality. Shorter laser vectors have been shown to alleviate internal stress of LPBF components, since longitudinal stress increases with scan vector length due to higher temperature gradients [85]. Scan rotation has been shown to reduce the directional warping in-process by rotating stress directionality each layer to avoid build up of stress in one particular direction [86]. Successive layers are routinely rotated 67° to achieve maximum misalignment of scan vectors throughout the layers, limiting preferential residual stress and grain growth.

2.2.4 Surface morphology

The surface morphology of PBF surfaces is formed as a result of several mechanisms: i) partially melted particles [87], whereby the heat affected zone outside of the melt pool captures partially sintered powder particles, primarily affecting all non-horizontal surfaces; ii) weld tracks [88], in which horizontal surfaces experience the peaks and troughs of each laser scan track due to surface tension of the melt pool causing rounding of the top surface, the extent of which depends on the nominal hatch distance; iii) staircasing [89], surfaces at angles $0 < \theta < 90$ to the substrate may only approximate linearity in increments equal to the nominal layer thickness, these steps comprise a rough surface; iv) balling [90], whereby surface

tension causes material in the melt pool to break up into periodic beads according to the Plateau-Rayleigh instability principle; v) dross [91], typically evident in overhangs, whereby the melt pool penetrates beyond the overhang surface and consolidates excess material; lastly, vi) surface porosity [92], pores captured in the surface of a part. Each type of LPBF surface roughness (except porosity found in section 2.2.2) can be seen in Figure 12 below.

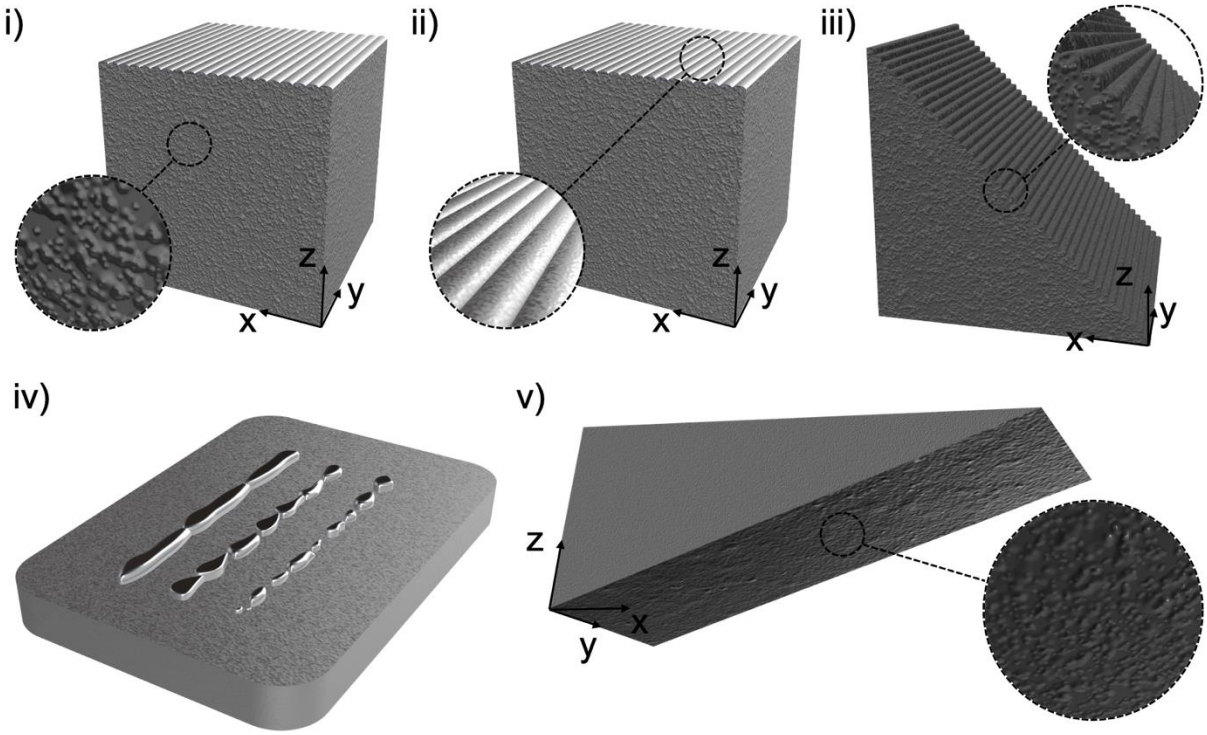

Figure 12 - 5 types of LPBF surface morphology: i) partially melted particles, ii) weld tracks, iii) staircasing, iv) balling, v) dross

In the as-built condition, surface roughness of LPBF components is poor – most studies report between 10 – 20 µm Ra values [93], however some studies range up to 50 µm [94]. While roughness can prove useful for cell regeneration in biomedical applications [95], rough surface features can act as crack initiation sites in many cases of mechanical testing in the literature, hence the skin laser strategy is generally optimised for surface roughness and parts are often machined post-build [93]. Naturally, machining surfaces post-build can be difficult, given the complex geometries often associated with AM techniques. Machining LPBF specimens to remove the rough surfaces has proven to significantly increase fatigue life and elongation to failure by removing surface defects that act as stress raisers to initiate fracture [96].

Laser power, scan speed, hatch distance, layer thickness and powder characteristics play a crucial role in surface roughness of LPBF parts [97]. High laser powers or slow scan

speeds result in a larger heat-affected zone, which is more likely to capture partially melted powder particles on vertical surfaces and thus increase surface roughness [98]; hence skin laser strategies often consist of lower laser powers compared with the volume strategy. However, high laser power also yields greater vapour recoil pressures that increases wettability of the melt pool to limit balling, as well as pressing the melt geometry downward to flatten the weld track morphology [99] – meaning the top surface roughness is reduced. Naturally, smaller hatch distances create greater overlap between laser passes to reduce weld track roughness, and finer layer thicknesses reduce roughness from staircasing. These parameters can be optimised for surface roughness, however, an optimal LPBF surface is typically still far rougher than a machined or cast surface and manufacturers elect to use post-process machining or electrochemical polishing [100].

2.2.5 Laser scan strategies

Scan strategy refers to the direction and pattern in which laser vectors process the select area of the powder bed, independent of process parameters. These scan strategies can provide local process control impossible through traditional techniques, enabling control over resultant microstructure [101], residual stress [102] and therefore mechanical properties. There are five scan patterns typically inherent in proprietary slicer software, used to discretise part files into layers for printing: i) raster, ii) meander, iii) offset-out, iv) offset-in, v) fractal [103]. Each of these patterns can be used to scan an entire area, or scan sub-areas sequentially in the form of a chessboard [104] or stripe pattern [105] to limit vector length and reduce residual stress. A chessboard strategy will discretise the area that requires processing into tiles of nominal size, whereby each tile is then processed individually in sequence. The stripe strategy performs similarly, using a stripe pattern that rotates along with the vectors each layer. This ensures laser vectors always scan the stripe width-wise to maintain short vectors and limit residual stress. Each strategy and an example of chessboard and stripes are pictured in Figure 13. A study by Parry et al. found that anisotropic residual stress is evident in LPBF components due to a non-uniform thermal history and that the effects were worsened as scan tracks became longer due to generating higher thermal gradients [73]. Cheng et al. demonstrated the ability of a chessboard strategy to combat this by maintaining shorter scan vectors to yield a more homogeneous stress distribution [106], where a similar premise can be achieved by the stripe pattern.

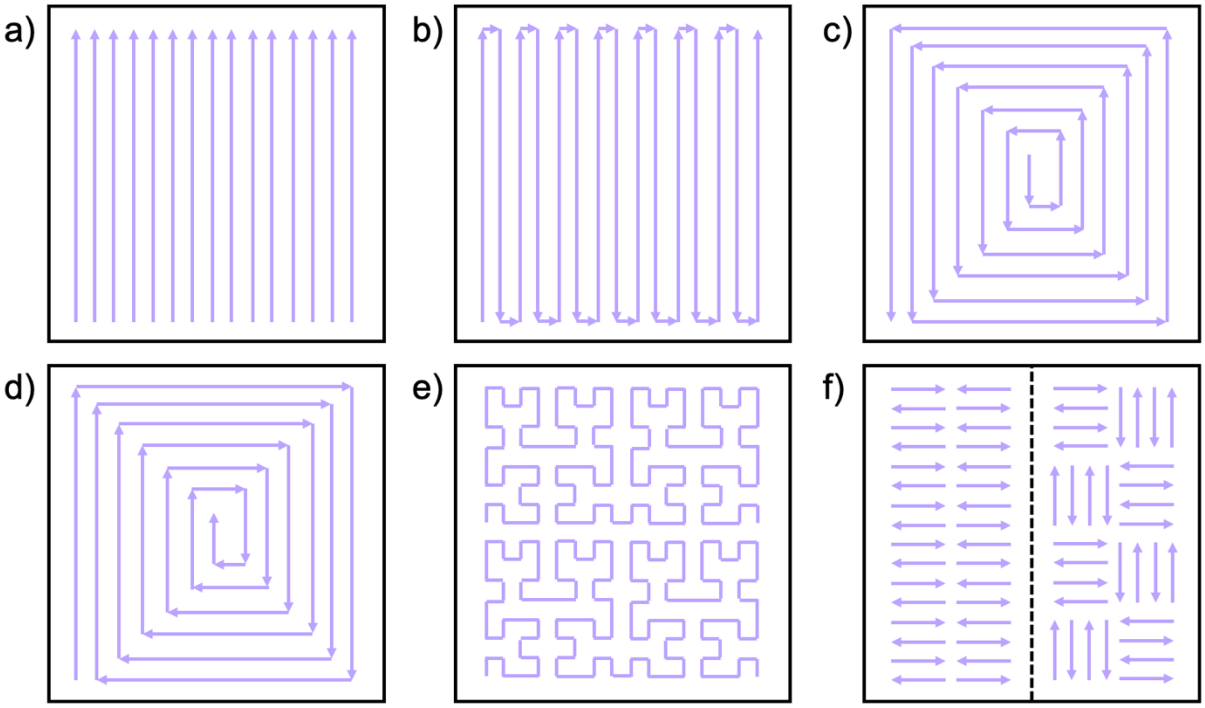

Figure 13 - Common LPBF laser scan strategies: a) raster, b) meander, c) offset-out, d) offset in, e) fractal, f) example of processing in stripes or checkerboard pattern

Some studies have investigated the use of laser remelting, in which a secondary pass of the laser is used to improve surface roughness or to reduce porosity. Kruth et al. were able reduce the top surface roughness (Ra) from 12 µm to 1.5 µm using laser remelting [107]. Since material has already been fused, parameters for remelting can be optimised for surface roughness without the need to consider material consolidation, enabling flatter melt pools and reduced roughness. Similar methods have been adopted to remelt already fused material to reduce the size of sub-surface pores. A blind method of this has been demonstrated by Qiu et al., in which the entire layer is rescanned with the intention of reducing pores that are likely to exist near the surface [108]. This was built on by Hirsch et al. in a study that locates individual pores near the surface and uses local laser 'rework' passes to target them, finding that large pores could be reduced in size significantly and small pores were relatively unaffected [109]. This is especially useful for future machine learning methods, whereby pores can be identified and fixed in-process. Due to the success of this research, laser rework passes are adopted in chapter 6 of the present thesis, as a method of reducing interfacial pores between component sub-volumes.

2.2.6 Common materials

The materials commonly used for LPBF feedstock are dictated primarily by the application and the 'printability' of the material. Printability refers to the ease with which the powder material can be consolidated to a near-fully dense component (99.9%), whereby materials considered to have poor printability are difficult to consolidate and will more than likely contain cracks or large pores. Common LPBF materials can be grouped into four categories: Titanium alloys, nickel-based super alloys, steel and ferrous alloys, other alloys. These categories are discussed in brief below:

i) Titanium alloys

Commercially pure titanium and titanium alloys are the second most researched LPBF materials after steels. Titanium is well-suited to laser processing, since it has relatively high absorptivity and the powder bed process removes some reactivity issues with liquid Ti when casting. The inert atmosphere and small, rapidly solidifying melt regions in LPBF are significantly less likely to capture interstitial elements that titanium is particularly sensitive too – oxygen, nitrogen, hydrogen and carbon. However, low thermal conductivity of titanium can induce large thermal gradients and give rise to warping of LPBF components. The most commonly researched Ti alloy is Ti6Al4V [110], however, there are also studies researching Ti6Al7Nb [111], Ti24Nb4Zr8Sn [112], Ti13ZrNb [113] and many more. Ti6Al4V is discussed in detail in section 2.3.

Ti alloys can routinely achieve high relative densities and are typically selected for airframe components due to its high specific strength, biomedical implants owing to high biocompatibility for bone approximation and cell regeneration, and marine applications due to high corrosion resistance.

ii) Steel and ferrous alloys

Steels received the majority of early attention within LPBF literature due to their wide range of applications and relatively low cost. Steels have good absorptivity and printability, hence relative densities of 99.9% have been routinely achieved since 2010 [114]. The most commonly researched alloy is 316L stainless steel [115], however, other studies investigate tool steels [116], maraging steels [117], and other ferrous alloys such as Fe-Ni [118].

Steels have a broad range of properties and hence also span a broad range of applications within LPBF, including lattice structures for biomedicine and aerospace [119] and ferromagnetic components for motors or generators [120].

iii) Nickel-based super alloys

Nickel-based super alloys are particularly difficult to work with by traditional means, given their high hardness and melting temperature. Hence LPBF presents a useful opportunity to produce net-shape components without the need for machining or casting. Inconel alloys have received the most attention in the literature and there are a examples of studies exhibiting sound process control to achieve high densities [121], however, some nickel-based superalloys are susceptible to cracking as a result of residual stress from the LPBF process. The most commonly researched alloy is IN718; other common alloys include IN625 [122] and Hastelloy X [123].

These alloys are primarily used for high temperature applications is combustion chambers, such as gas turbine blades in aerospace. This is due to having excellent fatigue strength at high temperatures and excellent corrosion resistance. LPBF enables these components to be fabricated with internal lattices to reduce weight, and internal cooling channels to reduce component operating temperatures.

iv) Other alloys

Outside of titanium, steel and nickel-based alloys, other metals of interest remain more difficult to laser process and, as such, have been grouped together. These include aluminium, copper, magnesium and tungsten. Aluminium and its alloys are especially prone to cracking when laser processed [124], and so many researchers have investigated Al alloys that are easier to process, such as AlSi10Mg [125], to improve the relative density of the material. Copper is highly reflective and has low absorptivity, as well as high susceptibility to oxidation during the LPBF process, making it difficult to achieve near-full densification. Hence many studies alloy small weight percentages of tin or chromium to improve the printability of copper, however, this reduces the thermal conductivity by approximately 10% [126]. Magnesium also has low absorptivity, and due to low evaporation temperature of magnesium, the high energy input required to offset the poor energy absorption causes excessive vaporisation and loss of material at the melt region [41]. Lastly, tungsten is especially difficult to machine or cast due to being exceptionally hard and having a melting temperature of 3422°C. Hence LPBF presents a new opportunity to melt small regions and

produce net-shape components. However, due to its high melting temperature, high thermal conductivity, high viscosity and brittle nature, the literature shows tungsten is difficult to laser process and most often produces crack and porous material below 90% relative density [127].

2.2.7 Productivity

LPBF productivity is often measured by 'build rate', defining the volume of processed material achieved per unit time. Build rate is generally represented in mm^3/s given the laser scan speed is typically measured in mm/s; however, cm^3/h is a more conceivable unit of measurement since components are typically to the order of centimetres and builds to the order of hours, hence data is represented in cm^3/h within this literature review. The build rate is a product of layer thickness, hatch distance and scan speed:

$$Build\ rate = lhv$$

Where l = layer thickness
h = hatch distance
v = scan speed

This equation also forms the basis for Volumetric Energy Density (VED), defining the energy supplied per unit volume of material. This serves as a useful metric to evaluate the combined effects of laser parameters on energy input, and is often used in literature to define an appropriate process window for a given alloy [128]. This value must remain within the appropriate process window to ensure quality material consolidation. The equation is stated:

$$VED = \frac{P}{lhv}$$

Where VED = volumetric energy density
P = laser power

LPBF benefits from greatly reduced times from part conception to part manufacture, in comparison to more conventional techniques. Traditional techniques such as die casting requires wait periods for the production of moulds and machining can involve complex tool paths requiring significant programming, whereas PBF simply requires a 3D part file. However, considering only the time to produce a component beyond initial setup time, LPBF is hindered by slow build rates. LPBF build rates vary greatly with process parameters and material requirements, falling within the range of 2 – 40 cm^3/h [129]; whereas a comparable wrought technique, such as high-pressure die casting, is likely to produce volumes to the order of tens of m^3/h.

Typical build rates for processing Ti6Al4V on an EOS M290 LPBF machine (EOS GmbH, Germany) with a 400 W laser are: 18 cm^3/h [130] for the low end of typical layer thicknesses (30 µm) and 32 cm^3/h [131] for the high end (60 µm). However, it is important to note that this method of build rate comparison does not factor in the time taken for powder recoating, where doubling layer thickness halves the number of layers and in turn approximately halves the collective time taken for recoating throughout the build. A typical powder recoating sequence takes 9 seconds, meaning hours of an LPBF build is dedicated to recoating across thousands of layers. Thus, processing with thicker layers is a powerful method of increasing productivity – discussed in greater detail in section 2.4.3 among other methods of LPBF productivity enhancements in section 2.4.

2.3 Laser Powder Bed Fusion Ti6Al4V

The experimental work within the present thesis focuses on process and process design modifications, hence it was necessary to select a relatively robust, well researched LPBF material to minimise any difficulties with materials processing and characterisation. This enabled confidence that any characterisation of process modifications was indeed a result of the process method and not due to material consolidation issues. Ti6Al4V was selected, as a well-researched and well-processed alloy.

Ti6Al4V is an α + β phase titanium alloy, meaning there are two distinct types of atomic bonding and arrangement present. The alloy comprises 5.5 – 6.75% Aluminium, 3.5 – 4.5% Vanadium, < 0.4% total Oxygen, Nitrogen, Carbon, Hydrogen, Iron and Yttrium, with a remaining balance of Titanium [132]. There is a wealth of LPBF research using Ti6Al4V feedstock, owing to a high strength-to-weight ratio, fracture toughness, corrosion resistance and biocompatibility [133], as well as relatively robust laser processability compared with other materials – aluminium alloys are notoriously difficult to process due to high reflectivity and cracking issues [134], for example. The applications are primarily in aerospace, for use in jet engines and airframe components [135], and biomedicine for bone implants, due to its biocompatibility [136]; however, there is some recent research into marine applications [137] due to its corrosion resistance.

2.3.1 Microstructure

The mechanical properties of Ti6Al4V are primarily dictated by the microstructure (i.e. present phases and grain structure), and the microstructure is dictated by the production process coupled with any heat treatment.

Titanium forms in two crystalline structures: α-Ti in a hexagonal close-packed (HCP) atom arrangement when formed below the β transus temperature, and β-Ti in a body-centred cubic (BCC) atom arrangement when formed above the β transus temperature. Ti6Al4V manages to maintain both α + β at room temperature due to the inclusion of Aluminium and Vanadium acting as α and β stabilisers respectively. However, phase transformation of Ti6Al4V is heavily dependent on cooling rate during the manufacturing process and the rapid cooling associated with LPBF creates a microstructure different to those seen in traditional methods [138]. The rapid cooling of Ti6Al4V during the LPBF process causes decomposition of the β phase by a non-equilibrium martensite reaction, to form an α' martensitic phase that exhibits very fine acicular grains [139]. This martensite typically yields high strength, brittle material and can be beneficial in certain applications [140]. Since the finishing temperature for martensite transformation is below room temperature, some β still exists in as-built Ti6Al4V, leaving an α + β/α' phase alloy.

As the LPBF melt pool approaches the solidus line, a prior β phase transformation takes place. Once the temperature begins to drop below the β transus temperature, the α/α' phase is formed within the prior β grains. Columnar β grains dominate as-built LPBF Ti6Al4V microstructure, and the β grain size and morphology dictates the size and morphology of the α/α' laths, which in turn affects the material behaviour [141]. Electron Back Scatter Diffraction (EBSD), SEM and optical microscopy data have regularly shown in the literature that epitaxial columnar grain growth occurs parallel to the build direction and spans across a number of layers [142]. A typical prior β grain is roughly 1 mm long and 100 µm wide, however this varies significantly depending on process variables [143], whereas the α laths within the prior β grains are typically 3 µm wide and up to 50 µm long. Images of both prior β columnar grains and α/α' lamellae can be seen in Figure 14.

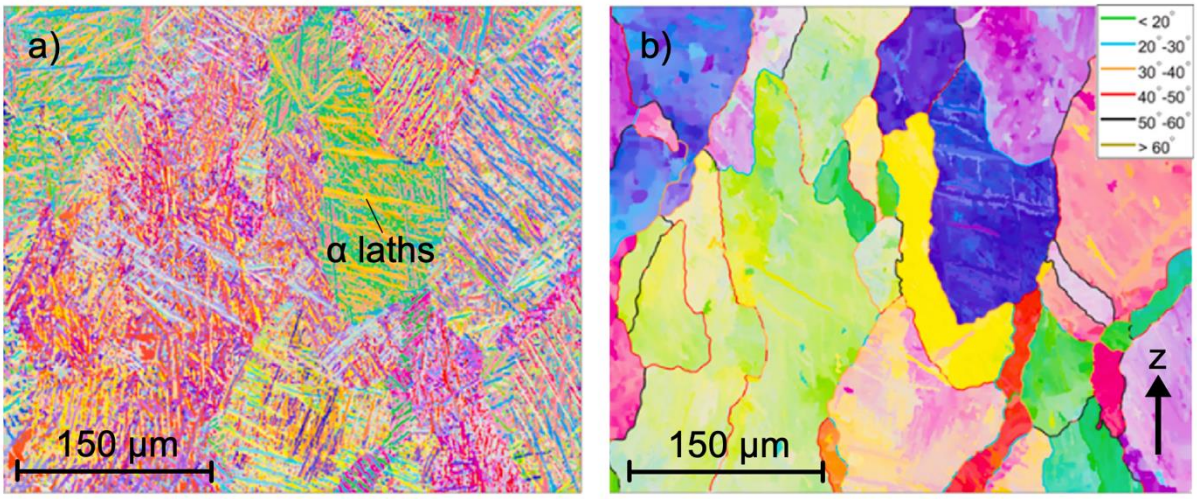

Figure 14 – EBSD images of as-built Ti6Al4V microstructure, adapted from [144]*: (a) α lamellae, (b) columnar prior β grains*

Grain size generally increases as the energy density of the laser source increases since the material spends more time at an elevated temperature, allowing more time for grain growth. During layer processing, the melt pool penetrates below into previously consolidated layers and grain coarsening occurs over a number of thermal cycles. Greater energy density yields greater melt penetration depth and hence more thermal cycles to generate grain coarsening, since a given layer will be remelted more times. This phenomenon can also play a role in producing varying grain size within different regions of a single component. For components with a large number of layers, the upper regions of the part will sustain higher temperatures for longer as the volume increases, due to the low thermal conductivity of Ti6Al4V, and hence there is more time at high temperature for grain coarsening.

The greater fraction of α' martensite phase found in as-built LPBF Ti6Al4V produces greater strength values than those of heat treated material with lower fractions. This strength comes from the fine lamellar microstructure of the martensite, however, the fine needle-shaped grains show very low plasticity and hence components are less ductile. Consequently, there is a wealth of literature investigating the heat treatment of LPBF Ti6Al4V to produce a microstructure with ductility close to that of wrought material, as well as reduce anisotropy and residual stress.

The heat treatment of LPBF Ti6Al4V can be divided into four common categories: i) stress relief below 700°C, in which the microstructure is unchanged but residual stress is reduced, ii) annealing below the β transus temperature (700 – 995°C), iii) annealing above the β transus temperature (> 995°C), and iv) hot isostatic pressing, below the β transus with the addition of extended pressure applied to the components before cooling.

There are many examples of stress relief in the literature that treat Ti6Al4V at 650°C for 1 – 2 hours, before allowing it to air cool [145]. This allows the entire component to reach an elevated temperature and cool at the same slower rate, producing a low thermal gradient that alleviates the residual stresses induced by high thermal gradients from laser processing. The literature agrees that heat treating below 700°C does not considerably alter the microstructure and hence material properties remain similar to as-built material.

Annealing below the transformation temperature results in decomposition of α'→α + β. Various temperatures between 700 – 900°C have shown the formation of lamellar α + β microstructure [146]. Increasing the temperature typically yields thicker α laths and agglomeration of precipitates in the β phase. Galarraga et al. also demonstrated that the duration of the heat treatment significantly affected α lath thickness, with 20 and 30hr treatments yielding 2.28 and 3.01 μm thick grains, compared with 0.66 μm as-built α laths [147]. It has also been shown that, below the transformation temperature, heat treatments produce similar microstructures regardless of cooling rate (air cooling, furnace cooling or water quenching) [148]. The coarser lamellar structure exhibits superior ductility at the cost of a reduction in strength.

Cooling rate has a significant effect on microstructure when annealing above the transformation temperature - often between 1000 – 1100°C. Furnace cooling, air cooling and water quenching result in α + β, α/α' + β and fully α' respectively. Annealing causes the full α' phase to transform to β phase, while the cooling rate dictates the final microstructure at room temperature. For example, rapid cooling by water quenching causes a new α' phase to form within new, equiaxed prior β grains [147]. In general, the greater presence of α' causes higher strength but more brittle material due to the finer lamellar structure.

Hot isostatic pressing (HIPing) is regularly studied as a method to enclose internal porosity within LPBF components, due to applying a uniform pressure to parts while at high temperatures – see section 2.4.2. Typically, parts are heat treated just below the transformation temperature at 900°C, before applying a pressure of around 150 MPa for 1-2 hours, followed by furnace cooling [149]. The microstructure is very similar to annealed Ti6Al4V at these temperatures, whereby the α' phase fully decomposes to form a lamellar α + β microstructure, with coarsened α laths roughly 2.5 μm thick. The primary difference is the reduction in pores and pore size possible through the HIP process [71], however, the applied pressure also has a negative effect on dimensional accuracy of the part. Due to α lath grain

coarsening, HIPed material experiences an increase in ductility with some penalties to strength, as well as improved fatigue life due to the reduction of pores that typically act as detrimental stress raisers under cyclic loading.

2.3.2 Mechanical properties

Due to the LPBF process forming atypical microstructures and defects in the form of porosity and residual stress, there are crucial differences between the mechanical properties of LPBF Ti6Al4V and wrought counterparts. Firstly, the introduction of α' martensite typically increases the strength of the material at the cost of reduced ductility [150]. Additionally, the as-built anisotropic grain structure yields unequal component performance when loaded in different directions [151]. Lastly, pores act as stress raisers under load and are regularly reported to initiate crack formation prematurely when compared with wrought material [152], after which the residual stress induced by fast cooling rates has been demonstrated to accelerate crack development since the material is essentially preloaded in tension [53].

The two most common mechanical testing techniques for LPBF Ti6Al4V are tensile testing and fatigue testing at room temperature. Fatigue testing is common since Ti6Al4V is often considered for components in active environments (aerospace components, bone implants) and knowledge of component service life under cyclic loading serves useful for such applications. Tensile testing is a quicker, easier, and necessary method to quantify the properties of LPBF Ti6Al4V compared with wrought material as well as other studies that have used different process parameters, machines and heat treatments. Figure 15 shows a violin plot of room temperature tensile properties collected from over 20 studies in the literature. Median values measure at 1165 MPa (range 960 – 1421 Mpa), 1016 MPa (range 664 – 1273 MPa) and 7% (range 1.6 – 12.7%) for ultimate tensile strength, yield strength and elongation to failure respectively. Large variation is evident in the data primarily due to variance in processing conditions, however, the violin plot is able to display the distribution of values found in the literature. Different machines, lasers and process parameters will produce significantly differing microstructure and porosity and thus yield disparate mechanical properties.

Table 1 - Tensile properties of as-built LPBF Ti6Al4V versus wrought Ti6Al4V

Condition	Avg. UTS (MPa)	Avg. Yield Stress (MPa)	Avg. elongation (%)
Wrought Ti6Al4V [153]	950	880	14
As-built LPBF Ti6Al4V [61], [110], [128], [140], [154]–[164]	960 - 1421	664 - 1273	1.6 – 12.7

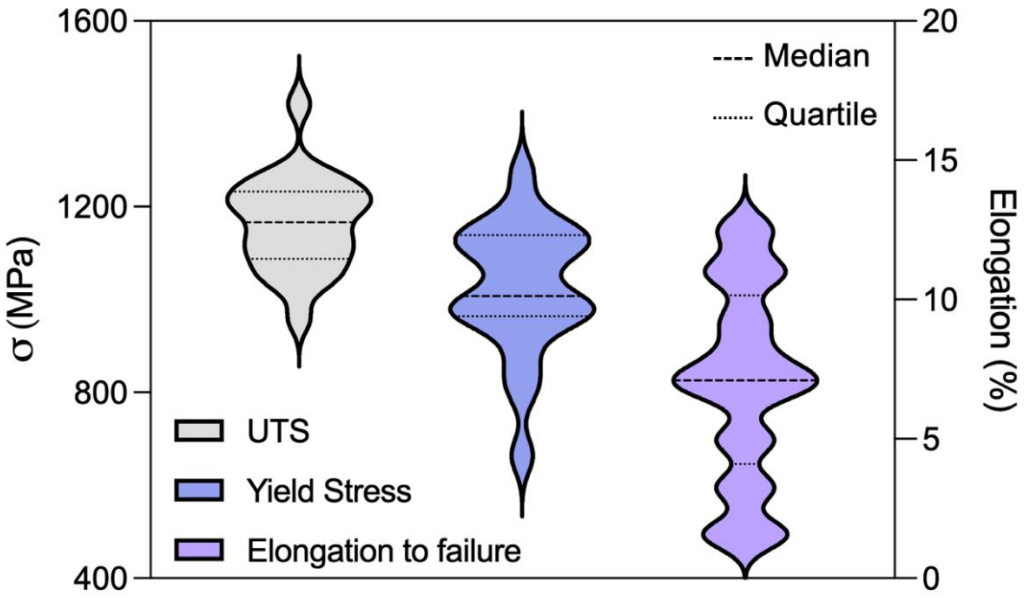

Figure 15 - A violin plot to show the distribution of 21 UTS, yield stress and elongation to failure data sets in the literature [61], [110], [128], [140], [154]–[164] *for as-built Ti6Al4V fabricated by LPBF*

Compared with wrought Ti6Al4V [153], the 21 data sets collected from the literature in Figure 15 for LPBF Ti6Al4V show a 22% and 14% increase in median UTS and yield strength respectively, mainly as a result of the fine acicular martensitic phase. However, the fine α' microstructure, and sometimes inclusion of oxygen contamination, results in a 50% reduction in elongation to failure and hence drastically reduced ductility. Ti6Al4V is incredibly sensitive to oxygen contamination and, since the LPBF process typically operates with some volume of oxygen (> 10 ppm), an increase in oxygen content is possible and is known to impose brittle behaviour on titanium [165].

Heat treatments are often selected to increase ductility. Stress relief is very commonly performed below 800°C. It has a limited effect on ductility since the temperature is not sufficient to cause significant grain coarsening – gaining roughly 1% elongation to failure at the expense of a small reduction in strength [166]. Annealing Ti6Al4V above 800°C has been

shown to drastically improve ductility through grain coarsening at a further penalty to strength. For example, Xingchen et al. were able to increase elongation to failure from 6% to 18% by heat treating at 900°C, while UTS fell from 1241 MPa to 945 MPa [166]. Further increases in temperature, below the transition point, caused decreases in both strength and elongation; whereas, above the transition temperature, a dominant α phase microstructure forms that yields poor elongation values (4%) and strength values over 20% lower than as-built LPBF Ti6Al4V.

Fracture typically occurs along both prior β and α grain boundaries, exhibiting ductile fracture surface characteristics in the form of a dimpled texture [167]. The columnar prior β grain orientation can influence crack formation, since cracks propagate preferentially along the long edge of the grains (intergranular as opposed to transgranular). This anisotropy contributes to causing different mechanical properties and crack growth rates when components are built in different orientations. Simonelli et al. reported superior ductility in specimens loaded parallel to columnar grain orientation (in the build direction) compared with those loaded perpendicular to columnar grain orientation [151]. However, each orientation yields similar elastic moduli, attributed to having a weak α' texture, where strong crystallographic texture can affect the modulus. While components loaded in the build direction exhibit superior ductility, Cain et al. have shown that residual stresses up to 200 MPa (forming dominantly in the build direction) accelerate crack growth in this build orientation by contributing to the applied load [81].

The fatigue properties of LPBF Ti6Al4V components are of particular interest to most manufacturers, since they are primarily considered for aerospace, automotive and biomedical applications – dynamic parts with long service life requirements. Due to stress raisers such as surface defects, internal pores and residual stresses, LPBF Ti6Al4V typically displays significantly shorter fatigue life than wrought counterparts [168]. Unlike tensile testing, the test parameters for fatigue testing vary significantly and often data is not comparable among some LPBF Ti6Al4V studies. Test parameters that vary in the literature are: i) loading direction, such as uniaxial, bending or torsional, ii) temperature, fatigue testing may be performed at elevated temperatures to simulate a service environment such as a combustion turbine, iii) stress cycle, a constant amplitude stress waveform is most commonly selected to apply cyclic load to a component, however, the minimum and maximum stress are at the discretion of the user; whereby a stress ratio of 0.1 achieves tensile cyclic loading and a stress ratio of -1

alternates tension and compression (these are the two most common choices), iv) frequency, the frequency of the stress waveform is also at the discretion of the user and can significantly affect the data – common values fall between 10 – 100 Hz depending on the loading direction.

Data has been collected from a number of studies in the literature that have conducted room temperature, uniaxial fatigue testing using a stress ratio R = 0.1. A violin plot has been generated to observe the range and distribution of fatigue limit collected from the literature, in both the as-built and HIPed condition (see Figure 16). HIPed specimens were included since HIPing is commonly used to repair defects with the intention of improving fatigue life and features in chapter 6. Only data from machined surfaces were collected, given that surface defects significantly reduce fatigue life and repeatability.

The median value of fatigue limit for as-built and machined specimens is 425 MPa (range 340 – 550 MPa) and the median value for HIPed and machined specimens is 570 MPa (range 430 – 690 MPa). When devoid of surface defects, fatigue fracture of LPBF components is typically found to be caused by pores or microstructural heterogeneities, and accelerated by residual stress [92].

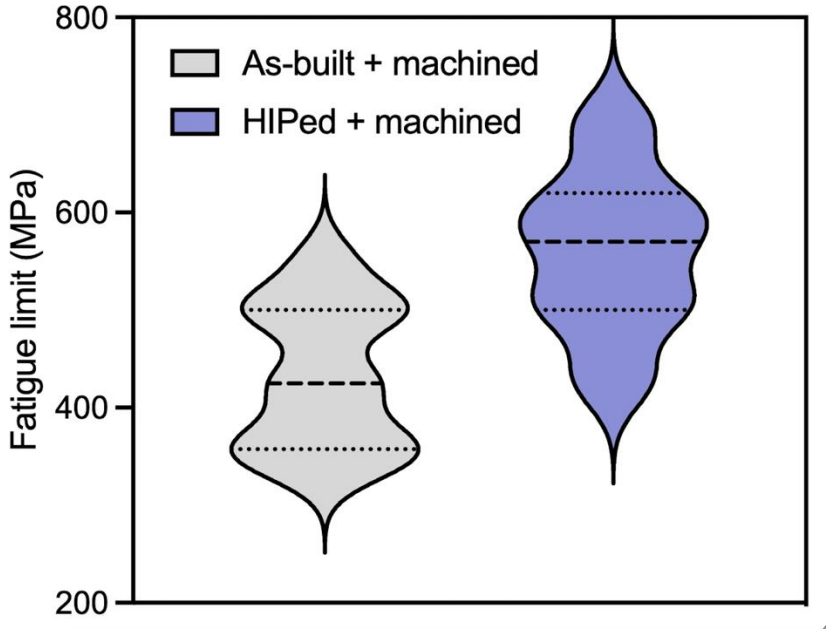

Figure 16 - A violin plot to show the distribution of high cycle fatigue limit for machined LPBF specimens, using a stress ratio of R = 0.1, in the as-built and HIPed condition across 17 studies [46], [53], [152], [159], [160], [169]–[176]

Internal pores and rough surface morphology (see sections 2.2.2 and 2.2.4 respectively) significantly reduce the fatigue performance of LPBF components by acting as stress raisers. For components with high relative densities (99.9% dense), poor surface finish can be more detrimental to fatigue life than pores [177], since the rough surface acts as

multiple stress points and behaves much like short cracks [178] - whereas internal pores act as single point stress raisers. Surface roughness issues can be resolved through machining or electrochemical or other polishing processes, however, a small fraction of internal pores will be evident in components and the impact on mechanical properties must be understood.

There are a number of studies investigating the effects of pore size on fatigue life of LPBF parts by engineering defects into component geometry [179]. However, many of these studies use geometrical design to achieve these voids and hence may behave differently to those that form via inherent melt pool phenomena. Both the literature and manufacturers are lacking threshold criteria when considering pore size, morphology, angle, frequency and proximity. While strict threshold limits are not yet commonplace, there are prevalent trends in pore behaviour that have been reported in the literature. For example, Murakami has stated that the cross sectional area of a defect, perpendicular to the loading direction, has a greater effect on mechanical response than the volume of the pore [180]. Fracture is most likely to occur at the largest pore, provided all pores have similar morphology; however, large aspect ratio lack of fusion defects can often dominate failure whereby the sharp edges accumulate very high stress concentrations, creating crack initiation sites.

2.4 Laser Powder Bed Fusion productivity enhancements

Compared with other AM techniques (Directed Energy Deposition for example), LPBF suffers from long build times owing to slower volumetric deposition rates, due to fine layer thicknesses, slow laser scan speeds and laser power limits [181]. Achieving greater throughput at no cost to the function or properties of a component is critical to the wider adoption of LPBF, and this area has been subject to significant research efforts. These efforts can generally be grouped into 4 categories: i) technology adaptations, introducing additional machinery to process faster or reduce inter-build turnaround, ii) process optimisation, to increase scan and recoating times within the confines of standard commercial LPBF machines, iii) post-build recovery, adopting fast scan methods and using heat treatments to repair the associated part defects, and iv) discretising components, dividing single parts into sub-volumes whereby some volumes maintain the required slower build rate but others can afford to utilise fast build rates.

2.4.1 Technology adaptations

Commercial quad-laser systems are now available to allow four times the laser utility and hence four areas of the powder bed can be processed simultaneously [182]. Large build volume [183], dual-hopper and automated powder reclamation [184] systems have all been introduced as methods of reducing time spent in between build cycles, by allowing greater component yield and reducing powder handling time respectively. These methods all aid in improving the economies of scale for LPBF, however at an increased cost and complexity of the process. Hence the work described in the present thesis explores novel techniques to increase productivity, solely available within the confines of a standard LPBF machine and at a reduced cost of operation.

2.4.2 Hot Isostatic Pressing porous material

Post process heat treatments can somewhat compensate for increased porosity associated with high build rate strategies. Herzog et al. knowingly tolerated poor relative densities when adopting high laser scan speeds, prior to Hot Isostatic Pressing (HIPing) to successfully reduce pores formed in the build process [131]. In this study, increasing the scan speed by 67% allowed the total build time to be reduced by 26% - the relationship is not directly proportional since recoating time is unaffected by scan speed. The high build-rate parameters produced components with 95% relative density, in which samples are rife with a combination of keyhole pores and lack of fusion. However, the HIP process was able to force the vast majority of these pores to close at high temperature, yielding a final part of 99.8% relative density. Du Plessis et al. took this concept further by producing shelled parts, i.e. with loose powder inside, relying on the HIP process to melt said powder and enclose the cavity [185]. XCT data showed HIPing was able to fully enclose the cavity and no pores were evident, however the data is limited by a voxel size of 5 µm. Additionally, the tensile response was very similar to specimens that were fully dense prior to HIPing. Only processing the shell of components allows for significantly reduced lasing time during builds. For the build produced for the study, a build time reduction of 12% was achieved; however, larger builds are likely to benefit more where larger volumes can be shelled.

This approach was not as successful, however, when specimens were subject to fatigue testing for shelled [186] or highly porous parts [187], where fatigue life suffered

significantly as a result. There is little evidence in the literature to confirm why the fatigue performance is poor, although it stands to reason there is likely a volume of small argon pores since the argon originally trapped prior to HIPing is unlikely to fully escape. There are also significant shrinkage factors to be considered when adopting this technique. In the case of du Plessis et al., the gauge volume shrunk by 10% and thicker volumes would shrink more given the greater ratio of powder-to-shell material. Additionally, some complex geometries associated with LPBF, such as internal lattices and cooling channels, are not appropriate for the HIP process, since the geometry is expected to morph drastically due to large shrinkage during the HIP process. Hence a solution to this issue is presented in chapter 6 of the thesis, in which semi-hollow components are subject to HIPing, enabling a solid region in areas of geometrical complexity and a shelled region in geometrically simple regions to reduce build time.

2.4.3 Layer thickness and variable layer thickness

It is possible to reduce build times within the confines of standard powder bed processing and without additional heat treatments, by selection of build parameters conducive to high build rates and accepting some penalties to mechanical performance. By increasing the layer thickness, a given component can be sliced into fewer layers that require processing and hence build times can be reduced. For example, a 30 mm build height sliced with 30 µm layers would require 1000 layers to be processed, and 1000 powder recoating cycles, whereas slicing at 60 µm layers only requires 500 layer scans and powder recoating cycles. In theory, build time can be halved in this manner. However, in practice, coarser layer thicknesses require slower scan speeds and hence time savings are slightly less than half.

Shi et al. used a 400 W laser to process at a nominal layer thickness of 250 µm, compared to a standard regime of typically 30 - 60 µm layers [188]. A build rate of 9 mm^3/s and relative density of 99.99% was achieved in 316L specimens through optimisation of process parameters. The ultimate tensile strength and yield stress featured at the low end of those described in the literature for LPBF 316L, however, the elongation to failure significantly improved. This is likely a result of the greater energy input required to consolidate a thicker layer producing slower cooling rates and thus more ductile material. Besides layer thickness, laser power, spot size and hatch distance can be varied to produce greater scan speeds. This

has been proven to reduce build time at the cost of dimensional accuracy, owing to the larger heat affected zone generated with greater energy input and a larger spot size [189].

Often, increasing layer thickness gives rise to reduced mechanical properties through introduction of porosity, whereby the high energy density required to consolidate a coarse layer induces high values of normalised enthalpy and thus less stable melt pools. This can lead to a higher fraction of keyhole pores and sometimes lack of fusion defects. For many applications where LPBF is considered, maintaining sound mechanical properties is crucial. A lack of porosity is the primary goal for attaining reasonable fatigue performance, for example. Hence manufacturers are generally unwilling to compromise component performance for productivity. As discussed in section 2.2.1, use of larger laser spot sizes (through beam shaping or through laser defocussing) has proven useful in establishing large melt pools with better stability that are suitable for coarser layers [23], however, scan tracks are often reported in the region of 600 µm in width [22], negating the feature resolutions afforded by LPBF whereby 200 – 300 µm thin walls are often used in lattices and heat exchangers.

There are scarce examples of researchers adopting multiple layer thicknesses within components to enable productivity increases while benefiting from finer layers in regions of interest. For example, De Formanoir et al. sought to avoid penalties to dimensional accuracy induced with coarse layers, by using a method called the 'hull-bulk' strategy. In which, the component shell was fabricated using a fine layer thickness to improve geometrical accuracy while the core was produced using a coarse layer thickness to increase production rate [190]. While this solves geometrical issues with high build rate parameters, it does not address the drop in mechanical performance associated with coarse layer thicknesses in the bulk material [191], and as such is still poorly suited to high performance part production. Hence the present thesis investigates using both fine and coarse layers in bulk regions of LPBF parts to maintain mechanical properties in volumes with high structural requirements and benefit from high throughput in volumes of low structural requirements. In this manner, LPBF components can be optimised for both performance and productivity simultaneously.

2.5 Research Gaps

The literature regularly cites the local process control enabled through laser processing as a primary benefit of LPBF, when compared with traditional manufacturing methods. However, the overwhelming majority of LPBF studies observe a single set of parameters for each component, selected solely to optimise one performance metric (most often mechanical strength), regardless of application or geometry. To fully exploit the design freedoms of LPBF, parameters should vary within sub-volumes of components to achieve the optimal part for service conditions and manufacturing productivity. This involves prioritising mechanical strength in areas of structural significance, higher volumetric build rates in areas of low structural significance, and considered surfaces for fluid dynamics or joining. Thus, LPBF components can be optimised for various performance metrics simultaneously.

Coarse layer thicknesses have been highlighted as an effective method to reduce build times by reducing the total number of layers required to produce a component. However, authors have reported penalties for use of coarse layers to mechanical strength, surface roughness, and dimensional accuracy. Experts in the field, such as de Formanoir, have highlighted the potential for combining both fine and coarse layer thicknesses to maintain superior part quality metrics associated with finer layers, while benefiting from the high build rates associated with coarser layers [190]. This study, however, uses fine layers to preserve surface roughness and dimensional accuracy, while tolerating a lesser bulk mechanical response from coarse-layer material. The present thesis builds on this by addressing the potential for discretising the bulk material into sub-volumes of both fine and coarse layer regions, whereby fine layers can be adopted in significant areas to maintain mechanical requirements and coarse layers can be used in insignificant areas to benefit from significantly reduced build times. Throughout the thesis, this method is established, characterised and developed further (chapters 4, 5 and 6 respectively).

HIPing of LPBF components containing cavities of varying proportions has also been identified as a method to increase build rates. HIPing has been shown to enclose pores and form parts with high relative densities. This has enabled experts, such as Herzog [131] and du Plessis [185], to adopt high build-rate laser strategies by tolerating porosity or designing shelled components, and relying on the HIP process to enclose the cavities post-process. In the case of both authors, the method successfully densified the components and produced

sound tensile properties; however, the fatigue life of the components was significantly reduced compared with standard LPBF processed material. Hence the present thesis builds on these studies by adopting a similar method to that described above for layer thickness, whereby components can be discretised into sub-volumes. In this manner, solid regions can be produced with standard LPBF processing to maintain fatigue properties in areas of high mechanical requirements and hollow regions can be produced in areas of lower mechanical requirements to significantly reduce lasing time, before HIPing to enclose the cavity.

The general principle of optimising LPBF components for both throughput and mechanical performance by discretising into sub-volumes can be seen in Figure 17 below. In the figure, a component exhibits a specific stress concentration for its application, using a Finite Element Analysis (FEA) model. Based on the stress response, the component is then sub-divided into volumes where it is crucial to maintain high mechanical performance, where build rate can be prioritised due to having lower material property requirements, and balanced volumes in between. In theory, a component that performs similar to a standard LPBF part can be produced in significantly less time. In practice, however, small discrepancies in material properties and fusion among the sub-volumes creates a new stress concentration, with higher stress experienced at the boundaries between regions (fourth image in Figure 17). Hence the present thesis seeks to characterise and understand both fabrication and the mechanical response of LPBF components such as these, with a key focus on the quality of fusion and fracture behaviour at the interface between sub-volumes.

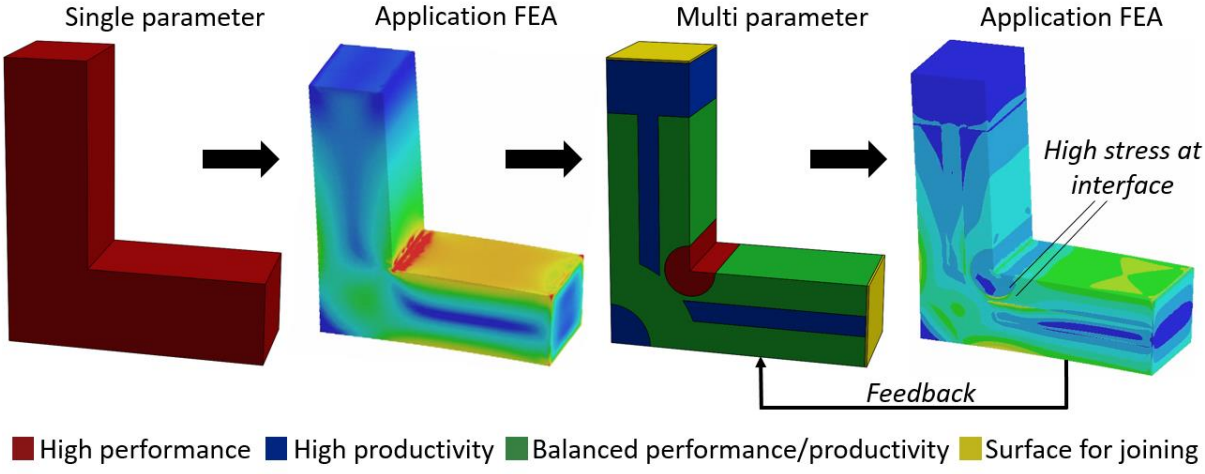

Figure 17 – An example of discretising LPBF components into distinct regions for a given application and the issues that arise at the interfaces between regions

Four areas have been identified to address the research gaps described above. They can be summarised as the following:

- The literature is yet to fully exploit local process control to optimise LPBF components for manufacture as well as part quality. There is evidence of varying skin parameters to improve surface roughness, however, authors have not explored the potential for discretising bulk material into various parameter sets to improve build rates. A novel build method is established here, discretising LPBF components into disparate layer thickness sub-volumes to optimise productivity while maintaining mechanical performance.
- Since only skin and bulk parameters are typically distinguished in the literature, the bulk mechanical response is dominated by material consolidated by a single parameter set. Hence there has been no critical analysis of the interface between regions of disparate parameters – especially different layer thicknesses. The interface between sub-volumes plays a crucial role in part performance, since there is discontinuity in laser processing and small discrepancies in resultant material properties. Fusion across these boundaries and mechanical behaviour of the interfaces are yet to be characterised and understood. Hence a detailed analysis of interface failure modes and defect formations is explored here.
- Typical LPBF slicer software has not been created with consideration for discretising components into sub-volumes of different process parameters. The software only allows for one set of parameters to be assigned to the bulk volume of a given component. This has hindered the potential for researchers to fully exploit the design freedoms of local laser control, by limiting the available laser strategies. Hence custom laser scan strategies are generated, tailored to joining of disparate parameter sub-volumes.
- HIPing of shelled material has been cited as an effective technique to reduce lasing time. However, authors have noted reduced fatigue life and reduced geometrical design freedom (due to shrinkage) as resultant limitations. This method can be built on using similar techniques to those described above, whereby a sub-volume is shelled to reduce build time and the remaining volume is processed as solid to maintain fatigue performance and greater design freedom in the necessary regions.

3 Methodology

This chapter describes the materials and characterisation techniques adopted to achieve the research presented within the thesis. This includes choice of powder feedstock, sample preparation, mechanical testing, and various imaging techniques.

3.1 Materials

3.1.1 LPBF feedstock material

Ti6Al4V was selected as the constant feedstock material throughout all experiments within the present thesis. Since the aims of the experiments are based on novel process adaptations and process design, it was necessary to select a well-understood LPBF alloy with relatively robust laser processability. This meant any issues with materials processing were minimised, to allow confidence that any variations in part quality metrics were as a result of the intended process variables and not a result of difficulties in laser processing of the alloy. A secondary reason for selecting Ti6Al4V was the high level of interest for this alloy in particular, having notable applications in aerospace, biomedicine, automotive and marine sectors.

Grade 5 Ti6Al4V with a particle size distribution (PSD) of 20 – 63 µm, sourced from EOS, was maintained across all manufacturing of test specimens to ensure all results were a fair comparison. Again, this is a common feedstock with a standard PSD and minimises risks for difficulties in materials processing. All reclaimed powder was sieved after each use to remove inclusion of spatter particles and the powder was routinely held at 60°C for over 6hrs, prior to builds, to remove any moisture introduced during storage at ambient temperature.

3.1.2 Metallographic sample preparation

Throughout the thesis, Ti6Al4V samples have been prepared for both optical and SEM imaging. In chapters 4 and 6, cube specimens were sectioned using a cutting wheel and mounted in conductive resin using a hot mounting press. The samples were then polished in the resin mounts using an automatic polisher, using silicon carbide abrasive paper. 500, 1200, 2000 and 4000 grit sizes were used before polishing on a polishing pad with 1 µm diamond suspension followed by colloidal silica. At this stage, samples were imaged for porosity before etching to ensure the etchant does not alter the size and morphology of the pores.

Commercially available Kroll's reagent was used to etch the sample surfaces to reveal the grain structure.

In chapter 5, an atypical polishing process was necessary to polish micro dog bones that were too long to mount in 30 mm diameter resin blocks, and too thin to grip by hand. Lengths of square section aluminium bar were cut to mount the dog bones. These blocks were placed on a hot plate and machine wax was applied to one surface until molten, the dog bones were then placed on the waxed surface and the blocks allowed to cool; thus setting the samples in the wax. The above polishing steps were used, however, the grinding and polishing discs were held stationary and the samples were moved back and forth by hand due to their fragility. The samples were also etched with Kroll's reagent in the same manner as above.

3.2 Manufacturing

All specimens investigated as part of the present research were produced by LPBF and mechanical test specimens were then machined to dimension to remove surface defects. This section details the manufacturing methods used to produce the specimens.

3.2.1 Laser powder bed fusion

A small volume of samples were produced on a Renishaw AM125 machine – strictly the proof of concept samples described in section 4.2.1. The system used a 200 W Yb-fibre laser with a spot size of 40 µm and a 125 x 125 x 125 mm build volume. Various parameter sets were used for layer thicknesses of 30, 60, 90, 120 and 150 µm.

The remainder of samples were produced on an EOS M290 LPBF machine, at Oerlikon AM Europe GmbH in Feldkirchen, Germany. The system uses a continuous 400 W Yb-fibre laser with an 85 µm spot size and 250 x 250 x 325 mm build volume. Optimised parameters were taken from the machine supplier (EOS) for each layer thickness investigated (30, 60 and 90 µm).

For dual layer thickness specimens in chapters 4 and 5, each sub-volume was sliced in EOSprint at the appropriate parameters and aligned by inputting coordinates in the software to share a boundary. For the dual layer thickness specimens in chapter 6, custom scan paths were generated (described in section 6.2.2) using a python script (available in appendix 10.1), and laser vectors were imported to EOSprint as cli. files, where the parameters were applied

to laser vectors with the corresponding ID number. Semi-hollow specimens were simply designed with a part-shelled region and sliced with a single set of parameters as standard.

3.2.2 Machining

For the macro dog bone specimens examined in chapters 4 and 6, specimens were simply machine to dimension using a standard lathe. Cylinders of 11 mm diameter and 70 mm length were produced by LPBF, before turning to ASTM E8 'reduced size' cylindrical dog bones specification for room temperature tensile testing . Due to the reduced size, production of a large batch of specimens was possible within the confines of a standard LPBF build volume. The remaining samples after tensile testing were used for fatigue testing, for which M10 x 1.5 mm threaded ends were machined to ensure there was no slippage within the grips.

For the micro tensile specimens in chapter 5, blocks of various orientations were produced with layer thickness interfaces at the mid-section. Tensile specimens were machined from these blocks by wire electrical discharge machining (EDM). Final dimensions were 45 x 5.8 x 0.4 mm and a 2 mm length gauge with 0.4 x 0.4 mm cross section. Specimen dimensions were limited micro tensile testing system, which is restrictive in both dimension and load cell capacity, and there are no notable standards for testing of this type. The 45 mm length was selected so the specimen tips lay flush with the far ends of each clamp to ensure sound gripping. The width was selected to achieve a sufficiently large surface for gripping and to maintain a similar aspect ratio to macro-scale dog bones of this type. The gauge cross-section, and subsequently sample thickness, was calculated by scaling down the ratio of maximum-load-to-cross-sectional-area from full scale specimens in chapter 4. The parts were built identically except for geometry.

3.3 Mechanical testing

Tensile testing, fatigue testing and micro tensile testing with in-situ optical microscopy were selected to characterise the mechanical performance and failure modes of the components manufactured. The methods and test parameters are detailed below.

3.3.1 Tensile testing

Tensile testing was selected to determine part properties (ultimate tensile strength, yield strength, elongation to failure and elastic modulus) and to compare these metrics with

reference samples, the wealth of available data in the literature and wrought material properties. A standard tensile testing system was used to measure the tensile response of cylindrical dog bones with a crosshead translation speed of 1 mm/min. A video extensometer was used to record the stress/strain response.

3.3.2 Fatigue testing

Fatigue testing was selected since cyclic loading is an accurate representation of common service conditions that Ti6Al4V parts are likely to experience, and since it is the most likely method to expose sensitivity to internal pores that arose as part of the proposed build methods. High-cycle fatigue tests were performed on standard fatigue testing machinery with a maximum stress amplitude of 840 MPa (80% of the yield stress), stress ratio of 0.1 and 30 Hz frequency. These test parameters are in keeping with those commonly found in the literature and enable high-cycle fatigue properties to be fairly compared.

3.3.3 Micro tensile testing with in-situ optical microscopy

Micro tensile testing was selected to focus on fracture occurring at the interface in real time using an in-situ optical microscope, enabling the role of individual pores to be tracked during plastic behaviour and failure. A Deben MicroTest 200N tensile stage was used, with a Leica M205 FA optical microscope in-situ. Tensile data points were recorded in the Deben MicroTest software with a sample time of 500 ms and a test speed of 0.2 mm/min, and a video recording of the microscope field of view was recorded at 60 fps. A slow test speed and high frame rate were selected to enable greater data capture during plastic behaviour and fracture, allowing more information on pore deformation, crack initiation and crack propagation to be understood.

3.4 Imaging and Image analysis

Optical, scanning electron and focus variation microscopy have all been used throughout the thesis experiments to image porosity, grain structure and fracture surfaces. The methods and equipment are discussed within this section.

3.4.1 Optical microscopy

Optical microscopy is a relatively simple technique for imaging features to the order of hundreds-of-microns. The microscopes use visible light and a series of lenses to magnify an area of the workpiece. Within the thesis, optical microscopes were used to focus on large pores and grain structure, since the resolution is sufficient for imaging larger defects and the large Ti6Al4V grain boundaries are more easily visualised on an optical microscope when compared with SEM. A Nikon eclipse LV100ND microscope was used for test cube specimens in chapters 4 and 6, whereas a Leica M205 FA microscope was used for in-situ imaging of micro tensile tests in chapter 5.

3.4.2 Scanning electron microscopy

Scanning electron microscopes use a focussed beam of electrons to scan sample surfaces, enabling resolutions down to single nanometres. These electrons interact with the atoms in the material surface and the resultant signals are collected by detectors in the chamber. These signals can provide information on both surface topography and material composition. The primary mode of scanning is secondary electron mode, in which atoms excited by the electron beam release secondary electrons to be measured by the detector. Secondary electron mode is used primarily for surface topography information, since the electrons only originate from shallow distances into the sample surface. Backscattered electron mode is also very common, involving detection of electrons emitted from the beam that have experienced an elastic interaction with the atoms of the workpiece and are 'backscattered' towards the detector. These electrons tend to scatter at greater depths than secondary electrons, and hence backscatter detection is primarily used for information below that of the topography, such as grain structure and composition.

Within the present thesis, SEM was used primarily for fracture surface analysis and imaging of small defects (< 20 µm), due to having significantly superior depth of field and resolution when compared with optical microscopes. An FEI XL30 SEM microscope was used in all cases found within the thesis. SEM was performed in secondary electron mode, using an acceleration voltage of 15 kV and working distance of 10 mm, since topographical information was required regarding porosity and fracture analysis.

3.4.3 X-ray computed tomography

XCT machines typically use rotating x-ray tubes to emit x-rays through a workpiece at various heights and turning through 360°. Depending on the density of the medium the material passes through, the x-rays are attenuated differently. This enables an accompanying algorithm to correlate data from various angles to construct a 3D representation of the workpiece, including subsurface information. Hence XCT is useful in detecting porosity in metal LPBF components, whereby pores have low density and material has high density.

Since there is a focus on internal porosity within the thesis, a Nikon MCT225 XCT system has been used as a powerful tool to provide non-destructive sub-surface information regarding pore characteristics, including size, morphology, and location. ImageJ was used to process the resultant image stack from the scans, in terms of selecting the appropriate volumes to focus on and thresholding the greyscale to better distinguish pore boundaries. BoneJ, an ImageJ plug-in, was used for particle analysis to measure pore information. Feret diameter was selected as the most comprehensive metric to measure pore size, describing the largest distance that exists between two points on the pore surface and effectively the largest diameter of the pore. ImageJ was also used to export an STL file of the pores to compare with STL files exported from focus variation data of fracture surfaces.

3.4.4 Focus variation microscopy

Focus variation uses similar technology to standard optical microscopes, using visible light and focal lenses to magnify a region of the sample. FVM builds on this, however, by varying the lens focus across a range of z-heights and relying on an algorithm to determine which regions of the sample are in focus for a given height. Hence topographical data can be extracted to measure surface roughness or, more importantly for the research contained within the present thesis, observe fracture surfaces inclusive of z-height information – a feature not possible using SEM.

An Alicona ‘Infinite Focus’ focus variation microscope has been used to measure fracture surfaces, in addition to SEM, to provide z-height information. Mountains surface metrology software was used to process the resultant data and generate height maps, as well as export 3D STL files for the surface reconstruction techniques described in chapter 5.

4 Multiple layer thicknesses within Laser Powder Bed Fusion and the effect on mechanical properties

4.1 Introduction

This chapter presents a novel method by which fine and coarse layer thicknesses can be interlaced into single LPBF parts, allowing for finer layers in regions of high specifications and coarse layers in regions of low interest or reduced mechanical requirements. This approach has several benefits. Firstly, it allows optimisation of parts for production rate by significantly reducing laser-on time, while maintaining part quality in the necessary areas. Secondly, it is a novel method to control property graduation, hence allowing control over fracture location and direction. The aim of this chapter is to demonstrate the viability of manufacturing single LPBF components divided into sub volumes with disparate layer thicknesses, and to characterise part quality compared with standard parts across select metrics.

Both 60 and 90 μm layers are interlaced with a benchmark 30 μm layer thickness, meaning these regions are only lased every second or third layer respectively. Flat and castellated interfaces are investigated. The castellated interface, featuring a grid arrangement of 'teeth' like a housing joint, is explored to improve fusion and exhibit the geometrical control enabled by this method. The quality of the union is characterised by porosity and microstructural analysis at the layer thickness boundary, as well as tensile testing and fatigue testing of specimens featuring layer thickness interfaces at the midpoint of the gauge length.

4.2 Methodology

4.2.1 Proof of concept and development

A proof of concept study of this research has been published [192], in which the principle of fabricating LPBF parts containing multiple layer thickness regions is demonstrated. The study explored a range of layer thicknesses (30, 60, 90, 120 and 150 μm) and the appropriate process parameters to fabricate them.

Volumetric energy density (VED) of a standard, optimised 30 µm layer thickness was calculated and used to identify a process parameter window when scaling up the layer thickness. In theory, VED should be constant, given it is energy per unit volume of a constant material. Hence, according to the equation described in section 2.2.7, doubling the layer thickness to 60 µm would require doubling the energy input by increasing laser power by a factor of 2 or halving the scan speed. However, once the process window had been refined in each case, the data showed that VED must be adapted for coarser layers. Figure 18 shows VED must increase to achieve high density parts as layer thickness increase above the standard regime, as powder layer shrinkage begins to play a larger role. Thicker layers will leave a greater layer height shrinkage. This additional height is then filled with loose powder for the successive layer and requires consolidation along with the nominal layer height; meaning as layer thickness increases, so does the disparity between nominal layer thickness and true layer thickness. Hence the according VED values must compensate.

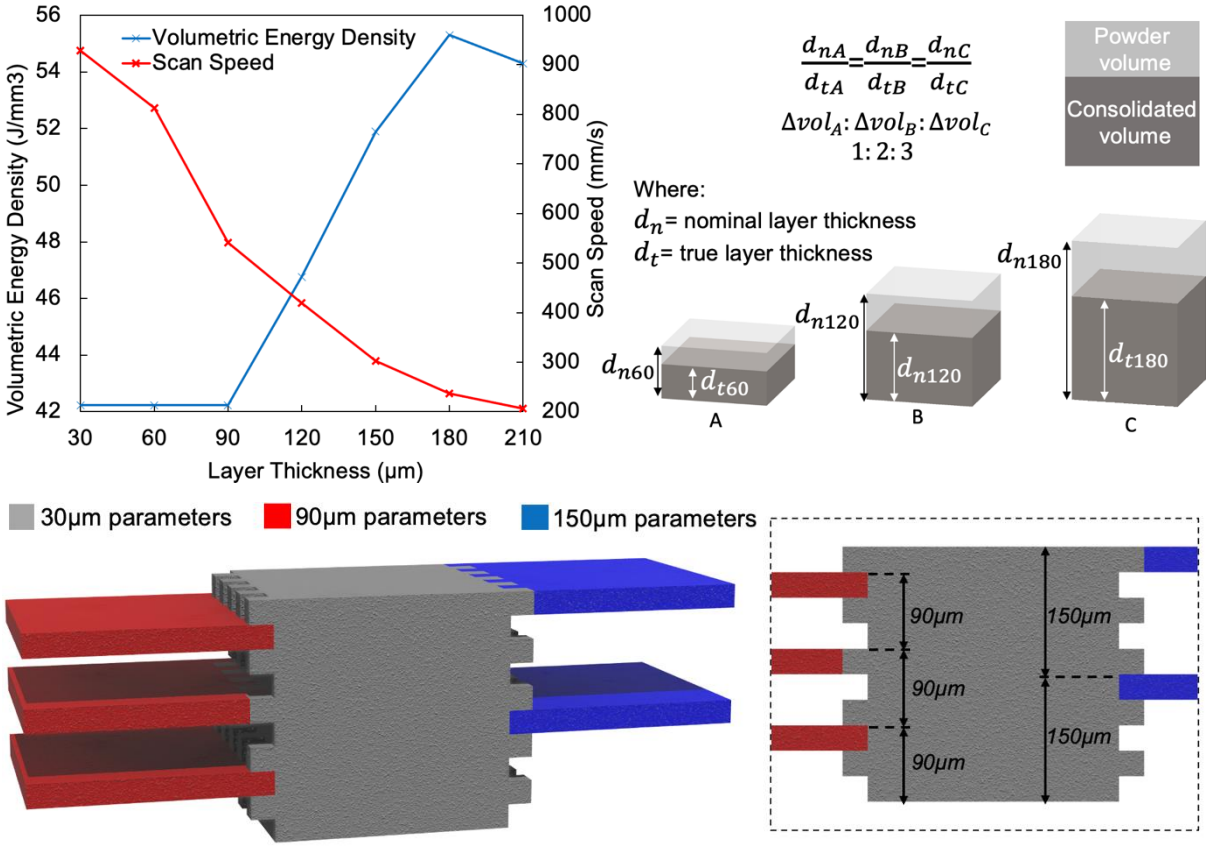

Figure 18 - Multi-layer thickness development: VED required for various layer thickness as shrinkage plays a growing role and a schematic to show trial specimen design

Cubes were manufactured to observe the boundaries among layer thickness volumes. Samples were prepared for polishing and optical imaging of both porosity and microstructure.

Dog bones were also produced with interfaces at the midpoint for tensile testing according to ASTM E8 for 'reduced size' specimens, suitable for LPBF since a greater quantity of specimens fit within the build chamber for a single build. The tensile response of these dual layer thickness specimens was compared with standard LPBF specimens of 30 µm layer thickness, and specimens built entirely of the maximum layer thickness investigated (150 µm). Excessive porosity dominated along the layer thickness interfaces, meaning joined samples failed well before reaching the plastic region and measuring interface design quality was not possible since all performed equally poorly. An example of this can be seen in Figure 19, whereby the tensile response can be seen in image (a) and extreme porosity following the castellated interlacing design is evident at the interface in image (b). Image (b) also shows a fracture surface measured by Focus Variation that displays two intact teeth where there has been clear large material discontinuity at the joint. Optimising the alignment of the two regions within the slicer software was crucial to improving the fusion between them. Cartesian coordinates were input to ensure each volume shared a border pass at the interface and further optimisation of bulk material parameters was also undertaken.

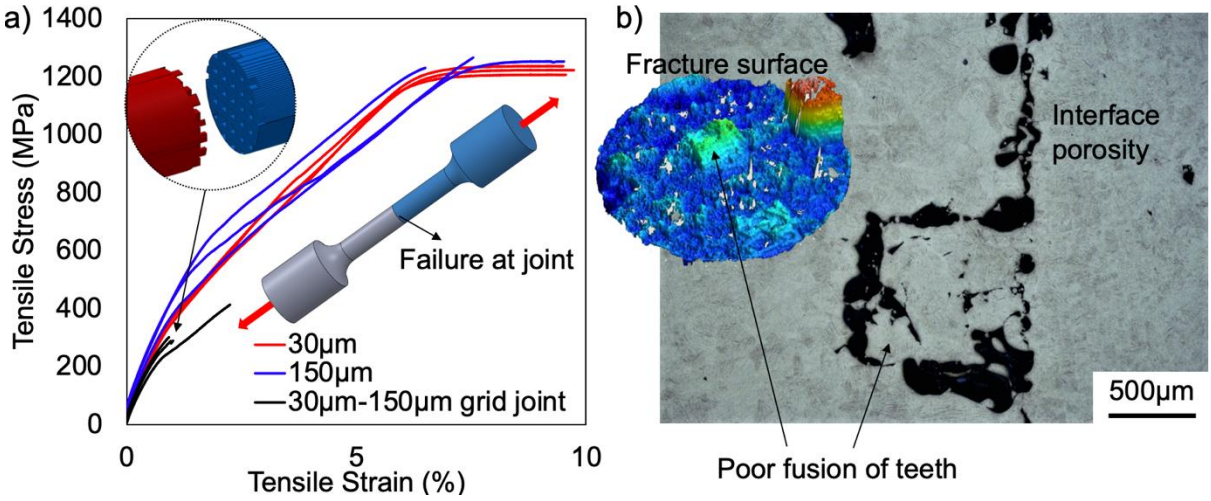

Figure 19 – Poor tensile response of proof-of-concept specimens as a result of interface porosity

The chapter hereafter built significantly on this proof-of-concept study by investigating samples in which part parameters have been optimised to hugely reduce interfacial porosity and allow a full mechanical response to be observed, thus tensile properties and fracture surfaces can be used to compare interface design quality.

4.2.2 Specimen fabrication

The experimental work hereafter in this chapter builds on the preliminary study described in section 4.2.1 with further optimised process parameters. The specimens were produced using a commercial EOS M290 LPBF system. These samples were designed and tested to characterise fusion of disparate layer thickness regions, interlaced within a single geometry, with 30, 60 and 90 µm layer regions being joined together. In each case, optimised build parameters were used to achieve near-fully dense consolidation of material (>99.9% relative density) and slicer software coordinates were used to align each region to share a laser border pass.

All specimens were produced using grade 5 Ti6Al4V feedstock, sourced from EOS, with a particle size distribution (PSD) of 20 – 63 µm. Since the study is based on a new processing technique, a standard, well-understood material was selected to remove any material risks and allow focus to remain on the process behaviour. Samples were produced on an EOS M290 LPBF machine, at Oerlikon AM Europe GmbH in Feldkirchen, Germany. The system uses a continuous 400 W Yb-fibre laser with an 85 µm spot size and 250 x 250 x 325 mm build volume. Specimens were manufactured containing regions of 30, 60 and 90 µm layer thicknesses.

Each region of a given part is sliced in EOSprint slicer software and discretised into the appropriate layer thickness and corresponding parameter set. Part regions were then arranged in the build volume within the software by inputting coordinates to ensure interfaces are perfectly aligned to form a 'single part', forming a cylinder lying horizontally on the substrate. The chamber conditions when processing parts were an oxygen content of 0.1% and platform temperature of < 45°C. The samples were stress relieved at 720°C for 2 hours post-build in order to relieve residual stresses and improve ductility [193].

Single parts were designed comprising two regions, one finer (30 µm) and one thicker layer (60 or 90 µm), to improve build rates through significantly reduced laser-on time. To achieve this, each region was designed separately in CAD software (SolidWorks, Dassault Systèmes, France) in order to slice the STL files at different nominal layer thicknesses using the optimised parameters in each case. Once sliced, the build files were aligned on the substrate within the slicer software to form one component comprised of two distinct regions. For this method to print successfully, increased layer thickness regions must be

divisible by the base layer thickness – in this case 60 and 90 µm, divisible by the 30 µm baseline – since the build is performed at the finest thickness and thicker layers are processed every second and third layer respectively. This method is depicted in Figure 20, along with the two joint geometries designed and fabricated within the study.

If half (or any appropriate fraction) of each sample is only lased every third layer, build times can be reduced significantly. Naturally, the amount of time saved is dependent on the size of the build. For example, take a build with the following parameters: 100 mm z-height + 5 mm support = 105 mm; 30 µm layers = 3500 layers; 30 seconds average laser-on time per layer; coarse layer scan speed 20% slower than fine layer scan speed. This means on layers where both halves are processed, the fine-layer region contributes 0.5 of the laser on time, while the coarse layer region contributes 0.6 of the laser on time compared to conventional processing. This equates to a time saving of 8hrs45mins or 22.5% build time reduction, accounting for 10 seconds recoater time per layer.

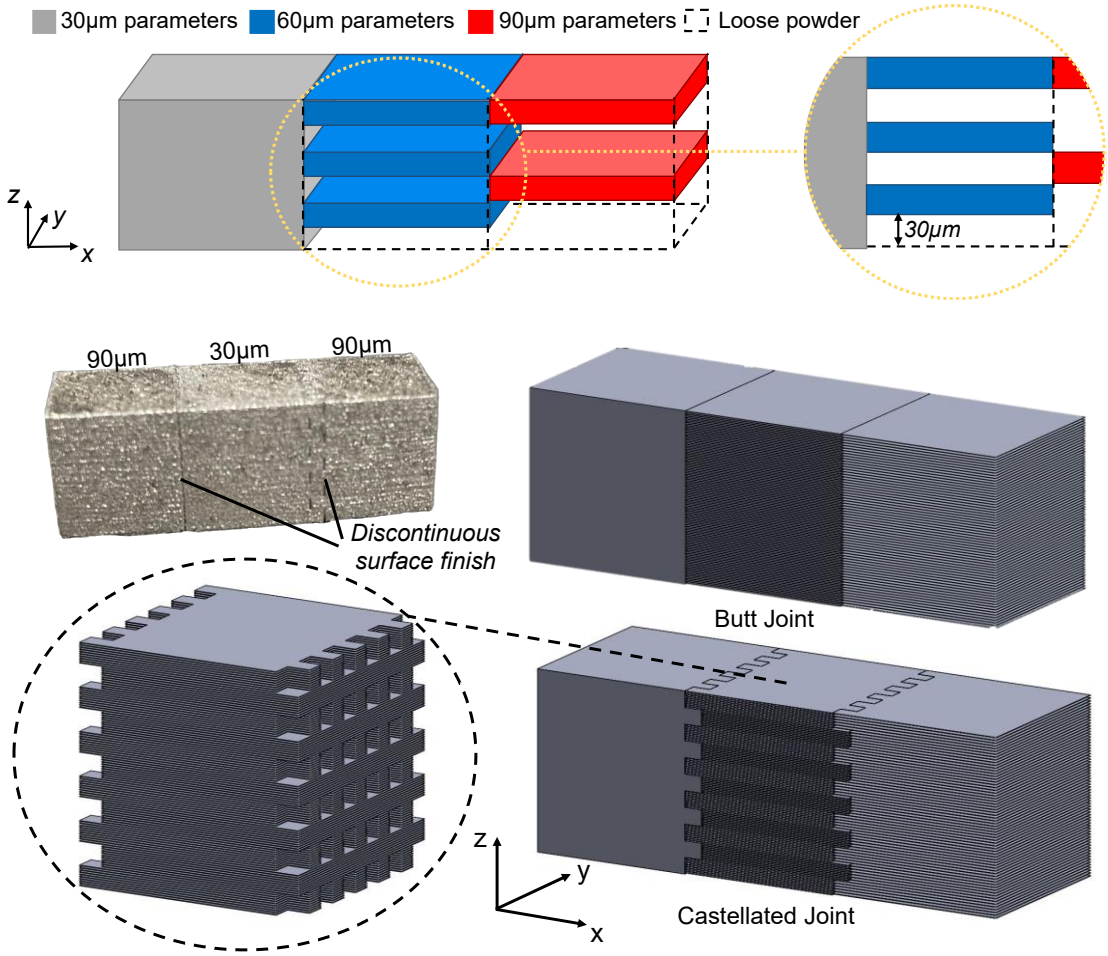

Figure 20 - A schematic showing the method by which multiple layer thicknesses can be interlaced within single LPBF geometries (top); CAD images of the two jointed geometries investigated as part of the study (butt and castellated joints) [192]

A series of cylindrical dog bone specimens were produced for mechanical testing according to ASTM E8M 16a, with 24 mm and 4mm gauge length and diameter respectively. 10 mm diameter grip sections were maintained from the standard. These were machined from blanks built as described above. Images of blanks, tensile specimens and specimen dimensions are shown in Figure 21. ASTM E8M 16a defines a series of standard specimen geometries for room temperature tensile testing; of which, the stated 'reduced size' geometry was deemed appropriate for AM samples to maximise the usage of the build envelope as well as material usage. Similarly, cubic specimens were manufactured with identical joint interfaces, for image analysis. The samples consist of 9 sample sets. As a baseline, single layer-thickness 30, 60 and 90 µm dog bones were produced (with no joints to serve as a comparison for the specimens that feature disparate layer thickness interfaces). Then two interface geometries were investigated; a flat joint much like a butt joint, and a castellated joint, interlacing the two regions to improve the weld region. Samples were manufactured exhibiting 30-30µm, 30-60µm and 30-90µm layer interfaces using both joint types, thus forming the nine sample sets along with the baseline specimens.

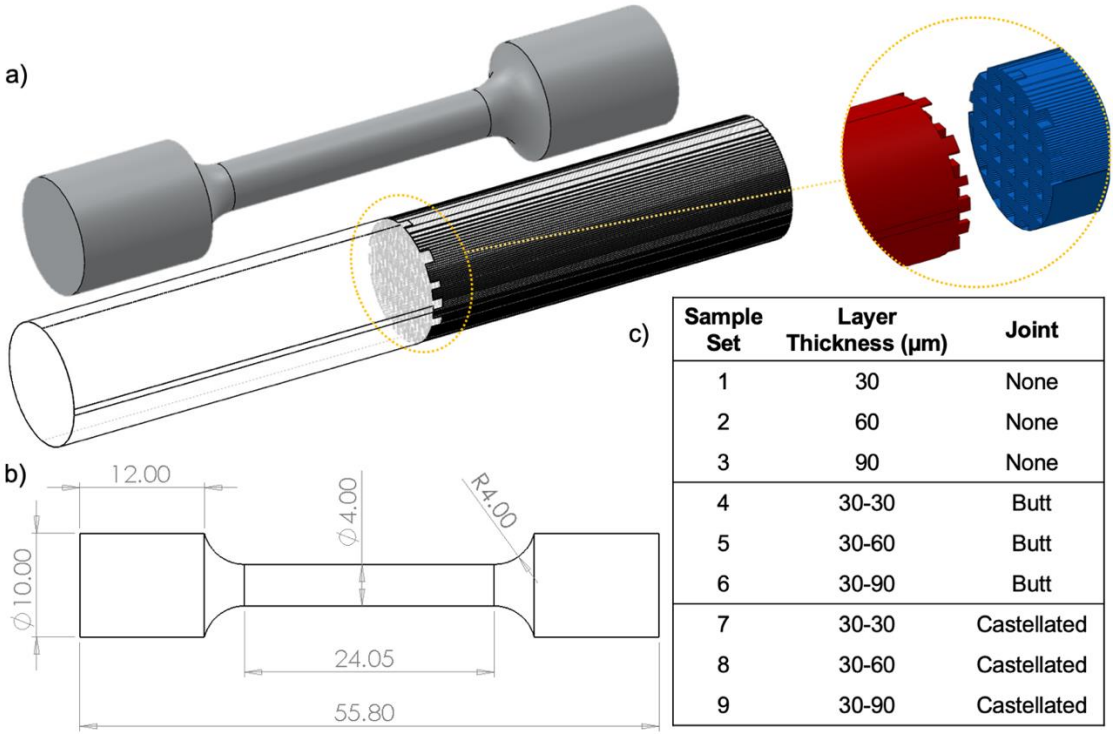

c)

Sample Set	Layer Thickness (µm)	Joint
1	30	None
2	60	None
3	90	None
4	30-30	Butt
5	30-60	Butt
6	30-90	Butt
7	30-30	Castellated
8	30-60	Castellated
9	30-90	Castellated

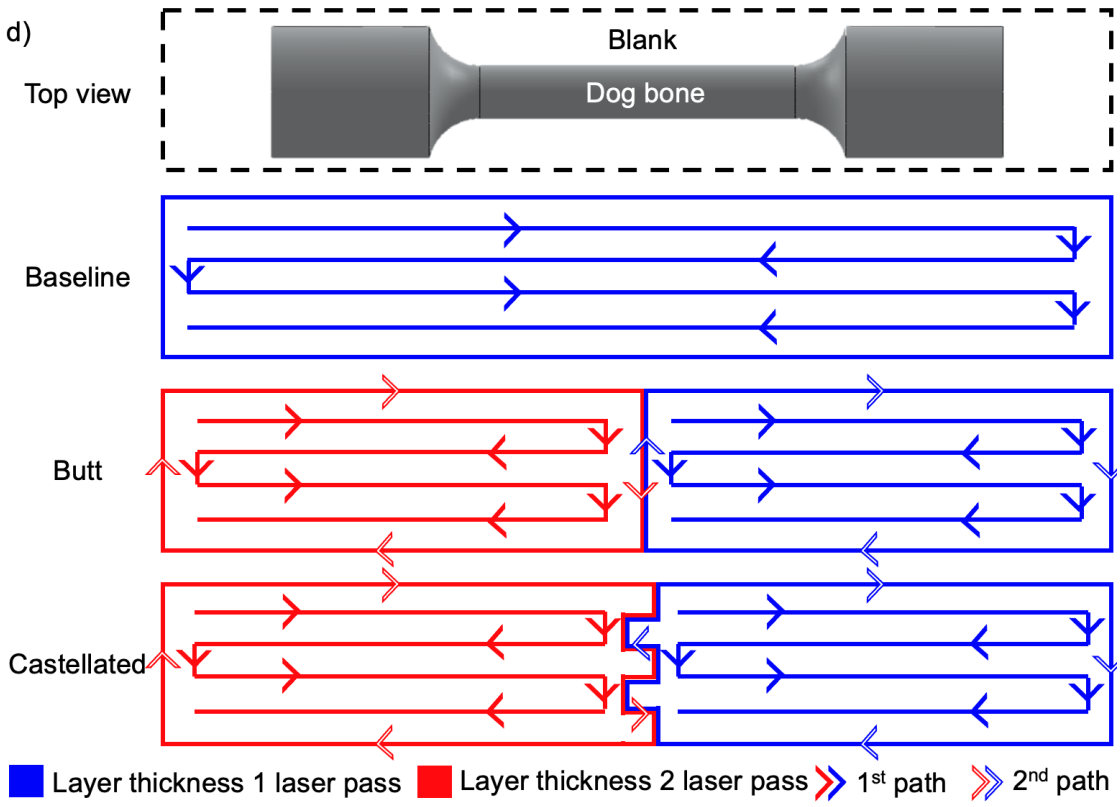

Figure 21 – a) CAD images of Ti6Al4V LPBF blanks featuring a castellated union of two regions built with different layer thicknesses and the final machined tensile specimens; b) dog bone dimensions according to ASTM E8M 16a; c) a table describing the nine sample sets investigated in terms of layer thickness and joint configuration; d) schematics to describe laser processing of the samples

4.2.3 Microstructural analysis

Cubic samples, including the joint configurations described above, were sectioned in both the x-z and x-y planes (*see* Figure 20 for cartesian axes with respect to build process) to observe interfacial porosity and blending of microstructure at the layer thickness interface. Samples were sectioned using abrasive cutting, and prepared via mechanical grinding followed by mechanical polishing down to colloidal silica. Samples were then imaged for porosity using a Nikon eclipse LV100ND optical microscope at 5-times magnification, prior to etching to avoid altering pore size and morphology by eroding pore boundaries with the etchant. Porosity analysis at the layer thickness boundary was necessary to understand whether this method of manufacture introduces defects at the interface and to correlate this information to the tensile results. ImageJ software was used to measure relative density across various 2 x 2 mm areas within each image and take an average reading in bulk regions compared to interface regions. Once porosity images were collected, the samples were then etched using Keller's reagent to reveal grain boundaries and imaged a second time on the optical microscope for

analysis of the grain structure at the layer thickness boundary. While the 30-30 µm jointed samples will contain the same structure in each region, these samples were manufactured to determine whether the introduction of a joint gives rise to other features in the material, potentially weakening the specimens, be it through interfacial porosity or a microstructural phenomenon brought about by parallel laser scans. In the case of 30-60 and 30-90 µm joints, one expected to observe similar large columnar prior- β grains in the build direction (z-direction)[194]. The microstructural analysis presented in this study aimed to observe the blending of two disparate grain structures across the joint interface, and whether the joint geometry could improve said blending. The castellated joint geometry features 900 µm teeth in an attempt to broaden the region of blending and improve the fusion by interlacing the two layer thickness regions.

4.2.4 Mechanical testing and fractography

Following the investigation of the quality and fusion of parts containing two disparate regions, the subsequent mechanical response is of primary concern. Both tensile testing and high cycle fatigue testing were selected as methods of characterising the mechanical performance of jointed samples, compared to baseline single-layer-thickness samples (those presented here and those found in the wealth of information surrounding tensile properties of LPBF Ti6Al4V in the literature [195][196][150]).

For tensile tests, three repeats were performed for each sample set to ensure reliability in the data and observe repeatability across the sample sets. The samples were uniaxially loaded on a standard tensile test system with a crosshead translation speed of 1 mm/min until specimen failure, using a video extensometer to measure the stress-strain response. All specimens failed within the gauge length. For fatigue tests, a sinusoidal stress waveform was applied uniaxially at a maximum stress of 840 MPa, R = 0.1 and a frequency of 30 Hz. 840 MPa was selected to maintain a maximum stress amplitude 20% below the yield stress of the material.

Following tensile testing, failed sample fracture surfaces were analysed using an Alicona ‘Infinite Focus’ focus variation microscope (FVM) at 10x magnification and post-processed using Mountains surface metrology software. Fracture surfaces were investigated for a number of reasons i) to observe the fracture behaviour in terms of ductility, since introduction of layer thickness boundaries has potential to cause more brittle failure at the

interface ii) to observe whether joint geometry relates to crack initiation and propagation, such as evidence of castellated teeth iii) to deduce whether samples failed at the joint interface, and hence determine whether interfaces introduce weak points in the parts and iv) to obtain supporting information as to why a sample may fail at the interface (e.g. internal defects). This information is used in conjunction with micrographs and tensile data to gain a deeper insight into the behaviour of parts containing interlaced layer thicknesses, and to understand why they may fail in the manner observed here.

4.3 Results

4.3.1 Porosity and grain structure

Optical micrographs of 30-30, 30-60 and 30-90 µm interfaces for both butt and castellated joined regions are presented both prior to and post etching to observe porosity and grain structure, respectively. Evidence of defects at the interface provides crucial information as to the quality of the fusion between the two regions of different layer thicknesses, and useful insight in to fracture locations of the tensile specimens. Grain structure analysis allows investigation of the blending of two parallel laser scans, producing two metal matrices that form one part.

Optical maging revealed an increase in porosity at the joint interfaces as opposed to the bulk regions, both in terms of frequency and size – highlighted in the micrographs in Figure 22. This finding suggests a phenomenon occurs during laser processing of two parallel scan paths that introduces defects otherwise not present in a single layer thickness, single meander laser pass. A trend is clear from the relative density data as well as visual inspection of the images (Figure 23), that an increase in layer thickness in the coarser layer region amplifies the increase in frequency and size of interfacial defects. In the bulk of 30, 60 and 90 µm regions measured 99.99, 99.99 and 99.98% relative densities respectively, while joining these regions with another 30 µm region and measuring at the interface gives 99.92, 99.88 and 99.77% respectively.

Across all samples, micrographs display typical prior- β grains that appear elongated in the xz-plane and equiaxed in the xy-plane as seen from Figure 24.This means columnar grain growth is evident in the build direction (z direction), as is typical in LPBF Ti6Al4V [197]. The microstructure observed in the 30-30 and 30-60 µm samples is very similar and can be

seen to share grains across the boundary interface that match the general size, morphology and direction of the remainder of the sample. This provides some insight that good fusion occurs across the interface, that did not significantly disrupt the grain growth of each region, but rather blended the two together. This is not the case for the 30-90 µm samples, in which there is a clear band at the boundary of the butt jointed samples and in which texture of the grains has been affected. Some finer horizontal grains can be seen to grow outward from the interface line into the bulk of each region either side.

Another identified phenomenon is a change in directionality of the columnar grains across the interface, observed in the xy-plane and evident only in the 30-60 and 30-90 µm samples – the 30-30 µm samples show a consistent directionality across the whole surface. Observed from the xz-plane, the columns appear unchanged and aligned vertically in the build direction. However, the xy-plane reveals disparate angles in the alignment of the cross section of the columnar grains when comparing the two regions each side of the interface. The samples showed an angle disparity across the interface of 3.9, 35 and 23.1° for the 30-30, 30-60 and 30-90 µm samples respectively.

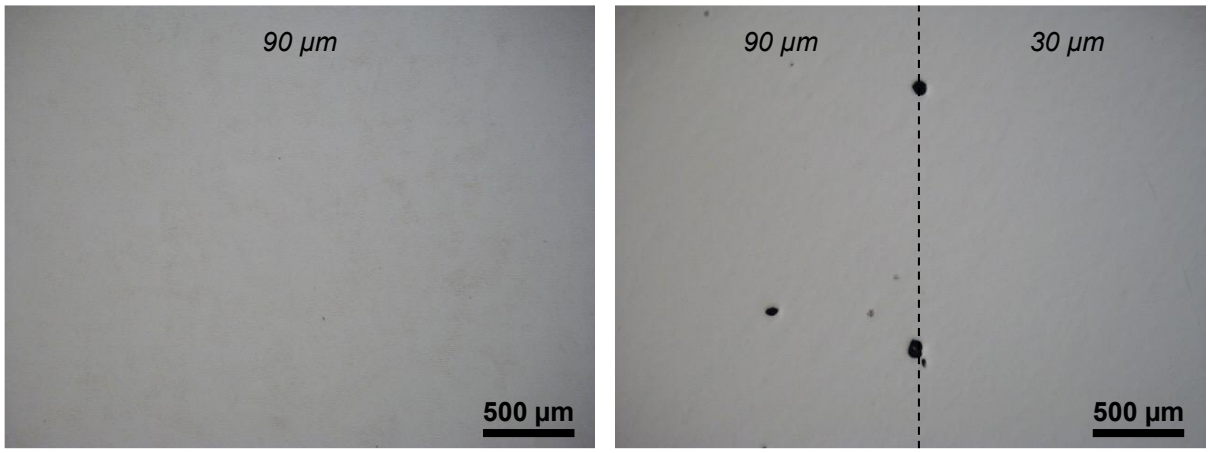

Figure 22 - 90 µm layer thickness bulk porosity compared with porosity at a 30-90 µm layer thickness interface, highlighting the increased presence in the region of interfaces

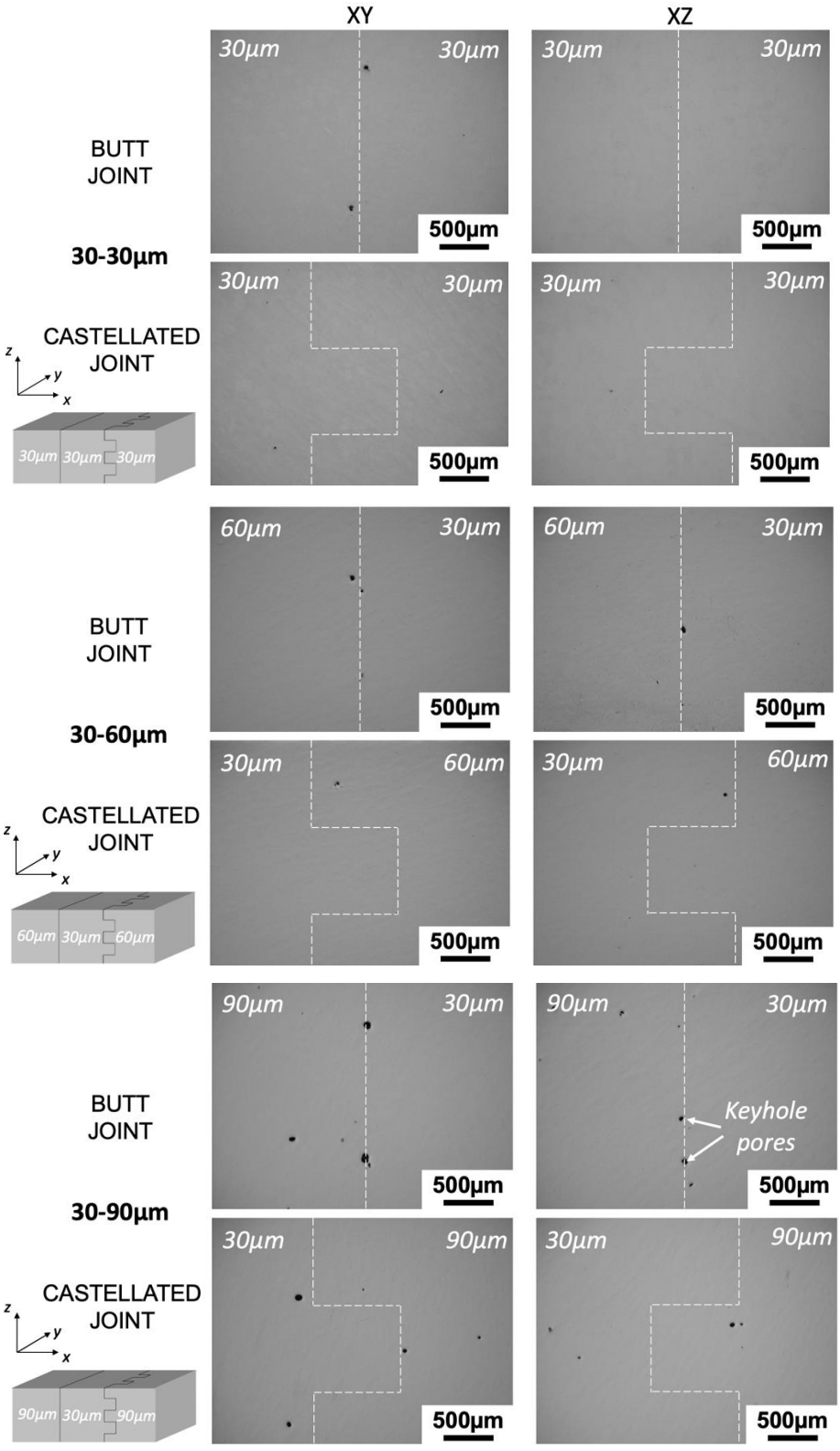

Figure 23 – Optical micrographs showing porosity at layer thickness interfaces in the xy plane (left column) and xz plane (right column) for butt joint and castellated joint boundaries; 30-30 µm regions (top rows), 30-60 µm regions (middle rows) and 30-90 µm regions (bottom rows); images depict an increase in defect presence and size at the interfaces, the extremity of which increases as layer thickness increases

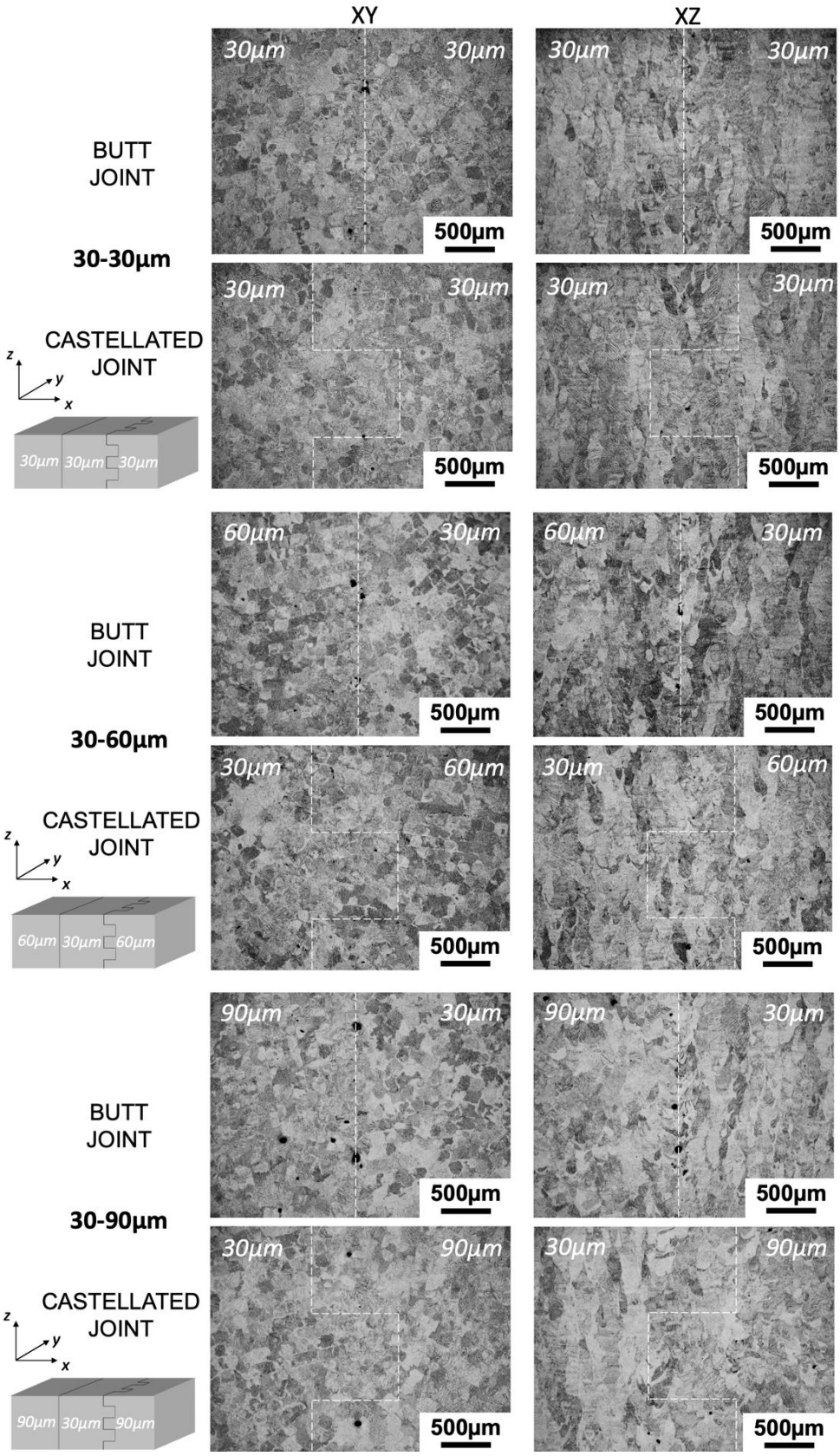

Figure 24 – Optical micrographs showing grain structure at layer thickness interfaces in the xy plane (left column) and xz plane (right column) for butt joint and castellated joint boundaries; 30-30 µm regions (top rows), 30-60 µm regions (middle rows) and 30-90 µm regions (bottom rows)

4.3.2 Tensile properties

Stress-strain curves and tabulated data are presented for baseline 30, 60 and 90 µm samples as well as 30-30, 30-60 and 30-90 µm samples featuring both butt and castellated joints between regions. Repeatability of the samples is good for AM parts, owing to two factors. Firstly, a very high relative density and hence lack of internal defects that would give rise to less consistent failure; secondly, robust melt pool control producing consistent grain size. Consequently, the scatter among repeats is difficult to discern. In addition, the tensile response of the 30, 60 and 90 µm baseline specimens are indistinguishable. As a result, the graphs included in Figure 25 display the stress range (depicted on the y-axes) magnified from 1060 to 1140 MPa to focus on the plastic region, in which ultimate tensile stress and fracture point is observed. In all cases, the elastic region is incredibly similar and does not require attention since there are no discrepancies among sample sets.

All tested samples exhibited failure within the gauge section. In the case of the baseline 30, 60 and 90 µm samples, fracture occurred at random points along the gauge. In the case of all jointed samples (30-30, 30-60 and 30-90 µm, butt and castellated), fracture occurred at the midpoint of the gauge - the location of the interface between the two regions.

Figure 25 (a) shows minor disparity amongst the tensile response of the baseline samples, showing an average UTS of 1126, 1131 and 1129 MPa for 30, 60 and 90 µm layer thicknesses respectively. This is explained by sound parameter optimisation and process control. There is no apparent trend in the baseline samples, and these minor changes (< 0.5%) can be attributed to wider manufacturing tolerances associated with AM techniques, such as minor discrepancies in porosity, microstructure and residual stress due to being built in a different area of the substrate. Elastic modulus (calculated from the gradient of the elastic region in the stress-strain graph), elongation to failure, strength and yield stress can also be considered comparable in each case – see Table 2.

Table 2 - Tensile properties of each design configuration compared with wrought and literature values

Sample Set	Avg. Young's modulus (GPa)	Avg. elongation (%)	Avg. UTS (MPa)	Avg. Yield Stress (MPa)
30µm	133.8	9.70	1126	1071
60µm	129.1	8.74	1131	1072
90µm	128.6	9.78	1129	1074
30-30µm butt	127.8	9.07	1130	1074
30-60µm butt	127.5	8.78	1135	1074
30-90µm butt	124.2	5.92	1129	1067
30-30µm castellated	130.4	6.71	1122	1067
30-60µm castellated	140.9	6.94	1128	1071
30-90µm castellated	127.0	6.15	1110	1052
Wrought Ti6Al4V [153]	113.8	14	950	880
LPBF Ti6Al4V [198]	94.4 – 110.9	2 – 19.7	840 - 1320	974

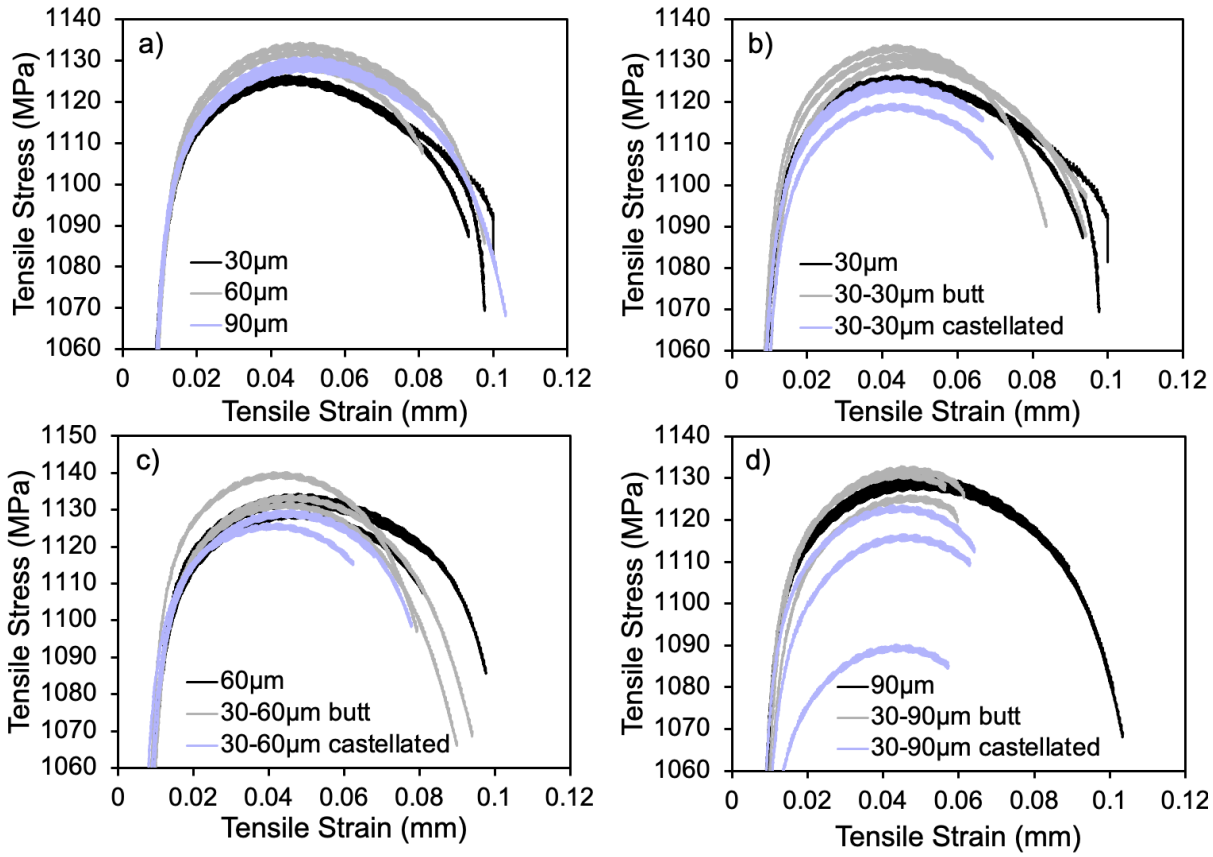

Figure 25 – Stress-strain curves displaying the tensile response of: a) baseline samples of 30, 60 and 90 µm layer thickness; b) 30-30 µm butt and castellated joins; c) 30-60 µm butt and castellated joins; d) 30-90 µm butt and castellated joins

It is clear from the graph that the 30 µm and two 30-30 µm jointed samples exhibit similar Young's modulus and UTS values - confirmed in Table 2 to range between 127.8-133.8 GPa and 1122-1130 MPa respectively for the three sample sets. However, while the butt jointed 30-30 µm samples perform very similarly to the standard 30 µm samples in terms of elongation (9.07% and 9.70% respectively), the castellated 30-30 µm joints exhibit failure at 6.71% elongation.

Figure 25 (c) depicts the performance of the 30-60 µm jointed samples compared with the baseline 60 µm layer thickness. The trend is comparable to the 30-30 µm joints, in that the butt jointed samples perform very similarly to the baseline samples; while the castellated joints, however, experience failure at 6.94% elongation compared with 8.74% and 8.78% for 60 µm baseline and 30-60 µm butt joints respectively. There was good quality blending of microstructure across the interface in these samples, as evidenced in section 4.3.1, with the only difference to the 30-30 jointed samples being a change in directionality observed in the xy-plane between the two regions (the angle of grain alignment differs). Since the performance of the 30-60 µm jointed samples appears very similar to the 30-30 µm counterparts, it would suggest this change in directionality does not affect the tensile performance when loaded in the y-direction as in this study.

Figure 25 (d) shows the samples with the largest disparity in layer thickness – the 30-90 µm jointed samples. The butt jointed samples, in this instance, give a similar Young's modulus, UTS and yield stress to the baseline samples; however, these specimens are the only butt jointed tests to yield premature failure and hence lower ductility in line with the castellated samples – dropping from the region of 9% elongation to failure to 5.92%. The 30-90 µm castellated samples again show premature failure and a reduction in ductility to the same extent as the 30-30 and 30-60 µm castellated interfaces. These are the first samples, however, to begin to show any depreciation in UTS and yield stress, as well as elongation (Young's modulus remains consistent). There is a marginal drop of around 1.4 and 1.6% in average UTS and yield stress respectively; while this is a very minor change, it is the first sign of any influence on stress response.

4.3.3 Fracture behaviour

Since the sample sets investigated are comprised of interfaces at the midpoint of the gauge, in two geometrical variations and three combinations of layer thickness (butt and castellated

joints featuring 30, 60 and 90 µm regions), the fracture locations and surfaces were investigated. The baseline samples, Figure 26 (a), (b) and (c), all failed at random points within the gauge length. This was expected due to the singular laser scan path producing a consistent grain structure and random porosity throughout the entire sample. The jointed samples, including butt joints and castellated joints featured in Figure 26 (d, e, f and g, h, i respectively), all fractured at the midpoint of the gauge where the joint interfaces are situated.

The baseline samples all exhibit a standard cup and cone fracture surface, in which the high lips (red) and low recesses (blue) indicate the moderate ductility reported in the tensile results. The rougher texture displayed in the 90 µm surface (top-right in Figure 26) is indicative of lower structural homogeneity brought about as a result of greater porosity within the sample, and thus yields a greater number of localised peaks and recesses, or 'dimples' – similar evidence was reported by Khalid Rafi et al. in 15-5 PH steel [199]. Despite this evidence, the 90 µm sample performed similarly with both the 30 and 60 µm samples under tension.

The butt jointed samples (Figure 26d, e and f) show the inverse relationship between layer thickness and ductility found in the tensile data. The 30-30 µm joint maintains the lips and recesses around the perimeter, characteristic of a ductile cup and cone fracture; this is less apparent in the 30-60, and the 30-90 joint shows very little evidence of ductility, implying the more brittle, premature failure reported in the mechanical data as a consequence of interfacial porosity. The rougher texture and dimples observed in the 30-30 µm butt joint fracture surface when compared with the baseline 30 µm surface suggest a greater presence of pores, each dimple representing localised brittle behaviour in the vicinity of a pore. This strongly supports the hypothesis that the jointed samples fail at the layer thickness boundary as a result of interfacial porosity. Nonetheless, the fracture surface of this sample implies superior material uniformity and load sharing capability when compared with all other jointed samples, as was supported by showing the least interfacial porosity and strongest grain blending at the boundary in the microstructural analysis.

In agreement with the mechanical data, more brittle failure is evident across the board for the 30-30, 30-60 and 30-90 µm castellated samples; less evidence of standard cup and cone failure is apparent since little deformation was achieved prior to failure. Dimples are evident in all three surfaces again, further supporting the theory that interfacial porosity is

the root cause of fracture occurring at the interface, as well as causing premature failure of the sample.

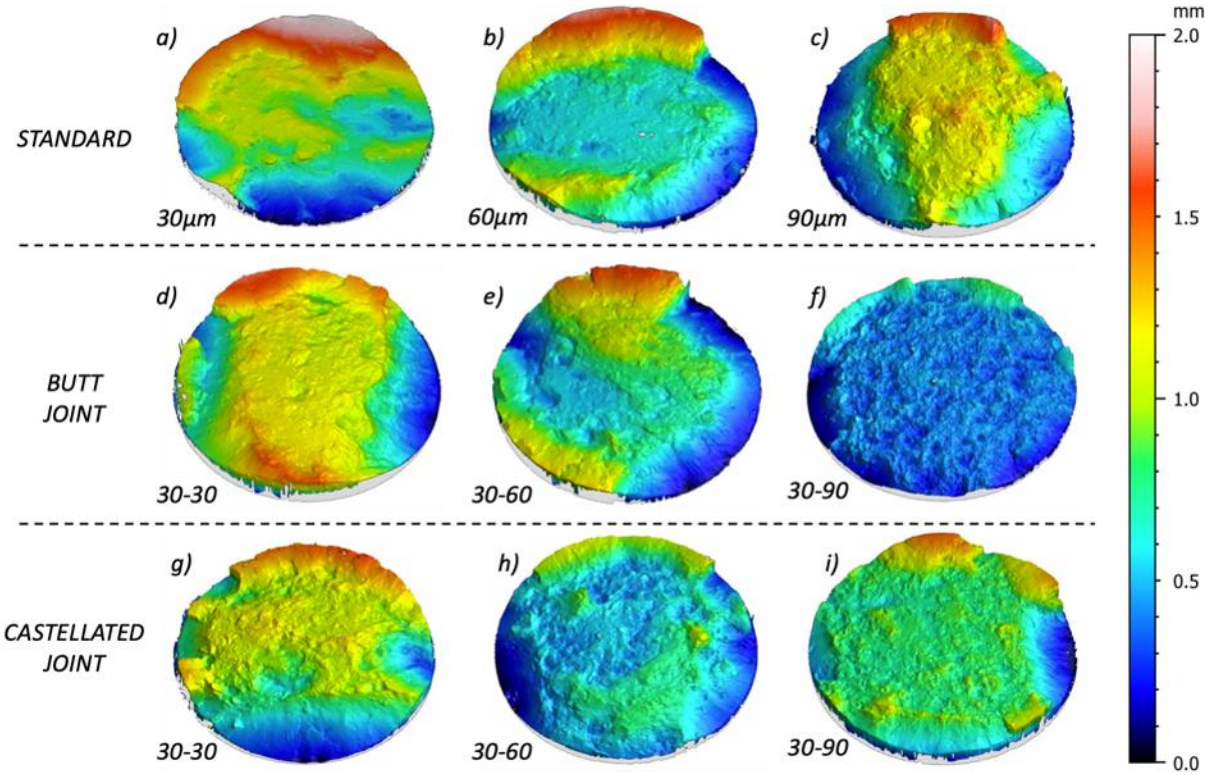

Figure 26 – Focus variation images of the fracture surfaces introduced when tensile testing the interlaced layer thickness LPBF specimens to failure; top row (a, b and c) includes baseline samples of singular layer thicknesses 30, 60 and 90 µm respectively; middle row (d, e and f) includes butt jointed layer thickness regions of 30-30, 30-60 and 30-90 µm respectively; bottom row (g, h and i) includes castellated joints between layer thickness regions of 30-30, 30-60, and 30-90 µm respectively.

4.3.4 Fatigue behaviour

The number of cycles to failure of each sample set can be seen in Figure 27, contrasted also with elongation to failure of the tensile specimens. The 30-30 µm sample sets exhibited the greatest fatigue life of the joined specimens, however, they experienced a drop in cycles to failure of 76.1% on average when compared with the standard samples. The disparate layer thickness joins of 30-60 and 30-90 µm sample sets displayed similar fatigue life and experienced a 95.2% average drop in cycles to failure. There are extreme penalties to fatigue life compared with the minor penalties to elongation to failure under tension.

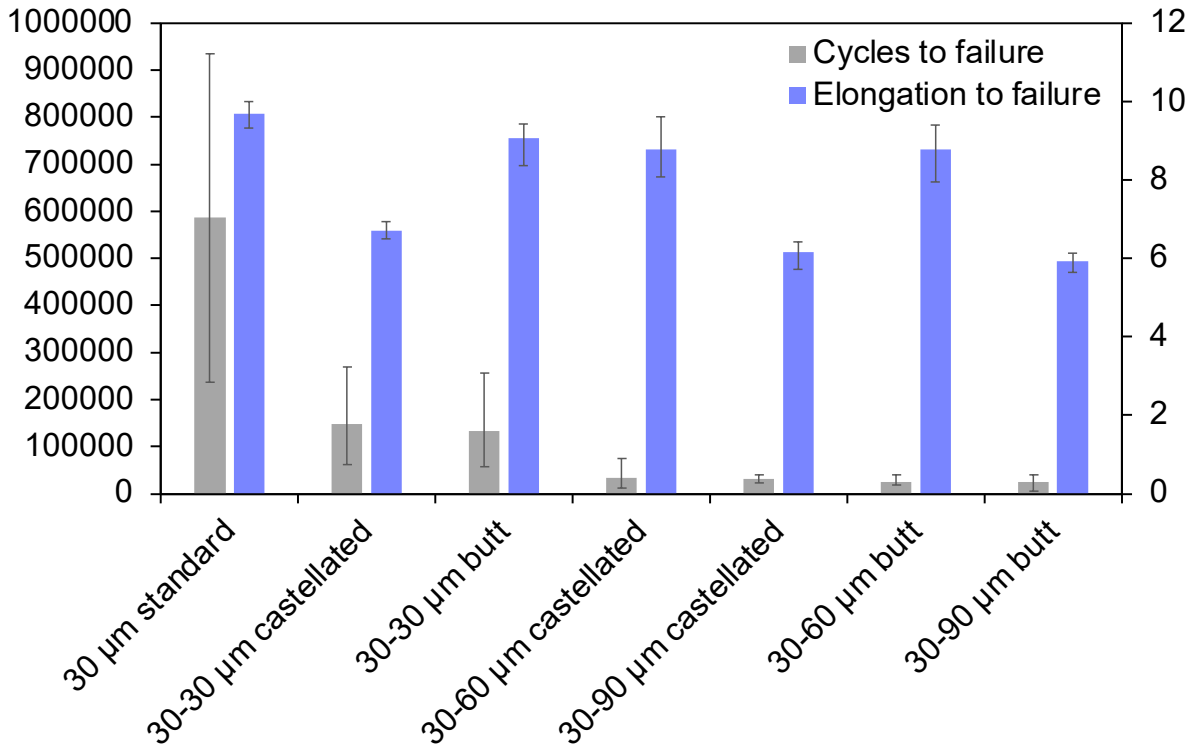

Figure 27 - Fatigue cycles to failure and elongation to failure compared among all joint designs

4.4 Discussion

4.4.1 Porosity and grain structure

The results suggest that producing LPBF parts comprising of different layer thickness regions gives rise to increased porosity (size and frequency) at the boundary. A trend is also evident in which increasing the thickness of the coarser layer region increases the extent of interfacial porosity. This trend can likely be attributed to two factors. Firstly, keyhole pores are increasingly more evident in LPBF parts as layer thickness increases, since melt pool stability becomes more difficult to maintain at greater depths of penetration. Thus, an increase in layer thickness in one or both regions is likely to give rise to a greater fraction of larger defects; especially since the border laser pass for each region is shared at the interface, and hence will be scanned twice over at a greater energy density input. Moreover, greater porosity exists at the interface in larger layer-thickness builds than exists in the bulk 60 and 90 µm regions, hence the introduction of a joint must be responsible for the presence of these interfacial pores. The trend also implies an increase in the coarse region layer-thickness increases the extent to which interfacial pores occur. The second contributing factor is thought to be the timing with which the two regions are processed. Since the 60 and 90 µm regions are only

lased every second or third layer respectively, while the 30 µm regions are lased every layer, one can expect a vertical wall of consolidated material against loose powder at the interface. For example, in layers where both a 30 µm and 90 µm layer region is processed, there exists a 60 µm consolidated region bordering 60 µm of loose powder beneath – where two 30 µm layers were processed, but the 90 µm layer is yet to be processed. This means when the border laser pass for the 60 or 90 µm regions is processed, a workpiece consisting of half consolidated material is produced (with near fully dense material) and half loose powder with a 65% packing density. The two are expected to exhibit significantly different laser absorptivities, with loose powder yielding superior energy absorption owing to the reflectivity of spherical Ti6Al4V powder particles enhancing laser irradiation [200][201]. It is possible, then, that the increased presence of keyhole pores can be attributed to a consistent remelting of previously consolidated material, since each 60 or 90 µm layer will require processing both a part-solid and part-loose-powder vertical interface below the current 30 µm layer being processed (one or two 30 µm layer region/s having been consolidated, and a loose powder 60 or 90 µm layer region). The parameters used to manufacture the specimens were optimised for consolidation of a uniform powder bed, hence further work modelling melt conditions at disparate layer-thickness interfaces (in which the powder bed is non-uniform) would likely inform methods to reduce interfacial porosity. Alternatively, custom scan paths can be explored to process each region as one continuous part to remove this phenomenon.

The presence of these larger pores aligned along the layer thickness interface is important, since it likely dictates both the fracture location and direction. In excess, this has potential to cause premature failure and hence lower ductility when compared with a single layer thickness, single region part, since keyhole pores accelerate crack initiation and propagation. This was confirmed by the tensile results and discussed in section 4.3.2.

The micrographs in Figure 24 show a band of fine grains growing out horizontally from the interface of the 30-90 µm butt jointed samples. This can likely be attributed to the remelting required of 90 µm layers. Since more time has passed to allow the previous two 30 µm layers to solidify, heat flux flows horizontally from the 90 µm layer of loose powder in to the 60 µm solid wall (plus 30 µm loose powder above) and encourages horizontal grain growth in the opposite direction. These finer horizontal grains are not evident in the castellated joint samples, possibly owing to the geometry of the teeth preventing a consistent vertical wall as it shifts 900 µm periodically. Apparent instead, is a clear arced interface in the microstructure

that highlights a harsher boundary between the two metal matrices (highlighted in Figure 24l), suggesting blending of the two is poor among these samples.

Another change observed in the micrographs is a change in alignment of the columnar grains. This was shown to have no bearing on the mechanical response and is attributed to the vector orientation of the laser path as opposed to having any link to the layer thickness or layer thickness interface.

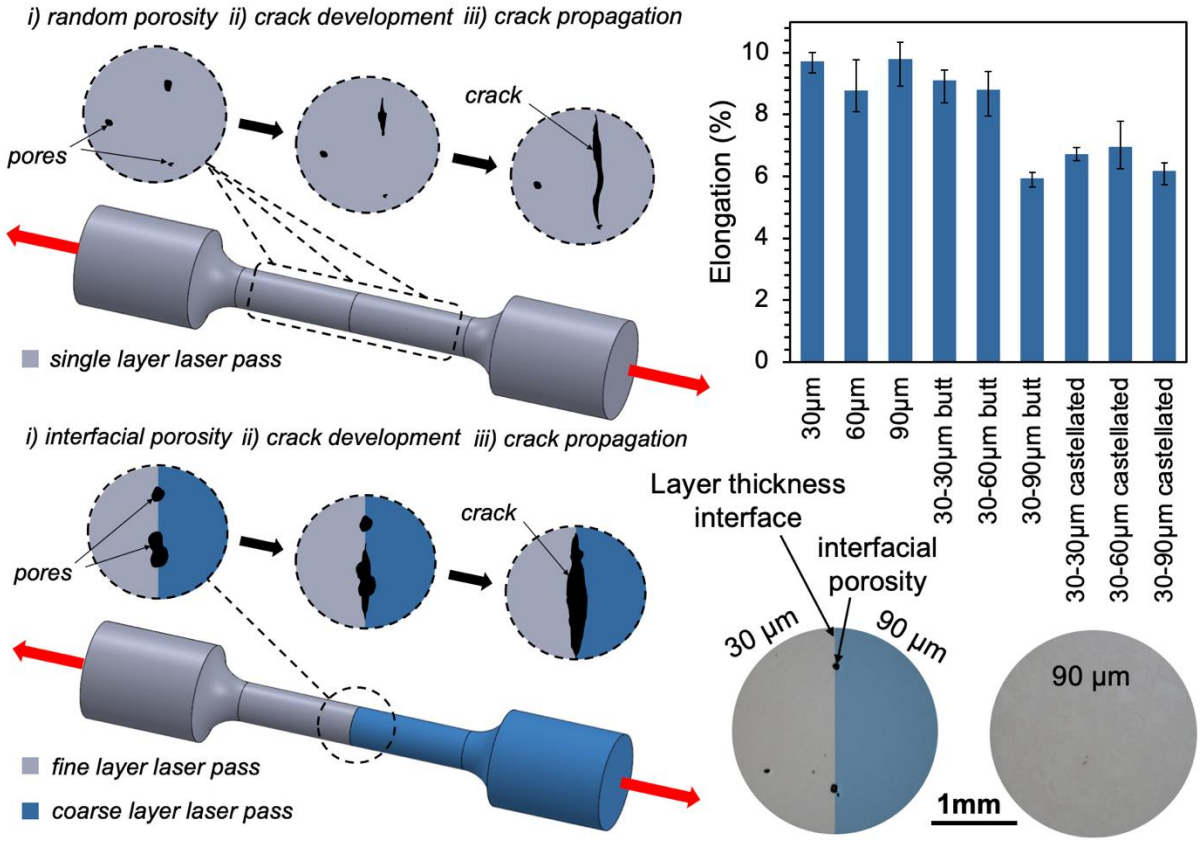

Figure 28 - A schematic to show the role of porosity in failure of samples featuring layer thickness interfaces compared with baseline samples, and the effect on ductility

4.4.2 Mechanical properties

It is clear the introduction of a joint reduces elongation to failure in the majority of samples. This may raise the point that a (single-layer-thickness) 90 µm layer part is the best option, since these samples exhibit the greatest productivity increase through processing the fewest layers, with no obvious penalty to mechanical response reported in the tensile data. However, mechanical performance is not the only reason one might limit thicker layers to regions of low interest as opposed to an entire part: surface finish, dimensional accuracy and staircasing are all worsened by significantly increasing layer thickness. To maintain higher part quality across various metrics then, it is important to maintain regions of finer layers in areas of high

interest; hence interlacing of 30-60 and 30-90 µm layers is deemed valid here despite identical tensile performance of the baseline samples.

The 30-30 µm jointed samples (top-right in Figures 5 and 6) were manufactured to isolate the introduction of a joint, and hence two parallel regions of one part, as the sole variable. In this way, layer thickness, build parameters and therefore grain structure remains similar either side of the join. Thus, observing any changes in mechanical response within the 30-30 µm jointed sample sets allows one to attribute said changes directly to the union of the two regions, since the bulk material is the same each side of the interface. Since these jointed samples failed exactly at the interface, despite the blending of grain structures at the boundary appearing to be seamless, it is thought that interfacial porosity is the root cause of the premature failure observed in the 30-30 µm castellated joins. By extension, all samples featuring an interface between two regions (30-30, 30-60 or 3-90 µm) likely fail due to interfacial porosity since they fail at the boundary location, however, the 30-30 and 30-60 µm butt jointed samples do not exhibit any penalty to elongation to failure, while the remaining 30-90 µm butt jointed samples and all three castellated samples do. One might anticipate the castellated joints provide a stronger union than butt jointed samples, due to the interlocking geometry increasing the region of blending between the two metal matrices, as was the intention with these designs. Nonetheless, it is hypothesised that, since interfacial porosity is likely the cause of premature failure, the significantly increased area of the castellated interface provides a larger region for defect formation when compared with the butt interface. This greater number of pores lends itself to accelerating crack initiation and propagation to a greater extent. We can therefore propose that interface design requires careful consideration with respect to the mating area between interfaces.

The 30-90 µm samples feature layer thickness boundaries displaying significantly greater interfacial porosity, both in terms of frequency and size as more keyhole pores became evident. Similarly, at 90 µm, these samples were the first to display evidence of an interface in the grain structure (section 4.3.1), exhibiting poorer fusion between the two regions. This could suggest 90 µm represents a critical layer thickness, at which the two metal matrices begin to show a clear microstructural boundary; this hypothesis may be supported further by the 30-90 µm castellated joins being the only sample set to show any reduction in UTS and yield stress, albeit very minor (1.4% and 1.6% respectively). It is possible that the observed microstructural boundaries have an effect on mechanical response of the joins;

nonetheless, the increase in interfacial porosity in the 90 μm sample sets likely dominates failure.

The method used to manufacture parts with multiple layer thicknesses in this study produces similar strength and elastic moduli in tension, with notable penalties to ductility. Hence the effects on tensile performance are likely to be tolerable, depending on the application. However, as evident in Figure 27, the presented production method is detrimental to the fatigue properties of the components and highly unlikely to be tolerated in any cyclical load service environment. As seen in the literature, internal pores play a far more crucial role in fracture under cyclic loading conditions when compared with standard tensile loading [152]. Given there are large pores identified along the joins of the samples that are also evident in fracture surfaces, the drop in fatigue life is attributed to their role as stress raisers that lead to fracture.

4.4.3 Fracture behaviour

Fracture surfaces indicative of more brittle failure are evident in the jointed samples as a whole, when compared with baseline samples. Similarly, an increase in layer thickness exhibits even less evidence of plasticity – indicated by flatter and rougher fracture surfaces as the coarser layer regions becomes thicker (30, 60 and 90 μm from left to right columns in Figure 26). As discussed in the tensile results section of the study (section 4.3.2), this is attributed to an increased fraction of internal defects at the interface between the two distinct regions of the part, using two parallel laser scan paths.

Simonelli et al. [154] reported that LPBF Ti6Al4V experiences intergranular fracture, owing to weak texture and α-laths arranged with high-angle boundaries. Since these samples were manufactured horizontally on the substrate, they feature large columnar prior-β grains perpendicular to the load direction. While interfacial porosity initiates crack growth in these samples, the crack propagates along the long edge of these prior-β grains (parallel) in the region of the interface. Altering the build orientation to angle the columnar grains will likely affect the failure of these samples. For example, vertically built samples will feature columnar grains parallel to the gauge length and thus fracture will likely occur perpendicularly through the cross sections of the grains. This has been shown in the literature to improve ductility at a small cost to strength since tensile residual stresses then act in the load direction [81].

4.5 Conclusions

A novel method to interlace multiple layer thicknesses within single LPBF components has been presented. This study characterises samples featuring a union between finer and coarser layer thickness regions to compare part quality with standard, single-layer thickness parts. This method enables increased build rates as thicker layers require significantly reduced laser-on time, while maintaining finer layers in regions of high interest to preserve part performance for specific load cases. Two interface geometries were examined - a flat surface join, or 'butt' joint, and interlocked teeth, or a 'castellated' joint. The samples were characterised by porosity analysis, microstructural analysis, tensile testing, fatigue testing and fractography.

While the findings here have demonstrated the validity of this method, some optimisation of the interfaces between disparate layer thickness regions is necessary, depending on the application. If adopted entirely for increasing throughput, further work is required to improve the fusion between the two regions to reduce interfacial porosity and therefore minimise penalties to mechanical performance (specifically fatigue life). The primary focus for achieving improved fusion is likely through custom laser scan paths, in which a tertiary laser pass may remelt the interface region to eliminate existing pores, the two regions may comprise of one continuous scan path as opposed to two parallel passes, or simply an optimised overlap between the two scan paths, for example. Further work is required to better understand the pore formation mechanisms before an informed decision can be made regarding a solution for eliminating them. Alternatively, this method may be adopted to tailor localised material properties at the interface, to achieve a desired mechanical response or to guide crack propagation under fatigue and creep conditions. For example, interface geometry can be designed to guide stress out of plane for a given service condition to improve part performance. There exists no one optimal interface geometry, but rather the design of the union must be optimised for each specific load case; for example, more complex load cases than that presented in this study may experience torsion as well as tension, and thus joint geometry will be required to combat sheer as well.

Dependent upon the application, the components investigated in this study may achieve a sufficient tensile response, given that Young's modulus, UTS and yield stress remain comparable across sample sets; however, a reduction in elongation of roughly one third must

be tolerated in the 30-90 µm butt joints and all castellated samples when compared with the baseline samples, 30-30 and 30-60 µm butt interfaces. While this response may be tolerable in uniaxial tension, the component designs had a more significant negative impact on fatigue life of the specimens due to the introduction of larger pores.

The conclusions are summarised as:

- Fabrication of components featuring regions of multiple layer thicknesses is possible, and geometry of the interfaces can be used to exploit design freedoms of LPBF.
- This method is capable of significantly reducing laser-scan times as well as manipulating metallurgy to control local part properties. Elongation to failure and UTS could be engineered into a given part.
- Further work is required to minimise interfacial porosity between two disparate layer thickness regions, as well as to tailor geometrical interface design for testing under a more complex load case, conducive to in-service conditions.
- Further analysis is required to understand the pore formation mechanisms at the layer thickness boundaries, in order to inform a solution.

In summary, this chapter has demonstrated a novel technique to significantly improve productivity of the LPBF process within the confines of standard machinery, with some penalties to mechanical performance due to induced porosity. Chapter 5 will investigate the formation of said pores and the failure modes at layer thickness interfaces in more detail, allowing for an informed adapted process solution to be devised and researched in chapter 6.

5 Failure modes in dual-layer-thickness Laser Powder Bed Fusion components

5.1 Introduction

In this study, an in-depth analysis of interfaces between disparate layer thickness volumes in single components was explored, to gain information vital to solving interface quality issues so that LPBF design freedoms can be fully exploited. This chapter builds on the previous by having conducted a detailed investigation into the interfacial porosity identified in chapter 4. The study aimed to characterise the pores, method of formation and failure modes of test specimens at the microstructural level. This information was crucial to understand the root cause of additional porosity and identify the necessary process adaptations most likely to reduce or eliminate them in the following chapter (chapter 6).

Interfaces were characterised in various planes to give greater information regarding formation of interfacial defects. XCT was used to characterise the pore signatures in each case, and tensile specimens were fabricated for micro tensile testing with in-situ microscopy to observe mechanical response at interfaces. Microscale dog bones have previously enabled tracking of all subsurface points of interest within small gauge volumes, such as pores and microstructural heterogeneities, so that individual contributions to failure can be assessed [202]. With the added benefit of in-situ microscopy during tensile testing, this method presents a powerful method of interface analysis for the research presented. Comparing XCT and fractography data meant that subsurface information could be related back to the tensile response and fracture location to determine the role of interfaces and interfacial porosity. Additionally, pre-test XCT and Focus Variation data of fracture surfaces were brought together to demonstrate an advanced 3D reconstruction technique to enable post-mortem evaluation of additively manufactured parts and track pore deformation. This method can be progressed to characterise transient defect behaviour, inform finite element models, and reverse engineer subsurface defect information from fracture surfaces without the need for XCT in due course.

5.2 Methodology

The methodology workflow used can be seen in Figure 29 and is detailed in the following sections (5.2.1 – 5.2.6). This workflow consists of: i) build preparation, in which dual layer thickness part files were prepared and sliced with two distinct parameter sets, ii) component fabrication, whereby wire electrical discharge machining was used to cut micro dog bones from blanks, iii) X-ray Computed Tomography to scan several samples at once to gather subsurface information, iv) sample preparation of the dog bones to ensure microstructure and pores were visible during testing, v) micro tensile testing with in-situ microscopy (fracture surface images were used to observe failure modes of the specimens) and vi) a 3D fracture reconstruction technique was developed to characterise pore behaviour.

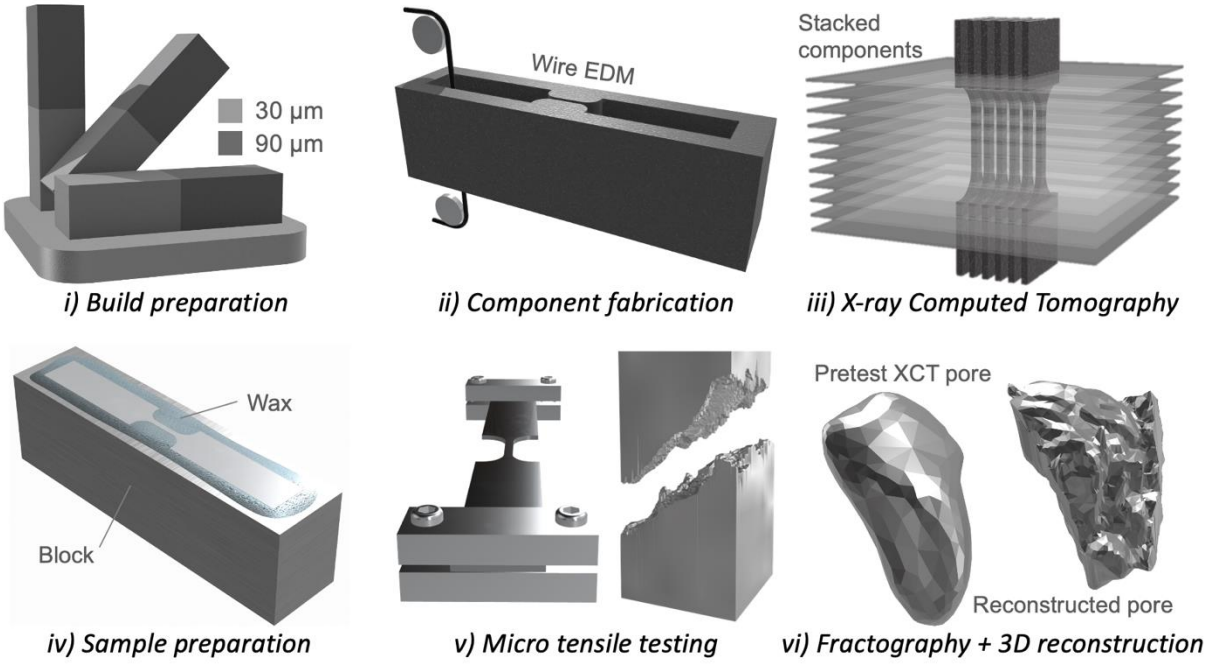

Figure 29 - The process workflow for achieving micro-tensile LPBF specimen geometry, subsurface pore information via XCT, subsequent mechanical data and 3D fracture surface reconstruction to further track pore behaviour

5.2.1 Build preparation

Specimens built entirely of 30 µm layers were produced as a reference, while counterparts comprised of both 30 and 90 µm layer regions with a boundary at the midsection. STL files of each half of the tensile specimens were sliced separately in EOSprint slicer software (EOS GmbH, Germany), according to the 30 and 90 µm parameter sets. These volumes were then brought together within the slicer software to form one volume, by ensuring the Cartesian coordinates align the interface to share a common border laser pass.

5.2.2 Component fabrication

LPBF specimens were produced on a commercial EOS M290 LPBF system (EOS GmbH, Germany), by Oerlikon AM Europe GmbH in Feldkirchen, Germany. The system uses a 250 x 250 x 325 mm build envelope, continuous 400 W Yb-fibre laser, and is operated with an 85 µm spot size. Grade 5 Ti6Al4V with a 20 – 63 µm particle size distribution, sourced from EOS, was used as the powder feedstock. A standard, well-understood material was selected to minimise material issues and allow focus to remain on the process design and behaviour that the study aimed to investigate. Optimised build parameters (to achieve relative densities >99.9%) were used for both 30 and 90 µm layer thicknesses - volumetric energy densities are 55.6 and 27.8 J/mm^3 respectively. Oxygen content within the build chamber was maintained at 0.1% and the temperature < 45°C.

Blocks were produced and 3 tensile specimens were machined from these blocks by wire electrical discharge machining (EDM) - 45 x 5.8 x 0.4 mm outer dimensions and a 2 mm length gauge with 0.4 x 0.4 mm cross section. Specimen dimensions were chosen according to the micro tensile testing system, which is restrictive in both dimension and load cell capacity. The 45 mm length was selected so the specimen tips lay flush with the far ends of each clamp to ensure sound gripping. The width was selected to achieve a sufficiently large surface for gripping and to maintain a similar aspect ratio to macro-scale dog bones of this type. The gauge cross-section, and subsequently sample thickness, was calculated by scaling down the ratio of maximum-load-to-cross-sectional-area from full scale specimens, built identically except for geometry.

The heat-affected zone created by the Wire EDM cutting process leaves a fine layer of recast that normally exhibits different characteristics to that of the bulk material, e.g. cracking and porosity [203]. This was removed from a series of trial specimens through hydrofluoric acid (HF) etching and the tensile responses were compared to counterparts still featuring a recast layer. Removing the recast layer had no effect on tensile response, and so it was tolerated in the specimens mechanically tested. One surface of each sample was ground and polished below the recast layer to examine as the surface of interest for optical imaging.

Six sample sets were produced for this study: standard 30 µm layer thickness samples as a reference, and samples with a 30-90 µm layer thickness interface at the midpoint of the gauge section, with the two variations built in 0°, 45° and 90° build orientations (see Figure

29). Build orientation is important here, since the orientation of the interface is also affected and as such is likely to impact the porosity and tensile data. It is also useful to observe real-time fracture of the anisotropic grain structure in different orientations at the microstructural level.

5.2.3 X-ray Computed Tomography

A Nikon MCT225 XCT machine (Nikon, Japan) was used to scan two samples per sample set (12 total) prior to tensile testing, to gather proximity, frequency, and size information regarding any pores in the gauge section captured in the scans. The voxel resolution of the scans was 6 µm – low resolution is a benefit of the micro-specimen geometry. The resultant image stack was processed in ImageJ software (ImageJ2 version 2.3.0, United States) to produce a 3D reconstruction of the gauge volume. BoneJ (an ImageJ plugin) was then used to run particle analysis on the XCT stack to count pores, create a surface mesh of each pore to measure enclosed volume, measure Feret diameter, and produce a 3D representation of porosity. Feret diameter represents the largest chord that can be fit between two points of the pore surface. BoneJ uses a greyscale thresholding criterion that is used to distinguish between pores and material. Relative density is also measured, representing the percentage volume of the gauge length comprising solid material, with the remaining percentage representing pores.

5.2.4 Sample Preparation

Dog-bone specimens were adhered to mounting blocks using wax and polished manually on stationary silicon carbide (SiC) abrasives due to the size, before polishing with 1 µm diamond suspension and colloidal silica. Additional dog bones were produced for microstructural analysis – primarily to observe microstructure at the interface and to visualise grain structure in each build orientation. The gauge sections were cut shorter to allow the specimens to be set within a 30 mm diameter resin block, before preparing using an automatic polisher and finally etching with Kroll's reagent (92.8% water, 6.1% nitric acid, 1.1% hydrofluoric acid) to reveal grain boundaries. Etching was performed at room temperature for approximately 10 seconds per sample. The samples were then imaged on a Nikon eclipse LV100ND optical microscope (Nikon, Japan) with a spatial resolution of 1 µm.

5.2.5 Micro tensile testing with in-situ microscopy

Tensile testing whilst recording the microscope field of view at 60 fps and capturing frequent images of the gauge section was conducted on a Deben MicroTest 200N tensile stage (Deben UK Ltd, United Kingdom), with a Leica M205 FA optical microscope (Leica Camera AG, Germany) in-situ. The microscope has a spatial resolution of 0.95 µm.

Tensile data points were recorded in the Deben MicroTest software with a sample time of 500 ms and a test speed of 0.2 mm/min. The cross-sectional area at the midpoint of each sample was measured prior to testing and this information inputted into the software to calculate stress-strain from load-displacement measurements. Two specimens from each sample set (those subject to XCT) were tested to failure under the optical microscope, and a third tested without microscopy.

5.2.6 Fractography and 3D pore reconstruction

SEM images of the fracture surfaces were collected using a JEOL JSM-6490LV Scanning Electron Microscope to provide additional insight into failure modes of the specimens. Fractography provided evidence of any sub-surface pores that may have instigated failure at that location and such was correlated to the XCT data to identify these pores. Fractography also supported any ductility discrepancies in the tensile data and enabled observation of fracture in different orientations across a small volume of material.

Fracture surfaces were also measured using an Alicona 'Infinite Focus' Focus Variation Microscope to gain 3D data and z-height information, with a lateral resolution of 176 nm and vertical resolution of 30 nm. STL files of the fracture surfaces were exported from focus variation data through Mountains surface metrology software, and STL files of subsurface defects were obtained by running the XCT data through a MATLAB script. This enabled a 3D reconstruction comparison for post-mortem evaluation of failed specimens, by aligning corresponding fracture surfaces and pore files in CAD software. By using fracture surface counterpart STLs, it was possible to also reconstruct the pores post-test from the fracture data by aligning the fracture surface and using Boolean operation to extract the voids. This method is successful in extracting medium-to-large pores (> 50 µm in this study), however, small pores are difficult to discern amongst the fracture surface texture.

5.3 Results

5.3.1 Porosity

Figure 30 below shows an example of XCT data for a 30-90 µm specimen with 45° build orientation. A 3D render of the XCT image stack provides a visualisation of the gauge section, while a second 3D render of strictly porosity is superimposed over it to provide trend and location information.

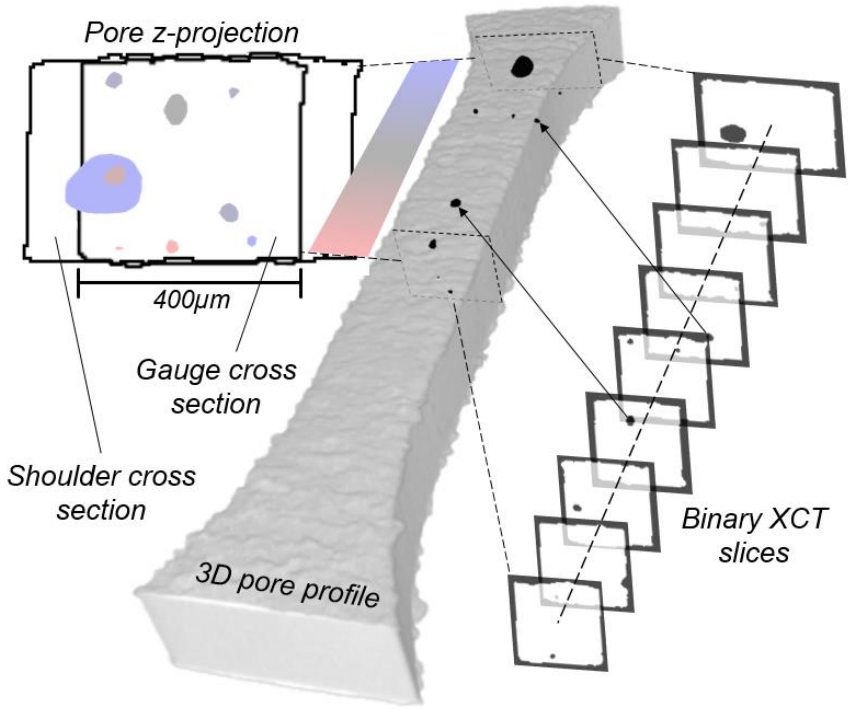

Figure 30 - A 3D XCT render of the dog bone gauge length for a 30-90 µm sample built at 45° orientation, with a 3D render of porosity superimposed over; a z-projection of porosity (top left) and XCT slices corresponding to pores (right) are shown

A comparison of porosity across sample sets can be seen in Figure 31 and numerical data in Table 3, detailing themean Feret diameter across all pores, with total number of pores present in each gauge volume. Only a small number of pores are evident in the specimens due to featuring geometry at the microscale, however, this enables individual defect contributions to failure to be observed. For the 30-90 µm jointed samples, 0° orientation shows a small number of large pores, concentrated at the interface location. XCT and particle analysis of the two samples investigated measured mean Feret diameters of 88.5 and 58.5 µm – the two largest of all samples measured. Despite the size, there were fewer pores than evident in the 45° orientation. The 45° specimens exhibited a greater number of pores, as well as showing a more sparse distribution over the gauge length that does not give a clear

indication of interface location. The mean Feret diameters for these two samples were 40.8 and 44.6 µm. Only one pore was evident between the two 90° joined specimens, with a small Feret diameter of 4.6 µm and located away from the interface location, implying the interface does not induce additional porosity in this build orientation. The single pore found amongst these specimens is likely a gas pore, given it is very small in size and is roughly spherical. A gas pore such as this will have been naturally produced during any standard laser processing and not a result of the dual-layer thickness method adopted in this study.

The 30 µm standard specimens serve as a comparison to confirm interfacial porosity in dual layer thickness specimens. The data confirms this, as no pores were evident in the 0° orientation and only 2 small keyhole pores were evident in the 45° orientation (based on size and morphology), attributed to formation during standard processing conditions. The 90° orientation, however, features more pores than all other sample sets, including jointed specimens – some of which reach Feret diameters in excess of 50 µm. Given that the large pores are aligned directly on top of each other in the build direction, it is most likely the gauge volume has captured an area of the powder bed that suffers from a recurring defect, hence the same area is affected at random layer intervals. Since both specimens subject to XCT were built adjoining and are only 400 µm thick, it appears both were affected by the problem area and display a large number of standard formed pores.

Table 3 - Porosity characteristics of specimens subject to mechanical testing

Sample Set	Sample No.	No. of pores	Mean Feret diameter (µm)	Avg. relative density (%)
0° jointed	1	3	88.5 ± 25.5	99.994
	2	7	58.5 ± 57.6	
45° jointed	1	8	40.8 ± 19	99.996
	2	9	44.6 ± 41.3	
90° jointed	1	0	0	100
	2	1	4.6	
0° reference	1	0	0	100
	2	0	0	
45° reference	1	2	32.45 ± 3	99.999
	2	2	23.7 ± 3.8	
90° reference	1	16	41.5 ± 14.1	99.995
	2	17	27.3 ± 29.8	

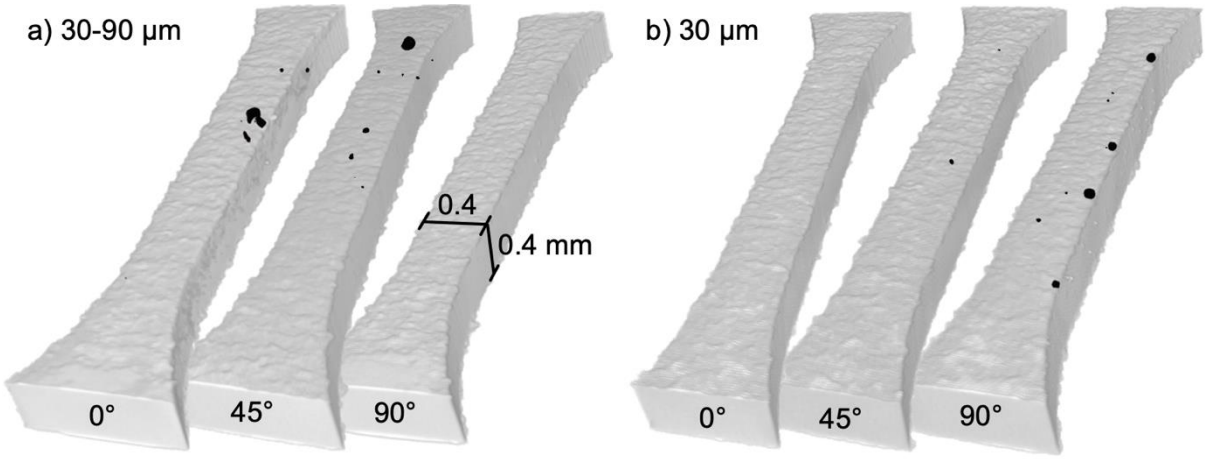

Figure 31 - 3D render of XCT scans showing gauge section and subsurface porosity in 0°, 45° and 90° build orientations for a) 30-90 µm joined specimens, and b) 30 µm standard specimens

5.3.2 Microstructure

Figure 32 shows the polished gauge sections of each 30-90 µm specimen in 0°, 45° and 90° build orientation. There is no evidence of poor fusion across the interfaces, such as grain discontinuity, nor appears any obvious disparity in grain size or texture between the 30 and 90 µm regions. As expected, columnar grains appear perpendicular to the gauge length in the 0° orientation, parallel in the 90° orientation, and 45° to the gauge length in the 45° orientation; however, this appears clearer in Figure 33 depicting the microstructure of the 30 µm reference samples due to the etch better highlighting the grain boundaries.

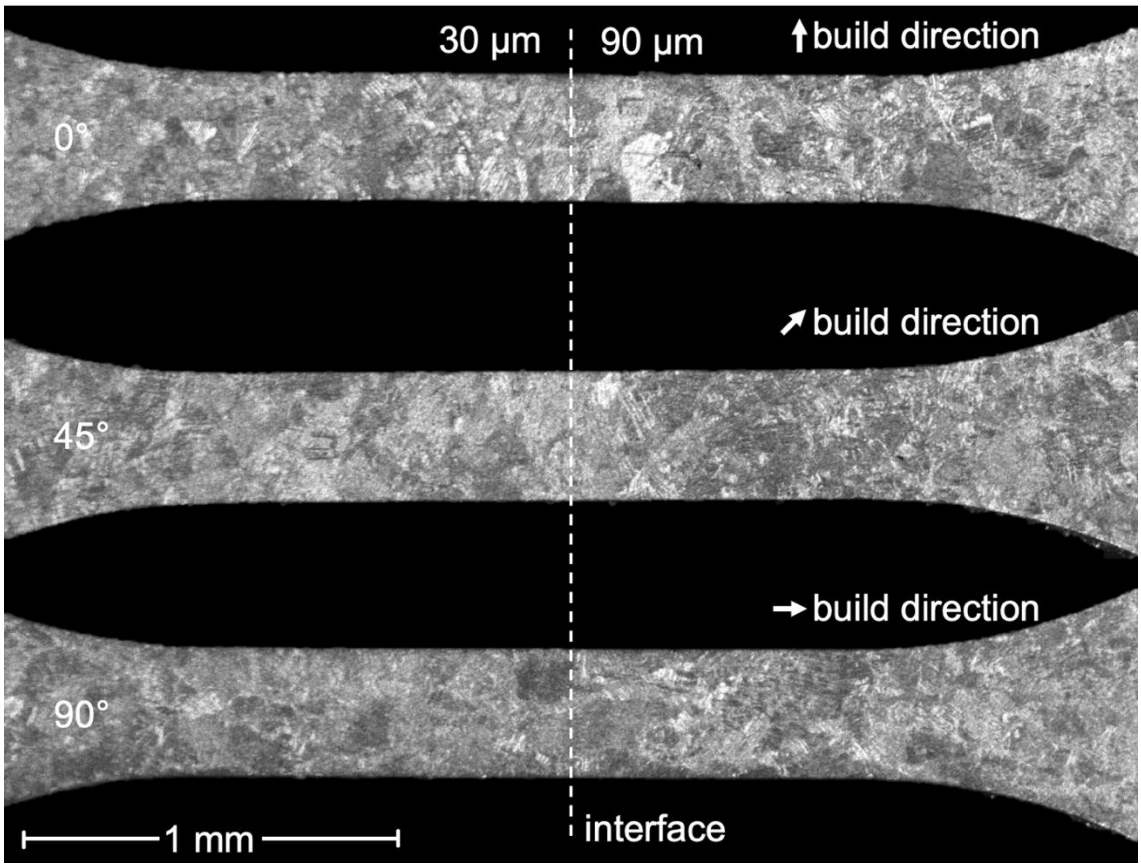

Figure 32 - Optical micrographs displaying microstructure in dog bone gauge lengths for 30-90 µm specimens; 0° (top), 45° (middle) and 90° (bottom) build orientations are shown; 30 µm regions are on the left and 90 µm regions are on the right

The image of the 30 µm reference samples gives a clearer indication of the number of grains represented in the gauge volume of the specimens, and more importantly, their distribution across the width of the gauge. In the 0° orientation, several grains can be seen with length > 400 µm and hence span the full width, meaning it is difficult to calculate an accurate average length. Of the grains for which length is measurable, the average grain is 266 µm in length. Each grain is 109 µm in width on average and so roughly 4 grains will stack throughout the thickness of the sample. A similar phenomenon is evident in the 45° build orientation specimen, with slightly more grains visible due to the orientation allowing greater lengths of columns to be captured. Lastly, the 90° build orientations capture the greatest number of grains since they are packed parallel to the gauge length. Nonetheless, it is important to note that even in the 90° orientation, tensile tests are evaluating roughly 16 grains at most for any given cross-section, and 4 in the case of 0° specimens. Therefore, this cannot be considered an accurate representation of bulk Ti6Al4V material, but rather the selection of grains.

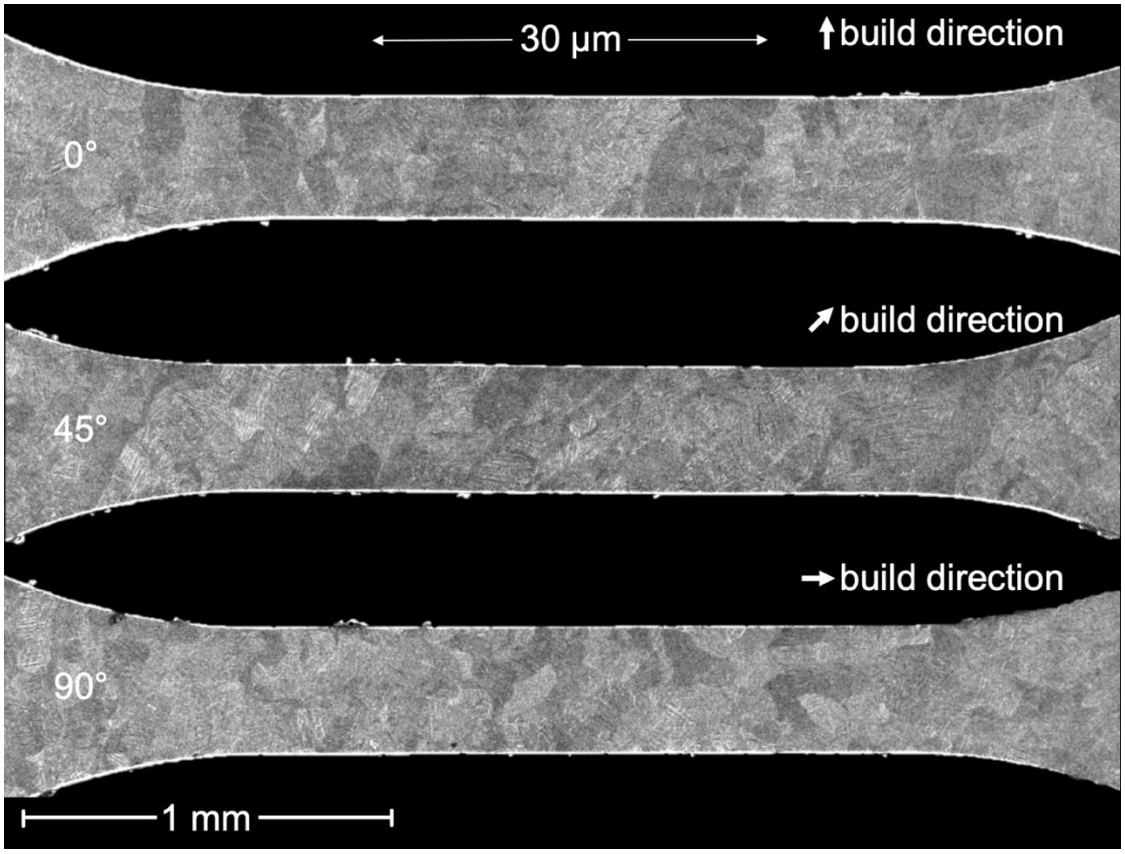

Figure 33 - Optical micrographs displaying microstructure in dog bone gauge lengths for standard 30 µm specimens; 0° (top), 45° (middle) and 90° (bottom) build orientations are shown

5.3.3 Micro tensile behaviour

The micro specimens display a typical elastic and then plastic tensile response. Low values for elastic modulus were recorded between 4.98 – 6.35 GPa, and high values of elongation to failure were recorded within 22.1 – 27.5%. This is attributed to the small number of grains captured within the micro gauge section (described in Section 5.3.2). Ultimate tensile strength and yield strength values were around 20 – 30% lower than is generally seen in full scale LPBF Ti6Al4V [198]. There is little to separate the responses of the 6 sample sets, nor the joined specimens with reference specimens – in part due to poor repeatability. The elongation value for the 30-90 µm specimens build at 0° is noticeably lower compared with 45° and 90° (22.1% compared with 27.1% and 26.4% respectively) and it is evident from the curves that the specimens fail quickly after entering the plastic region.

Table 4 – Micro tensile data for the 30-90 µm and reference specimens

Layer thickness (µm)	Build orientation (°)	Elastic modulus (GPa)	Elongation (%)	UTS (MPa)	Yield Stress (MPa)
30-90	0	4.98 ± 0.81	22.1 ± 4.1	857 ± 26	803 ± 53
30-90	45	5.37 ± 0.16	27.1 ± 1.1	883 ± 65	754 ± 145
30-90	90	5.54 ± 0.36	26.4 ± 1.1	901 ± 9	842 ± 6
30	0	5.59 ± 0.16	24.1 ± 0.9	870 ± 35	804 ± 31
30	45	6.35 ± 1.46	23.2 ± 0.9	855 ± 96	760 ± 124.5
30	90	5.19 ± 0.39	27.5 ± 1	814 ± 34	757 ± 37

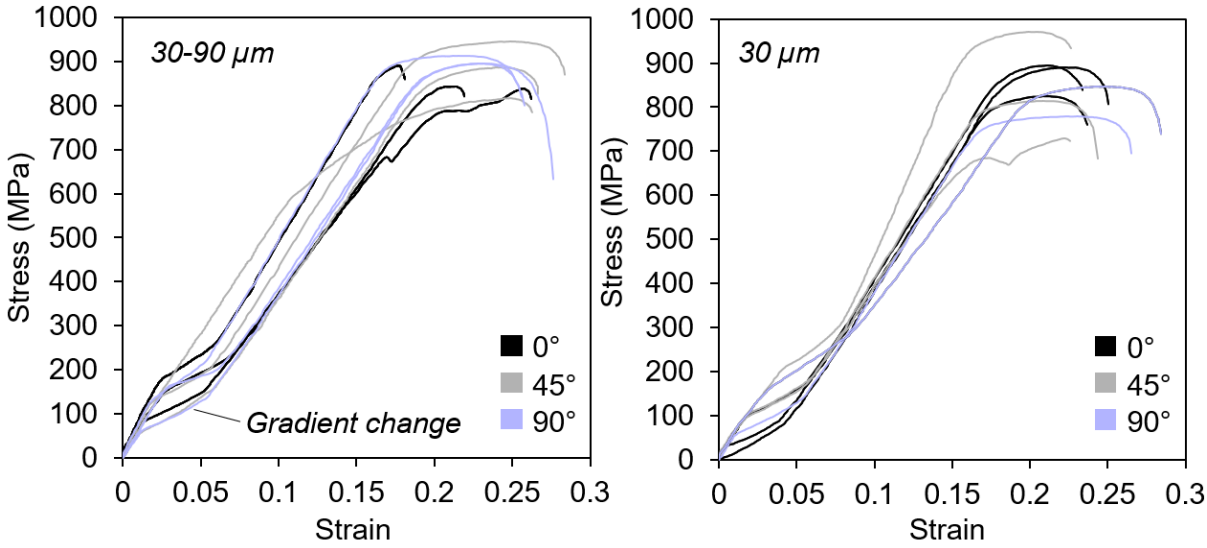

Figure 34 - Tensile curves of Ti6Al4V micro dog bones, built by LPBF in 0°, 45° and 90° build orientations; 30-90 µm dual layer thickness samples (left) and standard 30 µm samples (right)

Figure 35 gives an example of a 30-90 µm 0° orientation specimen, with a surface pore identified at the beginning of the test that ultimately leads to crack initiation and fracture. The figure displays this process in four stages: i) a small surface pore of Feret diameter 23 µm can be seen in the top image prior to testing; once in the plastic region, the pore has grown to 53 µm and begins to initiate a crack in the second image. In the third image, the crack has begun to develop and the pore measures 74 µm. There are visible signs of local plastic deformation surrounding the pore, indicated by a change in reflection of the light, and finally failure occurs at the pore location and propagates along the grain boundaries visible in the earlier images.

This behaviour can be contrasted with that shown in Figure 36, in which the same 0° build orientation is shown for a standard 30 µm specimen that exhibited no pores when subject to XCT. There is no pore location to focus on, however strain is visible in the second image when comparing a marker location with the first image. The third image shows signs of deformation and necking around one region of the specimen, not concentrated as seen with the pore in the previous figure. Lastly the final image shows fracture along the grain boundaries once again.

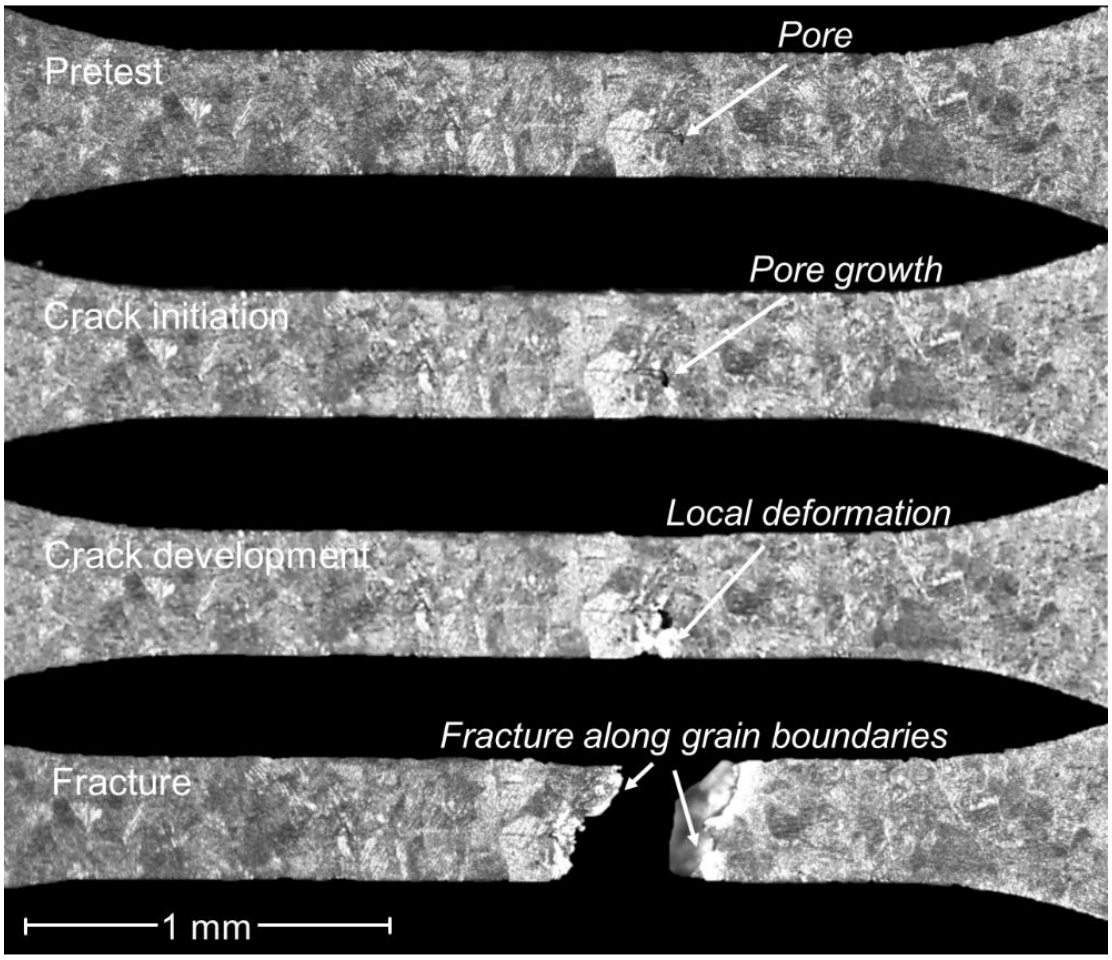

Figure 35 – Staged optical images during micro tensile testing of a 30-90 µm 0° build orientation specimen, showing evidence of an interfacial pore that leads to failure

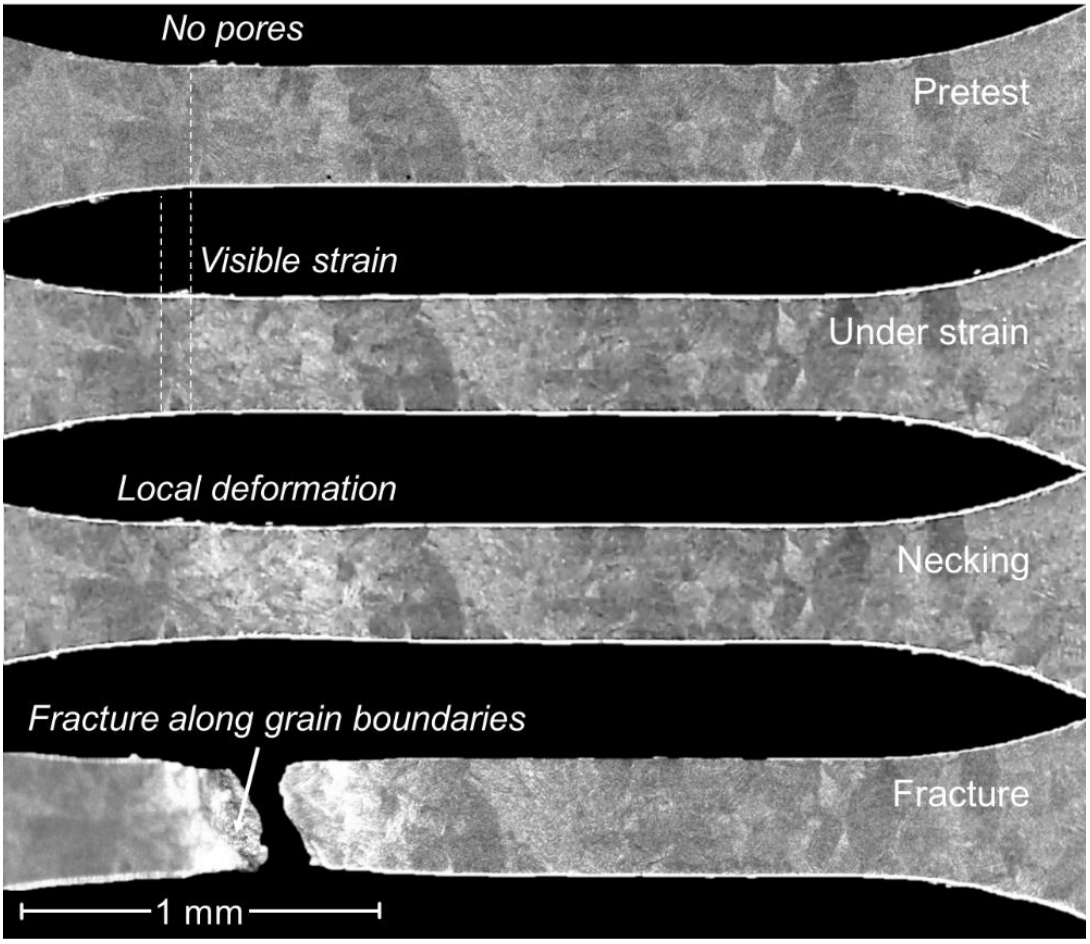

Figure 36 - Staged optical images during micro tensile testing of a standard 30 µm 0° build orientation specimen, showing failure of a dog bone containing no pores

5.3.4 Fracture behaviour

Figure 37 shows a fracture surface for each instance: 30-90 µm joined specimens in 0°, 45° and 90° build orientations (a, b and c respectively), and 30 µm standard specimens in 0°, 45° and 90° build orientations (d, e and f respectively). In image (a), multiple large pits can be seen with a smooth surface texture not thought to be generated via failure. This implies a material discontinuity and hence the pits are thought to represent pore locations. The same evidence was found at a smaller scale in images (b) and (f), implying that 30-90 µm 0° and 45°, as well as 30 µm 90° all failed at the site of an internal defect, with more extreme defects observed in the 30-90 0° specimen.

Images (c), (d) and (e), show no evidence of similar pits or evidence of discontinuity, implying failure was not initiated by an internal defect for 30-90 µm 90° and 30 µm 0° and 45°. In all cases, this agrees with the porosity trends found in the XCT analysis.

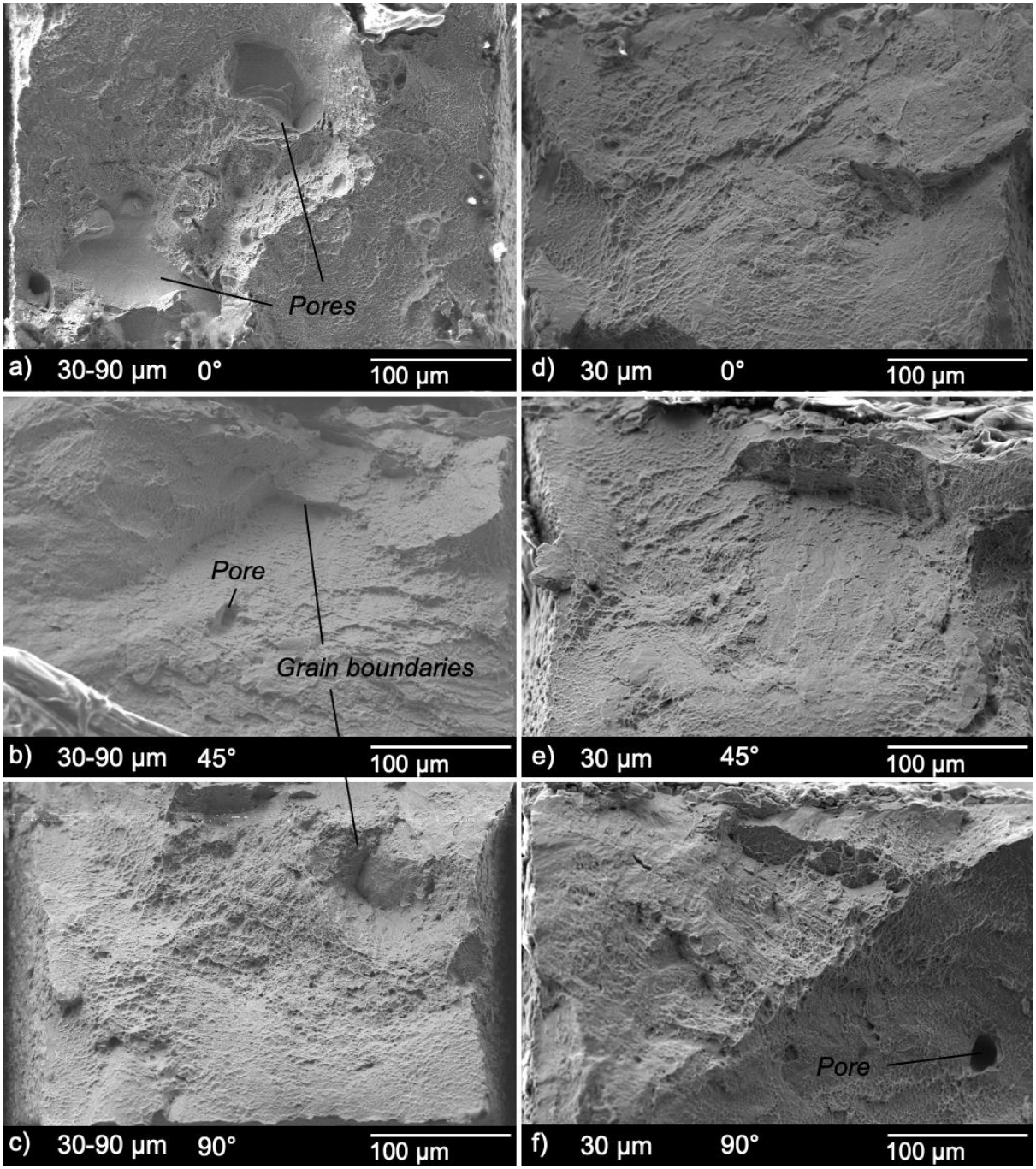

Figure 37 - Fracture surface images a) 30-90 µm 0° build orientation b) 30-90 µm 45° build orientation c) 30-90 µm 90° build orientation d) 30 µm 0° build orientation e) 30 µm 45° build orientation f) 30 µm 90° build orientation

All specimens exhibited a ductile fracture surface. Figure 38 shows evidence of the fine micro-dimples that describe ductile fracture, as well as highlighting some pore characteristics found in a 30-90 µm 0° build orientation specimen. Image (a) shows features of molten material that have remained intact, while image (b) displays partially melted powder particles and a martensitic grain structure from the underlying as-built microstructure, both preserved due to material discontinuity.

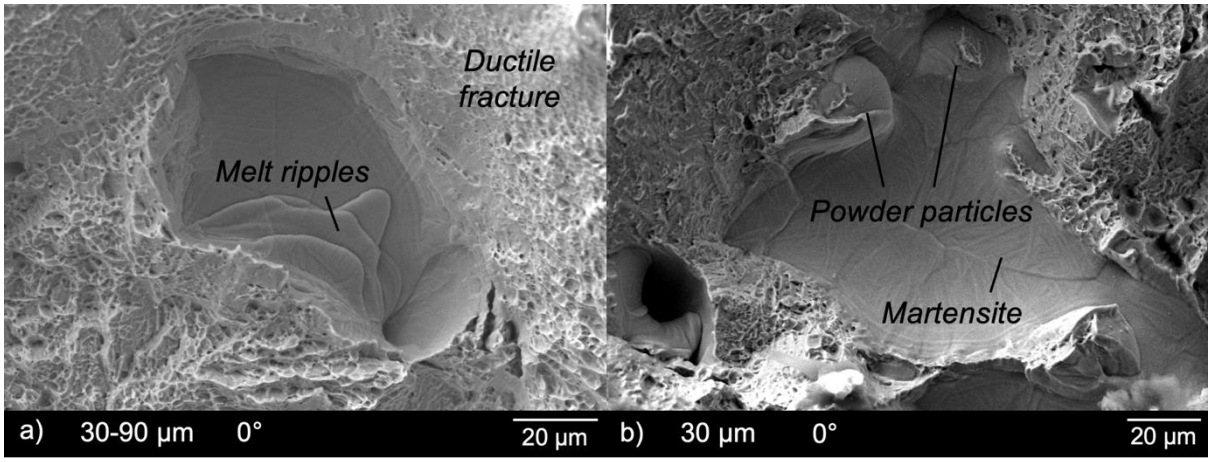

Figure 38 - Evidence of pores on the fracture surface of a 30-90 µm 0° build orientation specimen

5.4 Discussion

5.4.1 Porosity

This research provides significant evidence that discretising single components into sub-volumes with disparate layer thicknesses creates large pores at the interface between regions. It is clear this additional porosity is a result of introducing layer thickness interfaces and that process optimisation is necessary to better blend the 30 and 90 µm layer volumes together. Interlacing geometry using interlocking teeth (much like a housing joint) had little effect in chapter 4, however, optimised scan strategies that process the part in one continuous pass are likely to improve fusion. At present, this requires custom writing of scan vector files.

Interface build orientation has a direct effect on the extent of interfacial porosity. The 90° build orientation has not suffered from large interfacial porosity, likely due to featuring a horizontal interface (i.e. substrate or xy plane). Since the interface is parallel to the substrate, 30 µm layers have been processed up to the interface and 90 µm layers thereafter – there are no layers in which 30 and 90 µm regions are processed together. If the interface is taken out of a plane parallel to the substrate, 30 and 90 µm regions require processing in common layers. In these interfaces, such as the 0° and 45° part orientations presented here, interfacial porosity becomes an issue, implying laser processing of the 30 and 90 µm areas in mutual layers is the source issue. The route cause of these pores is likely one of two mechanisms: i) keyhole collapse occurring in vector end-points at the interface, whereby 90 µm layer vectors are lased up to the boundary of the previously consolidated 30 µm layer material; at which

point, the reflective bulk material causes a sudden drop in laser absorptivity and subsequent collapse of the melt depression, leading to keyhole pore formation (a similar phenomenon is sometimes seen when border contours are scanned prior to the infill hatches); or ii) the border pass of the first region causes powder denudation at the interface region, leaving a deficit of powder before the second region is exposed and leading to keyhole porosity due to excessive energy input into the thinner powder layer remaining. Each provides strong evidence that optimising laser scan strategy when processing both 30 and 90 µm regions in mutual layers is key to eliminating interfacial porosity.

This hypothesis agrees also with the distribution and size of pores across the specimen gauge length. In the 0° build orientation, the interface is processed at the same location on the substrate every layer and hence the porosity affected zone is limited to this area throughout the build – displayed in Figure 39. This gives rise to more concentrated pores seen in the XCT scans and large pore sizes since consistent defects in this area contribute to defects formed directly above in successive layers. The same effect is seen in the 45° specimens; interfacial pores affect successive layers and hence pores are grouped primarily in one half of the gauge section – since this half was positioned higher in the build volume and processed after interface areas. However, due to the angle of the part, the interface area translates laterally each layer, which in turn keeps pore sizes smaller than the 0° build orientation by avoiding stacking interfacial pores directly on top of each other. These affected zones are depicted in Figure 39 below. Standard pore formation mechanisms have been reported frequently, predominantly highlighting lack of fusion and keyhole pores as a function of volumetric energy density and varying process parameters [204]; however, the present study describes new pore formation mechanisms as a result of process parameter disparity among component sub-volumes.

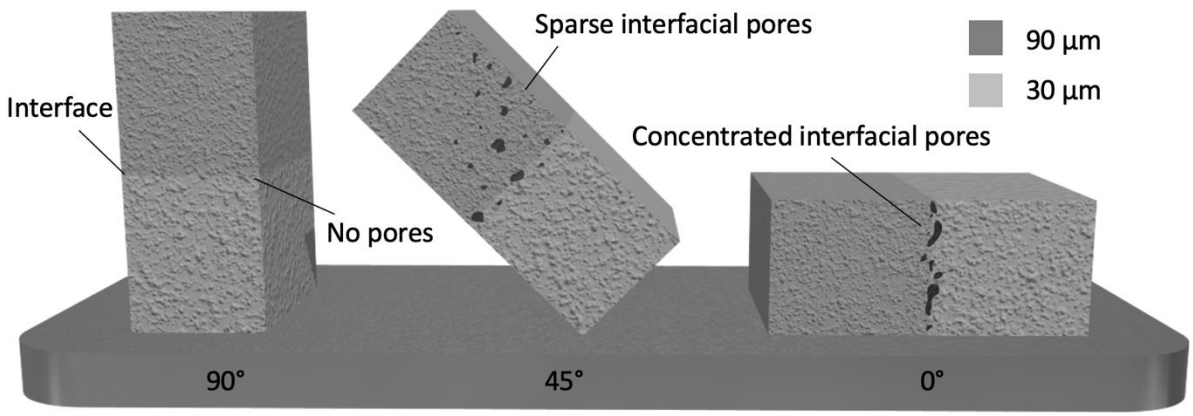

Figure 39 - The effect build orientation has on pore distribution throughout 30-90 µm specimens

5.4.2 Micro tensile behaviour

Due to porosity and microstructural discrepancies having an amplified effect at this scale, large errors were present in the tensile data making it difficult to compare sample sets. This was not the case in Chapter 4, in which full-size specimens were examined and discrepancies were clear with very low uncertainty compared to the present study. This was expected, due to the micro specimen geometry capturing only several grains in the cross section, exhibiting a very localised mechanical response as opposed to a typical bulk material response. Benzing et al. [202] have also reported differing tensile response in meso-scale additively manufactured Ti6Al4V components when compared with bulk material. However, this does not affect the research objectives of the study, since failure modes and fracture behaviour are the primary concern and micro tensile testing with optical microscopy in-situ has enabled the role of individual defects to be tracked and understood.

The data from the present study show superior elongation values in the 90° specimens when compared with the 0°. This is attributed to the columnar grain orientation, with longitudinal columns providing superior ductility, whereas transverse grains induce more brittle behaviour, as is displayed by the narrower plastic regions evident in the 0° tensile curves. This is more prevalent in the 30-90 µm 0° orientation curves, where failure can be seen to occur very quickly after entering the plastic region. Since this was not seen in the reference samples, the further increase in brittleness is directly attributed to the large pores.

The same premature failure was not seen in the 45° orientation 30-90 µm specimens despite a high number of large pores. It could be possible the critical pore size lies somewhere between 85.9 – 116.1 µm for these dog bone dimensions (the maximum for 45° and 0° build orientations respectively); however, it is more likely the premature failure in 0° orientation

specimens is a result of the combination of interfacial porosity and transverse grain orientation.

Figure 35 shows a pore on the surface of a 0° orientation 30-90 µm specimen that ultimately led to failure, the location of which strongly agrees with the location of concentrated pores in the XCT data, meaning it is more than likely an interfacial pore. This provided excellent proof in support of interfacial porosity being the root cause of premature failure in full scale samples. It is a good example of the role interfacial defects play as single point stress raisers that can lead to failure, and also evidence that failure location can be selected in components through interface placement. To this end, in the columnar grain structure in LPBF Ti6Al4V, cracks were found to propagate along the long edge of prior-β grains, parallel to grain growth in the build direction. Hence, with careful consideration, crack initiation site and propagation direction can be engineered into components.

5.4.3 Fracture behaviour

The three sample sets that exhibited a high number of large pores (30-90 µm 0°, 45° and 30 µm 90°) all showed specimens featuring evidence of internal defects in the fracture surfaces, consistent with other studies in the literature that have identified pores in LPBF fracture surfaces [125]. However, the additional benefit in this study is the small number of pores captured in the micro-specimens can be tracked from initial XCT to fracture signature with ease. This is further strong evidence that these pores typically invoke crack initiation. The 30 µm 90° orientation specimens are somewhat anomalous, given that very little porosity was evident in the other reference samples; the excessive porosity seen in these samples is likely a result of being built in an area of the substrate that suffered from a periodic defect, affecting all successive layers. This may have been caused by a spatter particle or an area of the powder bed in which layer height briefly fluctuates (a large particle removed by the recoater blade for example).

Fracture surface data has been compared with XCT data in the same location. Figure 40 shows this comparison for a 30-90 µm 0° build orientation specimen – the most extreme case and the scenario most representative of joining disparate layer thickness volumes with interfaces in xz or yz planes. This location in the XCT stack features the largest pore measured by particle analysis (175 µm Feret diameter), on the lower left of the images, and so is the primary defect likely responsible for crack initiation. The pore has a large keyhole morphology

spanning close to the surface polished for micro tensile testing and appears the polishing process removed sufficient material for the pore to become visible on the surface. The in-situ optical recordings showed this pore to be responsible for fracture; despite appearing small on the surface, fractography and XCT have shown that, subsurface, the interfacial pore was very large and extremely likely to have instigated fracture of the specimen.

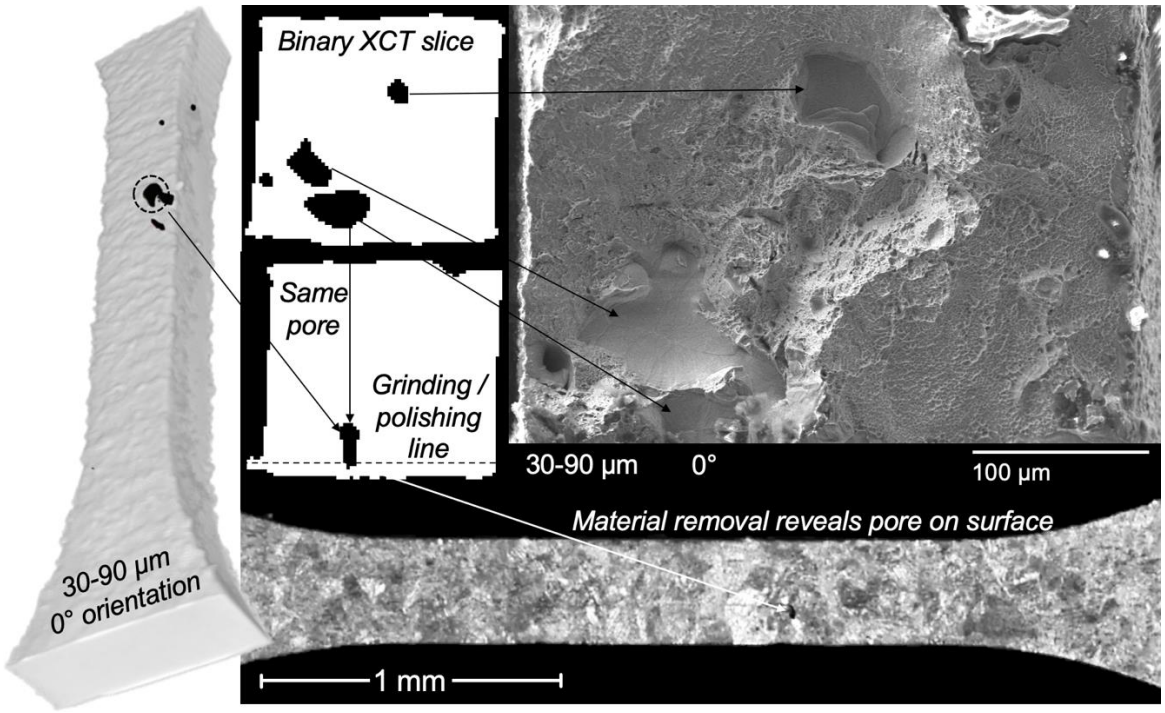

Figure 40 - A corelation of fractography, 3D and 2D XCT data, and in-situ microscopy of micro tension for a 30-90 µm 0° build orientation specimen; the figure highlights the interfacial defect responsible for failure of the specimen

Focus Variation data was collected to provide additional z-height information that was not available from two-dimensional SEM fractographs. Figure 41 shows the surface topography of fracture surfaces from each sample set. This method also clearly shows pore locations, as well as revealing additional grain boundary pits, owing to crack propagation adhering to grain boundaries in which tips of prior β grains create pits in the fracture surface. These pits show typical ductile fracture surface texture, hence it is clear homogenous material existed in these areas and not voids that would otherwise show smooth surface texture. Additionally, the pits believed to be caused by grain boundaries match columnar grain orientation; (a) and (d) do not show grain pits, since the grain boundaries span the full thickness perpendicular to the gauge section; (b) and (e) show elliptical pits as the columns cross the section at 45°; (c) and (f) show circular pits since the columnar grains run parallel to the gauge section. These microstructural features are consistent with the literature findings for Ti6Al4V crack

propagation in various orientations [154], with the addition of new pore formations found in the fracture surfaces of this study.

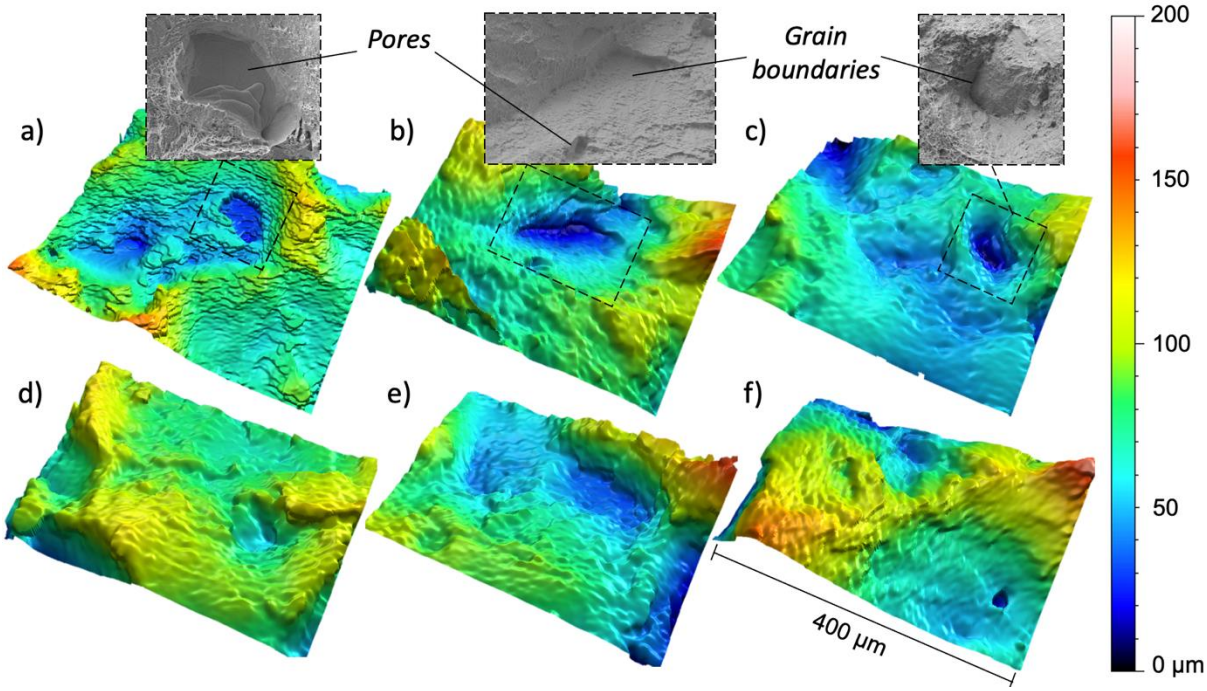

Figure 41 - Focus variation images of fracture surfaces compared with SEM fractographs for a) 30-90 µm 0°, b) 30-90 µm 45°, c) 30-90 µm 90°, d) 30 µm 0°, e) 30 µm 45°, f) 30 µm 90°

5.4.4 3D reconstruction

Figure 42 shows an example of interfacial pores (prior to tensile tests) aligned with pore location sites found in the fracture surface in 3D space. This technique presents an especially comprehensive way to visualise internal defects and their contribution to component failure. There was strong agreement in location, size, and morphology between the two; however, there were minor discrepancies given plastic deformation altered the geometry of defect sites in the fracture surface. Each pore was measured in x and y directions in pre-test XCT data and post-test fractographs. Pore sites were found to be 10.0 – 14.1% smaller in the x direction and 10.3 – 14.6% in the y direction. Larger pores generally exhibited the greatest reduction in size, likely due to experiencing plastic deformation earlier as an area of higher stress concentration. This technique has the significant benefit over the literature of measuring transient pore behaviour across the tensile test, whereby most studies have previously simply established pore size and location [59]. The method could also be extended to make use of more recent pore inspection techniques researched in the literature, such as acoustic wave spectroscopy [205] or pyrometry [206]. These methods typically exhibit greater scan speeds

at much lower cost compared with XCT, and are conducive to future in-situ inspection methods.

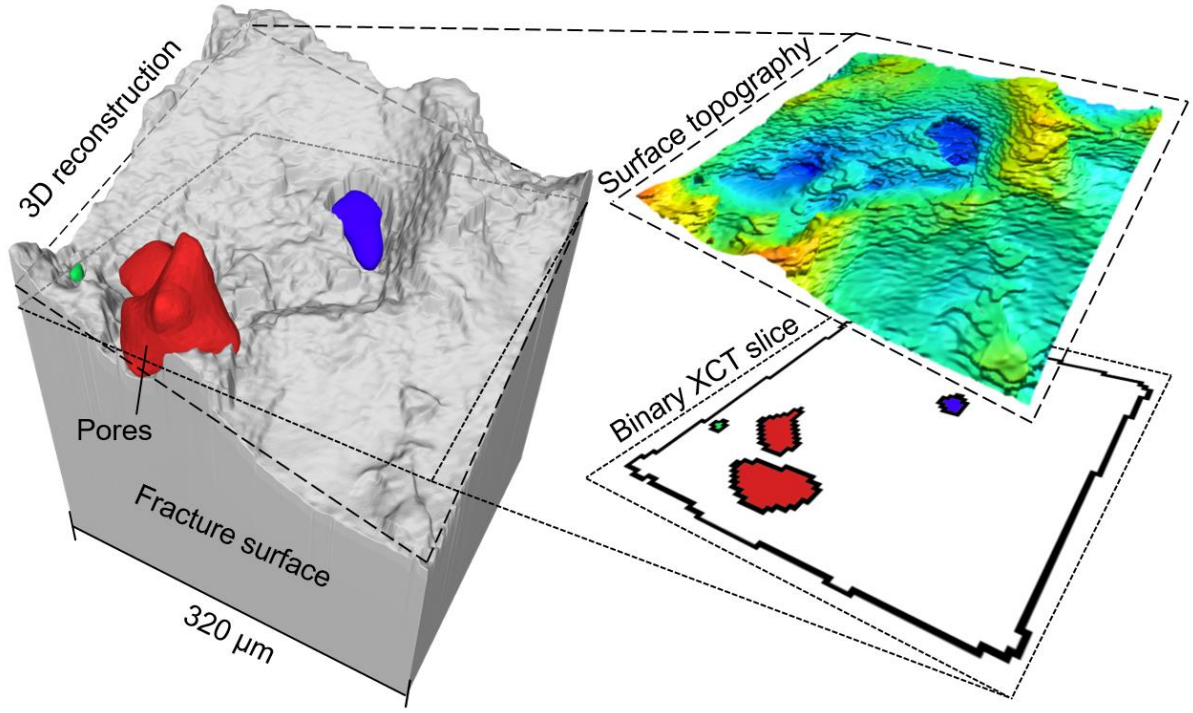

Figure 42 - A 3D STL reconstruction of fracture surface from focus variation data and subsurface pores from XCT data prior to testing, compared with surface topography map and XCT slice

A mesh comparison is shown in Figure 43 to display the discrepancy in size and morphology of pores in the pre-test state with the post-test state. Contrasting XCT measurements with FVM measurements yields a combined measurement uncertainty of 6.18 µm laterally and 6.03 µm vertically (i.e. a voxel resolution of 6.18 x 6.18 x 6.03 µm). The cross section (plane perpendicular to the gauge length) of the pores is seen to constrict, while elongating in the strain direction, as typical with tensile testing. The pore identified earlier as the crack initiation site shows additional deformation around the surface, where early stages of crack propagation have been captured in the fracture surface. This is not evident in other pores in this specimen, and so demonstrates the ability of this method to highlight defects responsible for instigating component failure.

Image (b) and (c) in Figure 43 shows the progression of pore morphology at crucial intervals of the tensile test i) pre-test, neutral state ii) elastic behaviour iii) plastic behaviour iv) fractured state, post-test. In the elastic region, the pore changes aspect ratio but mostly maintains the surface morphology; beyond the yield point, the pore begins to show rough plastic deformation around the surface. Observing 3D pore behaviour under load adds a new

dimension over current class pore characterisation that is typically limited to pre-test XCT or microscope imaging [125]. This method enables a finite element model to interpolate between test stages and observe the full progression of subsurface pores or cracks under given strain conditions and could be improved further with additional mid-test data. The information is likely to be more useful under cyclic loading conditions to aid in modelling fatigue response, since the role of internal defects is amplified and current state of the art is lacking in pore behaviour information [207]. With enough preliminary data, fracture surfaces can also be reverse engineered to approximate subsurface information around the failure location prior to mechanical testing, without the need for XCT data, and is significantly more time and cost effective.

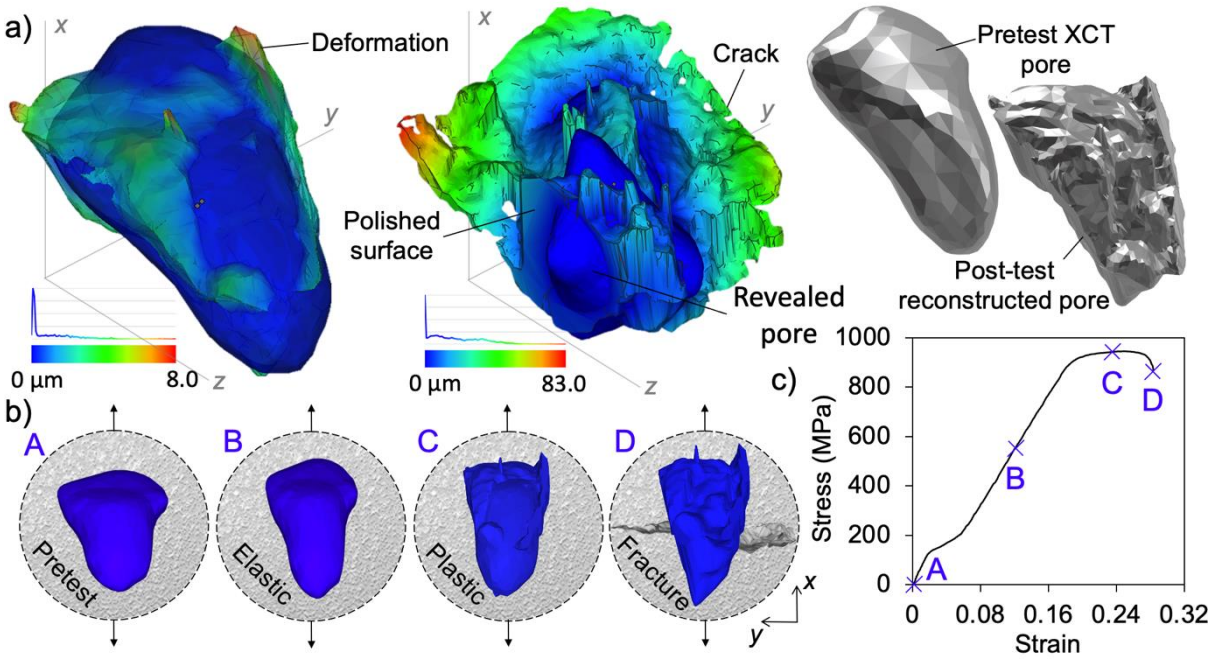

Figure 43 - A comparison of pores prior to testing (XCT data) and post-testing from reconstructed fracture surfaces, a) shows an STL mesh comparison of pores in both states and highlights the deformation in a colour map, b) and c) show the progression of pore deformation in various stages of tensile stress; A and D are empirical measurements where B and C are interpolations between the two

5.5 Conclusions

This study has built on chapter 4 by conducting a detailed investigation of the interface between layer thickness volumes, and identifying the root cause and characteristics of porosity formed as a direct result of the presented build techniques. The study presents dual layer thickness LPBF components with layer thickness interfaces in various planes. Discretising components into sub-volumes allows high stress areas under external load conditions to be processed with fine layers to maintain part performance, while using coarse layers in areas of

lesser importance to reduce build times – design freedoms and process control that is seldom exploited. This builds significantly on the current literature, whereby typically only skin strategies are varied (compared to the bulk) for improved surface roughness. The study has highlighted and characterised the prevalence of interfacial pores between sub-volumes as a result of adopting the presented build techniques, as a manner to inform a solution.

XCT and micro tensile testing with optical microscopy in-situ were used to gain a deeper understanding of defect formation at the interfaces between sub-volumes and the knock-on effect for tensile response. An advanced post-mortem evaluation technique has also been demonstrated to assemble fracture surface data and reconstruct subsurface pores in 3D for comparison with pre-test XCT data. This enables tracking of defect deformation under strain and can be used to inform finite element models, as well as reverse engineer subsurface defect state of components at the fracture location without the need for XCT.

The conclusions are summarised as:

- The presented method enables greater LPBF throughput and selection of component failure location.
- A 3D pore reconstruction methodology has been exhibited to compare defect state both pre-test and post-test that will prove useful for modelling and post-mortem defect inspection, reducing the need for more costly characterisation methods. The technique found that pores constricted 10.0 – 14.1% in the x direction and 10.3 – 14.6% in the y direction after fracture – normal to the loading direction.
- With current class scan strategies, interfacial pores (ranging from 10 – 170 µm Feret diameter) form at the boundary between layer thickness sub-volumes when both regions are lased in common layers. This includes all interfaces in planes > 0° from the xy substrate plane, with 90° exhibiting the largest interfacial defects in this study.
- These pores are likely a result of keyhole melt depression collapse as hatch vectors in the 90 µm layer region reach previously consolidated material in the 30 µm layer region, causing a drop in absorptivity where the material is more reflective, or due to powder denudation whereby each region is scanned sequentially.
- No additional porosity forms when only one layer thickness is processed per layer, as opposed to processing both 30 and 90 µm regions in common layers. This includes interfaces parallel to the xy substrate plane.

- XCT analysis, micro tensile testing with in-situ microscopy and fracture surface analysis provided strong evidence that interfacial porosity leads to fracture at the interface location. Material discontinuity reduces plasticity, leading to 2% lower elongation to failure values in specimens displaying the largest interfacial defects.
- New class scan strategies must be generated to improve consolidation of material at the interface when disparate parameter regions are combined in single layers.

In summary, large pores along the boundary of component sub-volumes have been confirmed as the root cause of test specimen failure. These pores have been characterised as keyhole pores, most likely formed as a consequence of a sequential laser scanning order. As a result, the following chapter will discuss creation of custom scan strategies with the aim of alleviating formation of interfacial pores through continuous laser scanning orders and laser remelting.

6 Custom laser scan strategies, shelled volumes and build data

6.1 Introduction

This chapter uses the information learned from fabricating multi-layer thickness specimens by means available in typical proprietary software (chapter 4), and the knowledge gained regarding failure modes and defect formation at the interfaces (chapter 5), to develop new process methods designed to improve interface quality and thus mechanical performance to an acceptable standard. Another method of discretising components into sub-volumes for improved throughput is also investigated that does not require disparate parameters or layer thicknesses. The two methods explored to achieve this are: i) custom laser scan strategies designed to accommodate layer thickness interfaces, and ii) semi-hollow components subject to Hot Isostatic Pressing (HIPing), in which the hollow section (containing trapped powder) is enclosed and consolidated during the HIP process.

Sequential scanning of disparate layer thickness regions, with abrupt parameter changes at the interfaces, has been highlighted in chapter 5 as a likely cause of poor fusion and porosity. Hence this study investigates custom scan strategies designed to improve fusion and reduce porosity by generating continuous laser scans that process both regions as one area, with laser vectors passing back and forth across the interface. This section also tackles the abrupt changes in laser parameters by investigating ramping of parameters across the boundary to enable more stability in the melt pool as it transitions from lower-to-higher energy density and vice versa. As a second resort, these custom scan strategies also explore use of a secondary 'rework' pass of the laser, to rescan the interface during mutual layers. This has been shown by Hirsch et al. to significantly reduce pore size [109] and is especially effective in targeting the large pores that have been highlighted earlier in dual-layer thickness parts (chapter 5).

An alternative method to reduce build times is producing shelled components and using HIPing post-process to consolidate the shelled region, as discussed in the literature review (section 2.4.2). This eliminates the issues with disparate layer thickness and parameter interfaces, however, the large-scale shrinkage means there are limitations in achievable geometries. This study builds on the literature by investigating a combination of solid and shelled regions, to enable design complexity in solid volumes and high-throughput shelling in

simple design regions. The interface remains a crucial area of interest in these components, since hollow regions will shrink during HIPing where the geometry of solid regions will remain intact.

Microscopy, XCT, tensile testing and fatigue testing are used to characterise all variations of specimen fabrication to assess component and interface quality in terms of porosity and mechanical performance. In addition, the benefits of these build methods in terms of increased productivity and reduced costs are yet to be quantified. This chapter establishes the throughput and cost data associated with introducing coarse layer or hollow volumes into components to significantly reduce lasing time – such as the components described in section 6.2.1. Time and cost data is presented for introducing coarse layer regions and shelled regions to components in various proportions (0%, 25%, 50%, 75%, and 100%) to quantify the benefits of these process techniques.

6.2 Manufacture and characterisation

6.2.1 Methodology

6.2.1.1 Specimen fabrication

Components for this study were designed to address both tensile properties and fatigue life of single LPBF parts, comprising of dual layer thickness volumes, as well as semi-hollow parts that were subject to HIPing – both methods investigated for ability to reduce build times while maintaining performance in areas of high stress concentration. The former has previously exhibited an increase in porosity at the interface between volumes, with tolerable penalties to tensile performance. Since these defects often have an amplified effect under cyclic loading, specimens in this study are subject to fatigue tests. This logic extends to semi-hollow HIPed samples, since the primary concern is whether the HIP process successfully melts the entrapped powder and compensates for the large volume of air that accompanies the powder.

All specimens were fabricated from grade 5 Ti6Al4V, sourced from EOS. The powder has a particle size distribution (PSD) of 20 – 63 µm and was used as feedstock for a commercial EOS M290 LPBF system - held by Oerlikon AM Europe GmbH in Feldkirchen, Germany. The system uses a 400 W continuous Yb-fibre laser with an 85 µm spot size and 250 x 250 x 325 mm build volume. A 30 µm layer thickness was used for reference samples and semi-hollow

samples, while 30-90 µm layer thickness combinations were investigated for joined specimens. In each layer thickness case, an optimised parameter set was used to achieve standalone relative densities of > 99.9% - volumetric energy densities were 55.6 and 27.8 J/mm^3 for 30 and 90 µm thicknesses respectively. The chamber conditions for the build were set to 0.1% oxygen content and a platform temperature of < 45 °C.

The specimens built with multiple layer thickness regions were machined down to dog bone dimensions according to ASTM E8M 16a, with 24 mm and 4mm gauge length and diameter respectively, to eliminate the likelihood of surface defects instigating failure of the specimens – the layer thickness interface was kept at the midpoint of the gauge length in all cases. This standard was maintained from a previous study [208] in order to characterise consistent components. The blanks for the custom scan strategy designs were built using methods described in section 6.2.2. The build ran at 30 µm layer intervals, and 90 µm layer regions were only processed every third layer.

For the semi-hollow HIPed specimens, blank cylinders of 15 mm diameter, 80 mm length and 2.6 mm shell thickness were produced and subject to Hot Isostatic Pressing for 2 hours at 900°C, before machining to dimension. The cylinders were built significantly above dimension to compensate for shrinkage due to the volume of air within the loose powder trapped internally.

6.2.1.2 Custom scan path design and manufacture

The aim of custom scan path design was to improve fusion between volumes built with different layer thicknesses and eliminate pores formed at the interface. The technique was applied to complex cases in which interfaces are in the xz/yz planes and interfacial porosity becomes a prevalent issue (where xy represents the substrate plane and z is the build direction), as learned in chapter 5. It is not applied to cases whereby interface planes are normal to the build direction (xy) and nominal layer thickness simply changes at an arbitrary layer number - this was shown not to increase porosity in chapter 5, owing to processing different layer thicknesses sequentially rather than simultaneously.

To do this, two schools of thought were introduced: i) one continuous laser strategy, in which laser vectors cross the boundary and transition into a different parameter set, as opposed to scanning each area in parallel previously, and ii) remedying pores introduced at the interface in-process with a ‘rework’ laser pass in layers where multiple layer thickness

areas are processed. Using these premises, 4 variations of scan strategies were designed to improve structural and microstructural part integrity and in turn improve fatigue life. Namely: 1) *continuous*, a single scan with vectors crossing the interface and changing parameters instantaneously at the border, 2) *continuous ramped*, a single continuous strategy with parameters ramped up and down between parameter sets to attain a smoother melt pool transition, 3) *continuous rework*, the continuous scan strategy and a secondary rework pass at the interface, and 4) *continuous ramped rework*, in which a secondary rework pass is added to the continuous ramped strategy. For mutual layers, in which both layer thickness regions are processed, the four scan strategies are depicted in Figure 44 below.

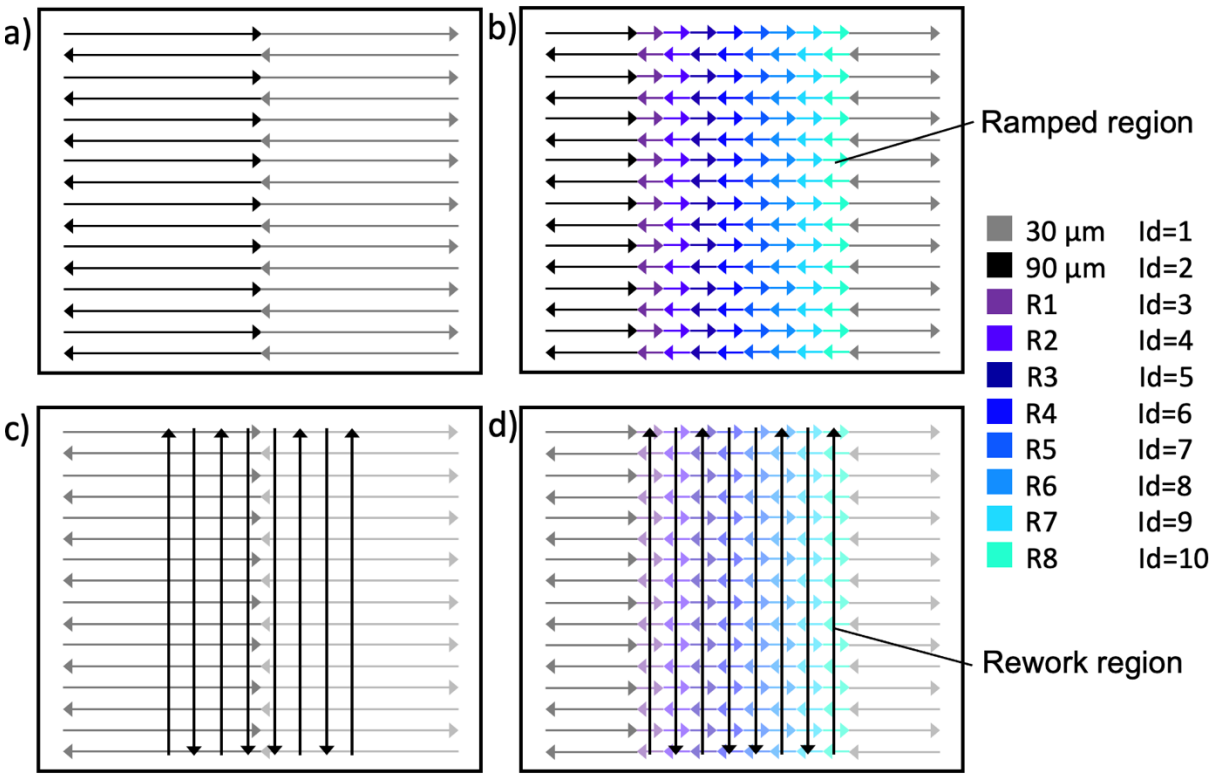

Figure 44 - Custom scan paths designed to improve fusion across multi-layer-thickness interfaces: a) continuous, b) continuous ramped, c) continuous rework, and d) continuous ramped rework

A Python script was written to generate laser vector files for each of the 5 scan strategy designs. The script defines position information for each laser vector (using part geometry, hatch spacing, layer thickness, angle of rotation), while the parameters are defined later in the slicer software by assigning ID numbers to vectors that correspond to a given parameter set. Each set of vectors corresponding to a parameter set was represented by a Common Layer Interface (cli) file, with numerous files allowing for multiple sets of parameters. The order in which the vectors are processed is defined in the slicer software. Laser output cannot be ramped linearly in this manner, hence ramping was achieved between

fine and coarse layers by incrementally varying parameters in small steps to approximate laser gradience. Each small step was represented by a laser vector file, and any vector within the sub-region (defined by distance from the interface) was assigned the same ID.

The script generated a catalogue of files, depending on the scan strategy selected. These files were then structured within the EOSprint slicer software, before build parameters for different layer thicknesses were applied to cli. files with the corresponding ID number. Blank cylinders were manufactured to be machined into dog bones, identical to those described for the standard strategy specimens. The cylinders were produced lying flat on the substrate, so that interfaces represented a vertical cross-section in the centre of the specimens. The 'reduced size' geometry was selected from the standard to optimise both material consumption and usage of the LPBF build volume. Cubes of 10 mm dimension were fabricated for imaging, again with interfaces at the midsection. A 30-90 µm layer thickness combination was produced, compared with the standard 30 µm specimens for reference.

6.2.1.3 Porosity and microstructure analysis

In the case of semi-hollow HIPed samples, X-ray Computed Tomography (XCT) was used to examine any subsurface cavities and pores, since there was a risk the HIP process would not trigger sufficient shrinkage to compensate for the large volume of air trapped in the internal powder. XCT scans were also performed custom laser strategy specimens to address whether interfacial porosity had been successfully removed or reduced.

A Nikon MCT225 was used to scan the dog bones; the resultant image stack was processed in ImageJ (including BoneJ plugin) to observe the specimens in 3D and measure pores using particle analysis. The key metrics of interest were proximity, frequency and size (Feret diameter) of pores. 10 mm cubes were also sectioned, polished by way of grinding, fine grinding, diamond suspension and colloidal silica, before optical imaging for porosity in the xz-plane using a Nikon eclipse LV100ND optical microscope.

The same cubes were then etched using Kroll's reagent to reveal grain boundaries and inspected for evidence of either i) a visible microstructural interface, seen previously and evidence of poor fusion, or ii) well-blended grain structure across the interface, evidence the custom scan paths have improved part quality as intended.

6.2.1.4 Mechanical testing and fractography

Both fatigue testing and tensile testing were conducted in this study. High cycle fatigue testing was selected as an appropriate method to measure mechanical performance of the specimens, since it is the most sensitive part property to the internal defects this study aims to eliminate. Uniaxial, high-cycle fatigue tests were performed at 840 MPa, a frequency of 30 Hz, and stress cycle of R = 0.1. All samples failed within the gauge and each test was repeated 3 times. The data collected compared the custom scan strategy specimens with that of standard strategies, in which parallel scans were utilised for the two layer thickness regions – the only method available within the confines of the slicer software without writing custom build files – as well as semi-hollow HIPed specimens. The aim was to achieve a significant increase in cycles to failure by processing with custom scan strategies, hence proving penalties to part quality can be removed by further optimisation of this method. Fractographs of the fatigue specimens were collected for all sample sets and analysed for failure mode information and evidence of defects that likely initiated crack growth.

Tensile data for specimens featuring dual layer thicknesses has been previously published and is drawn on for reference here [208]. The semi-hollow HIPed specimens have been tensile tested identically in this study, as a direct comparison to dual layer thickness dog bones and as-built reference specimens; the focus is to address whether there are penalties to tensile performance and compare the magnitude of these with any penalties identified in the fatigue response of the same samples. A standard tensile test system was used to uniaxially load the dog bones at a crosshead translation speed of 1 mm/min, recording stress-strain response using a video extensometer. The test was repeated 3 times, all samples were tested to failure and fracture occurred within the gauge length in each case.

6.2.2 Results

6.2.2.1 Porosity and microstructure

Optical images of porosity at the 30-90 µm layer thickness interface of the custom scan path samples can be seen in Figure 45. The continuous strategy, shown in image (a), shows a clear line of pores along the interface exhibiting poor material consolidation where the two regions meet.

Image (c) shows the continuous rework method, in which the scan strategy appears successful in removing the pores along the interface (seen in the continuous strategy); however, different pores are introduced by the rework pass at the sides of the rework band. The dispersion of pores from being perfectly aligned is preferable, although there still exists a cluster of relatively large pores within a 1.5 mm band across the full width of the sample.

Images (b) and (d) show the continuous ramped and continuous ramped rework strategies respectively. It is clear the addition of the ramped parameters has introduced extreme porosity across the 2 mm band ramping region, in both cases. The addition of a rework pass exhibited further effectiveness in reducing porosity, however, the bulk of large and frequent pores remain.

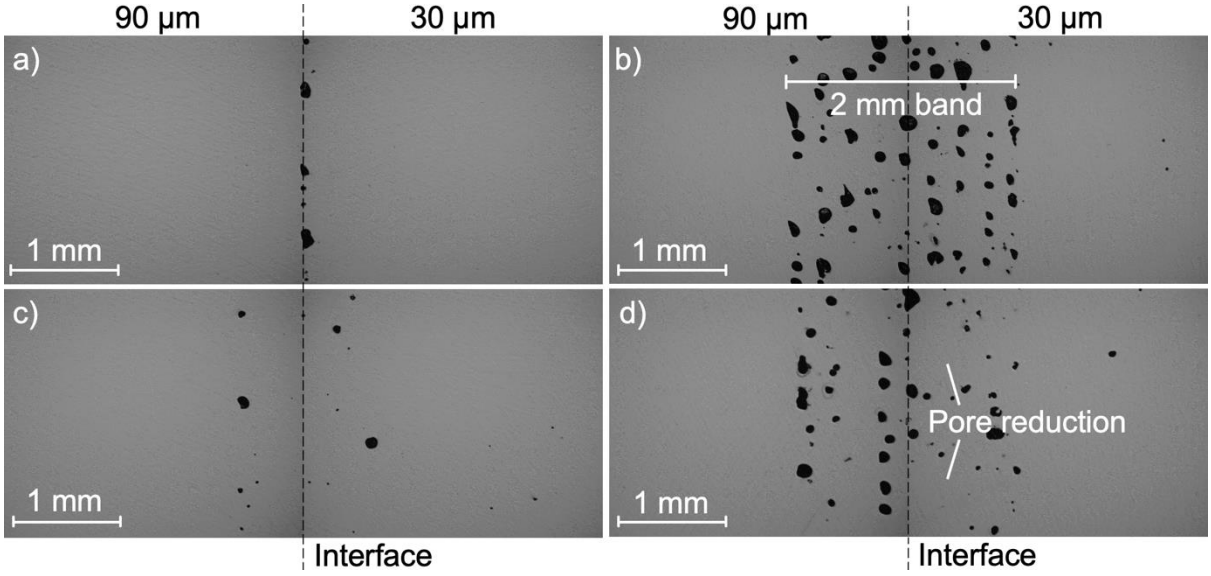

Figure 45 - Optical micrographs displaying porosity at the layer thickness interface (xz plane) of the following scan strategies: a) continuous, b) continuous ramped, c) continuous rework, d) continuous ramped rework

Figure 46 shows porosity in 3D from the XCT data, in which the extent of interfacial porosity is clearly visible with no or negligible porosity either side of the interface. The XCT data confirms the trends apparent in the optical images are consistent throughout the thickness of the specimens, with the continuous strategy showing a single plane of porosity, the rework strategy showing two distinct planes each side of the interface where new pores have been introduced, and both ramped and ramped rework strategies show a large 2 mm cylinder of dense distribution with 9 distinct planes of porosity. Figure 46 also shows a projected view along the gauge section, in which porosity is clearly aligned in the build direction in a stripe pattern for all scan strategies. The centre line of these stripes occurs in roughly 300 µm intervals.

The average pore size is considered similar across each scan strategy, ranging from 57.7 – 73.2 µm, given that the standard deviation also ranges from 31.7 – 45.3 µm – see Table 5. The continuous strategy exhibits 80 pores and the rework only reduced this to 71. However, the addition of a rework pass managed to reduce the number of pores in the ramped strategy by 53.7%, from 607 to 287, and exhibited the lowest average pore sizes.

Table 5 – XCT porosity data for each custom scan strategy

Scan strategy	No. of interfacial pores	Mean Feret diameter (µm)
Continuous	80	70.3 ± 39.8
Ramped	607	67.3 ± 42.7
Rework	71	73.2 ± 45.3
Ramped Rework	287	57.7 ± 31.7

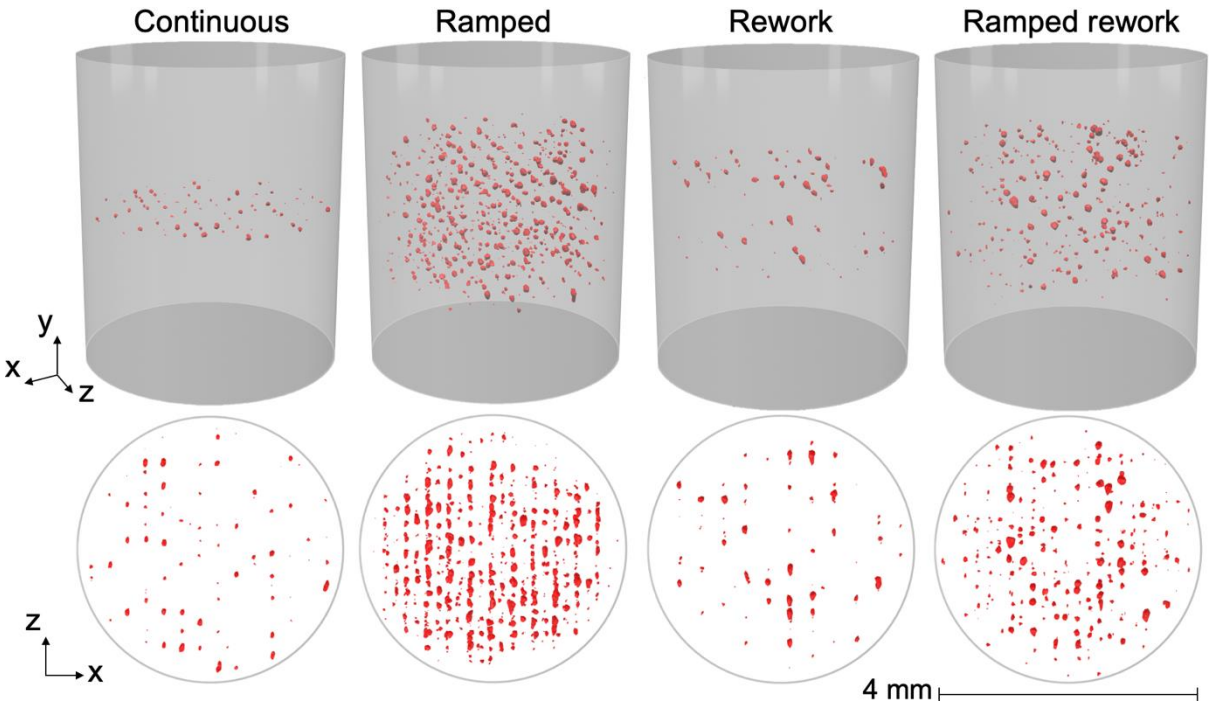

Figure 46 - XCT interface porosity data displayed in 3D within a portion of the gauge section (top row) and z-projection (bottom row) to show periodicity

The gauge sections of semi-hollow HIPed specimens exhibited no visible pores in the XCT scans, however, there are small pores evident in the optical and SEM images - as can be seen in Figure 47. These pores are consistently < 10 µm in diameter, meaning they are smaller than the voxel resolution of the XCT data and hence were not evident in the image stack. Although small, these pores are found very frequently and evenly spaced throughout the entirety of the hollow region (b and c), whereas very few pores were evident in the solid half

of the specimens (d and e). Since the Argon gas entrapped within the hollow section cannot escape, these small pores are likely Argon pockets that were evenly distributed throughout the hollow region during the HIP process.

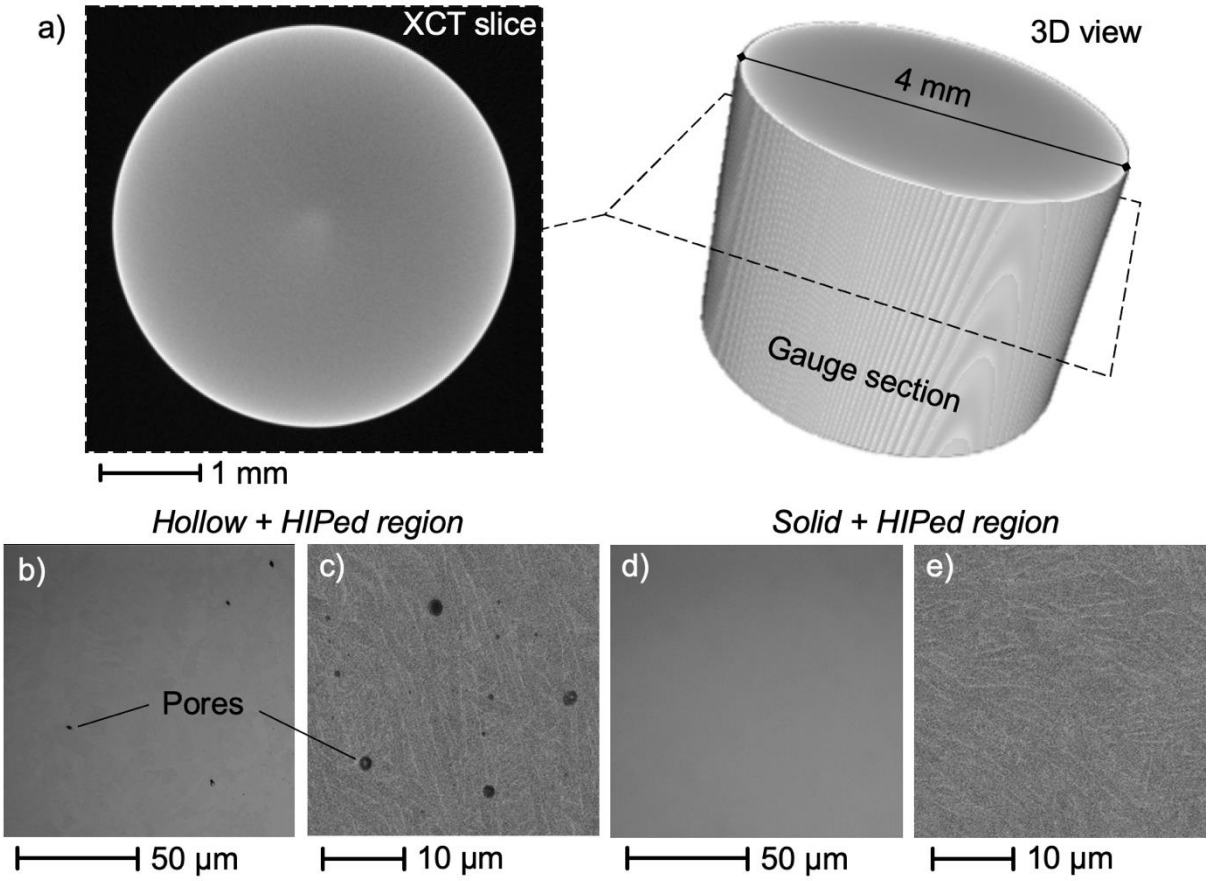

Figure 47 – a) XCT of semi-hollow HIPed specimen dog bones b) optical image of the hollow region at low magnification c) SEM image of the hollow region at high magnification d) optical image of the solid region at low magnification e) SEM image of the solid region at high magnification

Figure 48 displays the typical microstructure found in both the custom scan path specimens and the semi-hollow HIPed specimens. The custom scan paths show typical columnar prior-β grains oriented in the build direction (Images a and b). The 30 µm layer region shows columns around 500 µm in length and 120 µm wide, whereas the 90 µm region features grains in excess of 1 mm length and similar widths. The additional energy input of the 90 µm layer parameters is likely the source of elongated grain growth. HIPing has altered the texture of the microstructure (images c and d); however, the general columnar grain architecture is similar and grain size also remains similar to that of the as-built microstructure evident in the custom scan specimens. Figure 47 (images c and e) shows the lamellar microstructure of the HIPed material, in which the α laths measure an average of 1.86 µm thick. This shows grain

coarsening has occurred when compared with as-built material, exhibiting approximately 800 µm lath thickness.

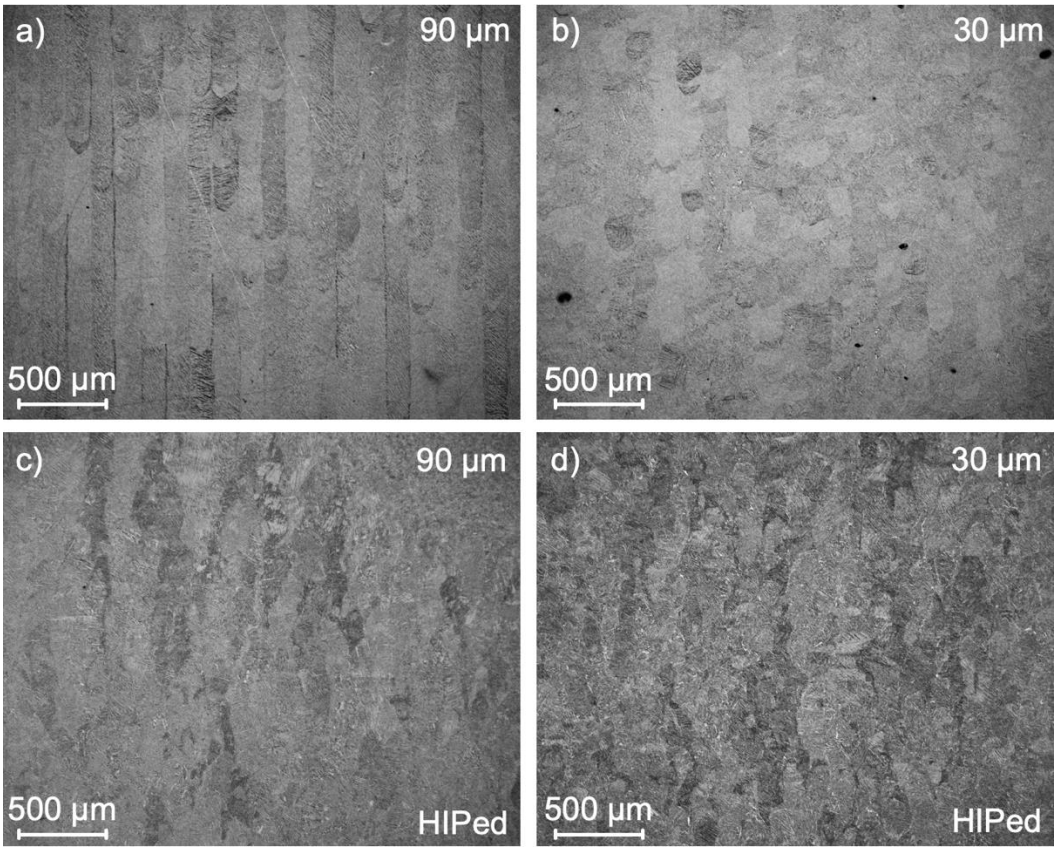

Figure 48 - Grain structure of: a) 90 µm layer region of a custom scan path specimen, b) 30 µm layer region of a custom scan path specimen, c) 90 µm layer region of a semi-hollow HIPed specimen, d) 30 µm layer region of a semi-hollow HIPed specimen

The microstructure across the interface in custom scan strategy specimens is visible in Figure 49, and accompanying grain size data in Table 6. The 30 µm and 90 µm layer regions show significantly different grain size and morphology. The 90 µm volume shows long and narrow columnar grains with a mean aspect ratio of 11.32, whereas the 30 µm volume grains are much closer to being equiaxed, with a mean aspect ratio of 1.47. The average grain is 1519 x 136 µm and 266 x 179 µm for 90 and 30 µm layer volumes respectively. The continuous strategy (image a) exhibits a harsh transition between the two grain structures and some discernible finer microstructure at the interface. The microstructure at the interface of the continuous ramped (image b) and continuous ramped rework (image d) strategies is difficult to observe given the extreme porosity evident across the region of interest; however, there is evidence of a wider band of blending between the two grain structures and a similar trend is visible in the rework strategy (image c).

Table 6 - Grain size data

Layer thickness (µm)	Avg. length (µm)	Avg. width (µm)	Avg. AR
30	266 ± 122	179 ± 49	1.47 ± 0.47
90	1519 ± 349	136 ± 13	11.32 ± 2.92

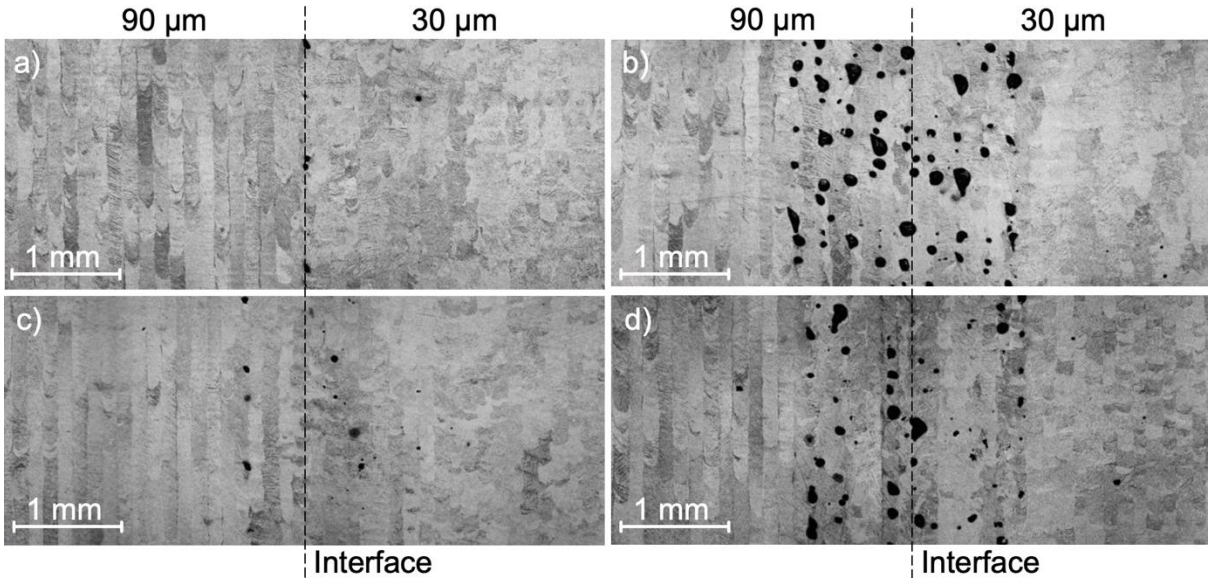

Figure 49 - Grain structure across the interface of each custom scan strategy (xz plane): a) continuous, b) continuous ramped, c) continuous rework, d) continuous ramped rework

6.2.2.2 Tensile behaviour

The tensile response of joined 30-90 µm layer thickness specimens, semi-hollow HIPed specimens, and standard reference specimens can be seen in Figure 50, with elastic modulus, elongation to failure, ultimate tensile strength and yield stress detailed in Table 7.

The data for the 30-90 µm specimens has been maintained from chapter 4. The elastic modulus, UTS and yield stress for 30-90 µm specimens were shown to remain very similar to the reference samples, while showing a significant reduction in ductility as elongation values dropped by 40% - attributed to interfacial pores. The data implies there is far less plastic behaviour at the failure location, allowing for a more brittle fracture.

The semi-hollow HIPed specimens exhibits a 14% lower modulus and 28% increase to elongation to failure, at the expense of 14% lower UTS and 15% lower yield stress when compared with the standard LPBF sample set – these values align much closer to that of wrought Ti6Al4V. The increase in ductility and loss in strength is attributed to the coarser α laths induced by the HIP process, identified in section 6.3.1. This increase in ductility is significant since it the main penalty for the dual layer thickness specimens was a reduction in

ductility, and ductile behaviour is beneficial under fatigue loading conditions. However, it is important to note that the reduction in strength is also crucial, given fatigue conditions maintain the same maximum stress for all sample sets.

Table 7 - Tensile data

Sample Set	Elastic modulus (GPa)	Avg. elongation (%)	Avg. UTS (MPa)	Avg. Yield Stress (MPa)
Standard	133.8 ± 1.01	9.70 ± 0.34	1126 ± 0.32	1071 ± 2.12
30-90 µm	124.2 ± 6.77	5.92 ± 0.25	1129 ± 3.68	1067 ± 8.83
Semi-hollow + HIP	115 ± 3	12.45 ± 0.35	979 ± 6	911 ± 5
Wrought Ti6Al4V [153]	113.8	14	950	880
LPBF Ti6Al4V [198]	94.4 – 110.9	2 – 19.7	840 - 1320	974

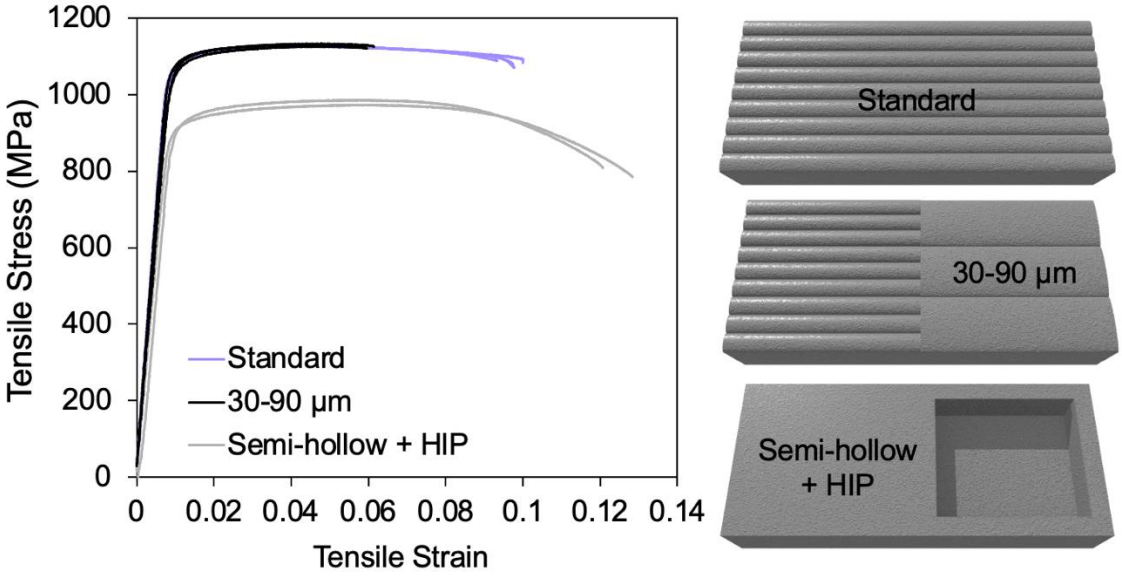

Figure 50 - A graph to show tensile response of standard specimens, 30-90 µm joined specimens, and HIPed semi hollow specimens

6.2.2.3 Fatigue behaviour

A comparison of cycles to failure between all sample sets and reference samples can be seen in Figure 51. Amongst the custom scan paths, the continuous strategy displayed the greatest mean cycles to failure (36,600), followed by the rework (27,100), ramped rework (18,100) and ramped (15,700) strategies. The large errors due to porosity must be considered when drawing comparisons.

The mean cycles to failure of the semi-hollow HIPed specimens was greater than all custom scan paths, however, the error range falls within the limits of the continuous, rework and 30-90 µm strategies. Moreover, the specimens exhibited a 93.5% drop in mean cycles to

failure when compared with the standard LPBF specimens, despite displaying no visible porosity in XCT scans and < 10 µm pores in the micrographs.

While there is a basis to compare the custom scan paths and semi-hollow HIPing amongst themselves, it must be noted that all sample sets performed poorly when compared with the standard LPBF specimen. The standard LPBF specimen exhibited a mean cycles to failure value of 585,800, outperforming all other specimens by at least a factor of 20. The 30-90 µm interfaces built with standard processing scan strategies falls in the middle of the group, although it is difficult to compare absolutely since there was very large error in the data.

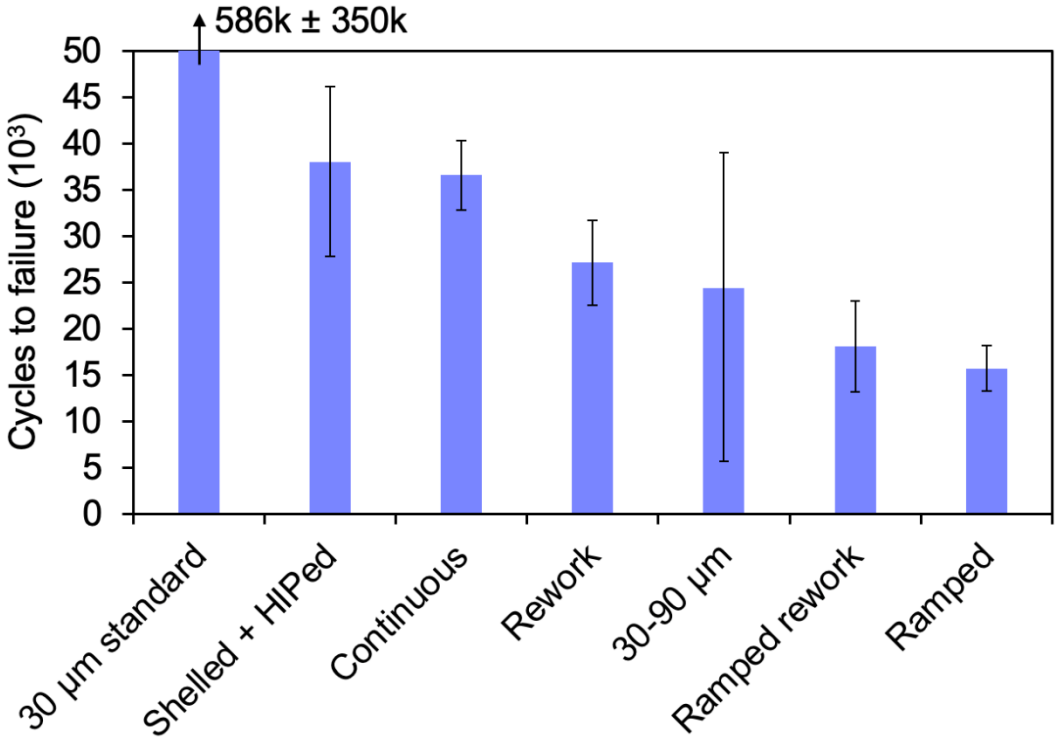

Figure 51 - A graph to show cycles to failure of components fabricated using each of the presented build methods

6.2.2.4 Fracture behaviour

Each of the custom scan strategy designs exhibited similar fracture surfaces, owing to exhibiting similar cross-sectional planes of porosity. These keyhole pores are clearly visible in image (a) of Figure 52 below (showing SEM images of the fracture surfaces), in which smooth material and evidence of melt morphology indicates material discontinuity in these regions. These pores measure approximately 80 µm Feret diameter, aligned with XCT data. In most cases, evidence of crack initiation was identified in the region of a large pore near the surface of the specimen. Image (b) shows an example of this, whereby a 400 µm Feret diameter lack

of fusion defect can be seen at the edge of the fracture surface at the crack initiation site. The defect is characteristic of lack of fusion due to having a high aspect ratio and evidence of partially sintered powder particles. Outside of pore locations, the material generally exhibits a dimpled ductile fracture surface, with a cup and cone fracture – consistent with the literature [199]. Image (c) highlights the cup and cone texture, including defect, crack initiation site and crack growth direction.

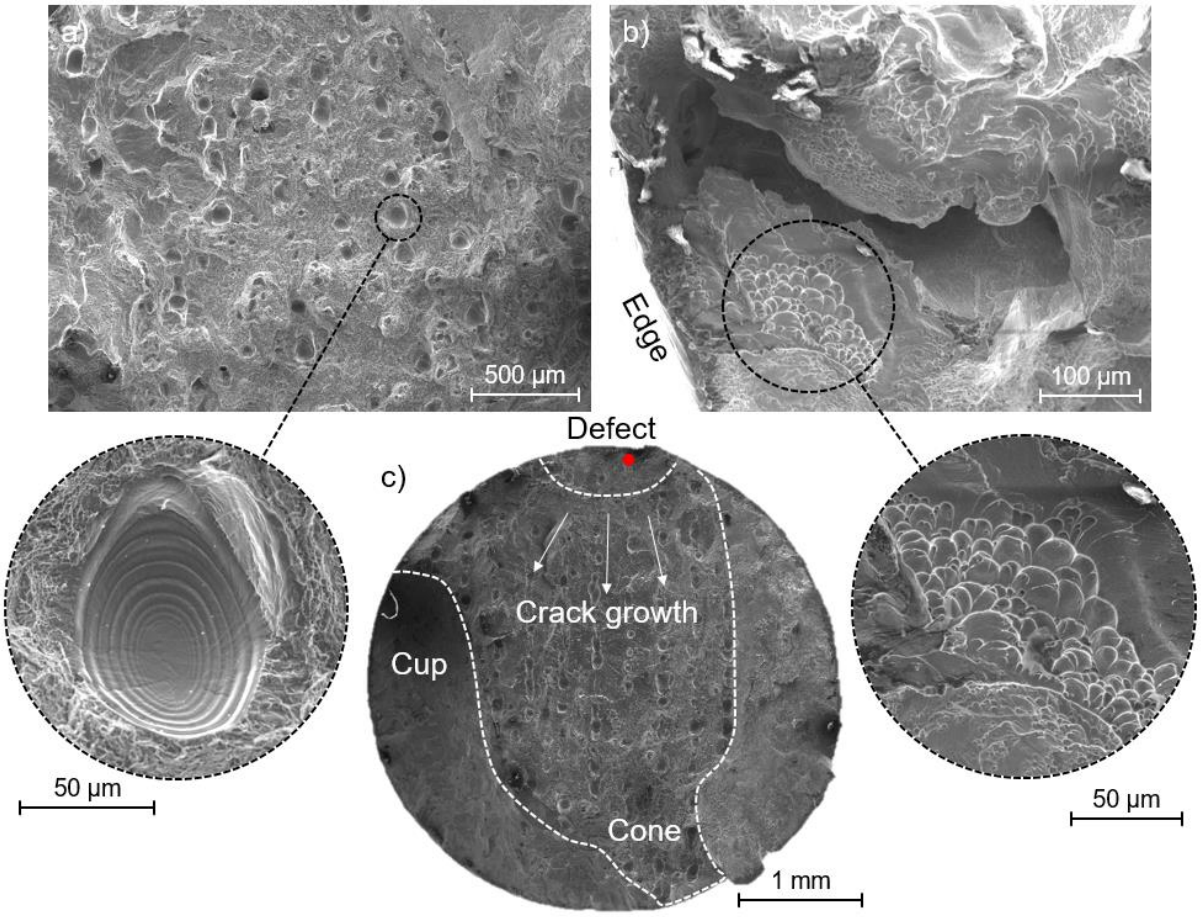

Figure 52 – SEM fracture surface images of custom scan strategy specimen: a) a trend of keyhole pores evident in the fracture surface, b) a crack initiation site initiated by lack of fusion – highlighting partially sintered powder, c) the general cup and cone fracture morphology and crack growth signature found in the specimens

The semi-hollow HIPed fracture surfaces exhibit ductile fracture characteristics, with rougher texture and fine pockets (dimples) providing stronger evidence of ductility compared with the standard specimens – see the left-hand image in Figure 53. This agrees with the superior ductility of the semi-hollow HIPed specimens reported in the tensile data of section 6.3.2. There are also deeper pores with diameters < 10 µm that are possibly Argon pockets similar to the pores highlighted in section 6.3.1.

The right-hand image in Figure 53 shows the likely crack initiation site of the specimen. A smoother surface, consistent with crack initiation in fatigue, can be seen. The surface

texture appears to fan out from a singular defect, supporting the premise that a crack grew from this location. The defect measures 13 µm diameter, which is consistent with gas pores sizes, and appears to be disconnected to the surrounding bulk material. There is material within the defect itself that has charged within the SEM chamber, suggesting it is not contamination but most likely lodged Ti6Al4V. There are also α-lath grain boundaries visible in the fracture surface texture fanning away from the defect (right hand image in Figure 53), suggesting the local microstructure has played a role in fracture of the specimen.

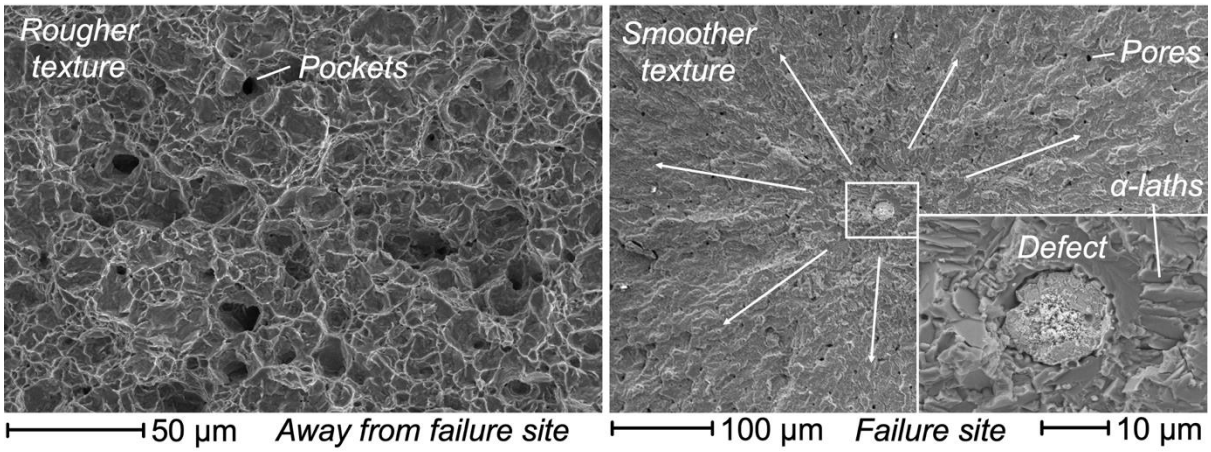

Figure 53 - Fracture surface images of the semi-hollow and HIPed specimens subject to fatigue testing: away from failure site (left), failure site with inset defect (right)

6.2.3 Discussion

6.2.3.1 Porosity

XCT imaging captured the size and trends in porosity at the layer thickness boundary and within the bulk material either side. There is 1 aligned plane of porosity for the continuous strategy, 2 for the rework and 9 for both ramped strategies – each forms in a plane in which parameters are changed. Averaging the number of pores per plane gives 80 and 67 for the continuous and ramped strategies and 36 and 32 for the rework and ramped rework strategies respectively. Hence the addition of a rework strategy at interfaces was successful in removing over half the pores per interface with no significant change to the average pore size.

The single plane of porosity in the continuous strategy is directly along the 30-90 µm layer thickness interface and the 2 planes in the rework strategy are introduced at the edges of the rework band. Moreover, the 9 planes of porosity seen in the ramped strategy specimens correlate to the 9 boundaries generated by the 8 ramping increments selected to

increment the process parameters between 30 and 90 µm layer volumes. This is highlighted in Figure 54, in which the yz plane image displays the clear transverse alignment of pores in 250 µm intervals across the 2 mm ramping region. The phenomenon is less clear in the xy plane since the pores are aligned in the z direction.

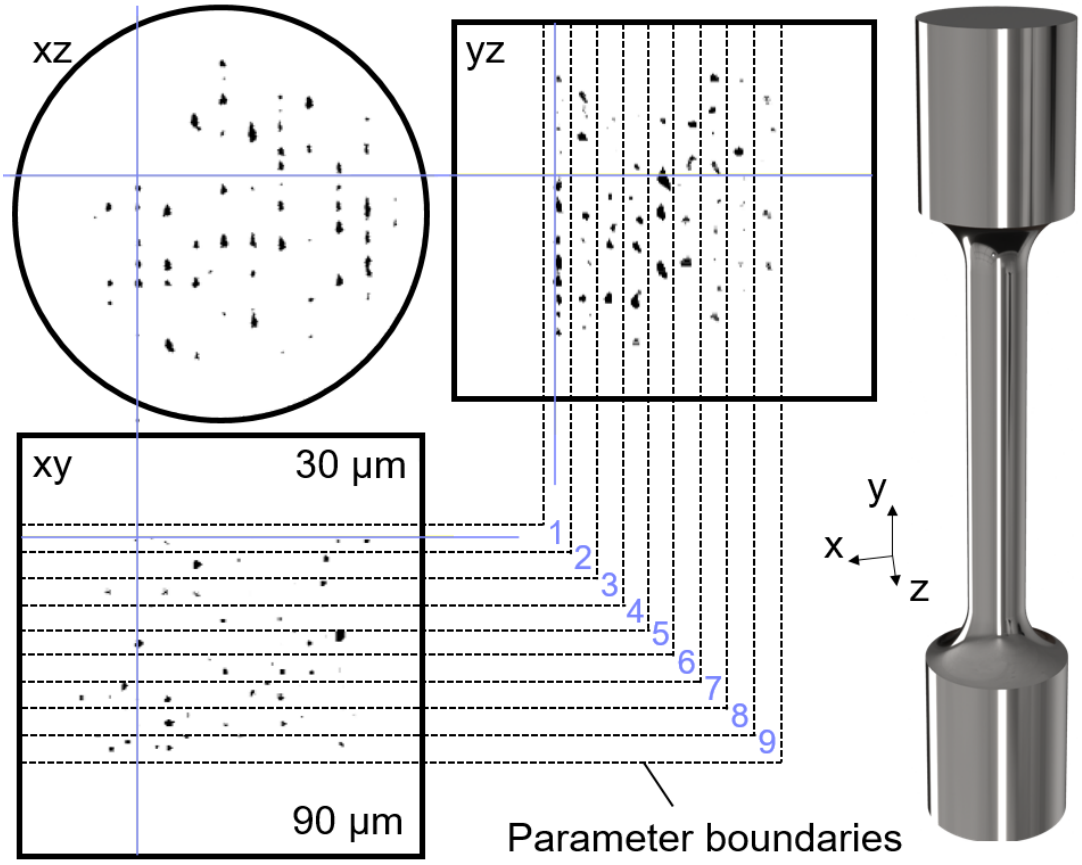

Figure 54 - XCT porosity pattern compared in xz, xy and yz planes with respect to parameter ramping increments

A possible explanation for the presence of porosity at the parameter increment boundaries is the deceleration and acceleration of the galvanometer-based scanning mirrors as one vector finishes and the successive vector begins. A similar phenomenon has been captured in standard scan strategies at the turn of the laser in meander scan paths, in which a keyhole depression forms as the scan slows and collapses as the scan accelerates again, causing large variations in normalised enthalpy in the melt pool and resultant keyhole pores similar to those found in this other work [54]. These keyhole pores are likely to form at the vector end points consistently throughout the layers, and the defects from previous layers will cause them to align in the build direction as the melt pool penetrates into the cavity below. This hypothesis could also explain why the defects appear to a lesser extent at boundaries 8 and 9 in the yz plane of Figure 54. Since the energy density increases towards the 90 µm layer volume, the slower cooling rates may delay the collapse of the keyhole and

reduce the drop in normalised enthalpy before the melt pool of the successive vector is re-established. It is possible this less harsh transition yields fewer pores than areas of lower energy density. Another contributing factor may simply be that there are only one-third of the layers processed in the 90 µm half (boundaries 6 – 9) and hence there are fewer opportunities for defects to form. There are 76 pores measuring 89.5 ± 57.0 µm at boundary 1 (where the 30 µm layer thickness bulk volume meets the ramping region) compared with only 49 pores measuring 54.8 ± 32.7 µm at boundary 9 (where the 90 µm layer thickness bulk volume meets the ramping region).

While this may explain the porosity patterns in longitudinal planes across the ramping region, it does not explain the alignment of pores in the build direction in transverse planes (xz plane in Figure 54). It is likely a series of pores were introduced in early layers of the build at the parameter increment boundary. As explained in Figure 39 in chapter 5, pores then affect successive layers directly above their location, since the melt pool penetrates down into a cavity. This creates a knock-on effect that causes periodic porosity aligned in the build direction.

6.2.3.2 Mechanical performance

The fatigue performance of the custom scan strategies directly correlates to the number of interfacial pores measured – the continuous and rework scan showed the least number of pores and performed the best, while the two ramped scans showed the most pores and performed the worst. The rework strategy exhibited a similar number of pores of a similar size to the continuous strategy and managed to split them across two planes; despite this, the rework specimens still showed mildly lesser fatigue performance. Similarly for the ramped strategies, the addition of a rework scan removed over half the pores (320) across the same number of interface planes. However, the fatigue performance of the ramped rework strategy is only mildly superior and, given the size of errors in the data, limited confidence can be had in this comparison. It is likely that the very frequent porosity across all custom scan components is sufficient to cause similar performance in all specimens, despite the great differences in defect patterns. The difference in cycles to failure between the continuous and ramped strategies is 57.1% relative to each other, which appears a large disparity. However, when measured relative to the LPBF reference specimens, the difference is only 3.8%. Similarly, the fatigue performance of the original 30-90 µm sequential strategy falls directly

in the middle of the custom scan path specimens; however, there is large error in the data and little confidence can be had in where this sample set falls in the order.

The significant drop in fatigue life of the semi-hollow HIPed specimens is attributed to a phenomenon called 'ratcheting', in which marginal plastic deformation accumulates with cyclic loading to the detriment of the component [209]. Since the yield stress of Ti6Al4V subject to HIPing is significantly lower compared with the as-built or stress relieved state, the appropriate maximum stress for fatigue testing all other sample sets falls too close to the yield stress of the semi-hollow specimens (840 MPa versus 911 MPa) and induces small plastic deformations that quickly build up over tens-of-thousands of cycles.

6.2.3.3 Fracture behaviour

The fracture surfaces of all custom scan specimens captured the same planes of pores as highlighted in the XCT data, exhibiting the same trend, alignment and size. Hence it is clear that failure occurred along these interfaces. Cracks initiated from larger pores located close to the specimen surface and propagated through the gauge section, as is regularly reported when fatigue testing LPBF components with internal defects [210].

The semi-hollow HIPed specimens clearly show a more ductile fracture, despite fatigue life being hindered by the ratcheting phenomenon. The defect (identified in Figure 53) meaures 13 µm diameter, consistent with the size of gas pores found in the specimens and considered small to instigate fracture. Similar fatigue crack initiation at gas pore locations has been reported by Gunther et al. [211], however, the pore in this study measures a diameter over 6 times larger at 80 µm. It is also possible a microstructural heterogeneity could have aided crack propagation in this location. The α-laths, highlighted in the inset image, appear to contribute to the texture fanning away from this singularity, supporting the likelihood of a microstructural issue being the root cause of failure. This has also been demonstrated by Gunther et al. [211], whereby an α phase microstructural defect is responsible for crack initiation and exhibits a smaller defect singularity. Given the size matches that of the identified gas pores and that some non-homogeneous materials appears to be residing in a pit, it is most likely the defect is a gas pore with the possibility that an α phase defect aided crack formation.

This result contributes further to the knowledge that LPBF components are especially sensitive to internal pores when subject to cyclical loading. Other studies on fatigue life of

LPBF materials have cited critical pore sizes around 20 µm [212] Feret diameter, however, the defect likely responsible for initiating failure in this case was 13 µm. The presence of α lamellae texture indicates there may be a coupling effect of porosity and microstructure that can initiate further premature failure, however, this information is lacking in the literature since the effects of each are difficult to decouple.

6.3 Build time and cost savings

6.3.1 Methodology

6.3.1.1 Build time

The time taken to complete a build was taken from the beginning of the initial laser vector of the first layer to the end of the final vector of the last layer. This model assumes the chamber conditions (oxygen content and temperature) are already achieved and maintained throughout, with no bearing on build time. The model also assumes there are no interruptions to the build that require it to be paused, such as a failed layer. Build time was calculated using the following equation:

$$t_{build} = \frac{N t_{wiper} + \frac{s_f}{v_f} + \frac{s_c}{v_c}}{3600}$$

Where: t_{build} = total build time (hrs)
N = number of layers
t_{wiper} = time taken to recoat the powder bed (s)
s_f = total build laser vector length of fine layer region (mm)
s_c = total build laser vector length of coarse layer region (mm)
v_f = fine layer laser scan speed (mm/s)
v_c = coarse layer laser scan speed (mm/s)

The number of layers required for the build, and the total laser vector length, were both extracted from the slicer software by slicing given components at the appropriate layer thickness, hatch distance and scan strategy. The time taken to recoat the powder bed was measured 10 times in practice and an average of 8.63 seconds was recorded. Nominal scan speed is dependent on the optimised parameter set of the operator; in this instance, 1200 mm/s and 800 mm/s for 30 and 90 µm layer thicknesses respectively.

Figure 55 below shows the build time function above plotted for the various build methods examined in the present thesis, up to and including a large build volume. Each vector

response is made up of lasing time and recoating time, hence a shorter vector represents a shorter build time. It is clear that the use of high-throughput sub-volumes significantly reduces lasing time, with no effect on recoating time since the total number of processable layers remains the same. Entirely shelled components show a further reduction in lasing time. Hence these build methods show a steeper gradient function compared with standard processing, whereby lasing time has been reduced while recoating time remains high. Entirely coarse layer builds, however, show a more shallow gradient response, in which recoating time has been significantly reduced by reducing the total number of layers to be processed by 67%. The gradient is not equal to the standard processing function, since coarse layers require slower scan speeds and thus lasing time is not reduced by 67%, but is still reduced by 53% since there are fewer layers to process. Again, shelling a coarse layer component significantly reduces lasing time and, combining the effects, produces a steeper gradient than standard and the shortest build time available.

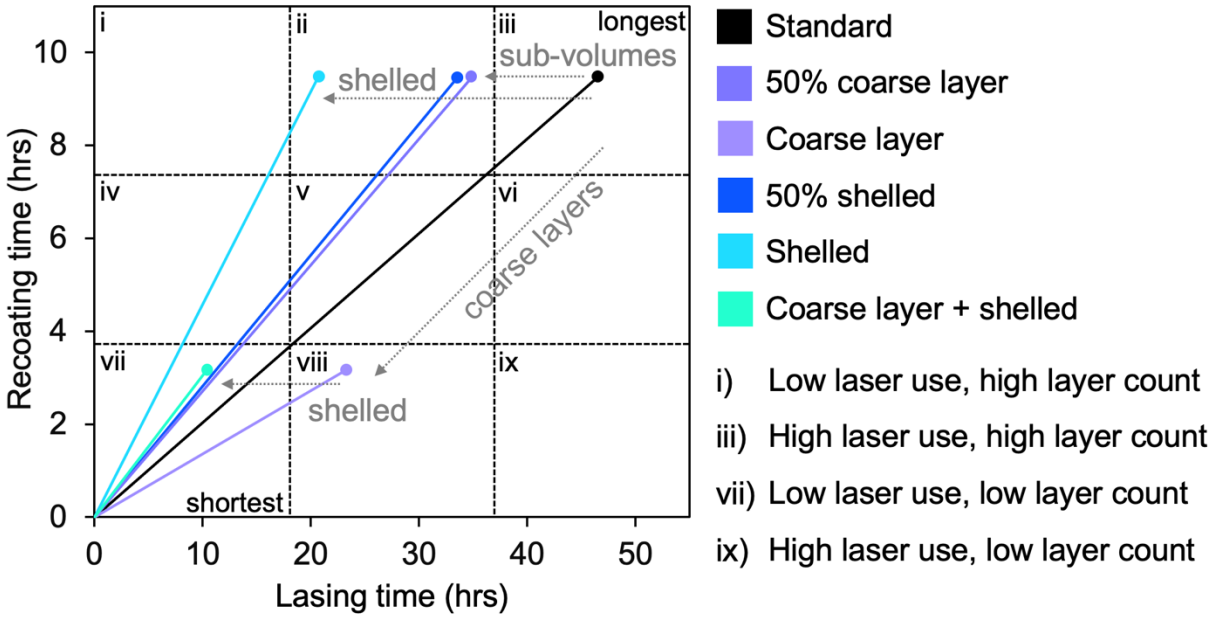

Figure 55 - A plotted build time function with increasing layer number to show how lasing time and recoating time are affected by the various build methods discussed within the thesis

This plotted function can also be used to envision other methods of increasing productivity. For examples, high scan speed strategies will shorten the total lasing time and hence produce a steeper gradient response. A similar effect would be apparent when addressing multi-laser systems, since a quad-laser LPBF machine could maintain the same scan speed using four lasers simultaneously, hence reducing the lasing time by 75% but maintaining the same total powder recoating time. Besides increasing layer thickness, there are also less common

methods to reduce the powder recoating time. At the simple end of the spectrum, many LPBF systems allow for the wiper blade speed to be adjusted. Provided a homogeneous powder bed was maintainable, increasing the wiper speed by 20% can save time to the order of hours for large builds. At the more complex end of the spectrum, there are examples of research and development systems that lase fresh areas of powder and recoat processed areas simultaneously [213]. This method would allow for a fraction of the lasing time to overlap with the recoating time, reducing the total build time.

6.3.1.2 Build cost

Costings were prepared for a medium-sized LPBF build (15 hours, 3kg Ti6Al4V) using information found in the literature, market research and some assumed standard practices. This was then combined with build time reduction data to quantify build cost, profit and margins for the various build methods investigated, both per build and per annum.

All values used to calculate build costs can be found in Table 8. Overhead values were taken from Baumers et al. [214] and Ruffo et al. [215], taking into account premises rent, admin, labour, machine costs (both LPBF and essential peripheral machinery, such as wire electrical discharge machining), and energy consumption. These studies also state machines are only utilised half of the available hours, and so the number of builds possible per year is calculated by dividing 50% of available hours by the respective build times of each method.

The current cost per kilogram of grade 5 Ti6Al4V powder, of typical particle size distribution, is around £250. 15 kg of feedstock is sufficient to reach a medium-sized build height of 50 mm, expecting to lose a small volume of powder to the overflow. Assuming only 20% of this volume is occupied by parts, 3 kg of material is directly consumed per build. Standard practice is typically to replenish the hopper with virgin feedstock after 10 builds due to powder degradation, hence one-tenth of this cost has been attributed to each build. It is worth noting that consumables and overheads (such as powder and energy) are variable and the costs are likely to change over time. It is possible material costs could come down as demand grows, however, most overheads such as building costs are likely to increase.

The profit margin of the standard processing method was taken as 40% - in keeping with values reported for 3D Systems Corp. for 2021 [216]. The sale price of components was assumed to remain constant, hence profit margin varied as cost per build varied across the various methods to achieve the same batch of parts.

Table 8 - LPBF costs [214][215]

Item	Value	Units
Cost of Ti6Al4V powder	250	£/kg
Ti64 powder per build (250 x 250 x 50 mm)	15	kg
Volume utilised	20	%
Mass of parts per build	3	kg
Material cost parts per build	750	£
1/10th replenishing feedstock after 10 uses	375	£
Total material cost per build	1125	£
Standard build time	15	hrs
Hourly costs	**Value**	**Units**
Building rent	4.53	£/h
Admin overhead	0.31	£/h
Production labour	6.14	£/h
Machine costs	15.66	£/h
Energy consumption	0.15	£/h
TOTAL	26.79	£/h

6.3.1.3 Build scenarios

Three build scenarios were investigated (small, medium, and large), since geometry and build height significantly affect build time and potential time savings. The three scenarios were selected to represent genuine LPBF builds that exhibit build times in which i) multiple builds can be produced in one day, ii) one build can be produced in one day, and iii) one build requires multiple days to complete. The small build is represented by 24 x 10 mm cubes, as is common for parameter optimisation; the medium build comprises of 6 mounting brackets; and the large build is a scaled down 6 cylinder engine block. Each build file is sliced at 30 µm layers and takes 2.2, 14.6 and 55.7 hours to complete respectively – information and images can be seen in Table 9 and Figure 56. Each of these components are then discretised into sub-volumes, comprised of 0, 25, 50, 75 or 100% standard processing, with the remaining fraction dedicated to coarse layer processing (90 µm layer thickness), shelled regions, or both. The total laser vector length for all variations of each component was found by loading the sub-volumes into slicer software with the appropriate parameters.

Table 9 - Build scenario comparison

Build size	Part/s	No. layers	Total vector length per build (m)	Total build time (hrs)
Small	24 x 10 mm cubes	333	5981	2.2
Medium	6 x mount brackets	2166	40574	14.6
Large	1 x engine block	3930	199869	55.7

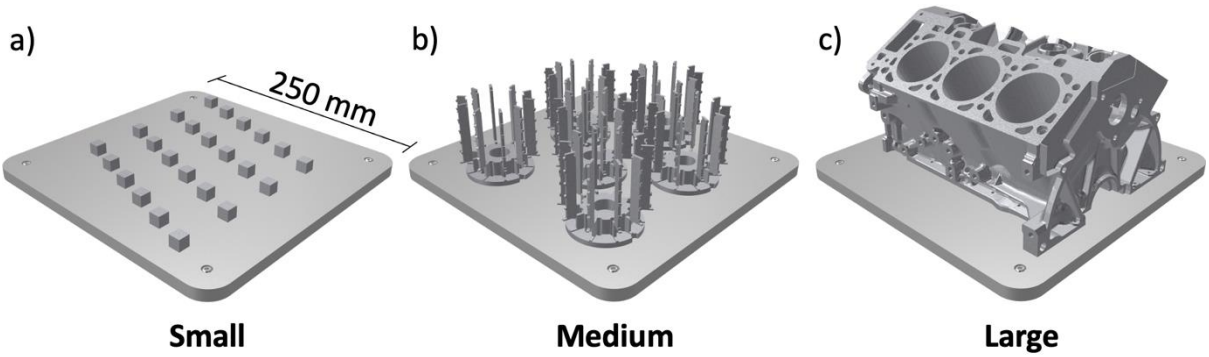

Figure 56 - Build scenarios for time and cost comparison a) small b) medium c) large

6.3.2 Results

6.3.2.1 Build time

A similar trend can be seen among each build scenario (small, medium, and large) in Figure 57, in which increasing the fraction of a build produced using coarse layers or shelled regions further reduces the build time. Time savings are between 0.2 – 1.6 hours for the small build, 0.9 – 9.9 hours for medium, and 5.8 – 42.3 hours for large. 100% coarse layer builds exhibit much shorter build times since the builds can be run at, in this case, 90 µm layer thickness instead of 30 µm – meaning total recoating time is one-third that of builds run at 30 µm layer thickness. Combining coarse layer thicknesses with shelled components shows a drastic reduction in build times since requirements from both powder recoating and laser processing are reduced to an absolute minimum. However, it is important to note in cases of 100% coarse layers or 100% shelled components, fine layers or solid regions cannot be used in areas of high structural significance to maintain part integrity – as is possible with 25/50/75% specimens.

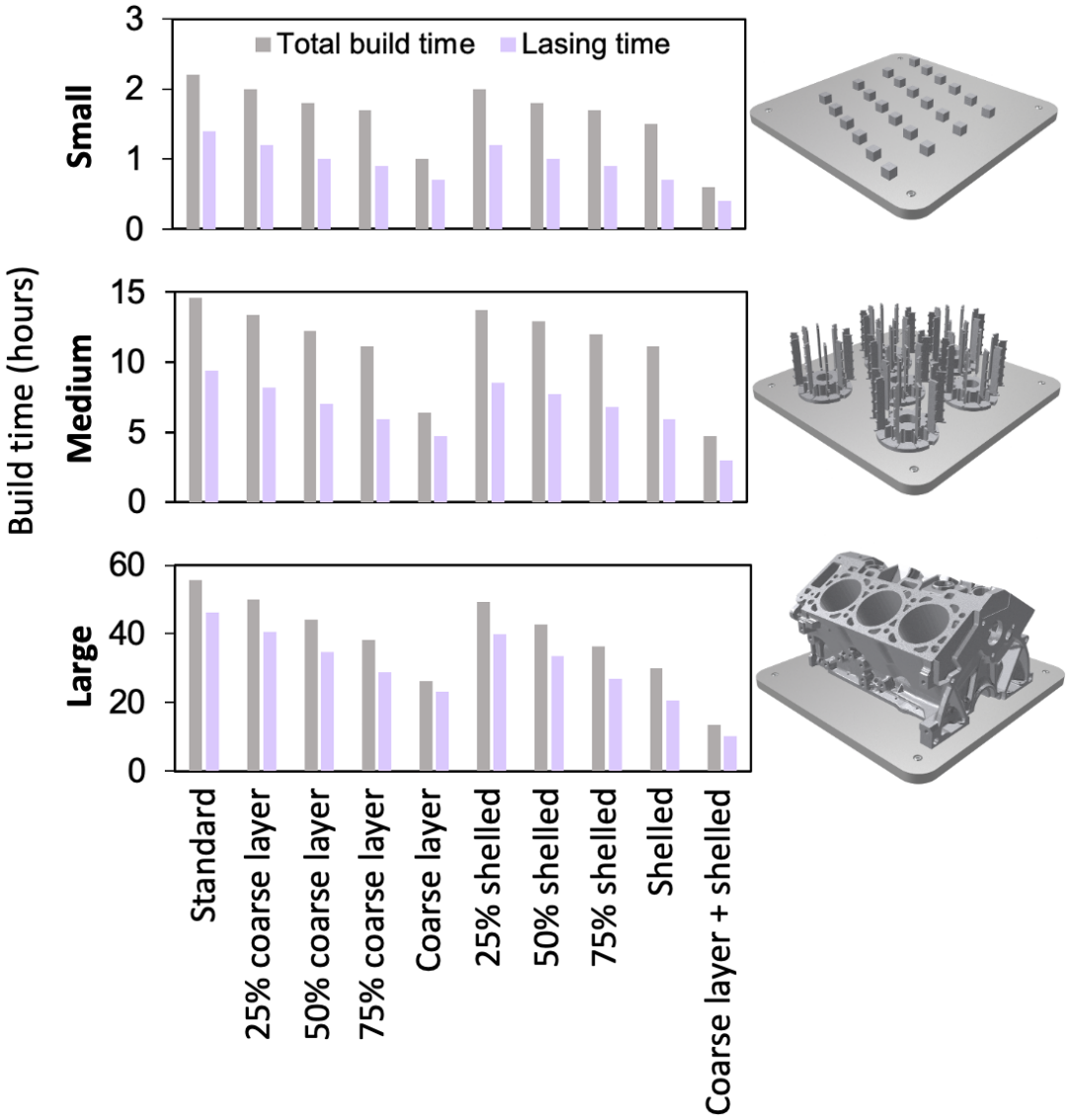

Figure 57 - Build time data comparison in hours: small build (top), medium build (middle), large build (bottom)

Although the large build shows drastically larger build time reductions in terms of hours, this is strictly due to the fact it has a large build duration. Figure 58 shows build time reduction as a percentage when compared with a standard process build of the same components. On average, the 50% coarse layer and 50% shelled components (as investigated throughout the thesis) exhibited 18.5% and 17.7% time reductions respectively; whereas 100% coarse layers, 100% shelled and a combination of coarse layers and shelled showed 54.5%, 34% and 72.2% respectively.

Time reductions are comparable for each method, however, there are some discernible trends with respect to the size and morphology of the build. In all cases where only a fraction of the build is produced using coarse layers or shelled regions, the large build exhibits the greatest build time reductions, since lasing time takes up a large fraction of this

build. The only exception to this is the 100% coarse layer method, in which the medium build shows mildly greater time reduction since powder recoating takes up a large fraction of this build. Since the medium build has relatively thin components, shelling is seen to be consistently less effective in reducing build time – 11.6% compared to 23.2% in the large build for the 50% shelled method, and 24% compared to 46.1% in the large build for the 100% shelled method.

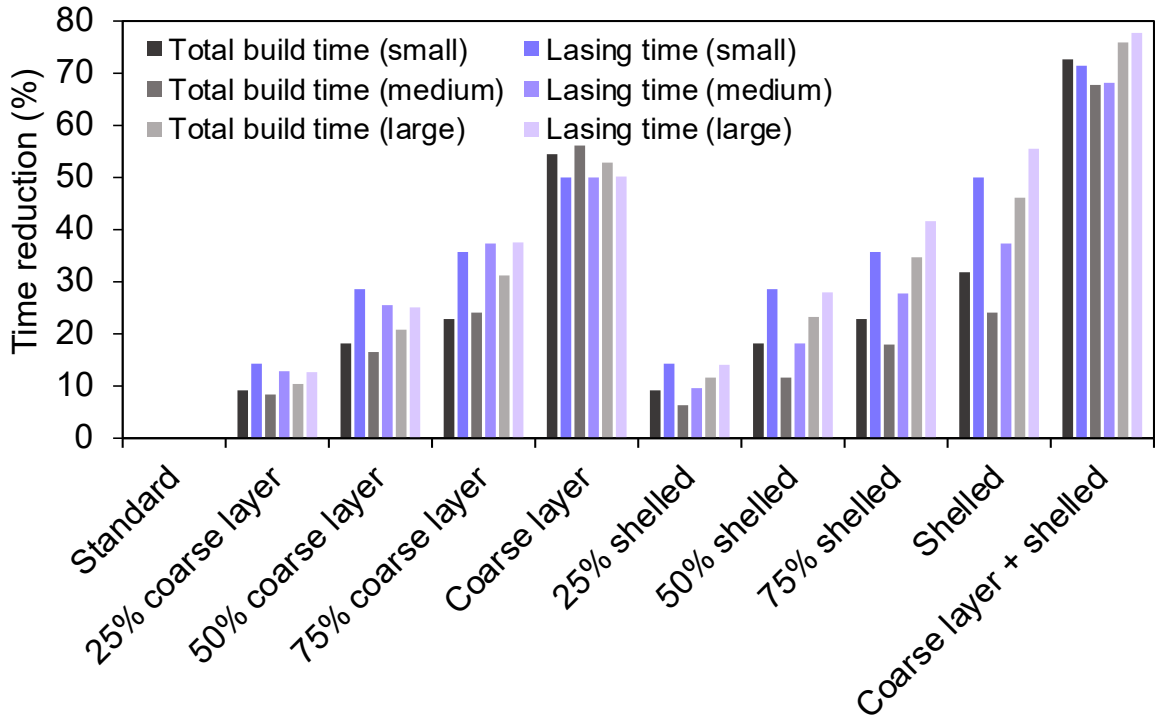

Figure 58 - Build time comparison data as a percentage

6.3.2.2 Build cost

Both cost and profit data associated with the various build methods are depicted in Table 10 and Figure 59. Although material costs remain the same per build, energy and other time-associated overheads allow for a cheaper cost per build when build time is reduced. £74.28 and £70.98 savings per build are possible for 50% coarse layer and 50% shelled builds respectively, amounting to £26,592 and £25,197 savings annually when builds are produced using half the available hours. Continuing observing the 50% scenarios, the additional possible builds per year (66 and 63) also allow for a 22.7% and 21.5% increase in annual profits, amounting to an additional £40,434 and £38,255 annually. Assuming the sale price of components remains constant, the profit margin increases by 2% in each case due to the lesser cost per build.

In the most extreme scenario, 'coarse layer + shelled', large financial gain is possible if lower part quality is tolerable. £290 can be saved per build, amounting to £304,220 saved annually given that 1049 builds are possible compared with 292 for standard LPBF processing. An annual profit increase of 259.2% is possible due to the high volume of builds, and profit margin increases by 9.4% given the lower cost per build.

Table 10 - Financial data of various build types

Build type		Cost per build (£)	Builds per year	Annual profit (£)	Profit increase (%)	Margin (%)
Standard		1526.90	292	178341.65	-	40.0
Coarse layer	**25%**	1489.76	322	196500.25	10.2	41.0
	50%	1452.62	358	218775.82	22.7	42.0
	75%	1422.49	394	240935.65	35.1	42.9
	100%	1307.87	642	391938.43	119.8	46.7
Shelled	**25%**	1491.07	321	195797.25	9.8	41.0
	50%	1455.92	355	216596.52	21.5	42.0
	75%	1426.17	390	237984.97	33.4	42.8
	100%	1390.35	442	270120.25	51.5	43.9
Coarse layer + shelled		1236.89	1049	640579.99	259.2	49.4

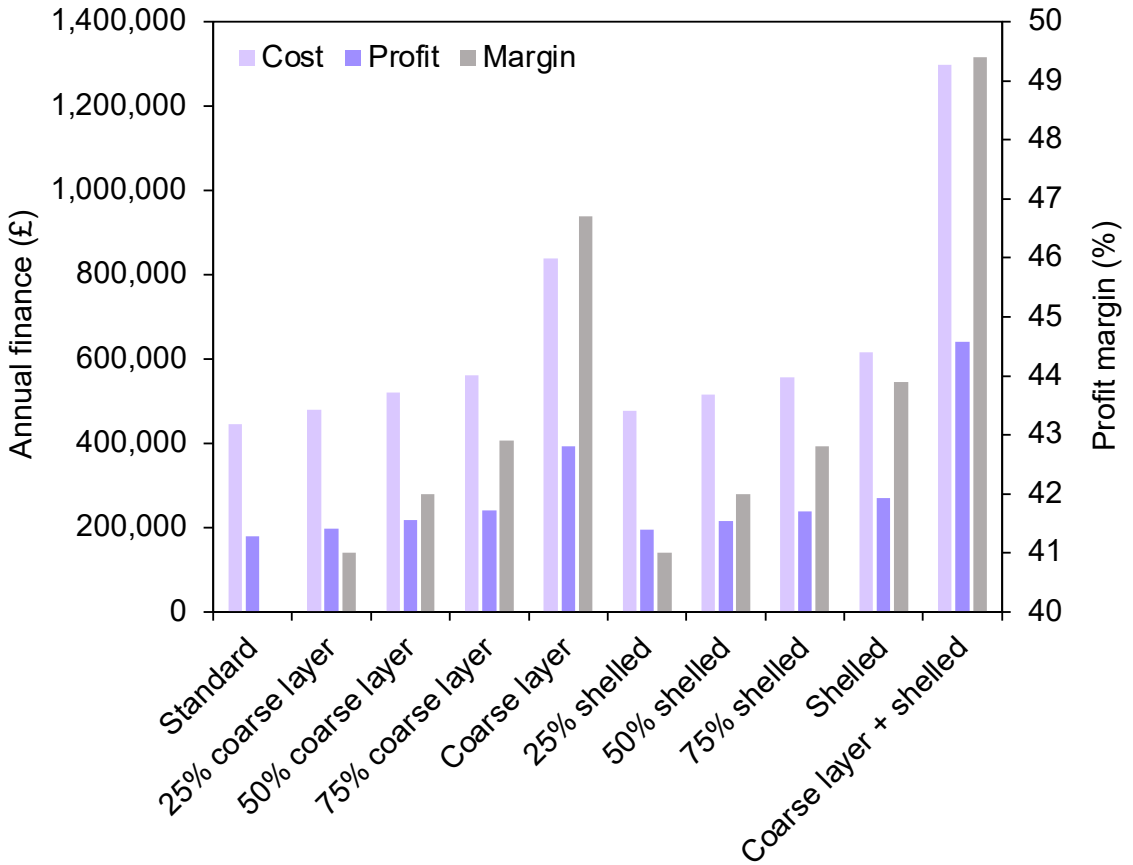

Figure 59 - Additional profit available from including coarse layer and/or shelled volumes in LPBF components

6.3.3 Discussion

It is clear from the data that both significant time can be saved and significant additional profit is available by introducing coarse layer or shelled regions into components. 25% volume produced with coarse layers or shelled is enough to save 10% build time and achieve an additional 10% profit annually, with additional volume achieving substantially more.

While the 100% coarse layer, 100% shelled and the coarse layer + shelled categories show 120%, 52% and 259% annual profit increase respectively, it is important to note that these build methods do not account for any volume to be produced by standard process parameters in order to maintain part integrity in said region. Components manufactured this way are likely to suffer from lesser part quality (mechanical strength, dimensional accuracy, surface roughness). However, for non-critical applications in which these penalties can be tolerated, these build methods are very effective in reducing build time and increasing potential revenue.

The monetary data presented is not absolute, given the amount of time saved using these techniques varies depending on the size of the builds and a single average-sized build is used here. For example, shelling regions of components had a much greater effect on build time in the large build scenario compared with the medium build, exhibiting roughly double the amount of time saved. This is due to the geometry of the components involved in the builds. The large build has a high volume-to-surface-area ratio due to the morphology and the fact it is a single part, meaning there is greater scope for internal voids; whereas the medium build has a low volume-to-surface-area ratio since there are multiple parts with thin section morphology, meaning there is less scope for internal voids given that shell thickness must occupy a greater fraction of the volume. By contrast, the coarse layer method is more consistent across build sizes given shell thickness is not an issue and the entire selected region can be represented by coarse layers.

The finance estimates greatly depend on the number of builds produced. This study assumes the machine is only in operation 50% of the time, in keeping with the literature [215]. However, there is capacity for the machine to operate almost constantly in a 24-hour, remote access, or automated facility – minus only the time required to replace substrates and consumables. In this instance, increase to annual profits could roughly double compared to those reported in the present study.

When considering productivity and cost, the processing methods described in this chapter are significantly beneficial, enabling production of the same geometries in a fraction of the time and at a fraction of the cost. However, there are penalties to adopting these techniques, described in detail in chapters 4 and 6. For components featuring multiple layer thicknesses, the boundary between layer thickness tends to yield large pores that act as stress raisers and crack initiation sites. Similar tensile properties can be achieved to standard LPBF components, at a small cost to ductility where the additional porosity causes premature fracture. For applications aligned with tensile loading, this build technique may be a viable method to reduce build time and cost if manufacturers are willing to tolerate some penalties to elongation to failure. However, for cyclic loading applications, the additional porosity has proven detrimental to fatigue life and the specimens are unsuitable at the present stage of development for applications such as these. The semi-hollow HIPed specimens achieved good quality builds with very high relative density. Ductility was significantly improved at some cost to strength of the material, and hence removes the issues with reduced ductility in the dual layer thickness samples for tensile loading applications. These components achieve near-full density and are hence better suited to fatigue conditions. Manufacturers must be willing to tolerate some reduction in strength due to the HIP process, however, properties are comparable with that of wrought material. Similarly, due to shrinkage, manufacturers must be willing to generate compensated geometries or machine final parts to dimension.

6.4 Conclusions

This chapter used the methods established in chapter 4 of building LPBF components using multiple layer thicknesses to increase productivity, and the lessons learned in chapter 5 regarding interfacial pore formation and failure modes, to develop a new process adaptation to tackle the prevalence of pores along the layer thickness boundaries. Custom LPBF scan strategies were designed to accommodate interfaces across disparate layer thickness sub-volumes of single components. Various scans were designed and tested to enable the laser to raster back and forth between regions of varying parameters, changing parameters both instantaneously and using a ramped region. A secondary rework pass was also applied to the interface region of each of these scan variations to reduce the number and size of interfacial pores. HIPing of semi-hollow specimens was also investigated as a method of reducing build time without concern over similar scanning issues since only a single parameter set was

necessary. Half the volume was dedicated to solid material that is capable of complex geometry during the LPBF process, while the remaining half was shelled to increase throughput but is limited to simple geometries. Both methods are effective in significantly increasing productivity, however, each presented notable issues in part quality when characterised for porosity using XCT and mechanical performance by way of tensile and fatigue testing.

Build times can be reduced as much as 31.2% and 34.6% using coarse layer or shelled regions respectively, while still dedicating at least a quarter of the component volume to optimal parameters to maintain part performance. It is also possible to increase annual profits by one-third by adopting this method – this may increase or decrease depending on the size and number of builds.

By producing entirely shelled components with coarse layers and using a post-process HIP treatment to enclose the void, it is possible to reduce build times by up to 76% and increase annual profit by 259%. This method may only be useful for non-critical applications since no region of the component is dedicated to optimal parameters.

There are some drawbacks to be considered when adopting these build techniques. For dual layer thickness components, pores exist along the interface between layer thicknesses at the current stage of development. Hence this method is currently unsuitable for cyclic loading conditions but is acceptable for tensile loading applications since high strength material is achievable at a small cost to ductility. HIPing of part-hollow components yields greater ductility at a small cost to material strength, hence this material is well suited to tensile loading applications in which a better balance of elongation to failure to yield strength is required. These parts have high relative densities and are better suited to fatigue conditions, however, still exhibit penalties to fatigue life. Additionally, compensated geometries are required to achieve net shape components.

The conclusions are summarised as:

- Novel scan strategies are presented that process multiple layer thicknesses as one area, using ramped parameters and secondary rework passes.
- Interfacial porosity remains prevalent at parameter increment boundaries for both instantaneous and ramped changes. This is attributed to the deceleration and subsequent acceleration of the continuous laser system, as one vector ends and the second begins, creating keyhole pores.

- These keyhole pores align vertically in the build direction.
- Further work is necessary to engineer porosity out of the samples at the parameter increment boundaries. Optimisation of laser delay or a pulsed laser system is likely to alleviate some of the issues with porosity at the end/start point of laser vectors.
- The rework pass was successful in halving the number of pores across the ramping region.
- Standard LPBF specimens exhibited cycles to failure greater than the custom scan specimens by a factor of 20, due to the prevalent interfacial porosity.
- HIPing successfully enclosed the semi-hollow region of components, exhibiting a very low volume of < 10 µm pores.
- Semi-hollow HIPed specimens showed a 30% increase in elongation to failure, however, a 15% reduction in yield stress meant the samples exhibited poor fatigue performance when tested under the same conditions as the other sample sets.
- Both build time and potential profit can be improved by over one-third while still dedicating sub-volumes of components to optimal parameters.
- Build times can be reduced by 76% when combining coarse layers and shelled regions.

In summary, various custom scan strategies have been demonstrated with porosity remaining an issue as process parameters are incremented using successive laser vectors. A further study is required to optimise laser transition among continuous vectors through laser delay time or pulsed laser strategies. The addition of a rework pass was successful in removing approximately half the pores, and HIPing of semi-hollow specimens was successful in densifying components. Significant productivity increases and cost reductions are possible by adopting the methods described in the present and previous chapters, provided manufacturers are willing to tolerate some cost to mechanical performance at the present stage of development.

7 Conclusions

7.1 General conclusions

Novel LPBF build techniques have been demonstrated, whereby components can be discretised into sub-volumes of varying process parameters to optimise for multiple metrics simultaneously. In the present thesis, this method is designed to maintain standard processing regimes aimed at maximising mechanical properties in volumes of high requirements, while introducing techniques associated with superior build rates in volumes with lower property requirements. This aims to alleviate the slow build rates associated with LPBF that act as a barrier to wider adoption of the technology and limits the number of components for which it is economical. The techniques investigated were coarser layer thicknesses and shelled regions that are subject to HIPing to enclose the cavity and melt the entrapped powder – both of which significantly reduce lasing time. The interface among sub-volumes has been characterised to understand fusion across the borders, and this information has been used to inform custom laser scan strategies, tailored directly to the presented build methods to address issues with fusion. Finally, the build time and cost savings possible through adopting these build methods has been quantified and presented.

The initial study in chapter 4 established that the method is valid, successfully producing test specimens in which the bulk material is split evenly between 30 and 90 µm layer volumes, and build time is significantly reduced within the confines of standard LPBF machinery. This study serves a strong basis for further development of the method, whereby LPBF specimens are no longer processed with a one-size-fits-all approach to parameter selection, as evident in the vast majority of the literature. Instead, manufacturers can adopt several sets of parameters in select regions of a part to optimise for strength, ductility, surface roughness (for dimensional accuracy or biocompatibility), and manufacturing productivity.

The test specimens performed well under uniaxial tensile tests, exhibiting similar UTS and elastic moduli to standard LPBF specimens. However, notable penalties to ductility must be tolerated with elongation to failure values dropping up to a maximum of one-third in the 30-90 µm specimens, as a result of an increased presence of pores along the boundary between sub-volumes. The role of interfacial pores as stress raisers was amplified under fatigue testing, in which the fatigue life of multi-layer-thickness specimens generally dropped

significantly compared with standard LPBF specimens. This result could be exploited to tailor localised material properties at the interface, to achieve a desired mechanical response or to guide crack propagation under fatigue and creep conditions. Moreover, for the technique to maximise both mechanical performance and manufacturing productivity to find place in industry, interfacial pore formation and failure modes required further understanding in the following chapter.

Prior to the present thesis, the interface between disparate layer thicknesses in single LPBF components had not been analysed. Chapter 5 sought to gain deeper understanding around fusion, defect formation and failure modes at the interfaces in order to inform a solution to reduce defects. XCT and micro tensile testing with in-situ optical microscopy were used to characterise pore formations at the boundary between sub-volumes and the knock-on effect for tensile response. A novel post-mortem evaluation technique was also demonstrated, in which 3D fracture surface data was collected and reconstructed to compare with pre-test pore XCT data. This method builds significantly on standard failure analysis methods found in the literature, whereby SEM is typically used to identify evidence of pores in 2D with no pre-test pore information available. This method enabled plastic deformation of defects to be measured and could be used in future studies to inform FEA models of transient pore behaviour, as well as use fracture surface information to reverse engineer the pre-test subsurface pore states without the need for more costly characterisation techniques.

This study found that large keyhole pores form along the interface between layer thickness volumes, most likely as a result of a sequential scan strategy, whereby the entire 30 µm layer area is scanned before the 90 µm layer area begins scanning, in mutual layers. This means the infill vectors of the second region end at previously consolidated material that is more reflective and a drop in absorptivity leads to collapse of the keyhole melt depression, introducing pores. Alternatively, the pores may be a result of powder denudation at the interface, during the border pass of the first region, leaving a deficit of powder for the second region the scan. Hence these pores were only found in components where both layer thicknesses are scanned in mutual layers (i.e. interfaces out of plane with the substrate). Interfaces parallel to the substrate exhibited no additional porosity since layer thickness simply changed at a given layer number and sub-volumes were not scanned in mutual layers. Micro tensile testing with in-situ optical microscopy provided real-time evidence of an interfacial pore initiating crack growth and fractography showed evidence of multiple pores

captured within the fracture surface, proving these pores are the root cause of fracture. The information found in this work is crucial to inform development of the build methods to eliminate stress raising at sub-volume boundaries, and to further understand the failure modes at interface locations so the design of interfaces can be harnessed for control of component fracture and local material properties.

It was clear that interfacial pores formed as a result of the build method, and these pores were responsible for initiating fracture in the specimens. Hence the final experimental chapter (chapter 6) investigated new-class, custom scan strategies designed to scan sub-volumes as one component, whereby laser vectors pass continuously back and forth across the boundaries. These custom scan strategies pose significant benefits over stock strategies found in proprietary slicer software, enabling the design freedoms and local process control of LPBF to be better exploited. Various scan strategies were designed and tested, changing parameters both instantaneously and using a ramped region. A secondary rework pass was also applied to the interface region of each of these scan variations to reduce the number and size of interfacial pores. For LPBF to progress to a stage where components can be discretised into sub-volumes, allowing multiple metrics to be optimised simultaneously, scan strategies such as these must be developed and available through standard software. Similarly, the addition of rework passes can have significant benefits on pore reduction, especially as machine learning research progresses and defects can be fixed in-situ with a secondary pass.

HIPing of semi-hollow specimens was also investigated to reduce build times without concern over similar scanning issues since only a single parameter set was necessary. Half the volume was dedicated to solid material that is capable of complex geometry during the LPBF process, while the remaining half was shelled to increase throughput but is limited to simple geometries. Since many LPBF components will require HIPing regardless, this presents a useful method to significantly reduce lasing time at no additional cost. Both layer thickness and HIP methods were effective in significantly increasing build rates and consolidating components; however, each requires further optimisation when considered for critical applications, since internal pores were still responsible for significantly reduced fatigue performance.

Despite laser scan vectors passing continuously across the boundary, interfacial porosity was still prevalent in the test specimens. This is attributed to the deceleration and subsequent acceleration of the laser scanning system, as one vector ends and another begins,

causing the keyhole melt depression to briefly collapse and create a keyhole pore. Hence each parameter increment generated a plane of aligned pores. The rework strategy was successful in halving the number of pores at the interface, however, the inclusion of interfacial pores saw fatigue life fall to around 5% of standard LPBF specimens. The semi-hollow HIPed specimens reached very high densities, with only a small volume of < 10 µm pores visible after HIPing. They exhibited a 30% increase in elongation to failure at the cost of a 15% reduction in yield stress.

This research has presented novel LPBF build methods, by which significant productivity increases and cost reductions are possible. Build times can be reduced as much as 31.2% and 34.6% using coarse layer or shelled regions respectively, while still dedicating at least a quarter of the component volume to optimal parameters to maintain part performance. Some development of the process is still required to maximise mechanical performance. It is also possible to increase annual profits by one-third by adopting this method – this may increase or decrease depending on the size and number of builds. By producing entirely shelled components with coarse layers and using a post-process HIP treatment to enclose the void, it is possible to reduce build times by up to 76% and increase annual profit by 259%. This method may only be useful for non-critical applications since no region of the component is dedicated to optimal parameters.

7.2 Future work

Several areas for future work have been identified that would build on the research topics contained within the thesis.

While new build methods have been established, characterised and developed within the thesis, further investigation into reducing interfacial porosity is required to reach the full potential of the methods described. The presence of keyhole pores at parameter increment boundaries is most likely a result of brief keyhole depression collapse as one laser vector ends and a new vector begins. Hence a study focussing on laser delay, or a study investigating use of a pulsed laser system, is likely to have a useful effect on the transition between laser vectors designed to increment parameters. A finite element model of the laser-material interaction as a fine-layer vector ends and a coarse-layer vector begins would enable the process window for delay or laser pulsing to be isolated (solutions that produce the least

pores), before running an optimisation build within this window and measuring interfacial porosity of the various parts. Once the custom laser scan strategies have been optimised, these designs can be incorporated into slicer software to enable widespread optimisations of LPBF components for multiple metrics, whereby a given stress concentration can be used to inform a LPBF processing topology optimisation to automatically generate the optical build file for the selected metrics (strength, ductility, dimensional accuracy, productivity). These strategies can also extend to multi-material processing.

Additionally, all mechanical testing contained within each study was carried out on test specimens featuring sub-volume interfaces at the midpoint of the gauge length. This design was selected to gain useful insight into the mechanical behaviour and failure modes at the interface location, however, this naturally places interfaces in areas that are most at risk of fracture. In practice, interfaces would be intentionally designed away from areas experiencing higher stress concentrations. Hence a further study would be useful, in which a case study component is discretised into sub-volumes and tested under more accurate service conditions, to determine whether the interfaces still dominate failure.

Sub-volume interface geometry can be designed to guide stress out of plane for a given service condition to improve part performance. In theory, mechanical properties could also be selected in specific areas: a bone implant can be engineered to yield at lower stress values to match bone in weaker areas, or an engine component can be designed to fracture at a safer location, for example. The design of the union must be optimised for each specific load case. For example, more complex load cases than that presented in this study may experience torsion as well as tension, and thus joint geometry will be required to consider sheer as well. Future work would entail a case study investigation of manipulating part properties and failure modes using joint design.

SEM images revealed a consistent distribution of micropores (< 10 μm) in the shelled regions of HIPed specimens that were not evident in the solid region (chapter 6). It stands to reason that argon gas remains trapped within the cavity when semi-hollow components were built, and that a volume of gas is unable to escape during the HIP process, breaking up into micropores throughout the specimens. However, there is little evidence to support this theory at present, and so a further study to investigate this is necessary. This study may also investigate the knock-on effects of these pores, and the potential for micro-cracks where argon pockets push back against the isostatic pressure applied during HIPing. It is necessary

to know the threshold criteria for which the volume of these pores becomes detrimental to fatigue life, after which, a study can be conducted to find the appropriate percentage infill of lattice material that enables minimal lasing time while keeping these pores below the maximum threshold. By maintaining fatigue life, the applications for this method would be broadened significantly.

Development of the 3D fracture reconstruction technique in chapter 5 was beyond the scope of the thesis, however, there are notable manners in which it can be progressed to better serve AM manufacturers. Firstly, the method can be furthered by conducting staged mechanical testing (tensile, fatigue or creep) and inspecting pore growth using XCT at each stage. This allows collection of pore state data at various stages throughout the test, in elastic, plastic and fractured states. Data such as this would enable the deformation behaviour of defects to be applied to computational models for a more accurate, transient stress response. Similarly, pore information could be reverse engineered from fracture surface data to interpret subsurface information prior to testing without the need for more costly characterisation techniques. Information regarding plastic behaviour of LPBF defects is crucial to further understand what constitutes a critical pore under various loading conditions. This data can be applied to future machine learning techniques, whereby threshold criteria can be varied depending upon the component service conditions.

8 References

[1] "Standard Terminology for Additive Manufacturing Technologies." [Online]. Available: https://www.astm.org/f2792-10.html. [Accessed: 06-Jun-2022].

[2] D. Wang, Y. Yang, R. Liu, D. Xiao, and J. Sun, "Study on the designing rules and processability of porous structure based on selective laser melting (SLM)," *J. Mater. Process. Technol.*, vol. 213, no. 10, pp. 1734–1742, Oct. 2013, doi: 10.1016/J.JMATPROTEC.2013.05.001.

[3] M.-S. Pham, C. Liu, I. Todd, and J. Lertthanasarn, "Damage-tolerant architected materials inspired by crystal microstructure," *Nature*, vol. 565, no. 7739, pp. 305–311, Jan. 2019, doi: 10.1038/s41586-018-0850-3.

[4] R. Liu, Z. Wang, T. Sparks, F. Liou, and J. Newkirk, "Aerospace applications of laser additive manufacturing," in *Laser Additive Manufacturing: Materials, Design, Technologies, and Applications*, Elsevier Inc., 2017, pp. 351–371.

[5] M. Munsch, "Laser additive manufacturing of customized prosthetics and implants for biomedical applications," *Laser Addit. Manuf. Mater. Des. Technol. Appl.*, pp. 399–420, Jan. 2017, doi: 10.1016/B978-0-08-100433-3.00015-4.

[6] V. Bhavar, P. Kattire, V. Patil, S. Khot, K. Gujar, and R. Singh, "A review on powder bed fusion technology of metal additive manufacturing," *Addit. Manuf. Handb.*, pp. 251–253, May 2017, doi: 10.1201/9781315119106-15.

[7] A. Saboori, A. Aversa, G. Marchese, S. Biamino, M. Lombardi, and P. Fino, "Application of Directed Energy Deposition-Based Additive Manufacturing in Repair," *Appl. Sci. 2019, Vol. 9, Page 3316*, vol. 9, no. 16, p. 3316, Aug. 2019, doi: 10.3390/APP9163316.

[8] D. R. Feenstra, R. Banerjee, H. L. Fraser, A. Huang, A. Molotnikov, and N. Birbilis, "Critical review of the state of the art in multi-material fabrication via directed energy deposition," *Curr. Opin. Solid State Mater. Sci.*, vol. 25, no. 4, p. 100924, Aug. 2021, doi: 10.1016/J.COSSMS.2021.100924.

[9] N. P. Taylor and R. Pampin, "Activation properties of tungsten as a first wall protection in fusion power plants," *Fusion Eng. Des.*, vol. 81, no. 8–14, pp. 1333–1338, Feb. 2006, doi: 10.1016/J.FUSENGDES.2005.05.010.

[10] J. Xie, H. Lu, J. Lu, X. Song, S. Wu, and J. Lei, "Additive manufacturing of tungsten using directed energy deposition for potential nuclear fusion application," *Surf. Coatings*

Technol., vol. 409, p. 126884, Mar. 2021, doi: 10.1016/J.SURFCOAT.2021.126884.

[11] D. Svetlizky *et al.*, "Directed energy deposition (DED) additive manufacturing: Physical characteristics, defects, challenges and applications," *Mater. Today*, vol. 49, pp. 271–295, Oct. 2021, doi: 10.1016/J.MATTOD.2021.03.020.

[12] M. Simonelli *et al.*, "Towards digital metal additive manufacturing via high-temperature drop-on-demand jetting," *Addit. Manuf.*, vol. 30, p. 100930, Dec. 2019, doi: 10.1016/J.ADDMA.2019.100930.

[13] M. Orme, Q. Liu, and R. Smith, "Molten Aluminum Micro-Droplet Formation and Deposition for Advanced Manufacturing Applications," *Alum. Trans. J.*, 2000.

[14] J. Luo, W. Wang, W. Xiong, H. Shen, and L. Qi, "Formation of uniform metal traces using alternate droplet printing," *Int. J. Mach. Tools Manuf.*, vol. 122, pp. 47–54, Nov. 2017, doi: 10.1016/J.IJMACHTOOLS.2017.05.004.

[15] A. Amirzadeh, M. Raessi, and S. Chandra, "Producing molten metal droplets smaller than the nozzle diameter using a pneumatic drop-on-demand generator," *Exp. Therm. Fluid Sci.*, vol. 47, pp. 26–33, May 2013, doi: 10.1016/J.EXPTHERMFLUSCI.2012.12.006.

[16] Z. Luo, X. Wang, L. Wang, D. Sun, and Z. Li, "Drop-on-demand electromagnetic printing of metallic droplets," *Mater. Lett.*, vol. 188, pp. 184–187, Feb. 2017, doi: 10.1016/J.MATLET.2016.11.021.

[17] N. Gilani, N. T. Aboulkhair, M. Simonelli, M. East, I. Ashcroft, and R. J. M. Hague, "Insights into drop-on-demand metal additive manufacturing through an integrated experimental and computational study," *Addit. Manuf.*, vol. 48, p. 102402, Dec. 2021, doi: 10.1016/J.ADDMA.2021.102402.

[18] T. Y. Ansell, H. Wang, and J. Fuh, "Current Status of Liquid Metal Printing," *J. Manuf. Mater. Process. 2021, Vol. 5, Page 31*, vol. 5, no. 2, p. 31, Apr. 2021, doi: 10.3390/JMMP5020031.

[19] D. Bergström, "The Absorption of Laser Light by Rough Metal Surfaces."

[20] C. Y. Yap *et al.*, "Review of selective laser melting: Materials and applications," *Appl. Phys. Rev.*, vol. 2, no. 4, p. 041101, Dec. 2015, doi: 10.1063/1.4935926.

[21] I. Yadroitsava, J. Els, G. Booysen, and I. Yadroitsev, "Peculiarities of single track formation from TI6Al4V alloy at different laser power densities by selective laser melting," *South African J. Ind. Eng.*, vol. 26, no. 3, pp. 86–95, Nov. 2015, doi: 10.7166/26-3-1185.

[22] X. Shi *et al.*, “Performance of High Layer Thickness in Selective Laser Melting of Ti6Al4V,” *Mater. 2016, Vol. 9, Page 975*, vol. 9, no. 12, p. 975, Dec. 2016, doi: 10.3390/MA9120975.

[23] J. Metelkova, Y. Kinds, K. Kempen, C. de Formanoir, A. Witvrouw, and B. Van Hooreweder, “On the influence of laser defocusing in Selective Laser Melting of 316L,” *Addit. Manuf.*, vol. 23, pp. 161–169, Oct. 2018, doi: 10.1016/J.ADDMA.2018.08.006.

[24] R. A. Rahman Rashid, H. Ali, S. Palanisamy, and S. H. Masood, “Effect of process parameters on the surface characteristics of AlSi12 samples made via Selective Laser Melting,” *Mater. Today Proc.*, vol. 4, no. 8, pp. 8724–8730, Jan. 2017, doi: 10.1016/J.MATPR.2017.07.221.

[25] W. King, A. T. Anderson, R. M. Ferencz, N. E. Hodge, C. Kamath, and S. A. Khairallah, “Overview of modelling and simulation of metal powder bed fusion process at Lawrence Livermore National Laboratory,” *Mater. Sci. Technol.*, vol. 31, no. 8, pp. 957–968, Jun. 2015, doi: 10.1179/1743284714Y.0000000728.

[26] T. Qi, H. Zhu, H. Zhang, J. Yin, L. Ke, and X. Zeng, “Selective laser melting of Al7050 powder: Melting mode transition and comparison of the characteristics between the keyhole and conduction mode,” *Mater. Des.*, vol. 135, pp. 257–266, Dec. 2017, doi: 10.1016/J.MATDES.2017.09.014.

[27] S. Patel and M. Vlasea, “Melting modes in laser powder bed fusion,” *Materialia*, vol. 9, Mar. 2020, doi: 10.1016/J.MTLA.2020.100591.

[28] D. Bäuerle, “Laser Processing and Chemistry,” *Laser Process. Chem.*, 2011, doi: 10.1007/978-3-642-17613-5.

[29] J. Blackburn, C. Allen, P. Hilton, and L. Li, “Nd:YAG laser welding of titanium alloys using a directed gas jet,” *J. Laser Appl.*, vol. 22, no. 2, pp. 71–78, May 2010, doi: 10.2351/1.3455825.

[30] I. Bitharas, N. Parab, C. Zhao, T. Sun, A. D. Rollett, and A. J. Moore, “The interplay between vapour, liquid, and solid phases in laser powder bed fusion,” *Nat. Commun. 2022 131*, vol. 13, no. 1, pp. 1–12, May 2022, doi: 10.1038/s41467-022-30667-z.

[31] W. E. King *et al.*, “Observation of keyhole-mode laser melting in laser powder-bed fusion additive manufacturing,” *J. Mater. Process. Technol.*, vol. 214, no. 12, pp. 2915–2925, Dec. 2014, doi: 10.1016/j.jmatprotec.2014.06.005.

[32] A. B. Spierings, N. Herres, G. Levy, and M. A. B. Spierings, “Influence of the particle size

distribution on surface quality and mechanical properties in AM steel parts ETH Library Influence of the particle size distribution on surface quality and mechanical properties in additive manufactured stainless steel parts," *Rapid Prototyp. J.*, vol. 17, no. 3, doi: 10.3929/ethz-a-006443611.

[33] J. Whiting and J. Fox, "Characterization of feedstock in the Powder Bed Fusion process: sources of variation in particle size distribution and the factors that influence them."

[34] A. Simchi, "The role of particle size on the laser sintering of iron powder," *Metall. Mater. Trans. B*, vol. 35, no. 5, pp. 937–948, Oct. 2004, doi: 10.1007/s11663-004-0088-3.

[35] A. Santomaso, P. Lazzaro, and P. Canu, "Powder flowability and density ratios: the impact of granules packing," *Chem. Eng. Sci.*, vol. 58, no. 13, pp. 2857–2874, Jul. 2003, doi: 10.1016/S0009-2509(03)00137-4.

[36] C. Yan, L. Hao, A. Hussein, and P. Young, "Ti–6Al–4V triply periodic minimal surface structures for bone implants fabricated via selective laser melting," *J. Mech. Behav. Biomed. Mater.*, vol. 51, pp. 61–73, Nov. 2015, doi: 10.1016/J.JMBBM.2015.06.024.

[37] S. A. Farzadfar, M. J. Murtagh, and N. Venugopal, "Impact of IN718 bimodal powder size distribution on the performance and productivity of laser powder bed fusion additive manufacturing process," *Powder Technol.*, vol. 375, pp. 60–80, Sep. 2020, doi: 10.1016/J.POWTEC.2020.07.092.

[38] S. Vock, B. Klöden, A. Kirchner, T. Weißgärber, and B. Kieback, "Powders for powder bed fusion: a review," *Prog. Addit. Manuf.*, vol. 4, no. 4, pp. 383–397, Dec. 2019, doi: 10.1007/S40964-019-00078-6/TABLES/3.

[39] J. H. Tan, W. L. E. Wong, and K. W. Dalgarno, "An overview of powder granulometry on feedstock and part performance in the selective laser melting process," *Addit. Manuf.*, vol. 18, pp. 228–255, Dec. 2017, doi: 10.1016/J.ADDMA.2017.10.011.

[40] J. Trapp, A. M. Rubenchik, G. Guss, and M. J. Matthews, "In situ absorptivity measurements of metallic powders during laser powder-bed fusion additive manufacturing," *Appl. Mater. Today*, vol. 9, pp. 341–349, Dec. 2017, doi: 10.1016/J.APMT.2017.08.006.

[41] V. Manakari, G. Parande, and M. Gupta, "Selective Laser Melting of Magnesium and Magnesium Alloy Powders: A Review," *Met. 2017, Vol. 7, Page 2*, vol. 7, no. 1, p. 2, Dec. 2016, doi: 10.3390/MET7010002.

[42] H. R. Kotadia, G. Gibbons, A. Das, and P. D. Howes, “A review of Laser Powder Bed Fusion Additive Manufacturing of aluminium alloys: Microstructure and properties,” *Addit. Manuf.*, vol. 46, p. 102155, Oct. 2021, doi: 10.1016/J.ADDMA.2021.102155.

[43] W. J. Reynolds, “Predicting melt pool behaviour in LPBF through high fidelity modelling,” Jul. 2022.

[44] A. M. Rubenchik, W. E. King, and S. S. Wu, “Scaling laws for the additive manufacturing,” *J. Mater. Process. Technol.*, vol. 257, pp. 234–243, Jul. 2018, doi: 10.1016/J.JMATPROTEC.2018.02.034.

[45] H. Gong, K. Rafi, H. Gu, T. Starr, and B. Stucker, “Analysis of defect generation in Ti–6Al–4V parts made using powder bed fusion additive manufacturing processes,” *Addit. Manuf.*, vol. 1–4, pp. 87–98, Oct. 2014, doi: 10.1016/J.ADDMA.2014.08.002.

[46] H. Gong, K. Rafi, H. Gu, G. D. Janaki Ram, T. Starr, and B. Stucker, “Influence of defects on mechanical properties of Ti-6Al-4V components produced by selective laser melting and electron beam melting,” *Mater. Des.*, vol. 86, pp. 545–554, Dec. 2015, doi: 10.1016/j.matdes.2015.07.147.

[47] J. R. Poulin, A. Kreitcberg, P. Terriault, and V. Brailovski, “Long fatigue crack propagation behavior of laser powder bed-fused inconel 625 with intentionally-seeded porosity,” *Int. J. Fatigue*, vol. 127, pp. 144–156, Oct. 2019, doi: 10.1016/j.ijfatigue.2019.06.008.

[48] N. Sanaei, A. Fatemi, and N. Phan, “Defect characteristics and analysis of their variability in metal L-PBF additive manufacturing,” *Mater. Des.*, vol. 182, p. 108091, Nov. 2019, doi: 10.1016/j.matdes.2019.108091.

[49] B. Zhang, Y. Li, and Q. Bai, “Defect Formation Mechanisms in Selective Laser Melting: A Review,” doi: 10.1007/s10033-017-0121-5.

[50] H. Gong, K. Rafi, N. V Karthik, T. Starr, and B. Stucker, “Defect Morphology in Ti-6Al-4V Parts Fabricated by Selective Laser Melting and Electron Beam Melting.”

[51] A. Matsunawa, J.-D. Kim, N. Seto, M. Mizutani, and S. Katayama, “Dynamics of keyhole and molten pool in laser welding,” *J. Laser Appl.*, vol. 10, no. 6, p. 247, Nov. 1998, doi: 10.2351/1.521858.

[52] V. Semak and A. Matsunawa, “The role of recoil pressure in energy balance during laser materials processing,” *J. Phys. D. Appl. Phys.*, vol. 30, no. 18, p. 2541, Sep. 1997, doi: 10.1088/0022-3727/30/18/008.

[53] S. Leuders *et al.*, “On the mechanical behaviour of titanium alloy TiAl6V4 manufactured

by selective laser melting: Fatigue resistance and crack growth performance," *Int. J. Fatigue*, vol. 48, pp. 300–307, Mar. 2013, doi: 10.1016/J.IJFATIGUE.2012.11.011.

[54] A. A. Martin *et al.*, "Dynamics of pore formation during laser powder bed fusion additive manufacturing," *Nat. Commun.*, vol. 10, no. 1, pp. 1–10, Dec. 2019, doi: 10.1038/s41467-019-10009-2.

[55] S. Shrestha and Y. Kevin Chou, "A Numerical Study on the Keyhole Formation During Laser Powder Bed Fusion Process," *J. Manuf. Sci. Eng.*, vol. 141, no. 10, Oct. 2019, doi: 10.1115/1.4044100.

[56] M. N. Ahsan, A. J. Pinkerton, R. J. Moat, and J. Shackleton, "A comparative study of laser direct metal deposition characteristics using gas and plasma-atomized Ti–6Al–4V powders," *Mater. Sci. Eng. A*, vol. 528, no. 25–26, pp. 7648–7657, Sep. 2011, doi: 10.1016/J.MSEA.2011.06.074.

[57] G. M. Janowski, F. S. Biancaniello, and S. D. Ridder, "Beneficial effects of nitrogen atomization on an austenitic stainless steel," *Metall. Trans. A 1992 2312*, vol. 23, no. 12, pp. 3263–3272, Dec. 1992, doi: 10.1007/BF02663435.

[58] S. K. Everton, M. Hirsch, P. Stravroulakis, R. K. Leach, and A. T. Clare, "Review of in-situ process monitoring and in-situ metrology for metal additive manufacturing," *Mater. Des.*, vol. 95, pp. 431–445, Apr. 2016, doi: 10.1016/J.MATDES.2016.01.099.

[59] A. Sola and A. Nouri, "Microstructural porosity in additive manufacturing: The formation and detection of pores in metal parts fabricated by powder bed fusion," *J. Adv. Manuf. Process.*, vol. 1, no. 3, p. e10021, Jul. 2019, doi: 10.1002/AMP2.10021.

[60] H. Galarraga, D. A. Lados, R. R. Dehoff, M. M. Kirka, and P. Nandwana, "Effects of the microstructure and porosity on properties of Ti-6Al-4V ELI alloy fabricated by electron beam melting (EBM)," *Addit. Manuf.*, vol. 10, pp. 47–57, Apr. 2016, doi: 10.1016/J.ADDMA.2016.02.003.

[61] T. Vilaro, C. Colin, and J. D. Bartout, "As-Fabricated and Heat-Treated Microstructures of the Ti-6Al-4V Alloy Processed by Selective Laser Melting," *Metall. Mater. Trans. A*, vol. 42, no. 10, pp. 3190–3199, Oct. 2011, doi: 10.1007/s11661-011-0731-y.

[62] M. Simonelli *et al.*, "A Study on the Laser Spatter and the Oxidation Reactions During Selective Laser Melting of 316L Stainless Steel, Al-Si10-Mg, and Ti-6Al-4V," *Metall. Mater. Trans. A*, vol. 46, no. 9, pp. 3842–3851, Sep. 2015, doi: 10.1007/s11661-015-2882-8.

[63] T. DebRoy *et al.*, “Additive manufacturing of metallic components – Process, structure and properties,” *Prog. Mater. Sci.*, vol. 92, pp. 112–224, Mar. 2018, doi: 10.1016/J.PMATSCI.2017.10.001.

[64] M. J. Zhang, G. Y. Chen, Y. Zhou, S. C. Li, and H. Deng, “Observation of spatter formation mechanisms in high-power fiber laser welding of thick plate,” *Appl. Surf. Sci.*, vol. 280, pp. 868–875, Sep. 2013, doi: 10.1016/J.APSUSC.2013.05.081.

[65] D. Wang *et al.*, “Mechanisms and characteristics of spatter generation in SLM processing and its effect on the properties,” *Mater. Des.*, vol. 117, pp. 121–130, Mar. 2017, doi: 10.1016/J.MATDES.2016.12.060.

[66] Z. A. Young *et al.*, “Types of spatter and their features and formation mechanisms in laser powder bed fusion additive manufacturing process,” *Addit. Manuf.*, vol. 36, p. 101438, Dec. 2020, doi: 10.1016/J.ADDMA.2020.101438.

[67] M. J. Matthews, G. Guss, S. A. Khairallah, A. M. Rubenchik, P. J. Depond, and W. E. King, “Denudation of metal powder layers in laser powder bed fusion processes,” *Acta Mater.*, vol. 114, pp. 33–42, Aug. 2016, doi: 10.1016/J.ACTAMAT.2016.05.017.

[68] G. Repossini, V. Laguzza, M. Grasso, and B. M. Colosimo, “On the use of spatter signature for in-situ monitoring of Laser Powder Bed Fusion,” *Addit. Manuf.*, vol. 16, pp. 35–48, Aug. 2017, doi: 10.1016/j.addma.2017.05.004.

[69] L. E. Criales, Y. M. Arısoy, B. Lane, S. Moylan, A. Donmez, and T. Özel, “Laser powder bed fusion of nickel alloy 625: Experimental investigations of effects of process parameters on melt pool size and shape with spatter analysis,” *Int. J. Mach. Tools Manuf.*, vol. 121, pp. 22–36, Oct. 2017, doi: 10.1016/j.ijmachtools.2017.03.004.

[70] C. M. Cepeda-Jiménez, F. Potenza, E. Magalini, V. Luchin, A. Molinari, and M. T. Pérez-Prado, “Effect of energy density on the microstructure and texture evolution of Ti-6Al-4V manufactured by laser powder bed fusion,” *Mater. Charact.*, vol. 163, p. 110238, May 2020, doi: 10.1016/j.matchar.2020.110238.

[71] C. Qiu, N. J. E. Adkins, and M. M. Attallah, “Microstructure and tensile properties of selectively laser-melted and of HIPed laser-melted Ti–6Al–4V,” *Mater. Sci. Eng. A*, vol. 578, pp. 230–239, Aug. 2013, doi: 10.1016/J.MSEA.2013.04.099.

[72] D. Gu *et al.*, “Densification behavior, microstructure evolution, and wear performance of selective laser melting processed commercially pure titanium,” *Acta Mater.*, vol. 60, no. 9, pp. 3849–3860, May 2012, doi: 10.1016/J.ACTAMAT.2012.04.006.

[73] L. Parry, I. A. Ashcroft, and R. D. Wildman, “Understanding the effect of laser scan strategy on residual stress in selective laser melting through thermo-mechanical simulation,” *Addit. Manuf.*, vol. 12, pp. 1–15, Oct. 2016, doi: 10.1016/J.ADDMA.2016.05.014.

[74] B. Vayssette, N. Saintier, C. Brugger, M. Elmay, and E. Pessard, “Surface roughness of Ti-6Al-4V parts obtained by SLM and EBM: Effect on the High Cycle Fatigue life,” *Procedia Eng.*, vol. 213, pp. 89–97, Jan. 2018, doi: 10.1016/J.PROENG.2018.02.010.

[75] P. Mercelis and J. P. Kruth, “Residual stresses in selective laser sintering and selective laser melting,” *Rapid Prototyp. J.*, vol. 12, no. 5, pp. 254–265, 2006, doi: 10.1108/13552540610707013/FULL/XML.

[76] Y. Liu, Y. Yang, and D. Wang, “A study on the residual stress during selective laser melting (SLM) of metallic powder,” *Int. J. Adv. Manuf. Technol. 2016 871*, vol. 87, no. 1, pp. 647–656, Feb. 2016, doi: 10.1007/S00170-016-8466-Y.

[77] T. Simson, A. Emmel, A. Dwars, and J. Böhm, “Residual stress measurements on AISI 316L samples manufactured by selective laser melting,” *Addit. Manuf.*, vol. 17, pp. 183–189, Oct. 2017, doi: 10.1016/J.ADDMA.2017.07.007.

[78] A. J. Dunbar *et al.*, “Development of experimental method for in situ distortion and temperature measurements during the laser powder bed fusion additive manufacturing process,” *Addit. Manuf.*, vol. 12, pp. 25–30, Oct. 2016, doi: 10.1016/J.ADDMA.2016.04.007.

[79] A. Bauereiß, T. Scharowsky, and C. Körner, “Defect generation and propagation mechanism during additive manufacturing by selective beam melting,” *J. Mater. Process. Technol.*, vol. 214, no. 11, pp. 2522–2528, Nov. 2014, doi: 10.1016/J.JMATPROTEC.2014.05.002.

[80] T. Craeghs, S. Clijsters, J. P. Kruth, F. Bechmann, and M. C. Ebert, “Detection of Process Failures in Layerwise Laser Melting with Optical Process Monitoring,” *Phys. Procedia*, vol. 39, pp. 753–759, Jan. 2012, doi: 10.1016/J.PHPRO.2012.10.097.

[81] V. Cain, L. Thijs, J. Van Humbeeck, B. Van Hooreweder, and R. Knutsen, “Crack propagation and fracture toughness of Ti6Al4V alloy produced by selective laser melting,” *Addit. Manuf.*, vol. 5, pp. 68–76, Jan. 2015, doi: 10.1016/J.ADDMA.2014.12.006.

[82] T. Mukherjee, W. Zhang, and T. DebRoy, “An improved prediction of residual stresses

and distortion in additive manufacturing," *Comput. Mater. Sci.*, vol. 126, pp. 360–372, Jan. 2017, doi: 10.1016/J.COMMATSCI.2016.10.003.

[83] J. P. Kruth, J. Deckers, E. Yasa, and R. Wauthlé, "Assessing and comparing influencing factors of residual stresses in selective laser melting using a novel analysis method:," *http://dx.doi.org/10.1177/0954405412437085*, vol. 226, no. 6, pp. 980–991, Mar. 2012, doi: 10.1177/0954405412437085.

[84] D. Buchbinder, W. Meiners, N. Pirch, K. Wissenbach, and J. Schrage, "Investigation on reducing distortion by preheating during manufacture of aluminum components using selective laser melting," *J. Laser Appl.*, vol. 26, no. 1, p. 012004, Nov. 2013, doi: 10.2351/1.4828755.

[85] Y. Lu *et al.*, "Study on the microstructure, mechanical property and residual stress of SLM Inconel-718 alloy manufactured by differing island scanning strategy," *Opt. Laser Technol.*, vol. 75, pp. 197–206, Dec. 2015, doi: 10.1016/J.OPTLASTEC.2015.07.009.

[86] H. Ali, H. Ghadbeigi, and K. Mumtaz, "Effect of scanning strategies on residual stress and mechanical properties of Selective Laser Melted Ti6Al4V," *Mater. Sci. Eng. A*, vol. 712, pp. 175–187, Jan. 2018, doi: 10.1016/J.MSEA.2017.11.103.

[87] T. Furumoto, S. Abe, M. Yamaguchi, and A. Hosokawa, "Improving surface quality using laser scanning and machining strategy combining powder bed fusion and machining processes," *Int. J. Adv. Manuf. Technol.*, vol. 117, no. 11–12, pp. 3405–3413, Dec. 2021, doi: 10.1007/S00170-021-07880-Z/FIGURES/14.

[88] I. Yadroitsev and I. Smurov, "Surface Morphology in Selective Laser Melting of Metal Powders," *Phys. Procedia*, vol. 12, no. PART 1, pp. 264–270, Jan. 2011, doi: 10.1016/J.PHPRO.2011.03.034.

[89] J. Metelkova, L. Vanmunster, H. Haitjema, and B. Van Hooreweder, "Texture of inclined up-facing surfaces in laser powder bed fusion of metals," *Addit. Manuf.*, vol. 42, p. 101970, Jun. 2021, doi: 10.1016/J.ADDMA.2021.101970.

[90] M. Grasso and B. M. Colosimo, "Process defects and in situ monitoring methods in metal powder bed fusion: a review," *Meas. Sci. Technol.*, vol. 28, no. 4, p. 044005, Feb. 2017, doi: 10.1088/1361-6501/AA5C4F.

[91] Y. Tian, D. Tomus, P. Rometsch, and X. Wu, "Influences of processing parameters on surface roughness of Hastelloy X produced by selective laser melting," *Addit. Manuf.*, vol. 13, pp. 103–112, Jan. 2017, doi: 10.1016/J.ADDMA.2016.10.010.

[92] P. Li, D. H. Warner, A. Fatemi, and N. Phan, “Critical assessment of the fatigue performance of additively manufactured Ti–6Al–4V and perspective for future research,” *Int. J. Fatigue*, vol. 85, pp. 130–143, Apr. 2016, doi: 10.1016/J.IJFATIGUE.2015.12.003.

[93] N. Sanaei and A. Fatemi, “Analysis of the effect of surface roughness on fatigue performance of powder bed fusion additive manufactured metals,” *Theor. Appl. Fract. Mech.*, vol. 108, p. 102638, Aug. 2020, doi: 10.1016/J.TAFMEC.2020.102638.

[94] K. S. Chan, M. Koike, R. L. Mason, and T. Okabe, “Fatigue life of titanium alloys fabricated by additive layer manufacturing techniques for dental implants,” *Metall. Mater. Trans. A Phys. Metall. Mater. Sci.*, vol. 44, no. 2, pp. 1010–1022, Feb. 2013, doi: 10.1007/S11661-012-1470-4/FIGURES/12.

[95] A. Nouri, A. Rohani Shirvan, Y. Li, and C. Wen, “Additive manufacturing of metallic and polymeric load-bearing biomaterials using laser powder bed fusion: A review,” *J. Mater. Sci. Technol.*, vol. 94, pp. 196–215, Dec. 2021, doi: 10.1016/J.JMST.2021.03.058.

[96] T. M. Mower and M. J. Long, “Mechanical behavior of additive manufactured, powder-bed laser-fused materials,” *Mater. Sci. Eng. A*, vol. 651, pp. 198–213, Jan. 2016, doi: 10.1016/j.msea.2015.10.068.

[97] G. Strano, L. Hao, R. M. Everson, and K. E. Evans, “Surface roughness analysis, modelling and prediction in selective laser melting,” *J. Mater. Process. Technol.*, vol. 213, no. 4, pp. 589–597, Apr. 2013, doi: 10.1016/J.JMATPROTEC.2012.11.011.

[98] K. Mumtaz and N. Hopkinson, “Top surface and side roughness of Inconel 625 parts processed using selective laser melting,” *Rapid Prototyp. J.*, vol. 15, no. 2, pp. 96–103, Mar. 2009, doi: 10.1108/13552540910943397/FULL/PDF.

[99] M. Elsayed, M. Ghazy, Y. Youssef, and K. Essa, “Optimization of SLM process parameters for Ti6Al4V medical implants,” *Rapid Prototyp. J.*, vol. 25, no. 3, pp. 433–447, Apr. 2019, doi: 10.1108/RPJ-05-2018-0112/FULL/PDF.

[100] H. Liu *et al.*, “High-quality surface smoothening of laser powder bed fusion additive manufacturing AlSi10Mg via intermittent electrochemical polishing,” *Surf. Coatings Technol.*, vol. 443, p. 128608, Aug. 2022, doi: 10.1016/J.SURFCOAT.2022.128608.

[101] E. H. Valente, C. Gundlach, T. L. Christiansen, and M. A. J. Somers, “Effect of Scanning Strategy During Selective Laser Melting on Surface Topography, Porosity, and Microstructure of Additively Manufactured Ti-6Al-4V,” *Appl. Sci. 2019, Vol. 9, Page*

5554, vol. 9, no. 24, p. 5554, Dec. 2019, doi: 10.3390/APP9245554.

[102] J. Robinson, I. Ashton, P. Fox, E. Jones, and C. Sutcliffe, "Determination of the effect of scan strategy on residual stress in laser powder bed fusion additive manufacturing," *Addit. Manuf.*, vol. 23, pp. 13–24, Oct. 2018, doi: 10.1016/J.ADDMA.2018.07.001.

[103] E. Malekipour and H. El-Mounayri, "Scanning Strategies in the PBF Process: A Critical Review," *ASME Int. Mech. Eng. Congr. Expo. Proc.*, vol. 2A-2020, Feb. 2021, doi: 10.1115/IMECE2020-24589.

[104] E. Yasa, J. Deckers, J. P. Kruth, M. Rombouts, and J. Luyten, "Investigation of Sectoral Scanning in Selective Laser Melting," *ASME 2010 10th Bienn. Conf. Eng. Syst. Des. Anal. ESDA2010*, vol. 4, pp. 695–703, Dec. 2010, doi: 10.1115/ESDA2010-24621.

[105] Y. M. Arısoy, L. E. Criales, T. Özel, B. Lane, S. Moylan, and A. Donmez, "Influence of scan strategy and process parameters on microstructure and its optimization in additively manufactured nickel alloy 625 via laser powder bed fusion," *Int. J. Adv. Manuf. Technol. 2016 905*, vol. 90, no. 5, pp. 1393–1417, Sep. 2016, doi: 10.1007/S00170-016-9429-Z.

[106] B. Cheng, S. Shrestha, and K. Chou, "Stress and deformation evaluations of scanning strategy effect in selective laser melting," *Addit. Manuf.*, vol. 12, pp. 240–251, Oct. 2016, doi: 10.1016/J.ADDMA.2016.05.007.

[107] J.-P. Kruth, M. Badrossamay, E. Yasa, J. Deckers, L. Thijs, and J. Van Humbeeck, "Part and material properties in selective laser melting of metals," *Proc. 16th Int. Symp. Electromachining (ISEM XVI)*, no. 9, pp. 3–14, 2010.

[108] C. Qiu *et al.*, "Influence of Laser Processing Strategy and Remelting on Surface Structure and Porosity Development during Selective Laser Melting of a Metallic Material," *Metall. Mater. Trans. A Phys. Metall. Mater. Sci.*, vol. 50, no. 9, pp. 4423–4434, Sep. 2019, doi: 10.1007/S11661-019-05348-0/FIGURES/9.

[109] M. Hirsch *et al.*, "Targeted rework strategies for powder bed additive manufacture," *Addit. Manuf.*, vol. 19, pp. 127–133, Jan. 2018, doi: 10.1016/J.ADDMA.2017.11.011.

[110] S. Liu and Y. C. Shin, "Additive manufacturing of Ti6Al4V alloy: A review," *Mater. Des.*, vol. 164, p. 107552, Feb. 2019, doi: 10.1016/J.MATDES.2018.107552.

[111] E. Chlebus, B. Kuźnicka, T. Kurzynowski, and B. Dybała, "Microstructure and mechanical behaviour of Ti—6Al—7Nb alloy produced by selective laser melting," *Mater. Charact.*, vol. 62, no. 5, pp. 488–495, May 2011, doi: 10.1016/J.MATCHAR.2011.03.006.

[112] L. C. Zhang, D. Klemm, J. Eckert, Y. L. Hao, and T. B. Sercombe, "Manufacture by

selective laser melting and mechanical behavior of a biomedical Ti–24Nb–4Zr–8Sn alloy," *Scr. Mater.*, vol. 65, no. 1, pp. 21–24, Jun. 2011, doi: 10.1016/J.SCRIPTAMAT.2011.03.024.

[113] L. Zhou, T. Yuan, R. Li, J. Tang, M. Wang, and F. Mei, "Microstructure and mechanical properties of selective laser melted biomaterial Ti-13Nb-13Zr compared to hot-forging," *Mater. Sci. Eng. A*, vol. 725, pp. 329–340, May 2018, doi: 10.1016/J.MSEA.2018.04.001.

[114] I. Tolosa, F. Garciandía, F. Zubiri, F. Zapirain, and A. Esnaola, "Study of mechanical properties of AISI 316 stainless steel processed by 'selective laser melting', following different manufacturing strategies," *Int. J. Adv. Manuf. Technol. 2010 515*, vol. 51, no. 5, pp. 639–647, Apr. 2010, doi: 10.1007/S00170-010-2631-5.

[115] N. Ahmed, I. Barsoum, G. Haidemenopoulos, and R. K. A. Al-Rub, "Process parameter selection and optimization of laser powder bed fusion for 316L stainless steel: A review," *J. Manuf. Process.*, vol. 75, pp. 415–434, Mar. 2022, doi: 10.1016/J.JMAPRO.2021.12.064.

[116] J. Sander, J. Hufenbach, L. Giebeler, H. Wendrock, U. Kühn, and J. Eckert, "Microstructure and properties of FeCrMoVC tool steel produced by selective laser melting," *Mater. Des.*, vol. 89, pp. 335–341, Jan. 2016, doi: 10.1016/J.MATDES.2015.09.148.

[117] Y. Bai, Y. Yang, D. Wang, and M. Zhang, "Influence mechanism of parameters process and mechanical properties evolution mechanism of maraging steel 300 by selective laser melting," *Mater. Sci. Eng. A*, vol. 703, pp. 116–123, Aug. 2017, doi: 10.1016/J.MSEA.2017.06.033.

[118] B. Zhang, N. E. Feninèche, H. Liao, and C. Coddet, "Microstructure and Magnetic Properties of Fe–Ni Alloy Fabricated by Selective Laser Melting Fe/Ni Mixed Powders," *J. Mater. Sci. Technol.*, vol. 29, no. 8, pp. 757–760, Aug. 2013, doi: 10.1016/J.JMST.2013.05.001.

[119] E. Yasa, G. M. Ay, and A. Türkseven, "Tribological and mechanical behavior of AISI 316L lattice-supported structures produced by laser powder bed fusion," *Int. J. Adv. Manuf. Technol.*, vol. 118, no. 5–6, pp. 1733–1748, Jan. 2022, doi: 10.1007/S00170-021-08069-0/FIGURES/19.

[120] M. Garibaldi, I. Ashcroft, M. Simonelli, and R. Hague, "Metallurgy of high-silicon steel

parts produced using Selective Laser Melting," *Acta Mater.*, vol. 110, pp. 207–216, May 2016, doi: 10.1016/J.ACTAMAT.2016.03.037.

[121] F. Caiazzo, V. Alfieri, G. Corrado, and P. Argenio, "Laser powder-bed fusion of Inconel 718 to manufacture turbine blades," *Int. J. Adv. Manuf. Technol. 2017 939*, vol. 93, no. 9, pp. 4023–4031, Aug. 2017, doi: 10.1007/S00170-017-0839-3.

[122] G. Marchese *et al.*, "Influence of heat treatments on microstructure evolution and mechanical properties of Inconel 625 processed by laser powder bed fusion," *Mater. Sci. Eng. A*, vol. 729, pp. 64–75, Jun. 2018, doi: 10.1016/J.MSEA.2018.05.044.

[123] G. Marchese *et al.*, "Study of the Microstructure and Cracking Mechanisms of Hastelloy X Produced by Laser Powder Bed Fusion," *Mater. 2018, Vol. 11, Page 106*, vol. 11, no. 1, p. 106, Jan. 2018, doi: 10.3390/MA11010106.

[124] G. Del Guercio *et al.*, "Cracking behaviour of high-strength AA2024 aluminium alloy produced by Laser Powder Bed Fusion," *Addit. Manuf.*, vol. 54, p. 102776, Jun. 2022, doi: 10.1016/J.ADDMA.2022.102776.

[125] Z. Wu *et al.*, "The effect of defect population on the anisotropic fatigue resistance of AlSi10Mg alloy fabricated by laser powder bed fusion," *Int. J. Fatigue*, vol. 151, p. 106317, Oct. 2021, doi: 10.1016/J.IJFATIGUE.2021.106317.

[126] T. T. Ikeshoji, K. Nakamura, M. Yonehara, K. Imai, and H. Kyogoku, "Selective Laser Melting of Pure Copper," *JOM*, vol. 70, no. 3, pp. 396–400, Mar. 2018, doi: 10.1007/S11837-017-2695-X/FIGURES/8.

[127] A. Iveković *et al.*, "Selective laser melting of tungsten and tungsten alloys," *Int. J. Refract. Met. Hard Mater.*, vol. 72, pp. 27–32, Apr. 2018, doi: 10.1016/J.IJRMHM.2017.12.005.

[128] R. Zhao *et al.*, "On the role of volumetric energy density in the microstructure and mechanical properties of laser powder bed fusion Ti-6Al-4V alloy," *Addit. Manuf.*, vol. 51, p. 102605, Mar. 2022, doi: 10.1016/J.ADDMA.2022.102605.

[129] M. Brandt, "The role of lasers in additive manufacturing," *Laser Addit. Manuf. Mater. Des. Technol. Appl.*, pp. 1–18, Jan. 2017, doi: 10.1016/B978-0-08-100433-3.02001-7.

[130] "Metal 3D printing materials and DMLS materials |EOS GmbH." [Online]. Available: https://www.eos.info/en/additive-manufacturing/3d-printing-metal/dmls-metal-materials. [Accessed: 26-Jul-2022].

[131] D. Herzog, K. Bartsch, and B. Bossen, "Productivity optimization of laser powder bed

fusion by hot isostatic pressing," *Addit. Manuf.*, vol. 36, p. 101494, Dec. 2020, doi: 10.1016/J.ADDMA.2020.101494.

[132] "EOS Titanium Ti64 Grade 5 Material Data Sheet Metal Solutions."

[133] C. Cui, B. M. Hu, L. Zhao, and S. Liu, "Titanium alloy production technology, market prospects and industry development," *Mater. Des.*, vol. 32, no. 3, pp. 1684–1691, Mar. 2011, doi: 10.1016/J.MATDES.2010.09.011.

[134] N. T. Aboulkhair, N. M. Everitt, I. Ashcroft, and C. Tuck, "Reducing porosity in AlSi10Mg parts processed by selective laser melting," *Addit. Manuf.*, vol. 1–4, pp. 77–86, Oct. 2014, doi: 10.1016/J.ADDMA.2014.08.001.

[135] P. Singh, H. Pungotra, and N. S. Kalsi, "On the characteristics of titanium alloys for the aircraft applications," *Mater. Today Proc.*, vol. 4, no. 8, pp. 8971–8982, Jan. 2017, doi: 10.1016/J.MATPR.2017.07.249.

[136] Y. L. Hao, S. J. Li, and R. Yang, "Biomedical titanium alloys and their additive manufacturing," *Rare Met.*, vol. 35, no. 9, pp. 661–671, Sep. 2016, doi: 10.1007/S12598-016-0793-5/FIGURES/8.

[137] A. S. Oryshchenko, I. V. Gorynin, V. P. Leonov, A. S. Kudryavtsev, V. I. Mikhailov, and E. V. Chudakov, "Marine titanium alloys: Present and future," *Inorg. Mater. Appl. Res. 2015 66*, vol. 6, no. 6, pp. 571–579, Dec. 2015, doi: 10.1134/S2075113315060106.

[138] D. Banerjee and J. C. Williams, "Perspectives on Titanium Science and Technology," *Acta Mater.*, vol. 61, no. 3, pp. 844–879, Feb. 2013, doi: 10.1016/J.ACTAMAT.2012.10.043.

[139] J. Yang, H. Yu, J. Yin, M. Gao, Z. Wang, and X. Zeng, "Formation and control of martensite in Ti-6Al-4V alloy produced by selective laser melting," *Mater. Des.*, vol. 108, pp. 308–318, Oct. 2016, doi: 10.1016/J.MATDES.2016.06.117.

[140] D. A. Hollander *et al.*, "Structural, mechanical and in vitro characterization of individually structured Ti–6Al–4V produced by direct laser forming," *Biomaterials*, vol. 27, no. 7, pp. 955–963, Mar. 2006, doi: 10.1016/J.BIOMATERIALS.2005.07.041.

[141] T. Wang, Y. Y. Zhu, S. Q. Zhang, H. B. Tang, and H. M. Wang, "Grain morphology evolution behavior of titanium alloy components during laser melting deposition additive manufacturing," *J. Alloys Compd.*, vol. 632, pp. 505–513, May 2015, doi: 10.1016/J.JALLCOM.2015.01.256.

[142] L. Thijs, F. Verhaeghe, T. Craeghs, J. Van Humbeeck, and J.-P. Kruth, "A study of the

microstructural evolution during selective laser melting of Ti–6Al–4V," *Acta Mater.*, vol. 58, no. 9, pp. 3303–3312, May 2010, doi: 10.1016/J.ACTAMAT.2010.02.004.

[143] M. Simonelli, Y. Y. Tse, and C. Tuck, "On the texture formation of selective laser melted Ti-6Al-4V," *Metall. Mater. Trans. A Phys. Metall. Mater. Sci.*, vol. 45, no. 6, pp. 2863–2872, Feb. 2014, doi: 10.1007/S11661-014-2218-0/TABLES/3.

[144] Z. Zou, M. Simonelli, J. Katrib, G. Dimitrakis, and R. Hague, "Microstructure and tensile properties of additive manufactured Ti-6Al-4V with refined prior-β grain structure obtained by rapid heat treatment," *Mater. Sci. Eng. A*, vol. 814, p. 141271, May 2021, doi: 10.1016/J.MSEA.2021.141271.

[145] E. Sallica-Leva, R. Caram, A. L. Jardini, and J. B. Fogagnolo, "Ductility improvement due to martensite α' decomposition in porous Ti–6Al–4V parts produced by selective laser melting for orthopedic implants," *J. Mech. Behav. Biomed. Mater.*, vol. 54, pp. 149–158, Feb. 2016, doi: 10.1016/J.JMBBM.2015.09.020.

[146] Y. Xu, Y. Lu, K. L. Sundberg, J. Liang, and R. D. Sisson, "Effect of Annealing Treatments on the Microstructure, Mechanical Properties and Corrosion Behavior of Direct Metal Laser Sintered Ti-6Al-4V," *J. Mater. Eng. Perform.*, vol. 26, no. 6, pp. 2572–2582, Jun. 2017, doi: 10.1007/S11665-017-2710-Y/TABLES/4.

[147] H. Galarraga, R. J. Warren, D. A. Lados, R. R. Dehoff, M. M. Kirka, and P. Nandwana, "Effects of heat treatments on microstructure and properties of Ti-6Al-4V ELI alloy fabricated by electron beam melting (EBM)," *Mater. Sci. Eng. A*, vol. 685, pp. 417–428, Feb. 2017, doi: 10.1016/J.MSEA.2017.01.019.

[148] B. Vrancken, L. Thijs, J. P. Kruth, and J. Van Humbeeck, "Heat treatment of Ti6Al4V produced by Selective Laser Melting: Microstructure and mechanical properties," *J. Alloys Compd.*, vol. 541, pp. 177–185, Nov. 2012, doi: 10.1016/J.JALLCOM.2012.07.022.

[149] X. Yan, S. Yue, J. Ge, C. Chen, R. Lupoi, and S. Yin, "Microstructural and mechanical optimization of selective laser melted Ti6Al4V lattices: Effect of hot isostatic pressing," *J. Manuf. Process.*, vol. 77, pp. 151–162, May 2022, doi: 10.1016/J.JMAPRO.2022.02.024.

[150] S. Cao *et al.*, "Role of martensite decomposition in tensile properties of selective laser melted Ti-6Al-4V," *J. Alloys Compd.*, vol. 744, pp. 357–363, May 2018, doi: 10.1016/j.jallcom.2018.02.111.

[151] M. Simonelli, Y. Y. Tse, and C. Tuck, "Effect of the build orientation on the mechanical

properties and fracture modes of SLM Ti–6Al–4V," *Mater. Sci. Eng. A*, vol. 616, pp. 1–11, Oct. 2014, doi: 10.1016/J.MSEA.2014.07.086.

[152] Y. N. Hu *et al.*, "A new approach to correlate the defect population with the fatigue life of selective laser melted Ti-6Al-4V alloy," *Int. J. Fatigue*, vol. 136, p. 105584, Jul. 2020, doi: 10.1016/J.IJFATIGUE.2020.105584.

[153] "ASM Material Data Sheet, Ti6Al4V (Grade 5), Annealed." [Online]. Available: http://asm.matweb.com/search/SpecificMaterial.asp?bassnum=MTP641. [Accessed: 13-Apr-2021].

[154] M. Simonelli, Y. Y. Tse, and C. Tuck, "Effect of the build orientation on the mechanical properties and fracture modes of SLM Ti–6Al–4V," *Mater. Sci. Eng. A*, vol. 616, pp. 1–11, Oct. 2014, doi: 10.1016/J.MSEA.2014.07.086.

[155] M. Koike *et al.*, "Evaluation of Titanium Alloys Fabricated Using Rapid Prototyping Technologies—Electron Beam Melting and Laser Beam Melting," *Mater. 2011, Vol. 4, Pages 1776-1792*, vol. 4, no. 10, pp. 1776–1792, Oct. 2011, doi: 10.3390/MA4101776.

[156] S. Leuders *et al.*, "On the mechanical behaviour of titanium alloy TiAl6V4 manufactured by selective laser melting: Fatigue resistance and crack growth performance," *Int. J. Fatigue*, vol. 48, pp. 300–307, Mar. 2013, doi: 10.1016/J.IJFATIGUE.2012.11.011.

[157] X. Shi, C. Yan, W. Feng, Y. Zhang, and Z. Leng, "Effect of high layer thickness on surface quality and defect behavior of Ti-6Al-4V fabricated by selective laser melting," *Opt. Laser Technol.*, vol. 132, p. 106471, Dec. 2020, doi: 10.1016/J.OPTLASTEC.2020.106471.

[158] L. L. Xing, W. J. Zhang, C. C. Zhao, W. Q. Gao, Z. J. Shen, and W. Liu, "Influence of Powder Bed Temperature on the Microstructure and Mechanical Properties of Ti-6Al-4V Alloy Fabricated via Laser Powder Bed Fusion," *Mater. 2021, Vol. 14, Page 2278*, vol. 14, no. 9, p. 2278, Apr. 2021, doi: 10.3390/MA14092278.

[159] G. Kasperovich and J. Hausmann, "Improvement of fatigue resistance and ductility of TiAl6V4 processed by selective laser melting," *J. Mater. Process. Technol.*, vol. 220, pp. 202–214, Jun. 2015, doi: 10.1016/J.JMATPROTEC.2015.01.025.

[160] H. K. Rafi, N. V. Karthik, H. Gong, T. L. Starr, and B. E. Stucker, "Microstructures and Mechanical Properties of Ti6Al4V Parts Fabricated by Selective Laser Melting and Electron Beam Melting," *J. Mater. Eng. Perform.*, vol. 22, no. 12, pp. 3872–3883, Dec. 2013, doi: 10.1007/s11665-013-0658-0.

[161] B. Vrancken, L. Thijs, J.-P. Kruth, and J. Van Humbeeck, “Heat treatment of Ti6Al4V produced by Selective Laser Melting: Microstructure and mechanical properties,” *J. Alloys Compd.*, vol. 541, pp. 177–185, Nov. 2012, doi: 10.1016/J.JALLCOM.2012.07.022.

[162] B. Wysocki, P. Maj, R. Sitek, J. Buhagiar, K. J. Kurzydłowski, and W. Świeszkowski, “Laser and Electron Beam Additive Manufacturing Methods of Fabricating Titanium Bone Implants,” *Appl. Sci. 2017, Vol. 7, Page 657*, vol. 7, no. 7, p. 657, Jun. 2017, doi: 10.3390/APP7070657.

[163] L. Facchini, E. Magalini, P. Robotti, A. Molinari, S. Höges, and K. Wissenbach, “Ductility of a Ti-6Al-4V alloy produced by selective laser melting of prealloyed powders,” *Rapid Prototyp. J.*, vol. 16, no. 6, pp. 450–459, Oct. 2010, doi: 10.1108/13552541011083371.

[164] P. Edwards and M. Ramulu, “Fatigue performance evaluation of selective laser melted Ti–6Al–4V,” *Mater. Sci. Eng. A*, vol. 598, pp. 327–337, Mar. 2014, doi: 10.1016/J.MSEA.2014.01.041.

[165] X. Li, J. Xie, and Y. Zhou, “Effects of oxygen contamination in the argon shielding gas in laser welding of commercially pure titanium thin sheet,” *J. Mater. Sci. 2005 4013*, vol. 40, no. 13, pp. 3437–3443, Jul. 2005, doi: 10.1007/S10853-005-0447-8.

[166] X. Yan *et al.*, “Effect of heat treatment on the phase transformation and mechanical properties of Ti6Al4V fabricated by selective laser melting,” *J. Alloys Compd.*, vol. 764, pp. 1056–1071, Oct. 2018, doi: 10.1016/J.JALLCOM.2018.06.076.

[167] I. Yadroitsev, P. Krakhmalev, I. Yadroitsava, and A. Du Plessis, “Qualification of Ti6Al4V ELI Alloy Produced by Laser Powder Bed Fusion for Biomedical Applications,” *JOM*, vol. 70, no. 3, pp. 372–377, Mar. 2018, doi: 10.1007/S11837-017-2655-5/FIGURES/3.

[168] E. Pessard, M. Lavialle, P. Laheurte, P. Didier, and M. Brochu, “High-cycle fatigue behavior of a laser powder bed fusion additive manufactured Ti-6Al-4V titanium: Effect of pores and tested volume size,” *Int. J. Fatigue*, vol. 149, p. 106206, Aug. 2021, doi: 10.1016/J.IJFATIGUE.2021.106206.

[169] H. Masuo *et al.*, “Effects of Defects, Surface Roughness and HIP on Fatigue Strength of Ti-6Al-4V manufactured by Additive Manufacturing,” *Procedia Struct. Integr.*, vol. 7, pp. 19–26, Jan. 2017, doi: 10.1016/J.PROSTR.2017.11.055.

[170] S. Bagehorn, J. Wehr, and H. J. Maier, “Application of mechanical surface finishing processes for roughness reduction and fatigue improvement of additively manufactured Ti-6Al-4V parts,” *Int. J. Fatigue*, vol. 102, pp. 135–142, Sep. 2017, doi:

10.1016/J.IJFATIGUE.2017.05.008.

[171] K. Zhang, J. Mei, N. Wain, and X. Wu, “Effect of hot-isostatic-pressing parameters on the microstructure and properties of powder Ti-6Al-4V hot-isostatically-pressed samples,” *Metall. Mater. Trans. A Phys. Metall. Mater. Sci.*, vol. 41, no. 4, pp. 1033–1045, Apr. 2010, doi: 10.1007/S11661-009-0149-Y/FIGURES/11.

[172] M. Kahlin *et al.*, “Improved fatigue strength of additively manufactured Ti6Al4V by surface post processing,” *Int. J. Fatigue*, vol. 134, p. 105497, May 2020, doi: 10.1016/J.IJFATIGUE.2020.105497.

[173] X. Zhao *et al.*, “Comparison of the microstructures and mechanical properties of Ti–6Al–4V fabricated by selective laser melting and electron beam melting,” *Mater. Des.*, vol. 95, pp. 21–31, Apr. 2016, doi: 10.1016/J.MATDES.2015.12.135.

[174] E. Wycisk, A. Solbach, S. Siddique, D. Herzog, F. Walther, and C. Emmelmann, “Effects of Defects in Laser Additive Manufactured Ti-6Al-4V on Fatigue Properties,” *Phys. Procedia*, vol. 56, no. C, pp. 371–378, Jan. 2014, doi: 10.1016/J.PHPRO.2014.08.120.

[175] D. Greitemeier, F. Palm, F. Syassen, and T. Melz, “Fatigue performance of additive manufactured TiAl6V4 using electron and laser beam melting,” *Int. J. Fatigue*, vol. 94, pp. 211–217, Jan. 2017, doi: 10.1016/J.IJFATIGUE.2016.05.001.

[176] W. Eric, E. Claus, S. Shafaqat, and W. Frank, “High Cycle Fatigue (HCF) Performance of Ti-6Al-4V Alloy Processed by Selective Laser Melting,” *Adv. Mater. Res.*, vol. 816–817, pp. 134–139, 2013, doi: 10.4028/WWW.SCIENTIFIC.NET/AMR.816-817.134.

[177] V. Chastand, P. Quaegebeur, W. Maia, and E. Charkaluk, “Comparative study of fatigue properties of Ti-6Al-4V specimens built by electron beam melting (EBM) and selective laser melting (SLM),” *Mater. Charact.*, vol. 143, pp. 76–81, Sep. 2018, doi: 10.1016/J.MATCHAR.2018.03.028.

[178] M. Suraratchai, J. Limido, C. Mabru, and R. Chieragatti, “Modelling the influence of machined surface roughness on the fatigue life of aluminium alloy,” *Int. J. Fatigue*, vol. 30, no. 12, pp. 2119–2126, Dec. 2008, doi: 10.1016/J.IJFATIGUE.2008.06.003.

[179] A. E. Wilson-Heid and A. M. Beese, “Combined effects of porosity and stress state on the failure behavior of laser powder bed fusion stainless steel 316L,” *Addit. Manuf.*, vol. 39, p. 101862, Mar. 2021, doi: 10.1016/j.addma.2021.101862.

[180] Y. Murakami, “Material defects as the basis of fatigue design,” *Int. J. Fatigue*, vol. 41, pp. 2–10, Aug. 2012, doi: 10.1016/J.IJFATIGUE.2011.12.001.

[181] A. V. Gusarov *et al.*, “On productivity of laser additive manufacturing,” *J. Mater. Process. Technol.*, vol. 261, pp. 213–232, Nov. 2018, doi: 10.1016/J.JMATPROTEC.2018.05.033.

[182] “High Volume Laser Melting 3D Printing - SLM®500 | SLM Solutions.” [Online]. Available: https://www.slm-solutions.com/products-and-solutions/machines/slm-500/. [Accessed: 15-Mar-2022].

[183] R. Poprawe, C. Hinke, W. Meiners, J. Schrage, S. Bremen, and S. Merkt, “SLM Production Systems: Recent Developments in Process Development, Machine Concepts and Component Design,” pp. 49–65, 2015, doi: 10.1007/978-3-319-12304-2_5.

[184] A. Khorasani, I. Gibson, J. K. Veetil, and A. H. Ghasemi, “A review of technological improvements in laser-based powder bed fusion of metal printers,” *Int. J. Adv. Manuf. Technol. 2020 1081*, vol. 108, no. 1, pp. 191–209, May 2020, doi: 10.1007/S00170-020-05361-3.

[185] A. Du Plessis *et al.*, “Productivity enhancement of laser powder bed fusion using compensated shelled geometries and hot isostatic pressing,” *Adv. Ind. Manuf. Eng.*, vol. 2, p. 100031, May 2021, doi: 10.1016/J.AIME.2021.100031.

[186] A. Kaletsch, S. Qin, S. Herzog, and C. Broeckmann, “Influence of high initial porosity introduced by laser powder bed fusion on the fatigue strength of Inconel 718 after post-processing with hot isostatic pressing,” *Addit. Manuf.*, vol. 47, p. 102331, Nov. 2021, doi: 10.1016/J.ADDMA.2021.102331.

[187] A. du Plessis *et al.*, “Fatigue performance of shelled additively manufactured parts subjected to hot isostatic pressing,” *Addit. Manuf.*, vol. 51, p. 102607, Mar. 2022, doi: 10.1016/J.ADDMA.2022.102607.

[188] W. Shi, P. Wang, Y. Liu, Y. Hou, and G. Han, “Properties of 316L formed by a 400 W power laser Selective Laser Melting with 250 μm layer thickness,” *Powder Technol.*, vol. 360, pp. 151–164, Jan. 2020, doi: 10.1016/j.powtec.2019.09.059.

[189] N. W. Makoana, I. Yadroitsava, H. Möller, and I. Yadroitsev, “Characterization of 17-4PH Single Tracks Produced at Different Parametric Conditions towards Increased Productivity of LPBF Systems—The Effect of Laser Power and Spot Size Upscaling,” *Met. 2018, Vol. 8, Page 475*, vol. 8, no. 7, p. 475, Jun. 2018, doi: 10.3390/MET8070475.

[190] C. de Formanoir *et al.*, “Increasing the productivity of laser powder bed fusion:

Influence of the hull-bulk strategy on part quality, microstructure and mechanical performance of Ti-6Al-4V," *Addit. Manuf.*, vol. 33, p. 101129, May 2020, doi: 10.1016/j.addma.2020.101129.

[191] H. Ali, H. Ghadbeigi, and K. Mumtaz, "Processing Parameter Effects on Residual Stress and Mechanical Properties of Selective Laser Melted Ti6Al4V," *J. Mater. Eng. Perform.*, vol. 27, no. 8, pp. 4059–4068, Aug. 2018, doi: 10.1007/s11665-018-3477-5.

[192] A. Clare, A. Gullane, C. Hyde, J. W. Murray, S. Sankare, and W. W. Wits, "Interlaced layer thicknesses within single laser powder bed fusion geometries," *CIRP Ann.*, Mar. 2021, doi: 10.1016/j.cirp.2021.03.001.

[193] A. M. Khorasani, I. Gibson, M. Goldberg, and G. Littlefair, "On the role of different annealing heat treatments on mechanical properties and microstructure of selective laser melted and conventional wrought Ti-6Al-4V," *Rapid Prototyp. J.*, vol. 23, no. 2, pp. 295–304, 2017, doi: 10.1108/RPJ-02-2016-0022.

[194] Q. Liu, M. Brandt, J. Elambasseril, P. K. Sharp, S. Sun, and R. Djugum, "Mechanical properties of selective laser melted Ti-6Al-4V with different layer thickness," 2018, pp. 819–824, doi: 10.2351/1.5063131.

[195] A. E. Wilson-Heid, Z. Wang, B. McCornac, and A. M. Beese, "Quantitative relationship between anisotropic strain to failure and grain morphology in additively manufactured Ti-6Al-4V," *Mater. Sci. Eng. A*, vol. 706, pp. 287–294, Oct. 2017, doi: 10.1016/j.msea.2017.09.017.

[196] Z. Xie, Y. Dai, X. Ou, S. Ni, and M. Song, "Effects of selective laser melting build orientations on the microstructure and tensile performance of Ti–6Al–4V alloy," *Mater. Sci. Eng. A*, vol. 776, p. 139001, Mar. 2020, doi: 10.1016/j.msea.2020.139001.

[197] B. Song *et al.*, "Differences in microstructure and properties between selective laser melting and traditional manufacturing for fabrication of metal parts: A review," *Front. Mech. Eng.*, vol. 10, no. 2, pp. 111–125, Jun. 2015, doi: 10.1007/s11465-015-0341-2.

[198] D. Bourell *et al.*, "Materials for additive manufacturing," *CIRP Ann. - Manuf. Technol.*, vol. 66, no. 2, pp. 659–681, Jan. 2017, doi: 10.1016/j.cirp.2017.05.009.

[199] H. K. Rafi, T. L. Starr, and B. E. Stucker, "A comparison of the tensile, fatigue, and fracture behavior of Ti-6Al-4V and 15-5 PH stainless steel parts made by selective laser melting," *Int. J. Adv. Manuf. Technol.*, vol. 69, no. 5–8, pp. 1299–1309, Nov. 2013, doi: 10.1007/s00170-013-5106-7.

[200] W. E. King *et al.*, “Laser powder bed fusion additive manufacturing of metals; physics, computational, and materials challenges,” *Appl. Phys. Rev.*, vol. 2, no. 4, p. 041304, Dec. 2015, doi: 10.1063/1.4937809.

[201] A. T. Clare *et al.*, “Laser calorimetry for assessment of melting behaviour in multi-walled carbon nanotube decorated aluminium by laser powder bed fusion,” *CIRP Ann.*, vol. 69, no. 1, pp. 197–200, Jan. 2020, doi: 10.1016/j.cirp.2020.04.053.

[202] J. T. Benzing, L. A. Liew, N. Hrabe, and F. W. DelRio, “Tracking Defects and Microstructural Heterogeneities in Meso-Scale Tensile Specimens Excised from Additively Manufactured Parts,” *Exp. Mech.*, vol. 60, no. 2, pp. 165–170, Feb. 2020, doi: 10.1007/S11340-019-00558-4/FIGURES/3.

[203] A. Pramanik, A. K. Basak, C. Prakash, S. Shankar, S. Sharma, and S. Narendranath, “Recast Layer Formation during Wire Electrical Discharge Machining of Titanium (Ti-Al6-V4) Alloy,” *J. Mater. Eng. Perform.*, vol. 30, no. 12, pp. 8926–8935, Dec. 2021, doi: 10.1007/S11665-021-06116-1/FIGURES/9.

[204] S. Zhang, S. Rauniyar, S. Shrestha, A. Ward, and K. Chou, “An experimental study of tensile property variability in selective laser melting,” *J. Manuf. Process.*, vol. 43, pp. 26–35, Jul. 2019, doi: 10.1016/J.JMAPRO.2019.03.045.

[205] J. R. Tempelman *et al.*, “Detection of keyhole pore formations in laser powder-bed fusion using acoustic process monitoring measurements,” *Addit. Manuf.*, vol. 55, p. 102735, Jul. 2022, doi: 10.1016/J.ADDMA.2022.102735.

[206] J. B. Forien, N. P. Calta, P. J. DePond, G. M. Guss, T. T. Roehling, and M. J. Matthews, “Detecting keyhole pore defects and monitoring process signatures during laser powder bed fusion: A correlation between in situ pyrometry and ex situ X-ray radiography,” *Addit. Manuf.*, vol. 35, p. 101336, Oct. 2020, doi: 10.1016/J.ADDMA.2020.101336.

[207] C. Elangeswaran *et al.*, “Predicting fatigue life of metal LPBF components by combining a large fatigue database for different sample conditions with novel simulation strategies,” *Addit. Manuf.*, vol. 50, p. 102570, Feb. 2022, doi: 10.1016/J.ADDMA.2021.102570.

[208] A. Gullane, J. W. Murray, C. J. Hyde, S. Sankare, A. Evirgen, and A. T. Clare, “On the use of multiple layer thicknesses within laser powder bed fusion and the effect on mechanical properties,” *Mater. Des.*, vol. 212, p. 110256, Dec. 2021, doi:

10.1016/J.MATDES.2021.110256.

[209] S. K. Paul, “A critical review of experimental aspects in ratcheting fatigue: microstructure to specimen to component,” *J. Mater. Res. Technol.*, vol. 8, no. 5, pp. 4894–4914, Sep. 2019, doi: 10.1016/J.JMRT.2019.06.014.

[210] C. Elangeswaran *et al.*, “Effect of post-treatments on the fatigue behaviour of 316L stainless steel manufactured by laser powder bed fusion,” *Int. J. Fatigue*, vol. 123, pp. 31–39, Jun. 2019, doi: 10.1016/J.IJFATIGUE.2019.01.013.

[211] J. Günther *et al.*, “Fatigue life of additively manufactured Ti–6Al–4V in the very high cycle fatigue regime,” *Int. J. Fatigue*, vol. 94, pp. 236–245, Jan. 2017, doi: 10.1016/J.IJFATIGUE.2016.05.018.

[212] V. Prithivirajan and M. D. Sangid, “The role of defects and critical pore size analysis in the fatigue response of additively manufactured IN718 via crystal plasticity,” *Mater. Des.*, vol. 150, pp. 139–153, Jul. 2018, doi: 10.1016/J.MATDES.2018.04.022.

[213] “Aurora Labs – High-Powered 3D Printing Technology for Industrial Applications.” [Online]. Available: https://www.auroralabs3d.com/. [Accessed: 01-Sep-2022].

[214] M. Baumers, P. Dickens, C. Tuck, and R. Hague, “The cost of additive manufacturing: Machine productivity, economies of scale and technology-push,” *Technol. Forecast. Soc. Change*, vol. 102, pp. 193–201, Jan. 2016, doi: 10.1016/j.techfore.2015.02.015.

[215] M. Ruffo, C. Tuck, and R. Hague, “Cost estimation for rapid manufacturing - laser sintering production for low to medium volumes:,” *http://dx.doi.org/10.1243/09544054JEM517*, vol. 220, no. 9, pp. 1417–1427, Dec. 2006, doi: 10.1243/09544054JEM517.

[216] “3D Systems Gross Profit Margin (Quarterly).” [Online]. Available: https://ycharts.com/companies/DDD/gross_profit_margin. [Accessed: 10-May-2022].

9 Appendix

9.1 Custom scan path generation

Two Python scripts were created for generating the laser vectors to achieve custom laser scan strategies. The initial script allows the user to select component geometry and apply the a select scan strategy to determine the appropriate laser vectors, while the second script generates the slices to form a 3D geometry and writes the laser vector files.

9.1.1 Part geometry and vector design

```
# -*-coding:latin-1 -*

import os
import matplotlib.pyplot as plt
import matplotlib.patches as mpatches
from matplotlib.patches import Circle
from matplotlib.collections import PatchCollection
import numpy as np

# Make sure the function file fct_cylinder90 is in the same directory as the main file (this file) :
from fctV12 import *
from math import pi, radians, cos, sin, tan, sqrt, radians, atan, asin, sqrt, floor, ceil

# ================================================ #
#                                  #
#             I. Explanation              #
#                                  #
# ================================================ #

# The V12-2 version of the script generates one cli file per sets of parameters (a certain scan speed coupled with a certain power), identified by their id.
# Some cli files might be empty, depending on the scan strategy chosen in Section V

# ================================================ #
#                                  #
#    II. Directory where the files will be saved   #
#                                  #
# ================================================ #


os.chdir('C:/Users/ezxsf3/OneDrive - The University of Nottingham/10 Python/02 Affichage cli/V12-2/100hatch/02 Continuous ramped')
```

```
# ================================================ #
#                                                  #
#          III. Creation of the domain             #
#                                                  #
# ================================================ #

L = 10                          # Length of the cylinder or the cube - X direction
H = 10                          # Heigth of the cylinder or the cube - Z direction

# === If cylinder (set w to 0 below)

r = 0                           # Radius of the cylinder

# === If cube (set r = 0 above)

w = 10.01                       # Width of the cube - Y direction

# ================================================ #
#                                                  #
#          IV. Creation of the variables           #
#                                                  #
# ================================================ #

e = 0.03                        # Layer thickness
h = 0.100                       # Hatching space
reworkL = 2                     # Length of the re-work pass
R = 8                           # Number of subdomain in the rework zone

theta = 90                      # First angle of the vectors

dtheta = 90                     # Rotation angle between each layers

nameFile = 'cube_hatch100_strat_2_id_'     # Name of the files (will be followed by the number
of the layer)
extension = '.cli'              # Extension of the file
unit = 1                        # For the cli files (1 = 1mm, 0.001 = 1 micron)
R5 = R + 5                      # For strat 3 (see below), rework will have the same parameter if
...
R6 = R + 6                      # ... R5 = R6

# ================================================ #
#                                                  #
#          V. Change the rework strategy           #
#                                                  #
# ================================================ #

strat = 2   ## 1 = continuous
            ## 2 = continuous ramped
```

```
        ## 3 = continuous rework
        ## 4 = continuous ramped rework

# ================================================ #
#                                                  #
#   VI. Creation of lists & iteration varaibles    #
#         DO NOT MODIFIY BELOW THIS POINT          #
#                                                  #
# ================================================ #

lay = (2 * r) / e       #Number of layers
l = 1                   #First layer
list_coord = []         #Creation of the empty list that will contain the width of the first half circle layers
list_temp = []          #Creation of the empty list that will contain the width of each layer for the matplotlib representation
list_w = []             #Creation of the empty list that will contain all of the layers' width
i = 0                   #iteration variable
j = 0                   #iteration variable
k = 1                   #iteration variable
total_layers = 0        #Number of layers in the slicing part
z = 0                   #Initialisation of the height of the layers
choice = 0

same_layer = z

if r != 0:
    cylindre = 1
    w = 0
else:
    cylindre = 0
    r = 0

cylindre = 0

if r != 0 and w != 0:
    print('You must set the radius to 0 if you want to print a cube, of the width of the cube to 0 if you want to print a cylinder')
    quit()

# ===== Creation of the first slice of the cylinder

if cylindre == 1:
    x2 = r
    x1 = - x2
    z1 = 0
    z2 = z1 + e
```

```
    X = [x1,x2,x2,x1,x1]
    Z = [z1,z1,z2,z2,z1]

    list_temp += X,Z
    list_coord.append(x2 - x1)


    # ==== While Loop : creation of the list containing the length of each
    #      layer for a cylinder

    while z2 + e < r + e:              # While next layer is within the circle
        z1 = z2                      # z1 becomes z2
        z2 = z2 + e                    # we had a layer thickness to z2
        x2 = (r**2 - z1**2)            # x2 increase along the circle
        x2 = - (x2**0.5)
        x1 = - x2                    # x1 is the opposite of x2
        X = [x1,x2,x2,x1,x1]
        Z = [z1,z1,z2,z2,z1]
        list_temp += X,Z
        list_coord.append(x2 - x1)      # We keep the width of the layer
        z += e
        total_layers +=1               # Next iteration

    # ===== Once we have every length of the top part of the circle, we create
    #       a list with the width of every layers

    list_coord.reverse()
    list_w += list_coord
    list_coord.reverse()
    list_w += list_coord

    # ===== Viewing of the circle with the different layers

    figure, axes = plt.subplots()
    c = plt.Circle( (0, 0 ), r, fill = False )

    while j <= total_layers:
        plt.plot(list_temp[i],list_temp[i+1])
        i += 2
        j += 1

    axes.add_artist( c )
    plt.axis('equal')
    #plt.show() # Comment this line to hide the slicing diagram
    plt.close()

# ===== Viewing of the cube with the different layers
```

```
if cylindre == 0:

    while z < H:
        X = [0,L,L,0,0]
        Z = [z,z,z+e,z+e,z]
        plt.plot(X,Z)
        z += e
        total_layers += 1

    plt.axis('equal')
    plt.show() # Comment this line to hide the slicing diagram
    plt.close()

# ===== Part. 2: creation of the cli file with each layer

# ~~~~~~~ Initialization of the variables

mid = 0             # Middle of the part (length)
plt.plot()          # Plot
list_coord2 = []    # Creation of an empty list which will return the coordinates\
#                    of the scan track
j = 0               # Number of iteration of while
layer = 0
z = 0
identifier = 1
# ~~~~~~~

# Creation of the outlines of the part

if cylindre == 1:
    X=[0,L,L,0,0]
    Y=[0,0,r,r,0]
    vari = (2*r-w)/2
else:
    X=[0,L,L,0,0]
    Y=[0,0,w,w,0]
    vari = w

mid = L / 2
aprime = int(mid-(reworkL/2))
bprime =  int(mid+(reworkL/2))
a = float(mid-(reworkL/2))
b = float(mid+(reworkL/2))
x = a
y = 0
dx = reworkL
dy = 0
lay = 1
```

```
list_fct = []
l = 1

# ~~~~~~~ Parameters for the .cli file

if cylindre == 1 :
   layer = ( 2 * r ) / e #total_layers * 2 #
else:
   layer = total_layers
print(' ')

n = 1
while n < R + 7:
   number = str(n)
   zprime = z + e
   with open(nameFile + number + extension, 'w') as myFile:
         myFile.write("$$HEADERSTART\n")
         myFile.write("$$ASCII\n")
         myFile.write("$$UNITS/")
         myFile.write(str(unit)[:])
         myFile.write("\n")
         myFile.write("$$LAYERS/")
         myFile.write(str(layer))
         myFile.write("\n")
         myFile.write("$$HEADEREND\n$$GEOMETRYSTART\n$$LAYER/"                    +
str(float(zprime))[:])
   n += 1

z += e # Add one empty layer at the bottom

# ~~~~~~~

## ===== Creation of the files

incrid = 1

while lay <= layer :

   if lay % 2 == 0 and lay != 0:

      if cylindre == 1:
         w = abs(float(list_w[lay - l]))

      if strat == 1 or strat == 3:

         direction = 1

         if theta == 0 or theta == 180:
```

```
            x1p = 0
            y1p = vari
            mid = L / 2
            dx1p = mid
            dy1p = 0
            count = 0 # count < 2 to have 2 arrows per line

            if cylindre == 1:
               top = vari + w
            else:
               top = w
               y1p = 0

            while y1p <= top:

               a = 0
               b =  L

               if direction == 1:

                  identifier = 1
                  x1p = a
                  dx1p = mid

                  while count < 2:

                     list_fct += x1p, y1p, x1p + dx1p, y1p + dy1p
                     plt.quiver(x1p, y1p, dx1p, dy1p, angles = 'xy', scale_units = 'xy', scale =1)
                     #print('direction',direction)
                     ecriture(nameFile, lay, unit,z, identifier, list_fct,extension, k, same_layer,
theta, w, h, b, condition)
                     x1p += dx1p
                     identifier += 1
                     k += 1
                     count += 1
                     list_fct = ()

                  y1p += h
                  direction = -1
                  count = 0

               if direction == -1 and y1p <= top:

                  #print('y1p = ',y1p, ' top = ', top)

                  identifier = 2

                  x1p = b
```

```
                dx1p = - mid

                while count < 2:

                    list_fct += x1p, y1p, x1p + dx1p, y1p + dy1p
                    plt.quiver(x1p, y1p, dx1p, dy1p, angles = 'xy', scale_units = 'xy', scale =1)
                    #print(direction)
                    ecriture(nameFile, lay, unit,z, identifier, list_fct,extension, k, same_layer,
theta, w, h, b, condition)
                    x1p = mid
                    identifier -= 1
                    k += 1
                    count += 1
                    list_fct = ()

                y1p += h
                direction = 1
                count = 0

        if theta == 90:
            if cylindre == 0:
                vari = 0
            x1p = 0
            y1p = vari
            mid = L / 2
            dx1p = 0
            dy1p = w
            count = 0 # count < 2 to have 2 arrows per line

            a = 0
            b = mid
            condition = b
            identifier = 1

            list_fct = zigzag(L, w, h, reworkL, theta, r, a, b, divzone, lay, vari)
            ecriture(nameFile, lay, unit,z, identifier, list_fct,extension, k, same_layer, theta, w,
h, b, condition)

            k += 1

            a = mid #+h
            b = L
            condition = b
            x1p = a

            identifier = 2

##              while x1p <= b:
```

```
            list_fct = zigzag(L, w, h, reworkL, theta, r, a, b, divzone, lay, vari)
            ecriture(nameFile, lay, unit,z, identifier, list_fct,extension, k, same_layer, theta, w,
h, b, condition)

            k += 1

        if theta == 0:
            X=[0,L,L,0,0]

            if cylindre == 1:
                Y=[ vari , vari , vari + w, vari + w , vari ]
            else:
                Y=[ 0,0,w,w,0 ]
            Xw =[a, b, b, a, a]

            plt.plot(X,Y)#, 'm')
            plt.plot(Xw,Y)#, 'c')
            plt.title("The angle is equal to {0} degrees, this is layer number
{1}.".format(theta,lay))
            plt.axis('equal')
            #plt.show() # Comment this line to hide the slicing diagram
            plt.close()

    if strat == 3:

        a = mid-(reworkL/2)
        b = mid+(reworkL/2)
        direction = 1

        if theta == 0 or theta == 180:
            x1p = 0
            if cylindre == 1:
                y1p = vari
            else:
                y1p = 0
            mid = L / 2
            dx1p = reworkL / 2
            dy1p = 0
            count = 0 # count < 2 to have 2 arrows per line

            while y1p  <= top : #w + vari:

                if direction == 1:

                    identifier = R5
                    x1p = a
                    dx1p = reworkL / 2
```

```
                while count < 2:

                    list_fct += x1p, y1p, x1p + dx1p, y1p + dy1p
                    plt.quiver(x1p, y1p, dx1p, dy1p, angles = 'xy', scale_units = 'xy', scale =1)
                    #print(direction)
                    ecriture(nameFile, lay, unit,z, identifier, list_fct,extension, k, same_layer,
theta, w, h, b, condition)
                    x1p += dx1p
                    identifier += 1
                    k += 1
                    count += 1
                    list_fct = ()

                y1p += h
                direction = -1
                count = 0

            if direction == -1 and y1p < top:

                identifier = R6

                x1p = b
                dx1p = - reworkL / 2

                while count < 2:

                    list_fct += x1p, y1p, x1p + dx1p, y1p + dy1p
                    plt.quiver(x1p, y1p, dx1p, dy1p, angles = 'xy', scale_units = 'xy', scale =1)
                    #print(direction)
                    ecriture(nameFile, lay, unit,z, identifier, list_fct,extension, k, same_layer,
theta, w, h, b, condition)
                    x1p = mid
                    identifier -= 1
                    k += 1
                    count += 1
                    list_fct = ()

                y1p += h
                direction = 1
                count = 0

        if theta == 90:

            x1p = a
            y1p = vari
            mid = L / 2
            condition = mid
```

```
            dx1p = 0
            dy1p = w
            count = 0 # count < 2 to have 2 arrows per line

            identifier = R5

            list_fct = zigzag(L, w, h, reworkL, theta, r, a, mid, divzone, lay, vari)
            ecriture(nameFile, lay, unit,z, identifier, list_fct,extension, k, same_layer, theta, w,
h, b, condition)

            k += 1

            identifier = R6

            mid2 = mid + h
            condition = b
            list_fct = zigzag(L, w, h, reworkL, theta, r, mid2, b, divzone, lay, vari)
            ecriture(nameFile, lay, unit,z, identifier, list_fct,extension, k, same_layer, theta, w,
h, b, condition)

            k += 1
            x1p += h

        if theta != 90 and strat != 3:
            if cylindre == 1:
                X=[0,L,L,0,0]
                Y=[ vari , vari , vari + w, vari + w , vari ]
                Xw =[a, b, b, a, a]
                Yw = [ vari , vari , vari + w, vari + w , vari ]
            else:
                X=[0,L,L,0,0]
                Y=[ 0 , 0 ,  w, w , 0 ]
                Xw =[a, b, b, a, a]
                Yw = [ 0 , 0 ,  w, w , 0 ]

            plt.plot(X,Y)#, 'm')
            plt.plot(Xw,Yw)#, 'c')
            plt.title("The angle is equal to {0} degrees, this is layer number {1}".format(theta,lay))
            plt.axis('equal')
            #plt.show() # Comment this line to hide the slicing diagram
            plt.close()

        if strat == 3 and theta == 0:
            if cylindre == 1:
                X=[0,L,L,0,0]
                Y=[ vari , vari , vari + w, vari + w , vari ]
                Xw =[a, b, b, a, a]
                Yw = [ vari , vari , vari + w, vari + w , vari ]
```

```
            else:
                X=[0,L,L,0,0]
                Y=[ 0 , 0 ,  w, w , 0 ]
                Xw =[a, b, b, a, a]
                Yw = [ 0 , 0 ,  w, w , 0 ]

            plt.plot(X,Y)#, 'm')
            plt.plot(Xw,Yw)#, 'c')
            plt.title("The angle is equal to {0} degrees, this is layer number {1}".format(theta,lay))
            plt.axis('equal')
            #plt.show() # Comment this line to hide the slicing diagram
            plt.close()

#########################################################################
#################################################################

        if strat == 2 or strat == 4:

##          if cylindre == 1:
##              w = abs(float(list_w[lay - l]))

          if theta == 0 or theta == 180:
              x1p = 0
              dy1p = 0
              direction = 1

##              if cylindre == 1:
##                  vari = (2*r - w)/2
##                  y1p = vari
##                  top = w + vari
##              else:
              y1p = 0
              top = vari

              while y1p  <= top:

                  if x1p == 0 and direction == 1: # If we are in the first part

                      dx1p = a
                      identifier = 3
                      list_fct += x1p, y1p, x1p + dx1p, y1p + dy1p
                      plt.quiver(x1p, y1p, dx1p, dy1p, angles = 'xy', scale_units = 'xy', scale =1)
                      ecriture(nameFile, lay, unit,z, identifier, list_fct,extension, k, same_layer, theta,
w, h, b, condition)
                      x1p = a
                      dx1p = reworkL / R
                      identifier += 1
                      k += 1
```

```
                list_fct = ()

            if a <= x1p < b and direction == 1: # If we are inside the rework zone

                while incrid < R and x1p < b:

                    list_fct += x1p, y1p, x1p + dx1p, y1p + dy1p
                    plt.quiver(x1p, y1p, dx1p, dy1p, angles = 'xy', scale_units = 'xy', scale =1)

                    ecriture(nameFile, lay, unit,z, identifier, list_fct,extension, k, same_layer,
theta, w, h, b, condition)

                    x1p += ( reworkL / R )
                    k += 1
                    identifier += 1
                    incrid += 1
                    list_fct = ()

                list_fct += x1p, y1p, x1p + dx1p, y1p + dy1p
                plt.quiver(x1p, y1p, dx1p, dy1p, angles = 'xy', scale_units = 'xy', scale =1)
                if identifier == 12:
                    list_fct = ()

                else:
                    ecriture(nameFile, lay, unit,z, identifier, list_fct,extension, k, same_layer,
theta, w, h, b, condition)
                identifier += 1

                incrid = 1
                x1p += ( reworkL / R )
                list_fct = ()

            if b <= x1p < L and direction == 1: # If we are in the last part
                list_fct = ()
                x1p = b
                dx1p = a
                dy1p = 0
                identifier = R + 4
                list_fct += x1p, y1p, x1p + dx1p, y1p + dy1p
                plt.quiver(x1p, y1p, dx1p, dy1p, angles = 'xy', scale_units = 'xy', scale =1)

                ecriture(nameFile, lay, unit,z, identifier, list_fct,extension, k, same_layer, theta,
w, h, b, condition)

                x1p = L
                y1p += h
                dx1p = - a
```

```
                direction = -1
                k += 1
                list_fct = ()

            if x1p == L and direction == -1 and y1p <= top: # Starting from the right

                list_fct += x1p, y1p, x1p + dx1p, y1p + dy1p
                plt.quiver(x1p, y1p, dx1p, dy1p, angles = 'xy', scale_units = 'xy', scale =1)
                dx1p = a
                ecriture(nameFile, lay, unit,z, identifier, list_fct,extension, k, same_layer, theta,
w, h, b, condition)

                x1p = b
                dx1p = - reworkL / R
                k += 1
                identifier -= 1
                list_fct = ()

            if a < x1p <= b and direction == -1: # If we are inside the rework zone, toward the
left

                while incrid < R:

                    list_fct += x1p, y1p, x1p + dx1p, y1p + dy1p
                    plt.quiver(x1p, y1p, dx1p, dy1p, angles = 'xy', scale_units = 'xy', scale =1)

                    ecriture(nameFile, lay, unit,z, identifier, list_fct,extension, k, same_layer,
theta, w, h, b, condition)
                    identifier -= 1

                    x1p -= ( reworkL / R )
                    k += 1
                    incrid += 1
                    list_fct = ()

##                  identifier -= 1
                list_fct += x1p, y1p, x1p + dx1p, y1p + dy1p
                plt.quiver(x1p, y1p, dx1p, dy1p, angles = 'xy', scale_units = 'xy', scale =1)

                ecriture(nameFile, lay, unit,z, identifier, list_fct,extension, k, same_layer, theta,
w, h, b, condition)

                incrid = 1
                x1p -= ( reworkL / R )
                list_fct = ()

            if x1p == a and direction == -1: # Last vector from direction = -1
```

```
                dx1p = - a
                identifier = 3
                list_fct += x1p, y1p, x1p + dx1p, y1p + dy1p
                plt.quiver(x1p, y1p, dx1p, dy1p, angles = 'xy', scale_units = 'xy', scale =1)
                ecriture(nameFile, lay, unit,z, identifier, list_fct,extension, k, same_layer, theta,
w, h, b, condition)

                x1p = 0
                y1p += h
                direction = 1
                k += 1
                list_fct = ()

        #######

            elif theta == 90:

                vari = 0
                top = vari

                x1p = 0
                y1p = 0 + vari
                dy1p = w
                dx1p = 0
                direction = 1
                incrid = 0
                interval = reworkL / R
                condition = a + incrid * interval #+ interval
                k = 1

                while 0 <= x1p < a:

                    identifier = 3
                    if direction == 1:

                        y1p = 0
                        dy1p = w

                        list_fct += x1p, y1p, x1p + dx1p, y1p + dy1p
                        plt.quiver(x1p, y1p, dx1p, dy1p, angles = 'xy', scale_units = 'xy', scale =1)
                        #print(x1p, "/", y1p, "/", x1p + dx1p, "/", y1p + dy1p, " / id = ", identifier)

                        direction = -1
                        x1p += h

                    elif direction == -1 and x1p < a:

                        y1p = w + vari
```

```
                dy1p = - w

                list_fct += x1p, y1p, x1p + dx1p, y1p + dy1p
                plt.quiver(x1p, y1p, dx1p, dy1p, angles = 'xy', scale_units = 'xy', scale =1)
                #print(x1p, "/", y1p, "/", x1p + dx1p, "/", y1p + dy1p, " / id = ", identifier)

                direction = 1
                x1p += h

        ecriture(nameFile, lay, unit,z, identifier, list_fct,extension, k, same_layer, theta, w,
h, b, condition)

        k += 1
        list_fct = ()

        rdm_var = 0

        while a <= x1p <= b:
           if condition <= x1p:

                if rdm_var != 0:
                   ecriture(nameFile, lay, unit,z, identifier, list_fct,extension, k, same_layer,
theta, w, h, b, condition)

                incrid += 1
                identifier += 1
                condition += interval
                list_fct = ()
                k += 1

           if direction == 1:

                y1p = 0
                dy1p = w
                list_fct += x1p, y1p, x1p + dx1p, y1p + dy1p
                plt.quiver(x1p, y1p, dx1p, dy1p, angles = 'xy', scale_units = 'xy', scale =1)

                direction = -1
                x1p += h
                rdm_var += 1

           else:

                y1p = w
                dy1p = - w

                list_fct += x1p, y1p, x1p + dx1p, y1p + dy1p
                plt.quiver(x1p, y1p, dx1p, dy1p, angles = 'xy', scale_units = 'xy', scale =1)
```

```
                direction = 1
                x1p += h
                rdm_var += 1


        rdm_var = 0

        while b < x1p <= L:

            if rdm_var == 0:
                ecriture(nameFile, lay, unit,z, identifier, list_fct,extension, k, same_layer, theta,
w, h, b, condition)
                list_fct = ()
                rdm_var = 10000

            condition = L
            identifier = R + 4

            if direction == 1:

                y1p = 0
                dy1p = w

                list_fct += x1p, y1p, x1p + dx1p, y1p + dy1p
                plt.quiver(x1p, y1p, dx1p, dy1p, angles = 'xy', scale_units = 'xy', scale =1)

                direction = -1
                x1p += h
                rdm_var += 1

            else:

                y1p = w
                dy1p = - w

                list_fct += x1p, y1p, x1p + dx1p, y1p + dy1p
                plt.quiver(x1p, y1p, dx1p, dy1p, angles = 'xy', scale_units = 'xy', scale =1)

                direction = 1
                x1p += h
                rdm_var += 1

        ecriture(nameFile, lay, unit,z, identifier, list_fct,extension, k, same_layer, theta, w,
h, b, condition)

        k += 1
        list_fct = ()
```

```
if strat == 2:

    X=[0,L,L,0,0]
    Xw =[a, b, b, a, a]
    if cylindre == 1:
        Y=[ vari , vari , vari + w, vari + w , vari ]
        Yw = [ vari , vari , vari + w, vari + w , vari ]
    else:
        Y = [0,0,w,w,0]

    Yw = [ vari , vari , vari + w, vari + w , vari ]

    plt.plot(X,Y)#, 'm')
    plt.plot(Xw,Y)#, 'c')
    plt.title("The engle is equal to {0} degrees, this is layer number {1}".format(theta,lay))
    plt.axis('equal')
    #plt.show() # Comment this line to hide the slicing diagram
    plt.close()

elif strat == 4:

    if cylindre == 1:
        X=[0,L,L,0,0]
        Y=[ vari , vari , vari + w, vari + w , vari ]
        Xw =[a, b, b, a, a]
        Yw = [ vari , vari , vari + w, vari + w , vari ]
    else:
        X=[0,L,L,0,0]
        Y=[ 0 , 0 ,  w, w , 0 ]
        Xw =[a, b, b, a, a]
        Yw = [ 0 , 0 ,  w, w , 0 ]

    plt.plot(X,Y)#, 'm')
    plt.plot(Xw,Yw)#, 'c')
    plt.title("The angle is equal to {0} degrees, this is layer number {1}".format(theta,lay))
    plt.axis('equal')
    #plt.show() # Comment this line to hide the slicing diagram
    plt.close()

if strat == 4:

    a = mid-(reworkL/2)
    b = mid+(reworkL/2)
    direction = 1

    if theta == 0 or theta == 180:
        x1p = 0
```

```
            if cylindre == 1:
                y1p = vari
            else:
                y1p = 0
            mid = L / 2
            dx1p = reworkL / 2
            dy1p = 0
            count = 0 # count < 2 to have 2 arrows per line

            while y1p  <= top : #w + vari:

                if direction == 1:

                    identifier = R5
                    x1p = a
                    dx1p = reworkL / 2

                    while count < 2:

                        list_fct += x1p, y1p, x1p + dx1p, y1p + dy1p
                        plt.quiver(x1p, y1p, dx1p, dy1p, angles = 'xy', scale_units = 'xy', scale =1)
                        #print(direction)
                        ecriture(nameFile, lay, unit,z, identifier, list_fct,extension, k, same_layer,
theta, w, h, b, condition)
                        x1p += dx1p
                        identifier += 1
                        k += 1
                        count += 1
                        list_fct = ()

                    y1p += h
                    direction = -1
                    count = 0

                if direction == -1 and y1p < top:

                    identifier = R6

                    x1p = b
                    dx1p = - reworkL / 2

                    while count < 2:

                        list_fct += x1p, y1p, x1p + dx1p, y1p + dy1p
                        plt.quiver(x1p, y1p, dx1p, dy1p, angles = 'xy', scale_units = 'xy', scale =1)
                        #print(direction)
                        ecriture(nameFile, lay, unit,z, identifier, list_fct,extension, k, same_layer,
theta, w, h, b, condition)
```

```
                    x1p = mid
                    identifier -= 1
                    k += 1
                    count += 1
                    list_fct = ()

                y1p += h
                direction = 1
                count = 0

        if theta == 90:

            x1p = a
            y1p = vari
            mid = L / 2
            condition = mid
            dx1p = 0
            dy1p = w
            count = 0 # count < 2 to have 2 arrows per line

            identifier = R5

            list_fct = zigzag(L, w, h, reworkL, theta, r, a, mid, divzone, lay, vari)
            ecriture(nameFile, lay, unit,z, identifier, list_fct,extension, k, same_layer, theta,
w, h, b, condition)

            k += 1

            identifier = R6

            mid2 = mid
            condition = mid + ( reworkL / 2 )
            list_fct = zigzag(L, w, h, reworkL, theta, r, mid2, b, divzone, lay, vari)
            ecriture(nameFile, lay, unit,z, identifier, list_fct,extension, k, same_layer, theta,
w, h, b, condition)

            k += 1
            x1p += h

    if strat == 4 and theta == 0 :

        if cylindre == 1:
            X=[0,L,L,0,0]
            Y=[ vari , vari , vari + w, vari + w , vari ]
            Xw =[a, b, b, a, a]
            Yw = [ vari , vari , vari + w, vari + w , vari ]
        else:
            X=[0,L,L,0,0]
```

```
            Y=[ 0 , 0 ,  w, w , 0 ]
            Xw =[a, b, b, a, a]
            Yw = [ 0 , 0 ,  w, w , 0 ]

        plt.plot(X,Y)#, 'm')
        plt.plot(Xw,Yw)#, 'c')
        plt.title("The angle is equal to {0} degrees, this is layer number {1}".format(theta,lay))
        plt.axis('equal')
        #plt.show() # Comment this line to hide the slicing diagram
        plt.close()

    zplus(nameFile,extension,z,e,R)
    z += e
    k = 1
    incrid = R5
    theta = theta + dtheta
    if theta >= 180:
        theta = theta - 180
    lay += 1

## ===== IF LAYER/3 !=/= 0

else:

    if cylindre == 1:
        w = abs(float(list_w[lay - l]))
        vari = (2*r-w)/2
    else:
        vari = 0
    a = 0    # beginning of the part
    b =  L/2   # middle of the part
    condition = b
    divzone = 0
    id_cst = 1

    list_fct = zigzag(L, w, h, reworkL, theta, r, a, b, divzone, lay, vari)
    ecriture(nameFile, lay, unit,z, id_cst, list_fct,extension, k, same_layer, theta, w, h, b,
condition)

    lay += 1
    zplus(nameFile,extension,z,e,R)
    z += e
    list_fct = ()
    theta = theta + dtheta
    if theta >= 180:
        theta = theta - 180
a = float(mid-(reworkL/2))
b =  float(mid+(reworkL/2))
```

```
    if cylindre == 0:
        vari = w
##    print(lay-1, layer)

n = 1
while n < R + 7:
    number = str(n)
    with open(nameFile + number + extension, 'a') as myFile:
        myFile.write("\n$$GEOMETRYEND")
        n += 1
```

9.1.2 Layering and file writing

```
# -*-coding:latin-1 -*

import os
import matplotlib.pyplot as plt
#import matplotlib
import numpy as np
from math import pi, radians, cos, sin, tan, floor, ceil

L = 100 # Part
w = 50
mid = L / 2
theta = 170 #degré

alpha = 180 - theta
reworkL = 30 #Probably no more than 2 mm
h = 1
j = 0
a = float(mid-(reworkL/2))
b =  float(mid+(reworkL/2))
X=[0,L,L,0,0]
Y=[0,0,w,w,0]
Xw =[a, b, b, a, a]
Yw = [0, 0, w, w, 0]

# ==== While Loop : creation of the list containing the length of each
#       layer

def view_slicing(r,i,j,k,list_coord):
    figure, axes = plt.subplots()
    c = plt.Circle( (0, 0 ), r, fill = False )

    while j <= k - 2:
        plt.plot(list_coord[i],list_coord[i+1])
        i += 2
        j += 1
```

```
    axes.add_artist( c )
    plt.axis('equal')
    #plt.show()
    plt.close()

def altern(r,x,y,dx,dy,h,reworkL):
    list_fct = []
    j = 0

    while y <= r:
        plt.quiver(x, y, dx, dy, angles = 'xy', scale_units = 'xy', scale = 1)
        list_fct.append(x)
        list_fct.append(y)
        list_fct.append(x+dx)
        list_fct.append(y+dy)
        y = y + h

        if y != r: # Avoid having an extra path outside the part
            plt.quiver(x+dx, y+dy, 0, dy+h, angles = 'xy', scale_units = 'xy', scale = 1)
            list_fct.append(x+dx)
            list_fct.append(y+dy)
            list_fct.append(x+dx)
            list_fct.append(y+dy+h)
        if j%2 != 0:
            x = a
            dx = reworkL
        else:
            x = b
            dx = - rework

    y = y + h
    #plt.quiver(a, i + h , reworkL, 0 , angles = 'xy', scale_units = 'xy', scale = 1)
    j += 1
    print(y)
    return(list_fct)

class return_values:
    def __init__(self,TheList,TheID):
        self.TheList = TheList
        self.TheID = TheID

def calcule_ID(list_fct, L, R, reworkL):
    identifier = 1
    a = 0
    b = ( L / 2 ) - ( reworkL / 2 )
    interval = reworkL / R
```

```
    if a <= list_fct[0] <= b and a <= list_fct[2] <= b: # If the vector is not in the rework zone
        identifier = 1

    else:

        a = b
        b = a + interval

        while identifier < R + 2:
            if  list_fct[0] > a and  list_fct[2] > b:
                a += interval
                b += interval
                identifier += 1
            elif a <= list_fct[0] <= b and a<= list_fct[2] <= b:
                break

    return(identifier)

def zplus(nameFile,extension,z,e,R):

    id_nb = 1
    z += e
    while id_nb < R + 7:
        with open(nameFile + str(id_nb) + extension, 'a') as myFile:
            myFile.write("\n$$LAYER/" + str(float(z))[:])

        id_nb += 1

def ecriture(nameFile, lay, unit,z, identifier, list_fct,extension, k, same_layer, theta, w, h, b,
condition):

##  A file per set of parameter -> with open(nameFile + '_' + identifier + extension, 'a') as
myFile
 #  Add  header as well (perhaps create the file in a loop, id from 1 to 12 id += 1

    vecalay = 0         # Number of vector per area per layer
    k = 0
    id_nb = str(int(identifier))
    last_line = ''

    if theta == 90:                                                  # We find the number of hatches
per area per layer
        try:
            xii = list_fct[0]
            while xii <= condition:
                xii += h
                vecalay += 1
```

```
        except IndexError:
            print('Value out of range')
            print(list_fct, lay, theta, identifier)

    else:
        vecalay = ceil(w/h) #len(list_fct)/4

    # Read the last line of the file

    with open(nameFile + id_nb + extension, 'r') as myFile:
        last_line = myFile.readlines()[-1]

    hatch = '$$HATCHES/' + str(identifier)[:] + str(int(len(list_fct)/4))

##    if last_line != hatch  :                          # If last line already contains hatch(es), we add
the new hatch(es) to the line
    if last_line[2] == 'H':
        #print('ERREUR') Next line led to error
        try:
            with open(nameFile + id_nb + extension, 'a') as myFile:
                #print('really')
                while k < len(list_fct):
                    myFile.write("," + str(list_fct[k]))
                    k += 1
        except PermissionError:
            return print('nameFile: ', nameFile, ', id_nb: ', id_nb, ', list_fct[k]: ', list_fct[k], 'k:', k, '
len(list_fct): ', len(list_fct));
    else:                                                 # Else we write $$HATCHES/id/vecalay
        with open(nameFile + id_nb + extension, 'a') as myFile:
            myFile.write("\n$$HATCHES/" + str(identifier)[:] + "," + str(int(vecalay)));
#str(int(len(list_fct)/4)))
            while k < len(list_fct):
                myFile.write("," + str(list_fct[k]))
                k += 1

def zigzag(L, w, h, reworkL, theta, r, a, b, divzone, lay, vari):

    alpha = 180 - theta
    mid = L / 2
    j = 0
##    a = int(mid-(reworkL/2))
##    b =  int(mid+(reworkL/2))
    X=[0,L,L,0,0]
    Y=[ vari , vari , vari + w, vari + w , vari ]
    Xw =[a, b, b, a, a]
    Yw = [ vari , vari , vari + w, vari + w , vari ]
    list_fct = []
```

```
    if 0 < theta < 90:
        V = w / sin(radians(theta)) # Norme vecteur jusqu'a dy = w
        D = (2 * h) / sin(radians(theta)) # Deplacement sur x
        adj = V * cos(radians(theta))
        x1 = - 10000 # Determine first value (issue with low angles)
        y1 = 0 + vari
        dx1 = adj #reworkL*cos(radians(theta))
        dx1p = dx1
        dy1 = w #reworkL*sin(radians(theta))

        while x1 <= b:
            if x1 < a and x1 + dx1 >= a: #Si début avant reworkL mais fin apres
                if x1 + dx1 <= b: #Si fin fleche avant fin reworkL
                    if j%2 == 0:
                        x1p = a
                        y1p = (x1p - x1)*tan(radians(theta)) + vari
                        dx1p = adj - a + x1 #(dx1 - x1) * sin(radians(theta))
                        dy1p = w - y1p + vari
                        plt.quiver(x1p,y1p,dx1p,dy1p, angles = 'xy', scale_units = 'xy', scale =1)
##                          print(j, " b4 up : ", x1p, "/", y1p, "/", dx1p, "/", dy1p)
                        list_fct += x1p, y1p, x1p + dx1p, y1p + dy1p
                        x1 += D
                        j += 1
                    else:
                        x1p = x1 + dx1
                        y1p = w + vari
                        dx1p = - (x1p - a) #(dx1 - x1) * sin(radians(theta))
                        dy1p = dx1p * tan(radians(theta))
                        plt.quiver(x1p,y1p,dx1p,dy1p, angles = 'xy', scale_units = 'xy', scale =1)
##                          print(j, " b4 down : ", x1p, "/", y1p, "/", x1p + dx1p, "/", y1p + dy1p)
                        list_fct += x1p, y1p, x1p + dx1p, y1p + dy1p
                        x1 += D
                        j += 1

                if x1 + dx1 >= b and x1 < a: #Si fin fleche apres reworkL
                    if j%2 == 0:
                        x1p = a
                        y1p = (x1p - x1)*tan(radians(theta)) + vari
                        dx1p = b - x1p
                        dy1p = (b - x1p) * tan(radians(theta))
                        plt.quiver(x1p,y1p,dx1p,dy1p, angles = 'xy', scale_units = 'xy', scale =1)
#                         print(j, " after up : ", x1, "/", y1, "/", x1 + dx1, "/", y1 + dy1)
                        list_fct += x1p, y1p, x1p + dx1p, y1p + dy1p
                        x1 += D
                        j += 1
                    else:
                        x1p = b
                        y1p = w - ((x1 + dx1 - b)*tan(radians(theta))) + vari
```

```
                dx1p = - (b - a)
                dy1p =  - (b - a) * tan(radians(theta))
                plt.quiver(x1p,y1p,dx1p,dy1p, angles = 'xy', scale_units = 'xy', scale =1)
#                 print(j, " after down : ", x1, "/", y1, "/", x1 + dx1, "/", y1 + dy1)
                list_fct += x1p, y1p, x1p + dx1p, y1p + dy1p
                x1 += D
                j += 1

        elif x1 >= a and x1 + dx1 <= b: # x1 & dx1 btw a & b
            if j%2 == 0:
                x1p = x1
                y1p = y1 #+ vari
                dx1p = dx1
                dy1p = dy1
                plt.quiver(x1p,y1p,dx1p,dy1p, angles = 'xy', scale_units = 'xy', scale =1)
##                 print(j, " norm up : ", x1, "/", y1, "/", x1 + dx1, "/", y1 + dy1)
                list_fct += x1p, y1p, x1p + dx1p, y1p + dy1p
                x1 += D
                j += 1
            else:
                x1p = x1 + dx1
                y1p = w + vari
                dx1p = - V * cos(radians(theta))
                dy1p = - w
                plt.quiver(x1p,y1p,dx1p,dy1p, angles = 'xy', scale_units = 'xy', scale =1)
##                 print(j, " norm down : ", x1, "/", y1, "/", x1 + dx1, "/", y1 + dy1)
                list_fct += x1p, y1p, x1p + dx1p, y1p + dy1p
                x1 += D
                j += 1
        elif x1 >= a and x1 + dx1 >= b: # Start before b, end after b
            if j%2 == 0:
                dx1p = b - x1
                dy1p = (b - x1) * tan(radians(theta))
                x1p = x1
                y1p = y1
                plt.quiver(x1p,y1p,dx1p,dy1p, angles = 'xy', scale_units = 'xy', scale =1)
##                 print(j, " after up: ", x1, "/", y1, "/", x1 + dx1, "/", y1 + dy1)
                list_fct += x1p, y1p, x1p + dx1p, y1p + dy1p
                x1 += D
                j += 1
            else:
                x1p = b
                y1p =  (b - x1) * tan(radians(theta)) + vari
                dx1p =  - (b - x1)
                dy1p = - (b - x1) * tan(radians(theta))
                plt.quiver(x1p,y1p,dx1p,dy1p, angles = 'xy', scale_units = 'xy', scale =1)
##                 print(j, " after down : ", x1, "/", y1, "/", x1 + dx1, "/", y1 + dy1)
                list_fct += x1p, y1p, x1p + dx1p, y1p + dy1p
```

```
                x1 += D
                j += 1
            else:
                x1 += D

    elif 90 < theta < 180:

        reworkL = (b - a)
        V = w / sin(radians(theta)) # Norme vecteur jusqu'a dy = w
        D = (2 * h) / sin(radians(theta)) # Deplacement sur x
        adj = V * cos(radians(theta))
        x1 = - 100000 # Determine first value (issue with low angles)
        y1 = 0 + vari
        dx1 = adj #reworkL*cos(radians(theta))
        dx1p = dx1
        dy1 = w #reworkL*sin(radians(theta))

        while x1 + dx1<= b: #x1 - (x1 - dx1) * sin(radians(alpha)) <= b :
            if x1 >= a and (x1 - a) * tan(radians(180 - theta)) <= w:
                if x1 >= b and dx1 <= a:
                    if j%2 == 0:
                        x1p = b
                        y1p = (x1 - b) * tan(radians(180 - theta)) + vari
                        dx1p = - reworkL
                        dy1p = reworkL * tan(radians(alpha))
                        plt.quiver(x1p, y1p, dx1p, dy1p, angles = 'xy', scale_units = 'xy', scale =1)
##                          print(j, " left1 up: ", x1, "/", y1, "/", x1 + dx1, "/", y1 + dy1)
                        list_fct += x1p, y1p, x1p + dx1p, y1p + dy1p
                        x1 += D
                        j += 1
                    else:
                        x1p = a
                        y1p = (x1 - a) * tan(radians(alpha)) + vari
                        dx1p = reworkL #(x1 - a)
                        dy1p =  - reworkL * tan(radians(alpha)) #- (x1 - a) * tan(radians(alpha))
                        plt.quiver(x1p, y1p, dx1p, dy1p, angles = 'xy', scale_units = 'xy', scale =1)
##                          print(j, " left1 down: ", x1, "/", y1, "/", x1 + dx1, "/", y1 + dy1)
                        list_fct += x1p, y1p, x1p + dx1p, y1p + dy1p
                        x1 += D
                        j += 1
                else:
                    if j%2 == 0:
                        dx1 = a - x1
                        dy1 = - (x1 - a) * tan(radians(theta))
                        plt.quiver(x1,y1,dx1,dy1, angles = 'xy', scale_units = 'xy', scale =1)
##                          print(j, " left2 up: ", x1, "/", y1, "/", x1 + dx1, "/", y1 + dy1)
                        list_fct += x1, y1, x1 + dx1, y1 + dy1
                        dy1 = w
```

```
                dx1  = adj
                x1 += D
                j += 1
            else:
                x1p = a
                y1p = (x1 - a) * tan(radians(alpha)) + vari
                dx1p = (x1 - a)
                dy1p =  - (x1 - a) * tan(radians(alpha))
                plt.quiver(x1p, y1p, dx1p, dy1p, angles = 'xy', scale_units = 'xy', scale =1)
##                  print(j, " left2 down: ", x1, "/", y1, "/", x1 + dx1, "/", y1 + dy1)
                list_fct += x1p, y1p, x1p + dx1p, y1p + dy1p
                x1 += D
                j += 1
        elif x1 >= a  and x1 <= b: #and x1 + dx1 <= b    x1 & dx1 btw a & b
            if j%2 == 0:
                dx1p = dx1
                plt.quiver(x1,y1,dx1p,dy1, angles = 'xy', scale_units = 'xy', scale =1)
##                  print(j, " norm up: ", x1, "/", y1, "/", x1 + dx1, "/", y1 + dy1)
                list_fct += x1, y1, x1 + dx1p, y1 + dy1
                x1 += D
                j += 1
            else:
                x1p = x1 + dx1
                y1p =  w + vari
                dx1p = - adj
                dy1p =  - w
                plt.quiver(x1p,y1p,dx1p,dy1p, angles = 'xy', scale_units = 'xy', scale =1)
##                  print(j, " norm down: ", x1, "/", y1, "/", x1 + dx1, "/", y1 + dy1)
                list_fct += x1p, y1p, x1p + dx1p, y1p + dy1p
                x1 += D
                j += 1
        elif x1 >= b:
            if j%2 == 0:
                x1p = b
                y1p =  - (x1 - b) * tan(radians(theta)) + vari
                dx1p = adj - b + x1
                dy1p = w - ( (x1 - b) * tan(radians(180 - theta)) ) #(b + dx1) * tan(radians(180 -
theta))
                plt.quiver(x1p, y1p, dx1p, dy1p, angles = 'xy', scale_units = 'xy', scale =1)
##                  print(j, " right up: ", x1, "/", y1, "/", x1 + dx1, "/", y1 + dy1)
                list_fct += x1p, y1p, x1p + dx1p, y1p + dy1p
                x1 += D
                j += 1
            else:
                x1p = x1 + dx1
                y1p =  w + vari
                dx1p =  b - x1p
                dy1p = - w + (x1 - b) * tan(radians(alpha)) #(b + dx1) * tan(radians(180 - theta))
```

```
            plt.quiver(x1p, y1p, dx1p, dy1p, angles = 'xy', scale_units = 'xy', scale =1)
##              print(j, " right down : ", x1, "/", y1, "/", x1 + dx1, "/", y1 + dy1)
            list_fct += x1p, y1p, x1p + dx1p, y1p + dy1p
            x1 += D
            j += 1
        else:
            x1 += D

##############################################

    else:
        reworkL = (b - a)
        y1 = 0 + vari
        if theta == 0:
            while y1  <= w + vari:
                if j%2 == 0:
                    x1p = a
                    y1p = y1
                    dx1p =  reworkL
                    dy1p = 0
                    plt.quiver(x1p, y1p, dx1p, dy1p, angles = 'xy', scale_units = 'xy', scale =1)
##                      print(j, "str8 0 paire : ", x1p, "/", y1p, "/", x1p + dx1p, "/", y1p + dy1p)
                    list_fct += x1p, y1p, x1p + dx1p, y1p + dy1p
                    y1 = y1 + h
                    j += 1
                else:
                    x1p = b
                    y1p = y1
                    dx1p =  - reworkL
                    dy1p = 0
                    plt.quiver(x1p, y1p, dx1p, dy1p, angles = 'xy', scale_units = 'xy', scale =1)
##                      print(j, " str8 0 impair : ", x1p, "/", y1p, "/", x1p + dx1p, "/", y1p + dy1p)
                    list_fct += x1p, y1p, x1p + dx1p, y1p + dy1p
                    y1 = y1 + h
                    j += 1
        elif theta == 180:
            while y1  <= w + vari:
                if j%2 != 0:

                    x1p = a
                    y1p = y1
                    dx1p =  reworkL
                    dy1p = 0
                    plt.quiver(x1p, y1p, dx1p, dy1p, angles = 'xy', scale_units = 'xy', scale =1)
    ##                  print(j, "str8 180 paire : ", x1p, "/", y1p, "/", x1p + dx1p, "/", y1p + dy1p)
                    list_fct += x1p, y1p, x1p + dx1p, y1p + dy1p
                    y1 = y1 + h
                    j += 1
```

```
            else:
                x1p = b
                y1p = y1
                dx1p =  - reworkL
                dy1p = 0
                plt.quiver(x1p, y1p, dx1p, dy1p, angles = 'xy', scale_units = 'xy', scale =1)
##                  print(j, " str8 180 impair : ",x1p, "/", y1p, "/", x1p + dx1p, "/", y1p + dy1p)
                list_fct += x1p, y1p, x1p + dx1p, y1p + dy1p
                y1 = y1 + h
                j += 1

        elif theta == 90:

            V = w / sin(radians(theta)) # Norme vecteur jusqu'a dy = w
            D = (2 * h) / sin(radians(theta)) # Deplacement sur x
            adj = V * cos(radians(theta))
            x1 = a # Determine first value (issue with low angles)
            y1 = 0 + vari
            dx1 = adj #reworkL*cos(radians(theta))
            dx1p = dx1
            dy1 = w #reworkL*sin(radians(theta))

            while x1 <= b:
                if x1 == a and divzone == 1:
                    pass
                else:
                    if j%2 == 0:

                        x1p = x1
                        y1p = y1
                        dx1p = 0
                        dy1p = w
                        plt.quiver(x1p, y1p, dx1p, dy1p, angles = 'xy', scale_units = 'xy', scale =1)
                        list_fct += x1p, y1p, x1p + dx1p, y1p + dy1p
##                          print(j, " 90 paire : ", x1p, "/", y1, "/", x1p + dx1p, "/", y1 + dy1p)
##                          j += 1

                    else:

                        x1p = x1
                        y1p = w + vari
                        dx1p = 0
                        dy1p = - w

                        plt.quiver(x1p, y1p, dx1p, dy1p, angles = 'xy', scale_units = 'xy', scale =1)
                        list_fct += x1p, y1p, x1p + dx1p, y1p + dy1p
##                          print(j, " 90 impaire : ", x1p, "/", y1, "/", x1p + dx1p, "/", y1 + dy1p)
```

```
##              print('     ', x1, ' ', b, ' ', divzone, ' ', ( 2*r - w ) / 2)
            j +=1
            x1 += h

    plt.plot(X,Y)
    plt.plot(Xw,Yw)
    plt.title("The angle is equal to {0} degrees, this is layer number {1}".format(theta,lay))
    plt.axis('equal')
    #plt.show() # Comment this line to hide the slicing diagram
    plt.close()

    if divzone == 0:
        return(list_fct)
    else:

        a = 0
        b = ( L / 2 ) - ( reworkL / 2 )
        interval = reworkL / R

        if a <= list_fct[0] <= b and a <= list_fct[2] <= b: # If the vector is not in the rework zone
            identifier = 1

        elif ((L / 2) + ( reworkL / 2 )) <= list_fct[0] <= L and ((L / 2) + ( reworkL / 2 )) <= list_fct[2]
<= L:
            identifier = R + 1

        else:

            a = b
            b = a + interval

            while identifier < R + 2:
                if  list_fct[0] > a and  list_fct[2] > b:
                    identifier += 1
                    a += interval
                    b += interval
                elif a <= list_fct[0] <= b and a<= list_fct[2] <= b:
                    identifier += 1
                    break
        t = return_values(list_fct,identifier)
        return(t)
    identifier = 1
```